A COMPREHENSIVE APPROACH FOR WAVEFIELD-BASED CHARACTERIZATION OF ULTRASONIC SHEAR WAVE SCATTERING IN PLATES

A Dissertation
Presented to
The Academic Faculty

By

Yu Weng

In Partial Fulfillment
of the Requirements for the Degree
Doctor of Philosophy in the
School of Electrical and Computer Engineering

Georgia Institute of Technology

May 2018

A COMPREHENSIVE APPROACH FOR WAVEFIELD-BASED CHARACTERIZATION OF ULTRASONIC SHEAR WAVE SCATTERING IN PLATES

Approved by:

Dr. Jennifer E. Michaels, Advisor
School of Electrical and Computer Engineering
Georgia Institute of Technology

Dr. Aaron D. Lanterman
School of Electrical and Computer Engineering
Georgia Institute of Technology

Dr. Ying Zhang
School of Electrical and Computer Engineering
Georgia Institute of Technology

Dr. Karim Sabra
School of Mechanical Engineering
Georgia Institute of Technology

Dr. Massimo Ruzzene
School of Aerospace Engineering
Georgia Institute of Technology

Date Approved: March 29, 2018

To my parents,

Yanheng and Ying,

for their unconditional and endless love throughout my life.

ACKNOWLEDGEMENTS

I would like to firstly express my appreciation and gratitude to my advisor, Dr. Jennifer E. Michaels for her continuous teaching, guidance, and support throughout my Ph.D. journey. It is absolutely my luck to be not only one of her students but the last one. I am impressed and significantly influenced by her meticulous attitude to the academic research and positivity to the daily life. I would also like to thank Dr. Thomas E. Michaels. I learn a lot how to be a better man from both his sayings and actions.

Secondly, thank you to all of the other committee members, Dr. Ying Zhang, Dr. Aaron D. Lanterman, Dr. Karim Sabra, and Dr. Massimo Ruzzene, for their time and efforts.

Thirdly, thank you to all of my colleagues and friends in the QUEST Laboratory. It is absolutely a treasured experience to work with Dr. Xin Chen, Dr. Alexander Dawson, Joe Kummer, Dr. Westin Williams, Dr. Hongye Liu, Carson Maki, and Dr. Jiadong Hua. Thank all of you for each talk and discussion on both technical and personal matters. Particularly, I would like to thank Westin for our wonderful friendship these years. I benefit a lot from our deep talks and discussions. With his care and company, my life becomes more colorful.

I especially appreciate the first teachers in my life. They are my incredibly amazing parents Mr. Yanheng Weng and Mrs. Ying Li. Studying abroad is undoubtedly an unforgettable experience in my life. At the same time, it is also truly a challenge for both my parents and me because of the long-time and long-distance separation. Without their unconditional love, support, understanding, and beliefs, I cannot be myself, finish my Ph.D. degree, and continue to pursue my dreams.

Lastly but not least, I sincerely thank my best friends Zhao Liu and Xiaoyi Li for their endless love and support. Even though we are far away with each other geographically, our hearts are even much closer.

The presented research was sponsored by the Air Force Research Laboratory (AFRL) under Contract Nos. FA8650-10-D-5210 and FA8650-15-D-5231. I would like to thank

the program manager, Dr. Eric Lindgren.

TABLE OF CONTENTS

LIST OF TABLES

LIST OF FIGURES

SUMMARY

This thesis presents a comprehensive approach for characterizing and quantifying the scattering of angle-beam ultrasonic shear waves with a variety of scatterers in plates. The motivation behind analyzing angle-beam shear wave propagation and scattering is to obtain a deep understanding of shear wave interaction with defects and improve the reliability and accuracy of actual inspection techniques for NDE applications. The scatterers investigated here include through-holes, part-through holes, and notches emanating from through-holes. Scattering from both through-holes and notches, aimed to mimic actual ultrasonic defects in practice, is particularly meaningful to the aerospace industry because crack-like defects usually grow from fastener holes, which presents a potential hazard to the aging aircraft components if undetected.

In general, two main research contributions are the acquisition of a comprehensive set of wavefield data in a variety of scattering scenarios via wavefield imaging and a reliable systematic methodology on ultrasonic shear wave scattering estimation. In terms of experimental wavefield data, a laser-based sensing technique was applied to an angle-beam inspection system. A laser Doppler vibrometer was used to measure the out-of-plane wave motion resulting from a fixed transmitting angle-beam probe (transducer+wedge) on the surface of a specimen. The obtained wavefield data sets include through-holes with various hole diameters and fill conditions, part-through holes with different hole depths, and quarter-circle notches emanating from through-holes with several notch lengths using different angle wedges aiming at various points.

The presented research develops a complete set of signal processing techniques, which include temporal and spatial windowing, spatial anti-aliasing, directional filtering, wavefield baseline subtraction, phase velocity filtering, dynamic ray tracing analysis, time-space windowing, and incident wave subtraction, for the sake of characterizing shear wave scattering from various scatterers. In terms of extracting waves of interest, directional filters are

effective to extract waves based on their propagation direction ranges. Phase velocity filters are useful to separate Rayleigh, shear, and longitudinal waves according to their respective phase velocity ranges. Although both filters have been previously applied to guided ultrasonic waves, their application and implementation for bulk waves are novel. Dynamic ray tracing analysis allows accurately tracking scattered waves directly in the time-space domain. Incident wave subtraction is particularly helpful for complicated scattering problems (e.g., compound scatterers) to remove unwanted incident waves by utilizing the current wavefield data itself instead of wavefield baseline subtraction. These signal processing techniques are quite general in nature and it is anticipated that they can be applied into a much wider variety of ultrasonic scattering problems.

Depending upon the proposed signal processing techniques, multiple methods for characterizing and quantifying shear wave scattering are performed. Scattering is characterized in both the frequency-wavenumber and time-space domains. The scattering patterns in both domains are described as energy versus direction curves. In the frequency-wavenumber domain, four methods, which combine two directions (observer direction and propagation direction) and two perspectives of characterizing scattered energy (energy of the residual wavefield and energy comparison), are presented. In the time-space domain, scattered waves caused by specific incident shear waves can be directly extracted and quantified by time-space windowing, which provides a group of time-dependent energy curves. This method is particularly useful because it is effective to show how scattered energy distributes at a specific time and how scattering evolves as time progresses. All methodologies presented in this thesis are reliable to show useful scattering information. The method efficacy and all results are discussed in detail and recommendations are made for future work.

CHAPTER 1
INTRODUCTION

Nowadays, periodic inspection has become important and necessary in many industries under the consideration of safety and cost. In particular, in the aerospace industry, periodic inspection of aircraft components is aimed to guarantee that fatigue cracks are detected in advance of failures in these aging structures. Motivated by the industry need, the objective of this thesis is to study ultrasonic shear wave scattering in plates. Two main research goals are proposed. One is to obtain experimental wavefield data by a combination of angle-beam inspection techniques and wavefield imaging. The other one is to characterize and quantify ultrasonic shear wave scattering. Research contributions summarize the improvements as compared to prior work by previous colleagues and other researchers. The thesis structure of the remaining chapters is described at the end.

1.1 Background and Motivation

Over the past 35 years, nondestructive evaluation (NDE), as a technology of testing, examining, or evaluating the properties of a given material, component or system without causing damage, has been significantly growing in terms of uniqueness and innovation [1]. Ultrasonic NDE, which uses ultrasonic waves, has become a valuable method for determining material characteristics and detecting defects in structures. S. Y. Sokolov, often hailed as the father of ultrasonic testing, firstly described the concept of ultrasonic waves for detecting discontinuities in metals in the late 1920s [1]. D. O. Sproule introduced the first ultrasonic flaw detector using pulse-echo in 1942 [1]. Nowadays, ultrasonic NDE has been widely used in virtually every major industry because ultrasonic waves can effectively penetrate into materials and quickly provide high-sensitivity results. In the field of ultrasonic NDE, one primary research focus is characterization and quantification of scattering

from specific types of damage. For example, in the aerospace industry, periodic inspection of aircraft components is needed for the sake of safety and cost. In fact, fatigue cracks usually emanate from fastener holes and present a potential hazard to these aging structures. Therefore, ultrasonic NDE of both fastener holes and notches is of practical interest.

Motivated by the industry need, this research investigates methodologies of scattering characterization and quantification. This thesis utilizes angle-beam technique [2], which uses oblique ultrasonic bulk waves to impinge upon the specimen at a desired angle. Here, angle-beam shear waves, generated by a longitudinal piezoelectric transducer and an angled acrylic wedge, penetrate into an aluminum plate. Scatterers presented in this thesis are through-holes, part-through holes, and notches, which aim to simulate defects in reality. The scattering analysis is valuable and meaningful to enrich ultrasonic scattering knowledge, strengthen the understanding of both the incident wave propagation process and scattering interactions with plate-like structures and scatterers, help simulated model validation, and further aid the reliability and accuracy of actual inspection methods.

1.2 Research Goals

The general purpose of this research is to characterize ultrasonic shear wave scattering from different scatterers in aluminum plates. This thesis focuses on three types of scatterers, which include through-holes, part-through holes, and notches emanating from through-holes. For each type, various scattering scenarios are discussed. For through-hole scattering, both hole diameter and fill condition are investigated. For part-through holes, scattering under different hole depths is analyzed. Damaged holes with notches are aimed to simulate actual cracks growing from fastener holes. This thesis focuses on how notch length, probe configuration, and wedge angle affect notch scattering. Here, two specific research goals are proposed to reach the targets. The first is experimental wavefield data acquisition in a variety of scattering scenarios described previously by a combination of angle-beam inspection techniques and wavefield imaging. The second one is to develop ef-

fective signal processing techniques and scattering characterization methodologies in both the frequency-wavenumber and time-space domains to characterize shear wave scattering and provide quantitative scattering information in detail.

1.3 Contributions

The main focus of this thesis is wavefield-based characterization of ultrasonic shear wave scattering from various scatterers of interest. Generally, both the obtained experimental wavefield data and the provided scattering analysis methods are invaluable and vital for getting more insights of bulk wave propagation process inside the plate-like structures and scattering behaviors as scatterers become more complex. Specifically, the first contribution is the acquisition of a comprehensive set of data as shown in wavefield snapshots of area scans, which is a straightforward and vivid means of visualizing both incident and scattered waves caused by different scatterers. Even before any methods and analyses, the obtained wavefield videos of the raw data provide instructive information such as when the scattering of interest occurs and where the subsequent scattered waves propagate with time.

The second contribution is a comprehensive set of signal processing technique, aimed to extract waves of interest. In terms of the obtained wavefield data, directional filtering is robust enough to extract specific waves based on any given angle ranges of propagation directions. Phase velocity filtering is effective to separate Rayleigh, shear, and longitudinal waves from total wavefields based on their respective phase velocity ranges. Even though both directional filtering and phase velocity filtering have been previously applied to guided ultrasonic waves, their application and implementation for bulk waves are novel. Dynamic ray tracing analysis is a new technique, which allows accurately tracking scattered waves caused by a specific incident wave in the time-space domain for all scatterers researched here. Incident wave subtraction, which combines directional filtering and spatial windowing, is powerful to remove unwanted incident waves by utilizing the current wavefield data itself instead of wavefield baseline subtraction. This technique is especially

useful for complex situations where either acquisition of damage-free baseline wavefields are not available or the baseline wavefields are not well time-space aligned to the current wavefields. All of the developed signal processing techniques are quite general in nature. It is anticipated that they can be applied to a much wider variety of ultrasonic scattering problems.

The third contribution of this thesis is comprehensively developing and comparing multiple methodologies for quantifying scattering in both the frequency-wavenumber and time-space domains. In the frequency-wavenumber domain, four methods are presented to characterize and quantify scattering by accumulating all scattered energy, each of which leads to a single scattering pattern of energy versus direction curves. The obtained scattering profiles are generally consistent and complementary if interpreted properly. However, such patterns cannot explain how waves are scattered by a specific incident shear wave and how scattering evolves as time progresses, which motivates the development of scattering characterization directly in the time-space domain. Based on dynamic ray tracing, time-space windowing is developed to extract and quantify scattered wavefronts caused by a specific incident shear wave in the time-space domain. A group of time-dependent energy curves completely show how scattered energy distributes and how scattering of interest changes with time.

1.4 Thesis Structure

The structure of the remaining chapters is organized as follows. Chapter 2 presents a literature review of the main topics related to this research in terms of ultrasonic nondestructive evaluation, angle-beam inspection, ultrasonic wavefield imaging, ultrasonic wavefield signal processing, and ultrasonic scattering. Chapter 3 introduces experimental procedures for angle-beam wavefield data acquisition and summarizes experiments of three types of scatterers: through-holes, part-through holes, and notches. Chapter 4 describes signal processing techniques in both the frequency-wavenumber and time-space domains, which are

the fundamental and useful tools applied to process and analyze the obtained wavefield data. In particular, a complete set of ray tracing analyses for pristine plates, through-holes, part-through holes, and notches is not only beneficial to build time-space filters for scattering characterization but also vital to get a deeper understanding of shear wave propagation between two plate surfaces and interaction with scatterers of interest. Chapter 5 provides specific scattering characterization methods in both the frequency-wavenumber and time-space domains. Chapter 6 summarizes quantification results and discuss efficacy of each provided method. Chapter 7 concludes remarks in this thesis and presents recommendations for future work.

CHAPTER 2
LITERATURE SURVEY

This literature survey introduces the fundamental background of nondestructive evaluation (NDE), ultrasonic NDE, angle-beam inspection, ultrasonic wavefield imaging, ultrasonic wavefield signal processing, and ultrasonic scattering in relation to this thesis. Section 2.1 provides an overview of NDE, which includes the definition and objectives of this technology and main testing methods in applications. Section 2.2 discusses types of ultrasonic waves and wave propagation fundamentals. Section 2.3 describes angle-beam probes and inspection techniques, which are used to angle-beam inspection techniques. Section 2.4 focuses on ultrasonic wavefield measurements and wavefield imaging. Section 2.5 introduces the 3-D Fourier transform and related frequency-wavenumber analysis techniques. In addition, this chapter reviews research efforts related to ultrasonic scattering from cylindrical holes and notches presented in Section 2.6. Lastly, a brief review in the context of the prior work using angle-beam inspection techniques in aluminum plates is summarized and research objectives of the present work are outlined in Section 2.7.

2.1 Overview of NDE

"Nondestructive evaluation (NDE) is the examination of an object with technology that does not affect the object's future usefulness", which is the definition of NDE provided by the American Society of Nondestructive Testing [3]. In general, for a testing object, three questions need to be answered: whether there is a defect and if yes, where the defect is and what its properties are, such as size, shape, and type. That is, NDE mainly focuses on detection, localization, and characterization of defects or flaws. The most widely used methods are visual testing, penetrant testing, magnetic particle testing, radiographic testing, ultrasonic testing, eddy current testing, thermal infrared testing, acoustic emission testing,

electromagnetic testing, and vibration analysis [1, 4]. In particular, ultrasonic testing is one of the most frequently used NDE methods because for many applications ultrasonic NDE is more sensitive, robust, and economical for inspecting a wide range of materials and structures as compared to other methods [5].

2.2 Ultrasonic NDE

In the NDE community, ultrasonic waves, which are mechanical waves with frequencies above the human-detectable limit ($\sim$20 kHz), have become critically important for characterization of material properties and defects. Because ultrasonic waves are sensitive to both surface and subsurface discontinuities, ultrasonic NDE plays a significant role in a wide range of industries (e.g., aerospace, transportation, and fabrication industries) [3, 4]. The fundamental theory of ultrasonic wave propagation in infinite, homogenous, isotropic, and elastic solids was established and developed in the 19^{th} century. In general, there are two types of ultrasonic waves: bulk waves, which propagate in bulk media, and guided waves, which are guided along interfaces. Nowadays, as NDE technologies grow and develop, both types of ultrasonic waves are applied to the NDE of engineering systems.

2.2.1 Types of Ultrasonic Waves

In general, both ultrasonic bulk waves and guided waves can propagate in gases, fluids, or solids. However, they are different in the nature of wave propagation. Unlike guided waves, which require boundaries for propagation, bulk waves propagate in infinite media without the influence of boundaries [6]. In addition, because bulk waves are nondispersive, the nature of the wave propagation process is relatively easy to understand. Moreover, ultrasonic bulk waves propagate within materials in three-dimensional space so that they are sensitive to defects and discontinuities both near surfaces and deep within the material. Specifically, there are two modes of bulk waves in a solid medium: shear (transverse) and longitudinal (compressional) [3]. In the shear wave mode, particle motion is perpendicular to the

direction of wave propagation resulting from an associated linear, elastic, shear stress. In addition, according to the polarization relative to a planar surface, shear waves are classified into shear-horizontal and shear-vertical waves [6]. In the longitudinal mode, particle motion is parallel to the propagation direction with the stress of the periodic compression and tension.

The interaction of shear and longitudinal waves with boundaries of a medium leads to ultrasonic guided waves. According to the boundary conditions, guided waves are generally categorized into five types: Rayleigh [7], Lamb [8], Stoneley [9], Scholte [10], and Love waves [11]. Rayleigh waves, sometimes also called surface waves, travel along a boundary between a semi-infinite solid medium and a vacuum; Lamb waves, sometimes also called plate waves, propagate in a solid plate or layer with free boundaries; Stoneley waves travel at the interface between two solid media; Scholte waves propagate on a water-solid interface; Love waves occur in a layer bonded to a half-surface. In current ultrasonic NDE research, guided waves have become one active subject for inspection purposes. For example, Rayleigh waves are sensitive to detect surface-breaking defects such as [12, 13] because they can travel along single free surfaces. In particular, Lamb waves are used in flaw detection such as [14, 15] because they can travel over long distances with little energy loss. However, Lamb waves are dispersive, which means both group and phase velocities are functions of the frequency rather than constants. Two Lamb wave modes (symmetrical and anti-symmetrical modes) have to be taken account and each mode has different dispersion curves, which can be found in [16].

2.2.2 Fundamentals of Ultrasonic Wave Propagation

Regardless of the type of ultrasonic wave, propagating waves in elastic solids lead to particle displacements, which are expressed by a three-dimensional vector,

$$\mathbf{u} = \begin{bmatrix} u_x(x,y,z,t) \\ u_y(x,y,z,t) \\ u_z(x,y,z,t) \end{bmatrix}. \tag{2.1}$$

Here, u_x, u_y, and u_z refer to particle displacements along the x, y, and z axes, respectively. Each displacement is described as a function of three-dimensional space (x, y, z) and time t. In a homogenous, isotropic, and elastic medium, propagating elastic waves obey the elastodynamic wave equation,

$$\frac{\partial^2 \mathbf{u}}{\partial t^2} = c_l^2 \bigtriangledown \big(\bigtriangledown \cdot \mathbf{u} \big) - c_s^2 \bigtriangledown \times \big(\bigtriangledown \times \mathbf{u} \big), \tag{2.2}$$

where c_s and c_l are shear and longitudinal wave speeds, respectively. The velocities of both waves largely rely on the properties of bulk materials. Given the density of isotropic materials, ρ, and the $Lam\acute{e}$ constants, λ and μ, which describe the stress-strain relation, propagation velocities of shear and longitudinal waves are calculated by,

$$c_s = \sqrt{\frac{\mu}{\rho}}, \tag{2.3}$$

and,

$$c_l = \sqrt{\frac{\lambda + 2\mu}{\rho}}, \tag{2.4}$$

respectively. As can be seen from equations above, longitudinal waves always propagate faster than shear waves in the same medium.

A plane wave solution for an infinite medium can be obtained based on the elastic wave equation of Eq. (2.2). The resulting displacement becomes a harmonic function,

$$\mathbf{u}\big(\mathbf{x}, t\big) = \boldsymbol{A} \cos\big(\omega t - \mathbf{k} \cdot \mathbf{x}\big), \tag{2.5}$$

where the vector $\boldsymbol{A}$ is the magnitude, ω is the angular frequency, and $\mathbf{k}$ is the 3-D wavenumber vector [17]. The propagation direction is the direction of the wavenumber vector, which is,

$$\mathbf{k} = \begin{bmatrix} k_x \\ k_y \\ k_z \end{bmatrix}, \tag{2.6}$$

where k_x, k_y, and k_z are components of $\mathbf{k}$ along the x, y, and z axes. The magnitude of the wavenumber vector is related to the angular frequency ω and the wave speed c calculated by the well-known relation,

$$|\mathbf{k}| = \frac{\omega}{c}, \tag{2.7}$$

where c is either the shear wave speed c_s or the longitudinal wave speed c_l. The angular frequency is related to the temporal frequency f by,

$$\omega = 2\pi f. \tag{2.8}$$

2.3 Angle-Beam Inspection

When using bulk waves, the angle-beam technique is one common NDE method to detect, localize, and characterize a variety of defects. Here, "angle-beam" means bulk waves that penetrate into a specimen at an oblique angle. Unlike normal incidence, which utilizes transducers to transmit a wave normal to an exposed surface, angle-beam inspection uses angle-beam probes to generate a transmitted wave propagating at a desired angle.

2.3.1 Angle-Beam Probe

An angle-beam probe consists of a piezoelectric transducer, which generates incident longitudinal waves, and an acrylic wedge, which refracts those incident waves with an expected angle at the wedge-specimen interface. Depending on the wedge angle, both refracted longitudinal and shear waves can be generated in the specimen. As shown in Figure 2.1(a), θ_i refers to the angle of the incident longitudinal wave, and θ_{rs} and θ_{rl} refer to the refracted shear and longitudinal angles, respectively. Based on Snell's law, the refracted angles are calculated by,

$$\frac{\sin\theta_i}{c_i} = \frac{\sin\theta_{rs}}{c_{rs}} = \frac{\sin\theta_{rl}}{c_{rl}}, \tag{2.9}$$

where c_i is the wave speed of the incident longitudinal wave, and c_{rs} and c_{rl} are the refracted shear and longitudinal wave speeds, respectively. As mentioned in Section 2.2.2, c_{rl} is always larger than c_{rs} in the same medium, so θ_{rl} is also larger than θ_{rs} based on this equation. Although Eq. (2.9) is the general relation, the incident angle determines the refracted wave types. As the incident angle increases, both the longitudinal and shear refracted angles will increase. When the refracted angle of the longitudinal wave firstly reaches 90°, the incident angle is called the first critical angle. If the incident angle increases more until the refracted shear angle is 90°, the incident angle is defined as the second critical angle. In practice, angle probes are manufactured with various angle wedges to generate longitudinal, shear, and/or Rayleigh waves [2]. If the angle of the probe is chosen less than the first critical angle, both refracted longitudinal and shear waves are present as shown in Figure 2.1(b); if the probe angle is between the first and second critical angles, then only mode-converted shear waves penetrate into the specimen shown in Figure 2.1(c); if the probe angle is designed more than the second critical angle, only Rayleigh waves are remaining as shown in Figure 2.1(d). In practice, because of beam spread, there are not abrupt cutoffs between these ranges.

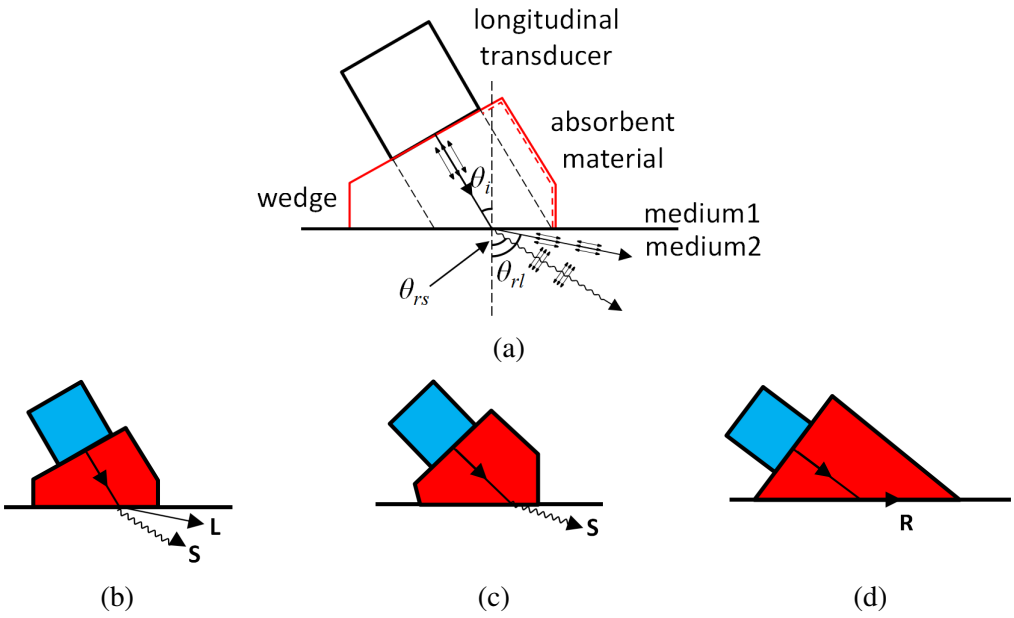

Figure 2.1: (a) Diagram of an angle-beam probe that consists of a longitudinal transducer and an acrylic wedge. Angle-beam probes for generating (b) longitudinal, (c) shear, and (d) Rayleigh waves.

This thesis utilizes a shear-wave probe designed at an expected wedge angle between the 1st and 2nd critical angles, which refract primary oblique shear waves into a specimen. In practice, probe angles of 45°, 60°, and 70° in steel are commonly used [18]. In this thesis, a probe of 60° is the one mainly used to generate shear waves, which results in a nominal refracted angle of 56.8° in aluminum, but both 45° and 70° wedges are also utilized. The top and side wedge surfaces are fabricated with plastic absorbent material, marked in red in Figure 2.1(a), to minimize the internally reflected waves inside the wedges leaking into a given material of interest. To enable transmission of ultrasonic waves across the transducer-wedge and wedge-specimen interfaces, an ultrasonic couplant is applied to both interfaces. Then, the incident beam of shear waves propagates around the nominal refracted angle into the specimen under test. Such waves are then reflected by the surfaces of the specimen.

2.3.2 Inspection Techniques

Most ultrasonic inspection applications utilize a transducer that transforms a voltage signal into an ultrasonic wave transmitted into a specimen. The wave travels through the specimen, responding to its geometry and material properties. The wave signal can be measured by either the original transducer (pulse-echo mode) or a different transducer (pitch-catch mode) [3]. As shown in Figure 2.2(a), because pulse-echo mode employs a single transducer that acts both the transmitter and receiver, only waves scattered back to the same transducer location are likely to be detected [19]. Based on the pulse-echo configuration, both monolithic transducers [20, 21] and phased array probes [22, 23, 24] are commonly used for ultrasonic defect detection. Unlike the pulse-echo mode, the pitch-catch mode uses separate transmitting and receiving transducers as shown in Figure 2.2(b). Thus, the receiver can be placed at an arbitrary location and orientation relative to the transmitter, which may measure both forward- and backward-scattered waves [25]. Regardless of mode, the measured signal is then transformed back into an electrical signal and displayed on an oscilloscope or otherwise recorded. This observed signal of the wave response at a specific location is used for detecting the presence of a defect, and its size, shape, and position [3]. In addition, the measured location can be extended from a single point to a two-dimensional space, which leads to an image of wave reflection and interaction with scatterers in the testing object. The format of this wave representation is also called as C-scans, which is usually used to localize defects in a variety of materials [26, 27].

2.4 Ultrasonic Wavefield Imaging

Ultrasonic wavefield imaging is an effective technique to visualize ultrasonic wave propagation and scattering on the surface of a specimen using a laser-based system. Both a scanning laser Doppler vibrometer (LDV) [28] and a scanning air-coupled ultrasonic transducer (AUT) [29] play a critical role in ultrasonic wavefield measurements. Depending

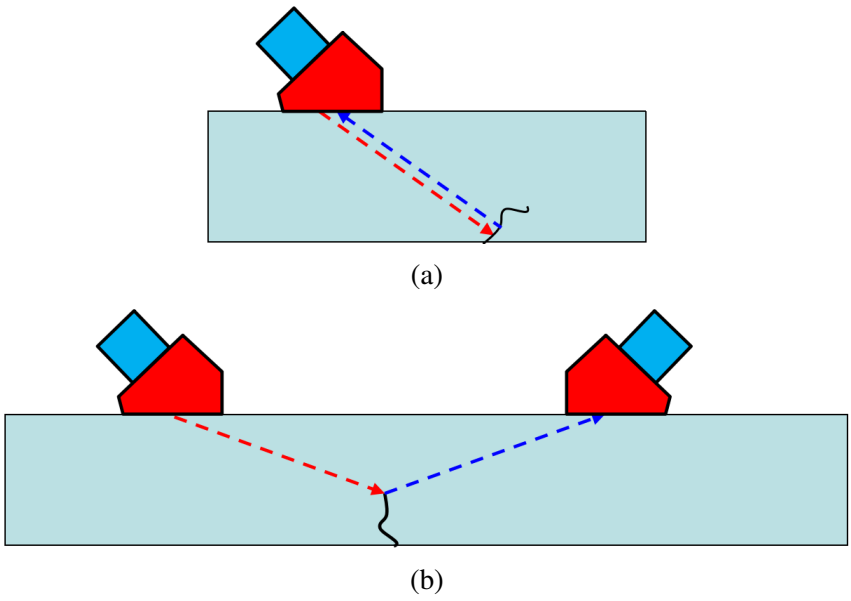

(a)

(b)

Figure 2.2: Diagram of probe placement using (a) pulse-echo and (b) pitch-catch modes.

on the use of lasers, either laser-based excitation or laser-based sensing technique can be applied to ultrasonic wave inspection systems. Laser-based excitation technique utilizes an excitation laser activated by a trigger signal to generate short pulses of high intensity to a specimen with a fixed scanning AUT to sense wave vibration on the surface. Flynn $et\ al.$ [30] used a scanning Q-switched laser system to excite the guided waves and a single fixed ultrasonic transducer to sense. Takatsubo $et\ al.$ [31] developed a measurement system that generates excitation ultrasonic signals by pulsed laser scanning and detects the propagation signals on a 3-D object by a reception transducer attached at a fixed point. In contrast, laser-based sensing technique uses a scanning LDV to sense wave motion resulting from a fixed transmitting AUT. Fukushima $et\ al.$ [32] evaluated the performance of a LDV for ultrasonic waveform measurements. Flynn $et\ al.$ [33] showed full-field ultrasonic steady-state response by a 2-D scanning LDV to the ultrasonic excitation from a piezoelectric transducer. In fact, based on the linear reciprocity in laser ultrasound, laser-based excitation and laser-based sensing techniques are equivalent. This thesis applies the laser-based sensing technique to measure wavefronts and visualize wave propagation on the exposed surface from a fixed transmitting transducer. A 2-D scanning LDV, as a moving receiver, is utilized

with repeated excitation waves to capture signals point by point over a 2-D rectilinear grid. Details of the measurement system can be found in the previous study [34].

Thanks to the availability of laser Doppler vibrometers, wave motion on the accessible surface of a specimen resulting from a spatially-fixed ultrasonic transducer is able to be effectively measured and recorded as a format of amplitude waveform signals of time, which allows to acquire full wavefield data over a two-dimensional rectilinear area of interest by wavefield imaging. The obtained wavefield data, formed in a three-dimensional format (time and two spatial dimensions) can be played as a wavefield video of time, which provides invaluable quantitative information of wave propagation and scattering process within the scan area. As a result, ultrasonic wavefield imaging has been widely used in a variety of research scenarios [35, 36].

There are many published wavefield imaging studies using both guided waves and bulk waves. Ultrasonic guided wavefield imaging has been a powerful research tool to determine propagation characteristics in various materials. Algernon $et\ al.$ [37] visualized surface wave propagation in concrete specimens. Rogge $et\ al.$ [38] investigated guided wave interaction in composites. Scales $et\ al.$ [39] studied ultrasonic wave propagation in heterogeneous media. In addition, wavefield imaging has been commonly applied into detect a variety of defects, such as impact damage [40, 41], cracks [42, 43], delaminations [44, 45], and corrosion [46, 47]. Compared to wavefield imaging research efforts of guided waves, the published work for wavefield imaging using bulk waves at typical frequencies in the 1-10 MHz range is limited since bulk wavefield acquisition requires finer temporal and spatial samples to avoid aliasing. The challenges are mitigated by using either lower frequencies under 1 MHz [32] or measuring wavefield within smaller scan areas.

2.5 Ultrasonic Wavefield Signal Processing

One fundamental mathematical tool in the field of signal processing is the Fourier transform, which decomposes a waveform (e.g., a signal or function of time) into the frequencies

expressed as the sum of sinusoidal functions. Here, the waveforms of interest are the experimental wavefield data of area scans described as a three-dimensional function (time and two spatial dimensions) as previously introduced in Section 2.4. The 3D wavefield data can be converted from the time-space domain (t, x, y) into the frequency-wavenumber domain (ω, k_x, k_y) via the three-dimensional Fourier transform,

$$W(\omega, k_x, k_y) = \iiint w(t, x, y) e^{-i(\omega t + k_x x + k_y y)} dt dx dy, \tag{2.10}$$

where ω is the angular frequency, and k_x and k_y are the wavenumber components along the x and y axes.

The 3-D Fourier transform allows the wavefield data being analyzed in the frequency-wavenumber domain. Two specific analysis techniques, which are directional filtering and frequency-wavenumber filtering, are effective on wave isolation and extraction. Both signal processing techniques have been performed numerous times to analyze ultrasonic guided wavefields. Directional filtering is powerful to extract waves based on the propagation direction. Ruzzene [48] isolated all propagating waves in the $x > 0$ direction by the elimination of the portion of the 3D spectrum corresponding to $k_x > 0$, which eventually enhances damage visualization using guided wavefield images. Michaels $et\ al.$ [49] extended this technique and effectively decoupled forward- and backward-propagating guided waves in both the 2-D and 3-D frequency-wavenumber domains. In addition to being used as a common analysis technique to identify different propagating waves, frequency-wavenumber analysis is helpful to separate guided wave modes. Tian and Yu [50] built 2-D frequency-wavenumber filters for decomposing the A_0 and S_0 modes of Lamb waves, which allows for analyzing each mode separately. Flynn $et\ al.$ [30] applied a frequency-dependent filter in the wavenumber domain about the estimated frequency-wavenumber curve to isolate guided wave modes. However, the published work of both signal processing techniques are limited on analyzing ultrasonic bulk wavefields.

2.6 Ultrasonic Scattering

The analysis of ultrasonic scattering has become one of the important ongoing research because it is helpful to obtain a deep understanding of the interaction of ultrasonic waves with both structural features and flaws, validate simulation models, and improve inspection techniques for NDE applications. There is a long history of quantifying ultrasonic scattering from a variety of scatterers. Many scattering studies focus on analytical, semi-analytical, and numerical modeling methods. Thanks to the computation capability improvement, the existing ultrasonic models are applicable to simulate realistic ultrasonic inspection scenarios and the interaction with flaws. Analytical models can be applied to analyze relatively simple scatterer shapes such as cylindrical, planar, or axisymmetric, e.g., [51, 52, 53].

For the sake of extending the applicability of the simulation tools, semi-analytical models are developed because of their lower computation complexity. Darmon $et\ al.$ [54] reported recent advances in semi-analytical models derived from the separation of variables and the geometrical theories of diffraction. Associated experimental validations of the creeping wave reflection simulation are provided. However, if scatterers become more complex, neither analytical nor semi-analytical models are effective. In this case, the scattering can be modeled by numerical methods such as finite element, finite difference, or boundary element modeling methods. Velichko $et\ al.$ [55] presented finite element modeling of elastodynamic scattering by the scattering matrix in isotropic material in both two and three dimensions. Harker [56] showed finite difference methods to model the scattering of elastic waves. This model was also used to study more complex systems including several defects.

This thesis focuses on scattering from through-holes, part-through holes, and damaged through-holes with notches. Both through-hole scattering and notch scattering are of particular interest. As mentioned previously in Section 1.1, cracks often tend to originate from fastener holes in aircraft components, so through-holes and notches aim to mimic fastener

holes and cracks. Their respective scattering is particularly important and beneficial to the periodic inspection of aircraft components in the aerospace industry.

2.6.1 Cylindrical Holes

A circular cylindrical cavity or side-drilled hole (SDH) is commonly used as a reference reflector in ultrasonic flaw detection. There are many scattering studies of a cylindrical hole or SDH by utilizing less or more sophisticated models over the years. The scattering problem can be solved analytically in 2D reported by White in [57]. An analytical model was presented to solve the transfer of energy in the scattering of compressional and shear elastic waves at a cylindrical discontinuity. For plane wave incidence, Flax $et\ al.$ [58] theoretically described the scattering of an infinite plane wave by an elastic cylinder. Niklasson $et\ al.$ [59] solved the scattering problem from an infinite circular cylinder by means of separation of variables. Boström and Bövik [60] characterized the SDH scattering by a combination of the analytical solution with realistic models of ultrasonic transmitting and receiving probes in transmission and reception, which is equivalent with the separation of variables solution.

Modeling efforts have been further put into a variety of semi-analytical approaches, which mainly include the Kirchhoff approximation, separation of variables (SOV), and distributed point source methods (DPSM). Schmitz $et\ al.$ [61] utilized Kirchhoff approximation and ray tracing to simulate scattered waves from different defects, which include flat bottom holes and SDHs. Ye $et\ al.$ [62] solved the theoretical evaluation of the elastic wave scattering from an SDH in the anisotropic media based on the Kirchhoff approximation. Lopez-Sanchez $et\ al.$ [63] performed measurement and scattering models to predict the ultrasonic pulse-echo response from an SDH using two scattering amplitude models that are based on the Kirchhoff approximation and a SOV solution, respectively. Placko and Kundu [64] developed the semi-analytical technique of DPSM, which was applied to investigate the scattering of elastic waves by a circular hole [65, 66]. With computational

power improving, some 3D scattering problems can be solved analytically. Aldrin $et\ al.$ [51] investigated a 3-D analytical model for the propagation and scattering of obliquely incident shear waves on a cylindrical hole. Darmon $et\ al.$ [54] extended a SOV method in 3D to simulate the scattering from a cylindrical cavity.

In addition to analytical modeling methods, purely numerical methods, such as the finite element method (FEM) [67] and the elastodynamic finite integration technique (EFIT) [68], are also in use for investigating scattering in anisotropic inhomogeneous media in 2D and 3D. Zhang $et\ al.$ computed the scattering coefficient matrix by a finite element model to distinguish a circular hole and a crack [69, 70]. Velichko $et\ al.$ [55] predicted 2-D and 3-D bulk wave scattering by the finite element method. Travaglini $et\ al.$ [71] developed on a 3-D finite element model to analyze the scattering of high order guided wave modes around a hole. Diligent $et\ al.$ [72] predicted the interaction of Lamb waves with a circular through-thickness hole. Aldrin and Knopp [73] studied the scattering of ultrasonic waves around fastener holes in three dimensions by finite element analysis.

2.6.2 Notches

In the NDE community, analysis of ultrasonic scattering by crack-like defects has become an important research focus because of the industry need for improved characterization. Similar to the research of hole-scattering, many studies of notch-scattering are developed using either analytical solutions or numerical modeling techniques. For example, many research efforts have been pursued to detect and characterize surface-breaking cracks. Mendelsohn $et\ al.$ [74] investigated scattering from surface-breaking cracks in two dimensions using a dual integral equation. Achenbach and Norris [75] applied ray methods to analyze backscattering of oblique longitudinal waves from a surface-breaking crack for the same 2-D configurations. Ray analysis was also used for surface wave interaction with an edge crack [76]. Angel and Achenbach [77] reported scattering of Rayleigh waves obliquely interrogating a surface-breaking crack. The elastodynamic representa-

tion integral was utilized for analyzing longitudinal and transverse wave scattering from inclined surface-breaking cracks in [78]. Finite difference methods were carried out to obtain numerical results for ultrasonic wave scattering from surface-breaking cracks such as [56, 79]. Datta and Shah [80] combined finite element and analytical expansion methods to research scattering for complex-geometry configurations, such as a branched surface-breaking crack. For the half-skip configuration, Felice $et\ al.$ [81] utilized finite element and ray tracing for sizing surface-breaking cracks.

There are also reported studies on fatigue cracks, elliptical cracks, planar cracks, crack-like notches, and buried cracks using both bulk waves and guided waves. Silk [82] investigated sizing fatigue cracks via the transfer of scattered shear and longitudinal energy. Ravenscroft $et\ al.$ [83] studied diffracted waves from fatigue crack tips in the context of the time-of-flight-diffraction (TOFD) method. Adler and Achenbach [84] provided analytical solutions to the diffraction of angle-beam longitudinal waves by elliptical cracks based on physical elastodynamic theory. Glushkov $et\ al.$ [52] applied an analytical model based on the integral equation technique to simulate the scattering of planar cracks. Chapman [53] modeled planar crack scattering by combining the elastodynamic geometrical theory of diffraction and Kirchhoff theory, which are two main theories applied to analytical modeling methods. Zhang $et\ al.$ [85] modeled local scattering of longitudinal waves from rough crack-like defects using the finite element method. Fromme and Rouge [86] experimentally investigated wave propagation and scattering of the A_0 Lamb wave mode at part-through and through thickness crack-like notches using FE simulations. Fellinger $et\ al.$ [68] showed scattering of normally-incident longitudinal waves from a buried crack in a transversely isotropic material in 2D using EFIT techniques. Shah $et\ al.$ [87] utilized the finite element method to model scattering from buried cracks in a half-space. Lu $et\ al.$ [88] used FEM methods to study the interaction of obliquely incident Lamb waves with through-thickness cracks of different lengths. Chang and Mal [89] theoretically and experimentally studied the scattering of Lamb waves interacting with a circular hole with or

without edge cracks in 3-D using the global local finite element method.

Over the years, a number of analytical, semi-analytical, and numerical modeling methods have been developed to simulate ultrasonic wave scattering from cracks and notches. However, limited results show full wavefield data, which consist of groups of wavefield snapshots. Each snapshot is an image of wave motion at a specific time. Harker [56] visualized compression and shear waves scattered from surface-breaking cracks and showed snapshot examples. More recently, Shi $et\ al.$ [90] showed the scattering of waves from an SDH, a smooth crack, and a rough crack. Darmon $et\ al.$ [91] showed FEM snapshots of 45° shear vertical waves interacting with 3D crack-like defects. These wavefield snapshots provide invaluable quantitative waveform information of the propagation and scattering process, which is beneficial to improve the understanding of ultrasonic wave interaction with the materials and defects.

2.7 Research Context and Objectives

The context of this thesis is applying wavefield methods to characterize scattering from holes and notches in aluminum plates. The experimental wavefield data are obtained by the laser-based sensing technique, which is described in Section 2.4, to record the full wavefield on the exposed surface resulting from an incident angle-beam shear wave interacting with scatterers in plates. The measured wavefield can provide quantitative information of both incident waves and scattered waves from defects, which is helpful to visualize wave components of interest and explain how scatterers affect ultrasonic wave propagation in a quantitative way.

The presented research builds upon prior work performed in the QUEST laboratory at Georgia Tech, which is summarized here. Dawson [92] presented reliable experimental procedures for high-quality measurement of angle-beam bulk wavefield data in aluminum plates via wavefield imaging and described a notch-scattering analysis methodology by isolating scattered waves via baseline subtraction. Kummer [93] developed two signal pro-

cessing methods to quantify the effect of various through-hole fill conditions on shear wave scattering. Maki [94] investigated shear wave scattering from complex compound scatterers (e.g., buried notches) in bonded specimens and obtained scattering patterns to quantify the effect of the bonded layer. Thanks to the previous research, this thesis improves signal processing techniques, develops comprehensive scattering characterization methodologies, analyze shear wave scattering from a variety of scatterers of interest, and research on how various factors affect scattering with different scattering scenarios in terms of sensitivity analysis.

The specific objectives of the presented research are to first acquire experimental angle-beam wavefield data from interactions with different scatterers, which include through-holes, part-through holes, and notches. Then, a complete set of signal processing techniques is presented in both the time-space and frequency-wavenumber domains, which aims to isolate and extract scattered waves of interest prior to scattering characterization and quantification. Next, multiple scattering characterization methodologies are developed to analyze the scattering behavior as scatterers become more complex. By a combination of various characterization methods, the quantified scattering profiles under different scattering scenarios can be analyzed and interpreted in more detail, which not only adds to ultrasonic scattering knowledge but also improves the understanding of bulk wave propagation and scattering in plate-like structures.

CHAPTER 3
EXPERIMENTAL PROCEDURES

This chapter presents the experimental setup, which includes sampling considerations, excitation methods, noise reduction, and wavefield visualization. Three wavefield representation perspectives, which are point, line, and area scans, are introduced. A detailed experiment summary is provided.

3.1 Experimental Setup

Wavefield measurements were performed on 6061 single-sided-mirror-finished aluminum plates of dimensions 305 mm $\times$ 305 mm $\times$ 6.35 mm. A conventional angle-beam shear probe, which consists of an ultrasonic transducer with a specified center frequency and an acrylic wedge with a designed angle, is used to generate angle-beam shear waves penetrating into a specimen obliquely. The wedges, Olympus part numbers ABWM-4T-45, ABWM-4T-60, and ABWM-4T-70, were designed to generate incident shear waves with refracted angles of 45°, 60°, and 70° in steel, which correspond to 43.1°, 56.8°, and 65.2° in aluminum. A 6.35 mm diameter, 5 MHz frequency broadband transducer (Olympus part number C543-SM) was used for all three wedges. The wedges were coupled to the plates using Sonotech Pyrogel ultrasonic couplant and were secured in place with adhesive mounts and plastic ties. A Polytec laser fiber vibrometer, model OFV-551, controlled by a Polytec vibrometer controller, model OFV-5000, was utilized to sense wave motion on the exposed surface resulting from the angle-beam probe. The output of the vibrometer controller was bandpass filtered between 1-10 MHz with a Panametrics (Olympus) model 5072PR pulser-receiver, and then subsequently digitized with a Cleverscope model CS328A digital oscilloscope at a sampling frequency of 100 MHz. All received signals were recorded from 0 to 100 μs.

3.1.1 Sampling Considerations

Wavefield data were measured in both time and space, so both temporal and spatial sampling intervals must be taken into account. As mentioned before, received signals of the vibrometer controller were bandpass filtered from 1-10 MHz before sampling, so the temporal sampling rate must be at least 20 MHz to avoid aliasing according to the Nyquist sampling theorem. Here, for the experimental setup, the digitizer clock is not synchronized with the excitation signal, so a sampling frequency of 100 MHz, which corresponds to 0.01 μs, well above the Nyquist rate, was used for the digital oscilloscope to minimize jitter. The spatial increment is chosen by considering the minimum wavelength, which corresponds to the wavelength of the slowest possible propagating waves. Here, the Rayleigh wave speed, which is taken to be 2.9 mm/μs, is the smallest. Then, the minimum wavelength of 0.29 mm is calculated by the equation of $\lambda = c/f$ at the frequency maximum of 10 MHz. Similarly, the Nyquist sampling theorem requires that the spatial sampling interval be at least two samples per wavelength to avoid spatial aliasing. Therefore, the spatial increment must be less than 0.145 mm. For the trade-off of the acquisition time, the spatial increment is taken to be 0.1 mm and 0.25 mm for line scans and area scans, respectively.

3.1.2 Excitation Methods

Two excitations were applied to the transducers. The first is a spike excitation using a Panametrics (Olympus) model 5072PR high voltage pulser-receiver at a repetition period of 1 ms. The 5058PR generates a typical negative spike signal whose amplitude can be adjusted from 100 to 900 V. The second one is a chirp excitation using an Agilent 33250A arbitrary waveform generator amplified with a Ritec RAM-5000 gated amplifier. The chirp was a linear frequency-modulated sine wave from 1-10 MHz with a duration of 180 μs and an amplitude of 200 V. This chirp duration was selected to fall within the 200 μs gate window of the RAM-5000. In the remainder of this thesis, both spike and chirp excitations are used. They were found to result in similar signal-to-noise ratios for similar acquisition

times, and there was no obvious advantage of using one versus over the other.

3.1.3 Wavefield Visualization

A laser Doppler vibrometer is a powerful tool to visualize waves propagating on the accessible plate surface and provide quantitative displacement information. Here, a Polytec laser fiber vibrometer, model OFV-551, was used to measure the out-of-plane displacement on the surface of a specimen caused by wave propagation resulting from a fixed ultrasonic transducer. The fiber optic sensor head was mounted on an XYZ scanner, programmed via a custom LabVIEW software, to perform point-by-point raster scans. The excitation was repeatedly generated as the scanner moved to each pixel.

3.1.4 Wavefield Representation

Generally, there are three ways to represent wavefield data. The first one is point scans. Given a single spatial point (pixel), wavefield data are expressed as amplitude versus time signals $w(t)$. Figure 3.1 shows several received waveform signals obtained from a shear wave probe of 56.8° excitated by spike signals at different distances. As can be seen from the figure, separate spike signals with different times of arrival are observed. Actually, the measured signals here are similar to the pitch-catch method. Wave components can be identified by calculating velocities. In practice, based on the geometric information, reflected pulses can be recognized, which is useful for defect detection. The amplitude signal of time at a specific location is straightforward, but point scan data cannot show comprehensive information of wave propagation.

The second perspective is line scans. Given a scan line, wavefield data can be described as a two-dimensional amplitude map that is a function of time and distance from the transducer location. Figure 3.2(a) shows wavefield data along a line from 10 to 100 mm. As can be seen from the figure, arrival time curves, which show the relation of wave propagation distance and arrival time, are clearly displayed. By taking the slope of one curve at a

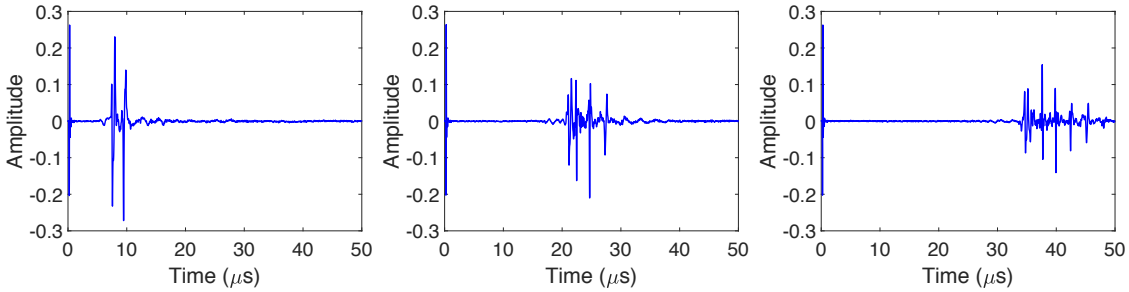

Figure 3.1: Point scans at a distance of (a) 10 mm, (b) 50 mm, and (c) 90 mm from the transducer location.

specific time or distance location, one can easily get the phase velocity. Line scan data are more informative than point scan data. However, for the sake of displaying full wavefield data, area scans are taken. Given a 2-D spatial region, wavefield data, formed in a 3-D format (t, x, y), can be displayed in a wavefield video of time, which is a vivid and straightforward means to show wave propagation and scattering behavior as time progresses. Each time snapshot is a 2-D image of wave motion at a specific time. Figures 3.2(b), 3.2(c), and 3.2(d) show wavefield snapshots at 17.6 μs, 18.6 μs, and 19.6 μs, respectively, in a scan area of 30 mm $\times$ 30 mm. As the figure shows, two wave trajectories are clearly observable in general. Wave trajectory movements are directly displayed by continuous time frames. Because area scan data provide comprehensive and quantitative waveform information over a 2-D rectilinear area of interest, this representation perspective is taken to be the primary means to visualize and analyze wavefield data in this thesis.

3.1.5 Noise Reduction

Laser Doppler vibrometer, as a tool to measure and record wavefields, is very sensitive to both temporal and spatial noise, particularly at the frequencies of interest for shear wave inspection. One solution is to utilize a chirp excitation and post-process the received signals to increase the signal-to-noise ratio (SNR). Here, the processing was performed via deconvolution as described in [95] where various target waveforms were performed. Signals

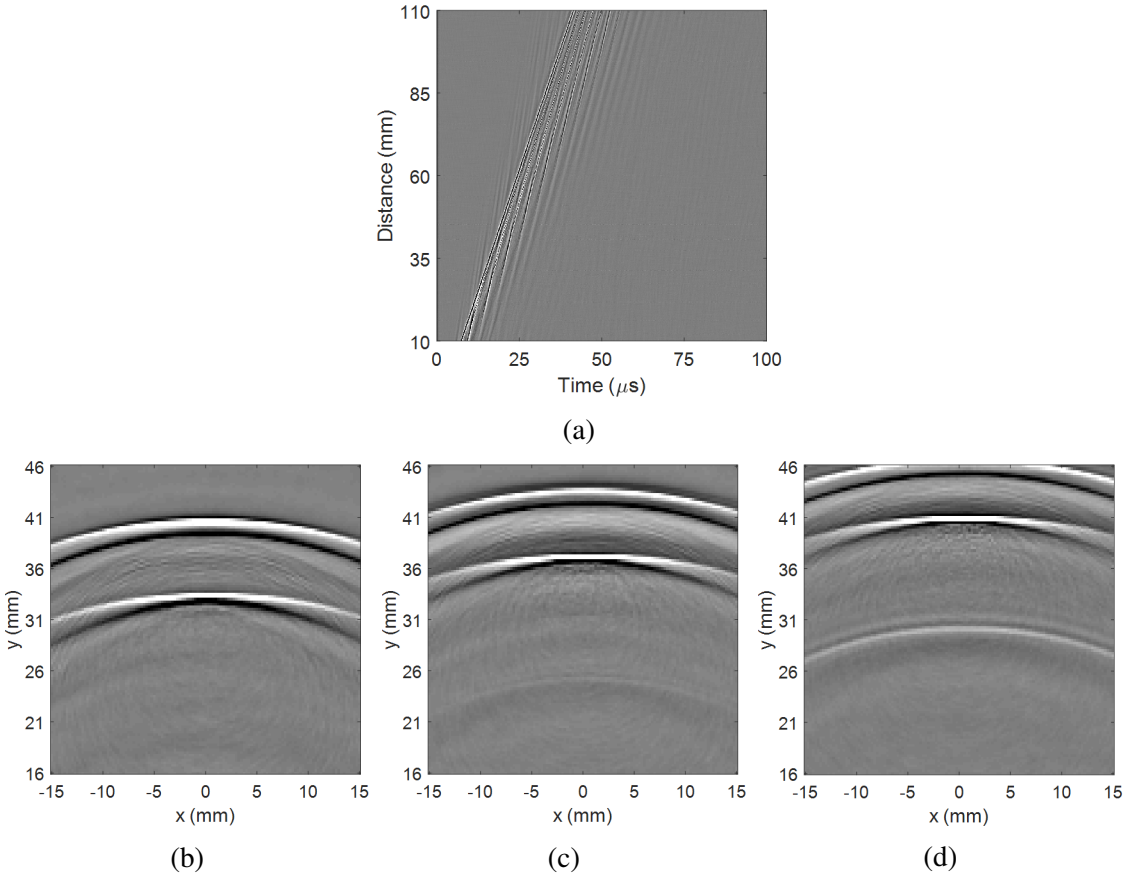

Figure 3.2: Wavefield data representation. (a) A line scan from 10 to 110 mm, and area scan snapshots at (b) 17.6 μs, (c) 18.6 μs, and (d) 19.6 μs.

were bandpass filtered after deconvolution by multiplication in the frequency domain by a tapered cosine window from 0 to 10 MHz with a taper width on each end of 1 MHz (20% Tukey window [96]). This technique yields the equivalent response to the target excitation but with a higher SNR because of both the larger energy of the chirp and the additional filtering. The other solution is signal averaging, which is an effective way to reduce both temporal and spatial noise, but it increases acquisition time.

Figure 3.3 shows several line scans at distances of 10 to 110 mm from a transducer with 0.1 mm increment. Each pixel was measured and averaged with various values by using a spike excitation. It is clearly to see that SNR is increased and wavefield images are cleaner as more averages are taken. However, acquisition time is also increased. Acquisition time increases from 673 to 750 s when the number of averages increases from 128 to 256. Under the consideration of the trade-off between SNR and acquisition time, averaging times are chosen to be 128 for each pixel when a spike excitation is used. For a chirp excitation, 64 averages are taken for each pixel, which can lead to similar signal-to-noise ratios with equivalent acquisition times. Regardless of the excitation method, with these averaging settings, each area scan, conducted over a 30 mm $\times$ 30 mm region with a pixel resolution of 0.25 mm in both the x and y directions, takes about 3.5 hours.

3.2 Summary of Experiments

A number of area scans were performed on plate specimens to characterize scattering from various scatterers, which include through-holes, part-through holes, and notches, in plate specimens. These scans can be divided into three categories of increasing scatterer complexity. The first is scattering from a through-hole (series "A"), the second is scattering from a part-through hole (series "B"), and the third is scattering from a notch emanating from a through-hole (series "C"). All wavefield scans were recorded under typical laboratory conditions, at nominally the same temperature. Although not measured for all scans, it is estimated that the temperature changed no more than $\pm 2^{\circ}$C during and between scans.

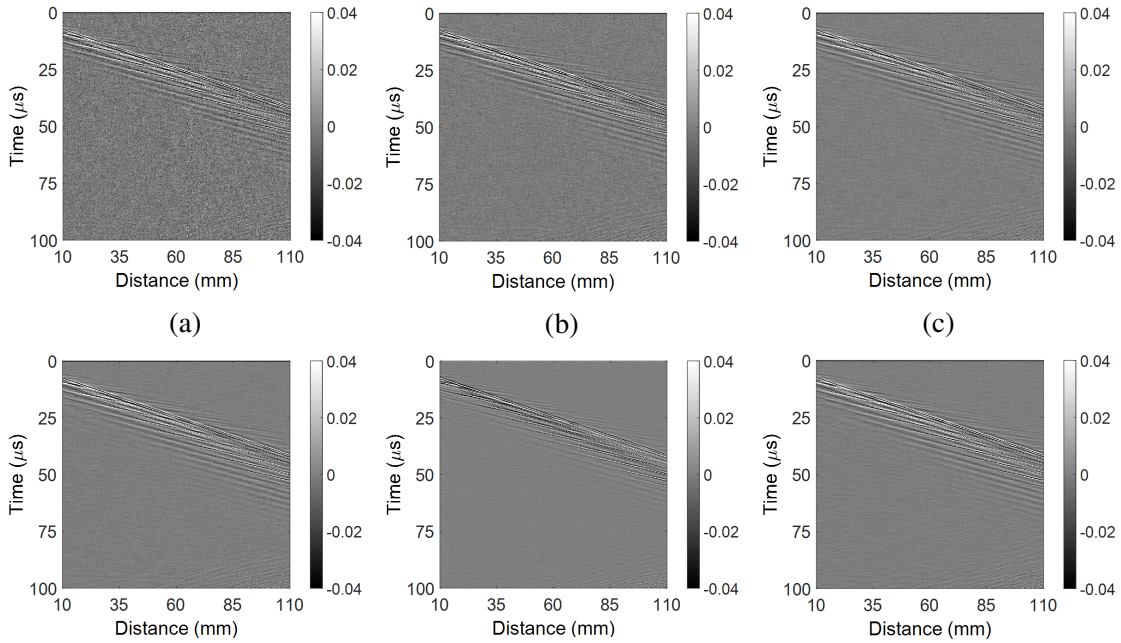

Figure 3.3: Line scan comparison by using different averages. Scans with (a) single average, (b) 4 averages, (c) 16 averages, (d) 64 averages, (e) 128 averages, and (f) 256 averages consume times of 626 s, 626 s, 626 s, 635 s, 673 s, and 750 s.

Wavefield amplitudes are reported in arbitrary units that are proportional to out-of-plane displacement and are consistent between measurements for each specimen.

3.2.1 Through-Hole Scans

Both spike and chirp excitations were used for three specimens with through-holes as summarized in Table 3.1. The first specimen corresponds to scans A1 and A2, which are used to present methodologies of through-hole scattering analysis. The second includes scans A3-A6, which are performed to investigate how hole sizes affect scattering. The third one includes scans A7-A14, designed for fill condition analysis. The plate was removed and remounted in between scans to drill or enlarge holes or to change the fill conditions, but the probe remained mounted in place.

Figures 3.4(a) and 3.4(b) show the through-hole configuration from the top and side views, respectively. The center of beam incidence (transducer) is taken to be the origin in

Table 3.1: Summary of scans from specimens with through-holes.

Scan Number	Description
A1	No hole (baseline), spike excitation
A2	3.18 mm diameter, empty through-hole, spike excitation
A3	No hole (baseline), chirp excitation
A4	1.59 mm diameter, empty through-hole, chirp excitation
A5	3.18 mm diameter, empty through-hole, chirp excitation
A6	6.35 mm diameter, empty through-hole, chirp excitation
A7	No hole (baseline), chirp excitation
A8	6.35 mm diameter, air-filled through-hole, chirp excitation
A9	6.35 mm diameter, epoxy-filled through-hole, chirp excitation
A10	6.35 mm diameter, steel-filled through-hole with epoxy coupling, chirp excitation
A11	6.35 mm diameter, aluminum-filled through-hole with epoxy coupling, chirp excitation
A12	6.35 mm diameter, half-steel-filled through-hole with oil coupling, chirp excitation
A13	6.35 mm diameter, steel-filled through-hole with oil coupling, chirp excitation
A14	6.35 mm diameter, aluminum-filled through-hole with oil coupling, chirp excitation

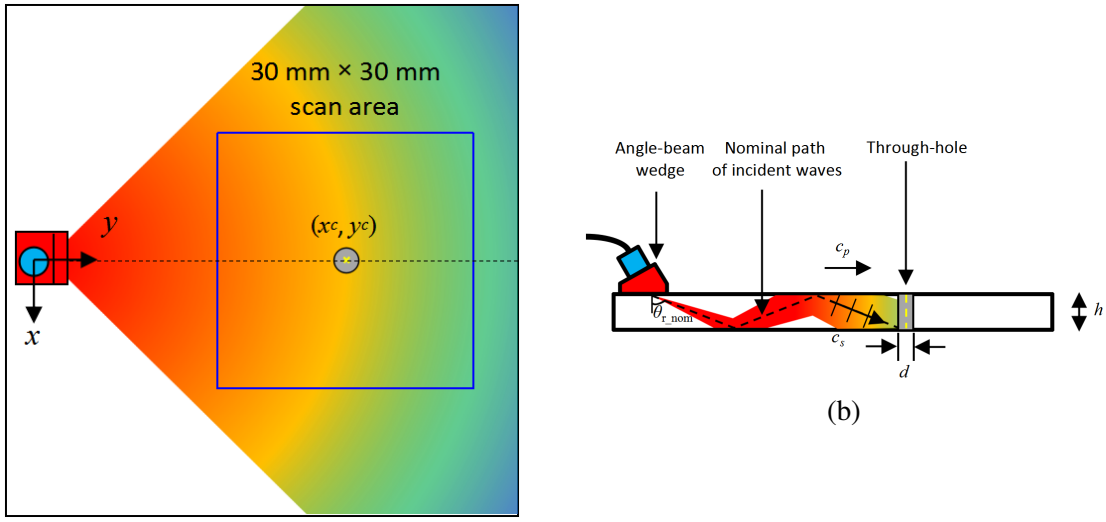

(a) (b)

Figure 3.4: Experimental setup for the acquisition of angle-beam wavefields in an aluminum plate with a through-hole. (a) Top view, and (b) side view (not to scale).

the x-y plane. Shear wave reflection between two plate surfaces leads to multiple skips. Here, one skip refers to a full V-path of shear waves traveling from the top surface, reflecting from the bottom surface, and returning to the top surface. A hole was drilled at a distance of 29.1 mm from the origin, which corresponds to 1.5 skips of a shear wave propagating at the nominal refracted angle, $\theta_{\text{r\_nom}} = 56.8°$, to ensure that the probe was not in the scan area. At this distance, the center of the incident beam interrogated the far surface at the desired location. Given the geometric information, the hole center coordinate y_c is given by,

$$y_c = 3h \cdot \tan\theta_{\text{r\_nom}} + d/2, \tag{3.1}$$

where h is the plate thickness and d is the hole diameter.

3.2.2 Part-Through Hole Scans

A spike excitation was applied to plate specimens with part-through holes of various hole depths as summarized in Table 3.2. Part-through holes were placed as same as through-

holes introduced previously and were drilled from the bottom plate surface.

Table 3.2: Summary of scans from specimens with part-through holes.

Scan Number	Hole Depth	Description
B1	0%	No hole (baseline)
B2	25%, 1.59 mm	3.18 mm diameter part-through hole
B3	50%, 3.18 mm	3.18 mm diameter part-through hole
B4	75%, 4.76 mm	3.18 mm diameter part-through hole

3.2.3 Scans of Through-Holes with Notches

A spike excitation was utilized for plate specimens with quarter-circle notches emanating from through-holes, which are aimed to mimic actual cracks growing from fastener holes in the aerospace industry. Notch length is a factor that leads to different notch-scattering behavior as well as transducer location and wedge angle. Therefore, for the sake of sensitivity analysis in terms of these factors, four groups of area scans in total were performed as summarized in Table 3.3. All wavefield scans were performed over a 30 mm $\times$ 30 mm area centered on the hole at a pixel resolution of 0.25 mm for each notch size (2 and 4 mm). The first one corresponds to scans C1-C3, which aim to present two methodologies to characterize notch-scattering and how does the notch length affect the scattering behavior. The probe was located at a distance of 29.1 mm (1.5 skips of a 56.8° shear wave) from the through-hole apex (lower edge of the hole) vertically below the hole (angle of $-90°$). Figure 3.5 illustrates this probe placement. A quarter-circular-profile, electric discharge machined (EDM) notch was made inside a 6.35 mm diameter through-hole at 0° relative to the $+x$-axis on the far-surface of the plate.

The second group, which includes scans C4-C6, aims to investigate how the probe placement (transducer location) influence notch scattering. Specifically, the probe is placed up and right both a distance of a hole radius (e.g., 3.18 mm for a 6.35 mm diameter through-hole) as compared to the fisrt probe placement so that the probe aimed at the hole-notch

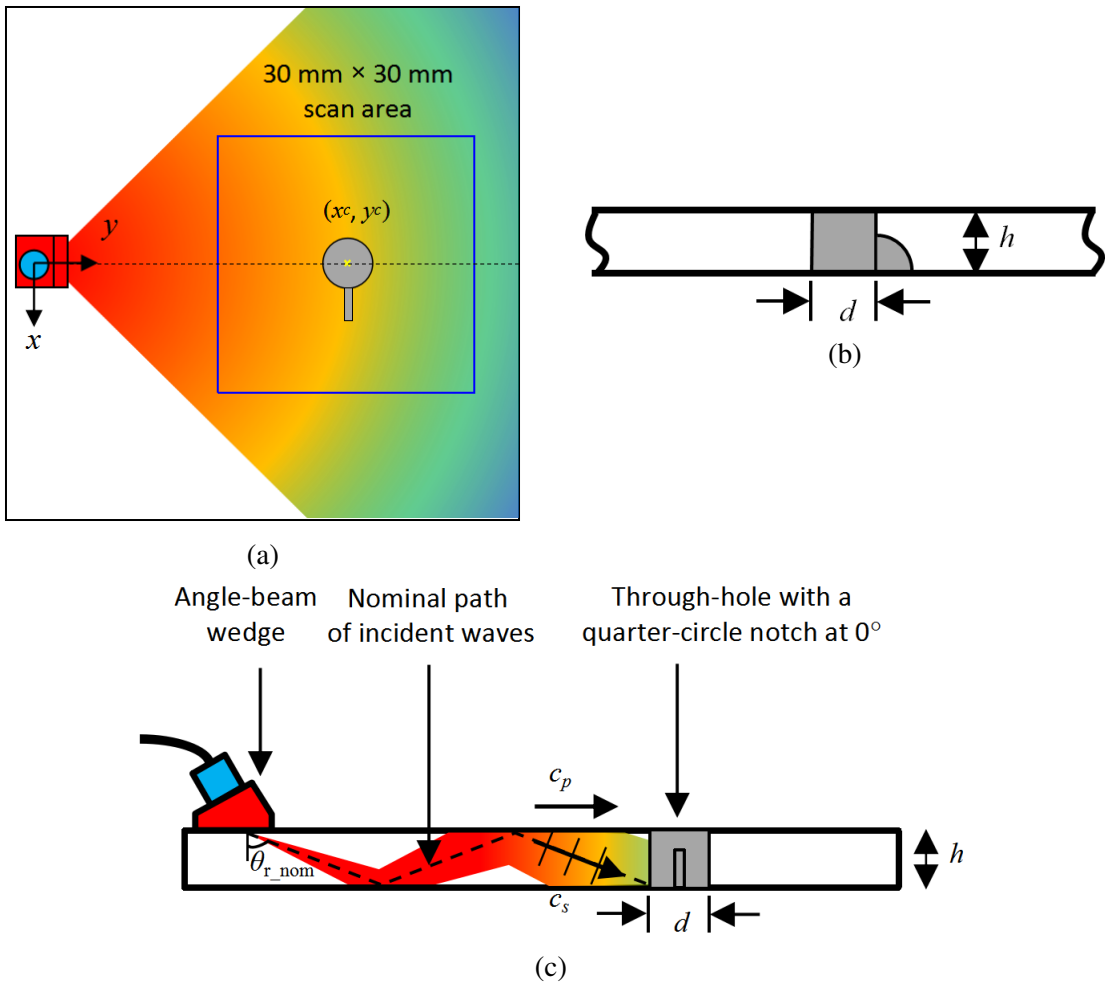

Figure 3.5: Diagram of the specimen with a through-hole and a quarter-circle notch showing angle-beam transducer locations. (a) Top view, (b) front view, and (c) side view (not to scale).

corner (right edge of the hole) with the same distance of 29.1 mm.

The third area scan group includes scans C7-C9, which utilize a 45° wedge aiming at the hole-notch corner as same as the second group but with a different distance of 29.7 mm, which corresponds to 2.5 skips of the nominal shear wave at 43.1° in aluminum. The purpose is to avoid that the probe was within the scan area. Similarly, the fourth group of scans C10-C12 uses a 70° wedge aiming at the hole-notch corner with a distance of 41 mm, which corresponds to 1.5 skips of the nominal shear wave at 65.2° in aluminum.

Table 3.3: Summary of scans from specimens with notches inside through-holes.

Scan Number	Aim Point	Wedge Angle	Description
C1	Hole apex	60°	6.35 mm diameter through-hole (baseline)
C2	Hole apex	60°	6.35 mm diameter through-hole with a 2 mm notch
C3	Hole apex	60°	6.35 mm diameter through-hole with a 4 mm notch
C4	Hole-notch corner	60°	6.35 mm diameter through-hole (baseline)
C5	Hole-notch corner	60°	6.35 mm diameter through-hole with a 2 mm notch
C6	Hole-notch corner	60°	6.35 mm diameter through-hole with a 4 mm notch
C7	Hole-notch corner	45°	6.35 mm diameter through-hole (baseline)
C8	Hole-notch corner	45°	6.35 mm diameter through-hole with a 2 mm notch
C9	Hole-notch corner	45°	6.35 mm diameter through-hole with a 4 mm notch
C10	Hole-notch corner	70°	6.35 mm diameter through-hole (baseline)
C11	Hole-notch corner	70°	6.35 mm diameter through-hole with a 2 mm notch
C12	Hole-notch corner	70°	6.35 mm diameter through-hole with a 4 mm notch

CHAPTER 4
SIGNAL PROCESSING TECHNIQUES

This chapter presents a set of signal processing techniques, which include temporal and spatial windowing, spatial anti-aliasing, directional filtering, wavefield baseline subtraction, phase velocity filtering, ray tracing analysis, and incident wave subtraction.

4.1 Temporal and Spatial Windowing

The purpose of temporal and spatial windowing is to smooth sharp transitions in both the time and space domains. The motivation behind the smoothing is to avoid spectral leakage in the Fourier domain. For the obtained wavefield data, incident and scattered waves are of interest in the first 30 μs even though the total time window is from 0 to 100 μs. To extract wavefield data in this 30 μs window without causing spectral leakage in the frequency domain, a 20% Tukey window is applied to smooth wavefields excited by chirp signals from 0 to 30 μs as shown in Figure 4.1. For wavefield data acquired by spike excitation, a 20% Tukey window is applied to wavefields from 1 to 30 μs, which excluded electromagnetic feedthrough of the excitation. For area scans, the spatial scan window results in discontinuities of the data at its edges, which causes spectral leakage in the wavenumber domain if not smoothed. Similarly, a 20% Tukey window is also applied along the 30 mm extent of each spatial dimension (x,y) to mitigate this effect.

A spatial window is also used to suppress noisy signals inside through-holes. The introduction of through-holes leads to a region where the laser Doppler vibrometer is out-of-focus. As a result, noisy signals with large amplitude are present inside the hole boundary. Here, through-hole windowing is performed to localize holes and remove through-hole noise. By displaying area scan data as wavefield videos, the noisy through-hole pixels can be identified. The centroid is estimated as the center of a circular spatial window to remove

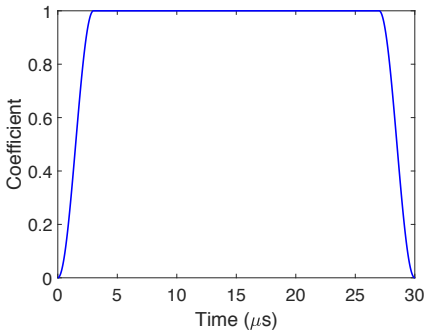

Figure 4.1: A 20% Tukey window along the time axis from 0 to 30 μs.

the hole noise. A 6$^{\text{th}}$ order circular Butterworth window with a specific radial cutoff is used to suppress the noisy signals, and is given by

$$w(x,y) = \frac{1}{\sqrt{1+\left(\frac{r_c}{\sqrt{x^2+y^2}}\right)^{2n}}}, \tag{4.1}$$

where r_c is the radial cutoff and n is the window order (n = 6). Table 4.1 summarizes radial cutoff parameters for different through-hole sizes.

Table 4.1: Radial cutoff setup for hole noise removal.

Hole Diameter (mm)	Radial Cutoff (mm)
1.59	1.5
3.18	2.5
6.35	5

Figure 4.2 shows the comparison of wavefield time snapshots from scan A2 before and after smoothing the time t, space (x, y), and hole boundaries. The hole center is marked with a yellow cross and the hole edge is shown with a solid red circle after through-hole windowing. As can be seen from the figure, the wavefield snapshots are clearly smoothed after temporal and spatial windowing. In addition, undesirable effects in the Fourier domain are mitigated.

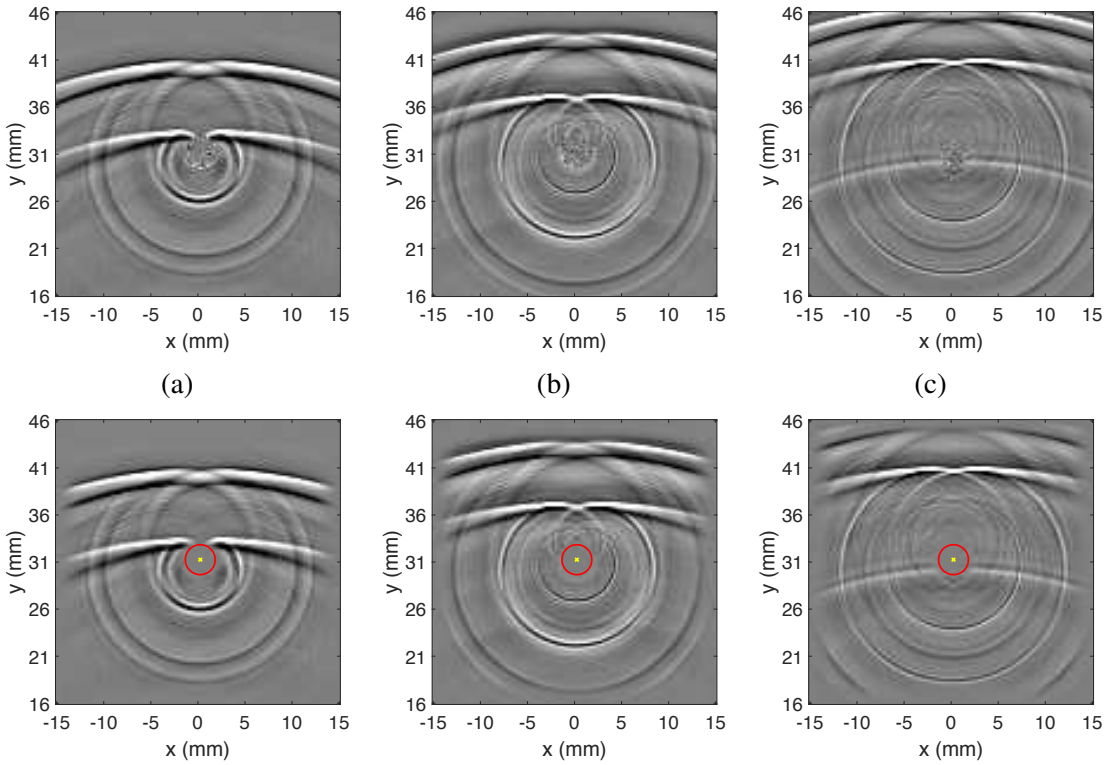

Figure 4.2: Raw wavefield snapshots at (a) 17.6 μs, (b) 18.6 μs, and (c) 19.6 μs. Wavefield snapshots after temporal and spatial windowing at (d) 17.6 μs, (e) 18.6 μs, and (f) 19.6 μs.

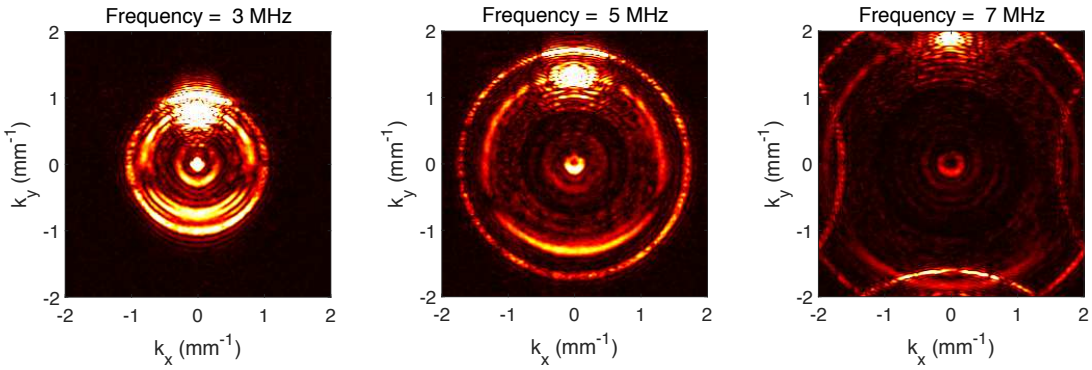

(a) (b) (c)

Figure 4.3: Fourier wavefield frequency snapshots (k_x-k_y slices) at (a) 3 MHz, (b) 5 MHz, and (c) 7 MHz.

4.2 Spatial Anti-Aliasing

Three-dimensional wavefield data (t, x, y) are transformed into the frequency-wavenumber domain (ω, k_x, k_y) via the 3-D Fourier transform after smoothing the data in the time-space domain as described previously. Similar to the wavefield data displayed as videos of time in the time-space domain, Fourier wavefield data can be displayed as videos of frequency. Each frequency snapshot refers to a 2-D k_x-k_y slice of the Fourier data. Figure 4.3 shows several frequency snapshots from scan A2. As can be seen from the figure, the wavefield data appear in circular patterns in the Fourier domain. As the frequency increases, the radii of these circles become larger and larger. After frequency values exceed the Nyquist frequency, the radii of these circles are larger than the wavenumber boundaries in both the k_x and k_y axes and spatial aliasing occurs as shown in Figure 4.3(c). According to the Nyquist sampling theorem, spatial increments in both the x and y directions must be less than half of the smallest wavelength,

$$dx, dy \leq \frac{1}{2}\lambda_{\min}, \tag{4.2}$$

In the experimental wavefield data, Rayleigh waves, whose wave speed is 2.9 mm/μs, are the slowest waves, and thus have the smallest wavelength. Based on the relation of

$\lambda = c/f$, the Nyquist frequency, which is the maximum frequency without causing spatial aliasing, is calculated by,

$$f_{\max} = \frac{\frac{1}{2}c_{p\_\text{Rayleigh}}}{dx}. \tag{4.3}$$

Given a spatial increment of 0.25 mm, the Nyquist frequency is 5.8 MHz. Figure 4.4(a) shows the actual Fourier data (k_x-k_y slice) at the calculated critical frequency of 5.8 MHz and Figure 4.4(b) shows the simulated wavenumber contour (k_r =2 mm^{-1}) at the same frequency. As can be from the figure, the contour is well matched with the actual k_x-k_y slice. Figures 4.4(c) and 4.4(d) show the comparison between the actual and simulated k_x-k_y slices at a frequency of 7.5 MHz after spatial aliasing occurs. As can be seen from the comparison, simulated contours are in good agreement with the actual Fourier data. For the sake of spatial anti-aliasing, a 20% Tukey window along the frequency axis from 0 to 6 MHz is applied to filter the Fourier data. This processing step is immediately implemented once a Fourier transform is taken.

4.3 Directional Filtering

The aim of directional filtering is to extract waves propagating with a specified range of directions. Here, the propagation direction is defined in the 3-D frequency-wavenumber domain. Specifically, the wavefield data are transformed from the time-space domain (t, x, y) into the frequency-wavenumber domain (ω, k_x, k_y) via the 3-D Fourier transform. Here, ω is the angular frequency, and k_x and k_y are components of the wavenumber vector k_r along the x and y axes, respectively. The actual wave propagation direction in the time-space domain can be estimated by the direction of wavenumber vector, $\boldsymbol{k_r} = k_x\hat{\boldsymbol{e}}_{\boldsymbol{x}} + k_y\hat{\boldsymbol{e}}_{\boldsymbol{y}}$, which is calculated by,

$$\theta_p = \arctan\left(\frac{k_y}{k_x}\right), \tag{4.4}$$

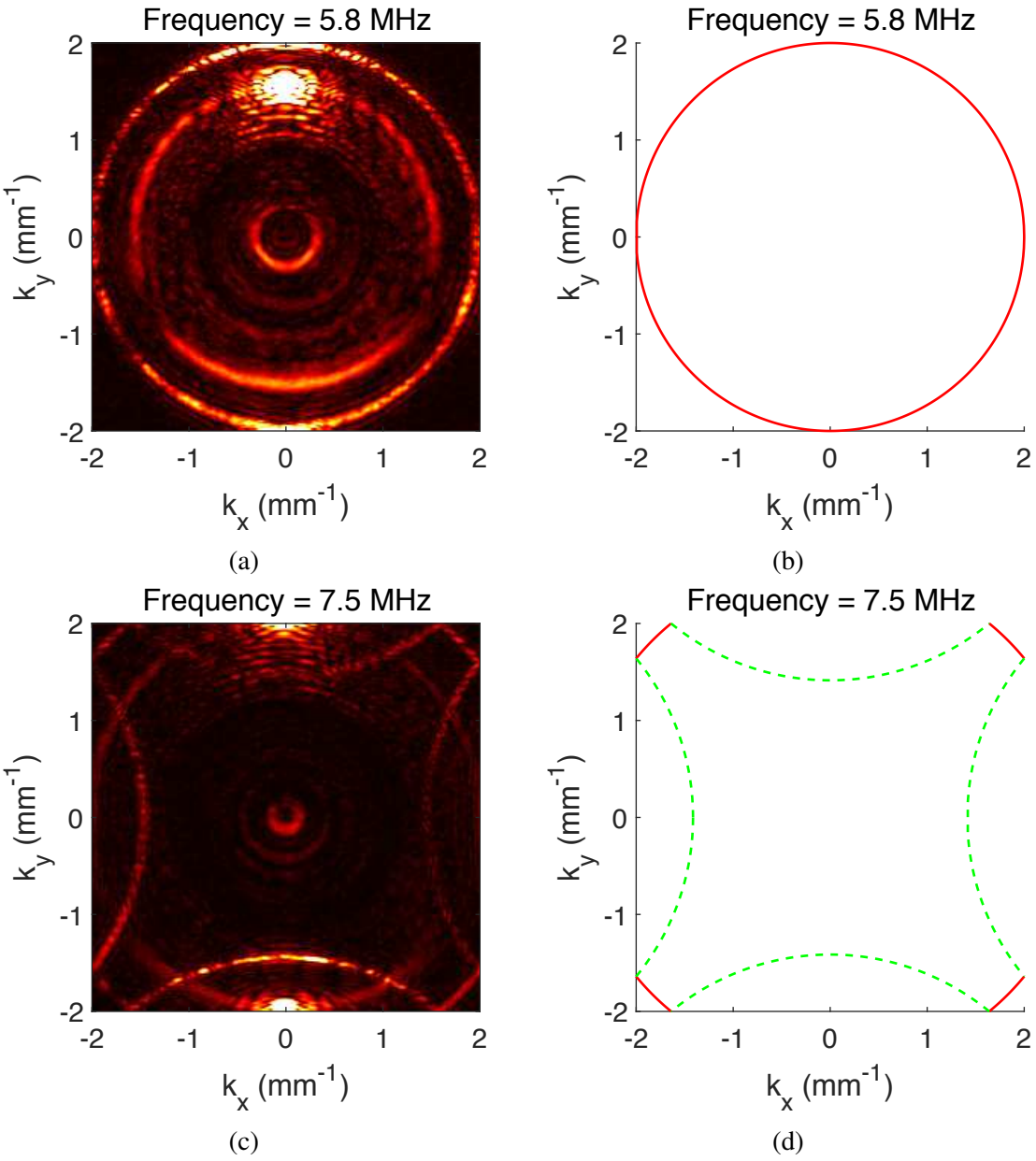

Figure 4.4: (a) Actual and (b) simulated k_x-k_y slices at a frequency of 5.8 MHz; (c) actual and (d) simulated k_x-k_y slices at a frequency of 7.5 MHz.

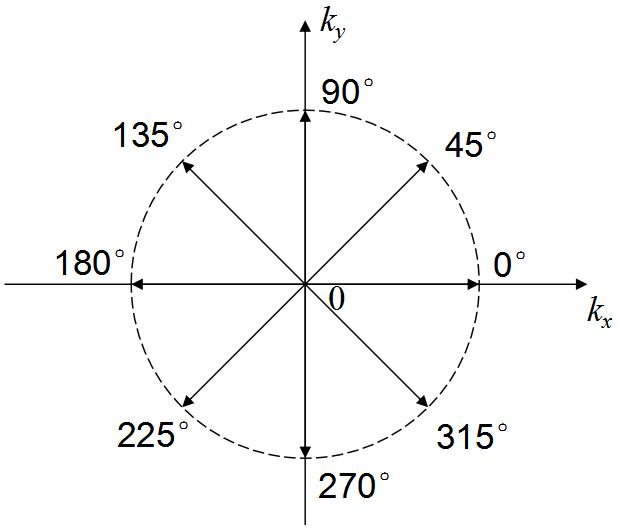

Figure 4.5: Diagram of wavenumber vectors in the k_x-k_y plane.

Figure 4.5 shows several wavenumber vectors marked with their respective propagation directions. As shown in the figure, 90° and 270° refer to vertically forward and backward propagation directions, respectively; 0° and 180° refer to propagation directions horizontally to the right and left, respectively.

Given the definition of the propagation direction, directional filtering can be built to extract waves with a specific propagation direction range. The general idea is to construct a 2-D directional k_x-k_y filter, multiply it with the wavefield data in the Fourier domain, and reconstruct the filtered directional waves in the time-space domain via the inverse FFT. The specific processing steps are illustrated by separating and extracting forward-propagating waves from the total wavefield using the total wavefield from scan A2. The propagation direction range of forward-propagating waves is from 0 to 180°. Based on the mapping relation between the time-space and frequency-wavenumber domains, the corresponding data distribute in the first and second quadrant where k_y is positive in the k_x-k_y plane. A k_x-k_y window can be built to filter in the data ($k_y > 0$), however, the edge effect around the k_x axis ($k_y = 0$) has to be addressed. Here, a one-sided 50% Tukey window is applied along the k_y axis from 0 to 2 mm^{-1} to make a smooth transition from 0 to 1 as shown in Figure 4.6(a). The 1-D positive k_y window is extended to the entire k_x-k_y plane (each k_x

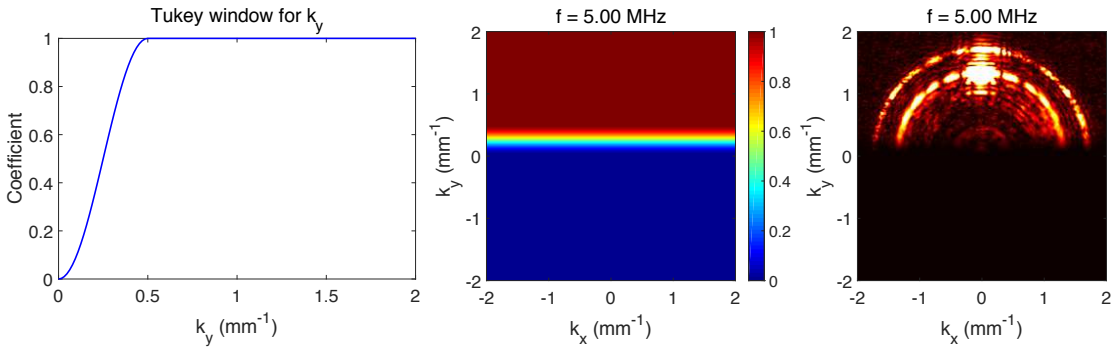

(a) (b) (c)

Figure 4.6: Forward-propagating wave filtering process: (a) a Tukey window for the +k_y axis, (b) k_x-k_y filter, and (c) filtered forward-propagating data at a frequency of 5 MHz.

value) shown in Figure 4.6(b). A direct multiplication of the smoothed k_x-k_y window and the Fourier wavefield data at each frequency value (each k_x-k_y slice) leads to the filtered data; an example is shown in Figure 4.6(c) at 5 MHz. The filtered forward-propagating waves in the time-space domain are reconstructed via the inverse 3-D Fourier transform. Figures 4.7(a) and 4.7(b) show the time snapshot comparison before and after directional filtering ($k_y > 0$). As shown in Figure 4.7(b), only forward-propagating waves are remaining. In addition, there are no obvious artifacts in the time-space domain caused by sharp edge effects in the Fourier domain. In a similar way, backward-propagating waves can be extracted by directional filtering ($k_y < 0$). Figure 4.7(c) shows the wavefield snapshot after extracting backward-propagating waves at 18.6 μs. As can be seen from the figure, all forward-propagating waves, which include incident waves and forward hole-scattered waves, are fully removed.

Directional filters can be built with any propagation direction range. Figure 4.8 shows more examples of directional filters with various propagation directions and their respective filtered wavefield snapshots at 18.6 μs. As can be seen from the figure, directional filtering is effective and robust to decompose wavefields by propagation directions. Here, the angle ranges of all provided directional filters equal to 180 degrees, but the angle ranges can be designed either more or less than 180 degrees based on the filtering purpose. However, narrower angle ranges may lead to more unexpected Fourier artifacts after reconstructing

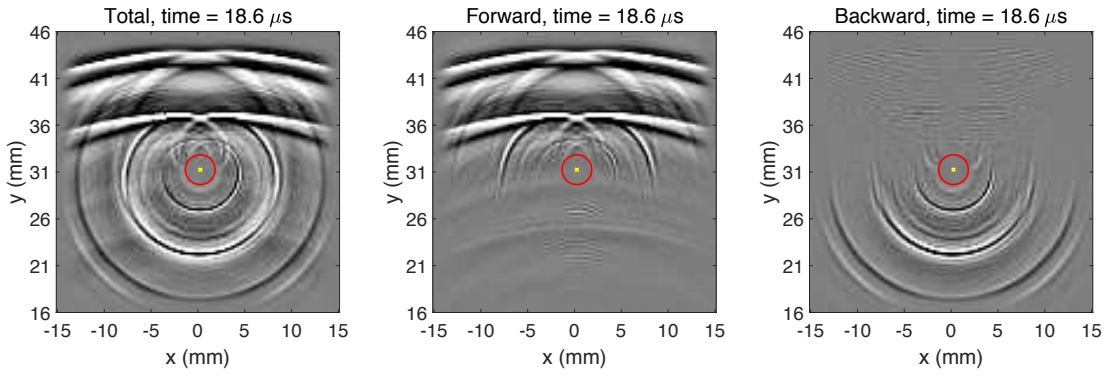

(a) (b) (c)

Figure 4.7: (a) Total wavefield snapshot at 18.6 μs, wavefield snapshots after (b) forward-, and (c) backward-propagating-wave filtering at 18.6 μs.

extracted wavefields in the time-space domain.

4.4 Wavefield Baseline Subtraction

The objective of wavefield baseline subtraction (WBS) is to isolate differences between baseline and current wavefields, which are recorded before and after a change (e.g., damage) is introduced. The baseline from an undamaged specimen, $w_B(t, x, y)$, is subtracted from the current wavefield, $w_C(t, x, y)$, acquired after the damage is introduced, which leads to the residual wavefield, $w_R(t, x, y)$,

$$w_R(t, x, y) = w_C(t, x, y) - w_B(t, x, y). \tag{4.5}$$

However, variations in both experimental and operational conditions between baseline and current wavefields are inevitable, which leads to temporal and spatial misalignment between two sets of wavefield data. As a consequence, direct WBS is usually not effective to remove incident waves and isolate scattered waves. Figure 4.9 shows time snapshots of current, unaligned baseline, and residual wavefields after direct WBS at 12 μs. As shown in Figure 4.9(c), incident waves are not fully removed.

For the sake of compensating for temporal and spatial misalignment, baseline alignment, which aims to find a baseline that is well-aligned to the current wavefield, is devel-

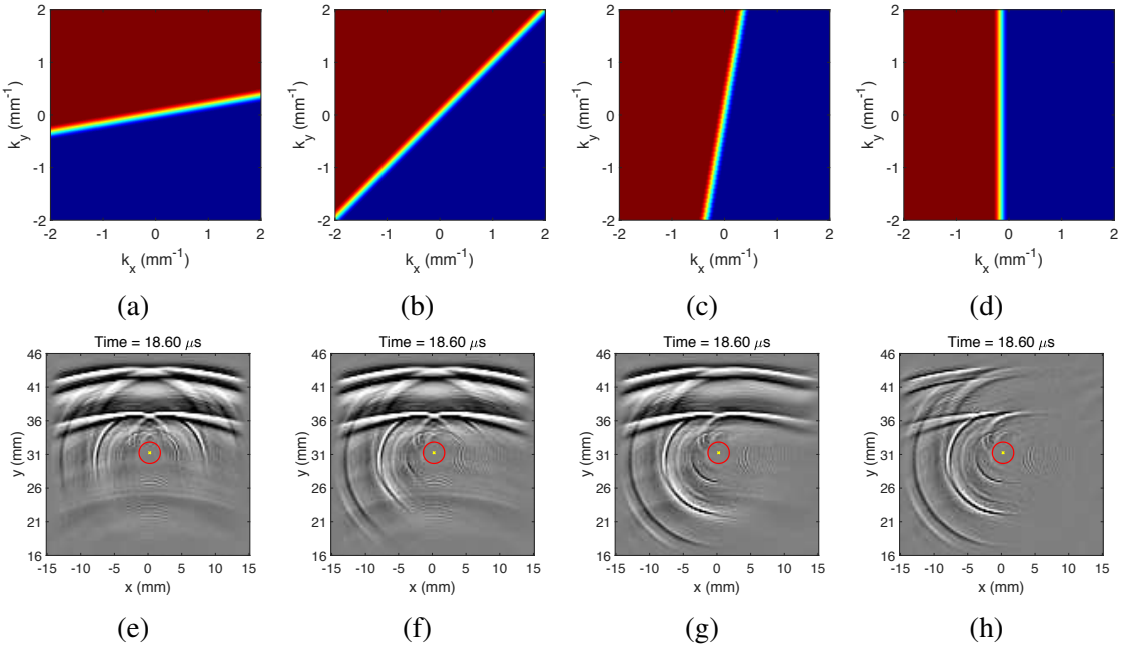

Figure 4.8: Directional filters whose propagation direction ranges are from (a) 10 to 190°, (b) 45 to 225°, (c) 80 to 260°, and (d) 90 to 270°, and their respective reconstructed wavefield snapshots (e)-(h) at 18.6 μs.

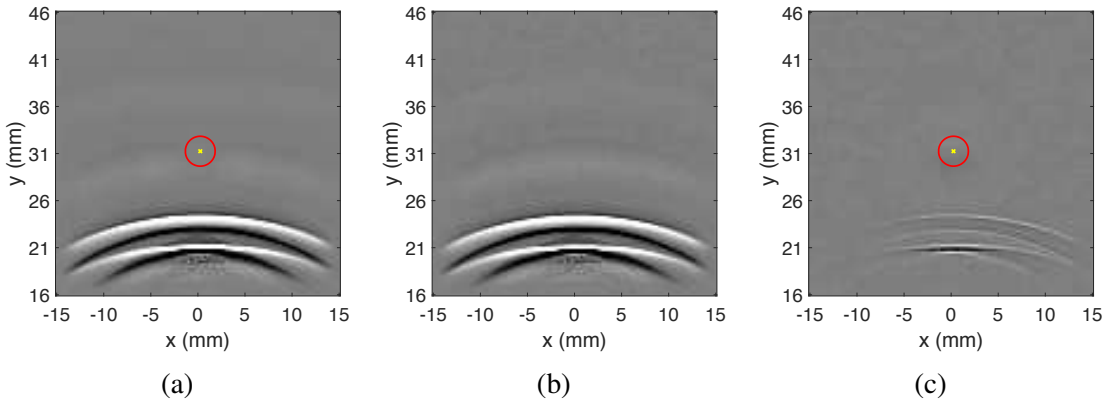

Figure 4.9: Wavefield baseline subtraction. (a) Current, (b) unaligned baseline, and (c) residual wavefield snapshots at 12 μs.

oped to improve the performance of WBS. Here, global space-time alignment (GSTA), a method developed previously by Dawson $et\ al.$ [97], is utilized to align the baseline wavefield. Basically, the strategy is to minimize the residual energy over the full extents of time and space by searching for the optimal time and space shifts $(\Delta t, \Delta x, \Delta y)$ of the baseline wavefield. However, the strategy here is modified to utilize only the incident waves prior to impinging upon a scatterer of interest for baseline alignment, which is expected to improve the baseline subtraction performance because these are the primary waves that are supposed to be removed after subtraction. The general idea is to firstly isolate incident waves before hitting any scatterer for both baseline and current wavefields, then implement GSTA to the two sets of filtered wavefields to find optimal shifts of time and space, and finally apply the acquired optimal shifts to the entire baseline wavefield to get the aligned baseline for subtraction. All processing steps are illustrated by scans A1 and A2 acquired before and after introducing a 3.18 mm diameter through-hole.

Firstly, two signal processing techniques as previously described, directional filtering and spatial windowing, are applied to extract incident waves before hitting the hole. Here, $+k_y$ filtering is designed to filter in waves propagating from 0 to 180° as shown in Figure 4.10(a). Figures 4.10(b) and 4.10(c) show the wavefield comparison at 16 μs before and after $+k_y$ filtering. As shown in Figure 4.10(c), a spatial window, smoothed by a 20% Tukey window at it edges marked with a green rectangle, is applied to extract only incident waves before hitting the hole (below the hole). The same directional filter and spatial window are also applied to process the baseline wavefield even though there are no backscattered waves for a pristine plate. Figure 4.10(d) shows the filtered baseline wavefield at the same time after $+k_y$ filtering.

GSTA is then performed to get the optimal shifts $(\Delta t, \Delta x, \Delta y)$ by using the filtered and windowed current and baseline wavefield data. The aligned baseline wavefield is obtained by applying the shifts to the total baseline wavefield. Compensation coefficient α, which is aimed to compensate for amplitude differences between baseline and current wavefields,

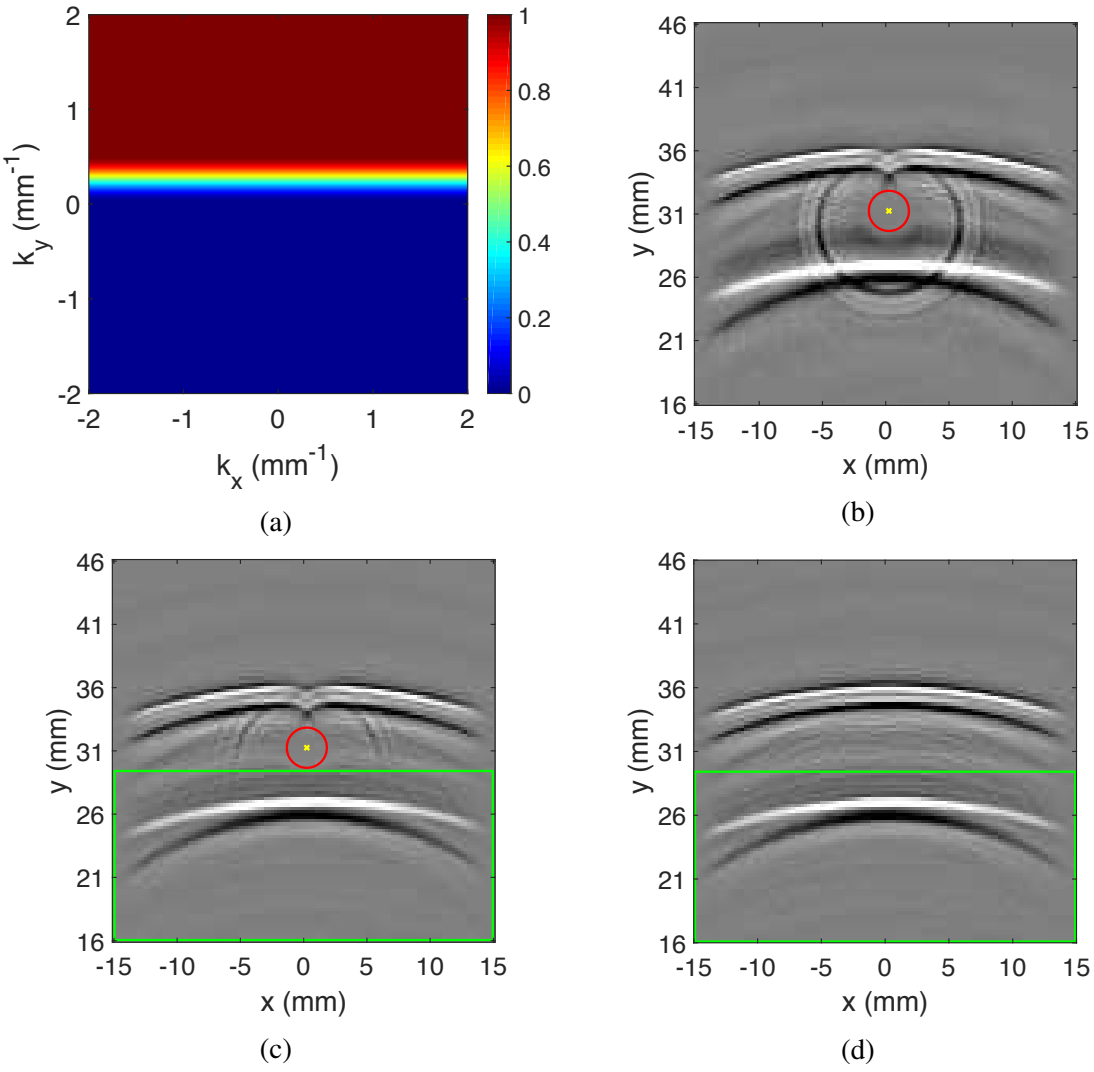

Figure 4.10: (a) Forward propagating k_x-k_y filter, current wavefield snapshots after at 16 μs (b) before and (c) after forward directional filtering, (d) baseline wavefield snapshot of 16 μs after the same forward directional filtering. Spatial windows are marked by green rectangles.

is calculated by minimizing the mean squared error of the residual energy of two sets of wavefield data. After baseline alignment and scaling, the residual wavefield is obtained by WBS. The complete wavefield baseline subtraction procedure is summarized as follows:

- Apply a 20% Tukey window to smooth the data along the t, x and y axes to avoid edge effects.
- Apply a 6$^{\text{th}}$ order circular Butterworth window to remove the through-hole noise.
- Take the 3-D Fourier transform: $w(t,x,y) \xrightarrow{\mathcal{F}} W(\omega,k_x,k_y)$.
- Apply $+k_y$ filtering: $W(\omega,k_x,k_y) \rightarrow W_{k_y>0}(\omega,k_x,k_y)$.
  - Apply a 20% Tukey window to smooth the data in frequency from 0 to 6 MHz to minimize spatial aliasing.
  - Apply a one-sided 50% Tukey window to smooth the data in k_y axis from 0 to 2 mm^{-1}.
- Take the inverse 3-D Fourier transform: $W_{k_y>0}(\omega,k_x,k_y) \xrightarrow{\mathcal{F}^{-1}} w_{\text{forward}}(t,x,y)$.
- Apply spatial windowing to isolate incident waves below the hole.
- Use GSTA to get the optimal shifts of time and space:

$$[\Delta t,\Delta x,\Delta y] = \arg\min \|W'_C(\omega,k_x,k_y) - W'_B(\omega,k_x,k_y)e^{-i(\omega\Delta t+k_x\Delta x+k_y\Delta y)}\|.$$

- Apply the optimal shifts to the entire baseline wavefield:

$$\hat{w}_B(t,x,y) = \mathcal{F}^{-1}\Big\{W_B(\omega,k_x,k_y)e^{-i(\omega\Delta t+k_x\Delta x+k_y\Delta y)}\Big\}.$$

- Calculate compensation coefficient α,

$$\alpha = \frac{\sum_{t,x,y} w_C\cdot\hat{w}_B}{\sum_{t,x,y}\hat{w}_B^2}.$$

- Calculate the residual wavefield $w_R(t,x,y)$,

$$w_R(t,x,y) = w_C(t,x,y) - \alpha\cdot\hat{w}_B(t,x,y).$$

Figures 4.11(a)-(c) show current, aligned baseline, and residual wavefield snapshots at 18.6 μs after applying the WBS procedures. As can be seen from Figure 4.11(c), most of incident waves are removed and hole-scattered waves are dominant. Figure 4.11(d) shows the residual wavefield snapshot at 12 μs before any incident shear waves hit the hole. As can be seen from the figure, only a slight amount of incident waves remains after the

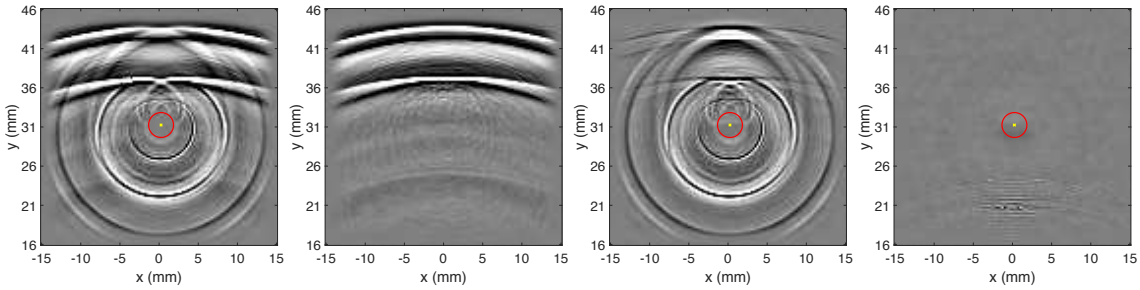

(a) (b) (c) (d)

Figure 4.11: Wavefield baseline subtraction. (a) Current and (b) aligned baseline wavefield snapshots at 18.6 μs. Residual wavefield snapshots at (c) 18.6 μs and (d) 12 μs, respectively, after baseline alignment.

WBS procedures. As compared to Figure 4.9(c), which shows the same residual wavefield snapshot after direct WBS, WBS after baseline alignment provides better performance than direct WBS. Therefore, wavefield baseline subtraction after baseline alignment is effective to isolate scattered waves from a single scatterer. This technique will be used for through-hole scattering analysis.

4.5 Phase Velocity Filtering

Three wave modes, Rayleigh, shear, and longitudinal, are observed in the obtained experimental wavefield data. Phase velocity filtering, as its name implies, is aimed to separate wave modes by their respective phase velocity ranges. Motivated by frequency-wavenumber filtering applied to separate guided wave modes by their dispersion curves [48, 49], phase velocity filters are developed in the frequency-wavenumber domain for isolating and separating Rayleigh, shear, and longitudinal waves. In general, there are three processing steps: transform the wavefield data from the time-space domain (t, x, y) into the frequency-wavenumber domain (ω, k_x, k_y) via the 3-D fast Fourier transform (FFT), build a 3-D frequency-wavenumber filter based on a specified phase velocity range, and reconstruct the extracted wave mode in the time-space domain via the inverse 3-D FFT. The following detailed procedures are illustrated by the residual wavefield from scans A1 and A2 after WBS.

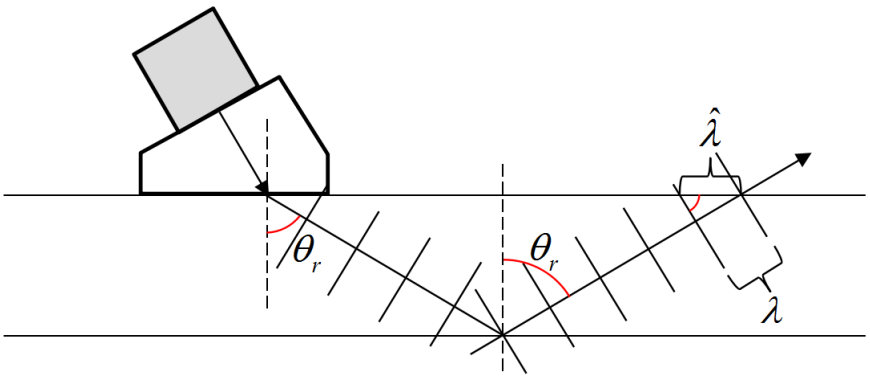

Figure 4.12: Diagram of the plate specimen from the side view for illustrating the apparent wavelength and phase velocity of bulk waves.

4.5.1 Phase Velocity as Measured on the Surface

Phase velocities of Rayleigh, shear, and longitudinal waves are key for building frequency-wavenumber filters for wave mode separation. Here, their respective wave speeds are taken to be 2.9, 3.1, and 6.3 mm/μs. Rayleigh waves, as a type of surface wave, propagate along the surface of a solid, so the measured phase velocity on the surface is very close to the nominal Rayleigh wave speed, 2.9 mm/μs. Unlike Rayleigh waves, shear and longitudinal waves propagate within the material in three spatial dimensions because of the nature of bulk wave propagation. However, wavefield measurements are performed on the exposed surface of a specimen in two spatial dimensions. Figure 4.12 illustrates bulk wave propagation by showing the traveling path of a single incident ray of a refracted angle θ_r from the side view. As can be seen from the figure, the apparent wavelength projected on the surface $\hat{\lambda}$ is longer than the actual wavelength λ and it is weighted by $1/\sin(\theta_r)$,

$$\hat{\lambda} = \frac{\lambda}{\sin(\theta_r)}. \tag{4.6}$$

As a consequence, the measured phase velocity is not the same as the bulk wave speed itself. According to the relation of $c = \lambda f$, the apparent phase velocity on the surface is calculated by,

$$c_p = \frac{c}{\sin(\theta_r)}, \tag{4.7}$$

which is also inversely proportional to $\sin(\theta_r)$. Therefore, shear and longitudinal phase velocities are larger than 3.1 and 6.3 mm/μs, respectively. As θ_r approaches zero (normal incidence), both phase velocities theoretically approach infinity. Thus, phase velocities are ambiguous for shear waves with small refracted angles and longitudinal waves with large refracted angles. The apparent surface shear wave velocity shifts into the longitudinal regime as $\sin(\theta_r)$ approaches zero. For example, both a shear wave with a refracted angle of 8.92° and a longitudinal wave with a larger refracted angle of 18.36° have the same apparent phase velocity of 20 mm/μs on the measurement surface. Despite this velocity ambiguity, the phase velocity range of shear waves is set from 3.1 to 6.3 mm/μs for shear mode extraction [98] since there are no Rayleigh or longitudinal waves present in this range; that is, only shear waves are remaining even though some may be missed. The phase velocity range of longitudinal waves is then set from 6.3 mm/μs to infinity to include all waves with high phase velocities in spite of small-refracted-angle shear waves involved. For convenience, they will still be referred to "longitudinal" waves. For Rayleigh waves, because Rayleigh waves cannot be faster than the shear wave speed, the phase velocity range is set from 2 to 3.1 mm/μs to guarantee that all Rayleigh energy is captured. All phase velocity ranges for filtering are summarized in Table 4.2.

Table 4.2: Phase velocity ranges.

Wave Mode	Bulk Wave Speed (mm/μs)	Phase Velocity Range (mm/μs)
Rayleigh	2.9	2-3.1
Shear	3.1	3.1-6.3
Longitudinal	6.3	6.3-∞

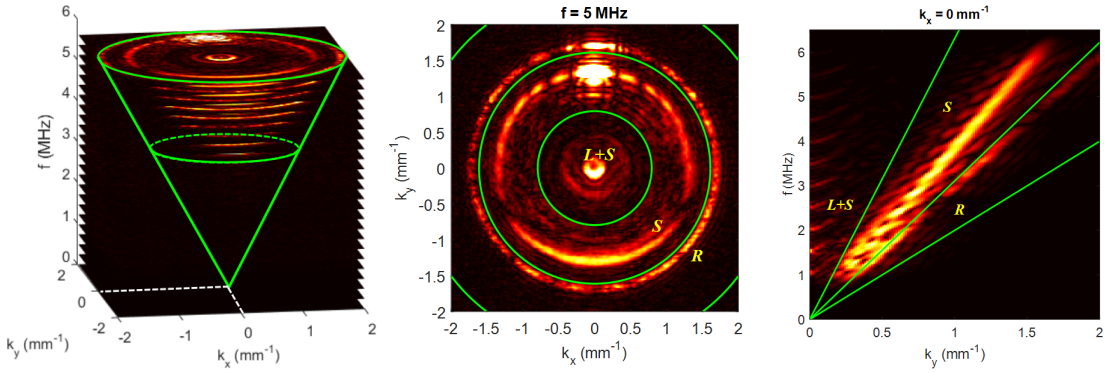

(a) (b) (c)

Figure 4.13: Wavefield data representation in the Fourier domain. (a) The 3-D frequency-wavenumber domain, (b) a k_x-k_y slice at a frequency of 5 MHz, and (c) a k_r-f slice at k_x = 0 mm^{-1}, $k_y > 0$.

4.5.2 Frequency-Wavenumber Boundaries in the 3-D Fourier Domain

This section presents how to build the frequency-wavenumber boundaries based on the phase velocity ranges. Wavefield data are transformed from the time-space domain (t, x, y) into the frequency-wavenumber domain (ω, k_x, k_y) via the 3-D Fourier transform. Figure 4.13(a) shows the 3-D cone-like Fourier data; that is, at each frequency level, the data appear in circular patterns as shown in Figure 4.13(b), and the radii of these circles become larger as the frequency increases as shown in Figure 4.13(c). The explanation of this distribution pattern depends on the well-defined relation among the angular frequency, wavenumber, and phase velocity,

$$c_p = \frac{\omega}{k_r}. \tag{4.8}$$

For a k_x-k_y slice at a specific frequency value, each wavenumber radius $k_r = \sqrt{k_x^2 + k_y^2}$ corresponds to specific wave components with a constant phase velocity c_p. Moreover, the wavenumber is inversely proportional to the phase velocity; larger phase velocities correspond to smaller wavenumber values. Similarly, for a k_r-f slice, a constant phase velocity corresponds to a specific line of a constant slope; larger phase velocities correspond to steeper lines. Given phase velocity ranges of each wave mode presented in Section 4.5.1,

their corresponding k_x-k_y and k_r-f boundaries in the 3-D frequency-wavenumber domain are built as marked in green circles in Figure 4.13(b) and green lines in Figure 4.13(c). For example, $c_{\min}$ and $c_{\max}$ are taken to be 3.1 and 6.3 mm/μs for the shear wave mode. Given a specific frequency value (ω or f), their respective wavenumber boundaries can be calculated by $k_{\max} = \frac{\omega}{c_{\min}}$ and $k_{\min} = \frac{\omega}{c_{\max}}$.

4.5.3 Build Frequency-Wavenumber Filters

The approach here is to build an annular k_x-k_y filter at each discrete frequency for a specific wave mode in the Fourier domain. As mentioned previously, for each frequency value, wavenumber boundaries ($k_{\min}$, $k_{\max}$) can be calculated as shown in Figure 4.14(a) by the green circles. Annular filters of each wave mode are then constructed in the k_x-k_y plane. Here, the edges of each k_x-k_y filter are smoothed by a 33% radial Tukey window between $k_{\min}$ and $k_{\max}$ to mitigate the Fourier artifacts caused by sharp edges. Figures 4.14(b), 4.14(c), and 4.14(d) show the k_x-k_y filters of Rayleigh, shear, and longitudinal waves, respectively, at 5 MHz. Filtered Fourier data of each wave mode are obtained by multiplication with their respective smoothed k_x-k_y filters along the frequency axis. Then, the reconstructed wavefield data of each mode in the time-space domain are acquired via the inverse 3-D Fourier transform. Figure 4.15 shows time snapshots at 18.6 μs before and after phase velocity filtering of each wave mode. As can be seen from the figure, phase velocity filtering is helpful to separate wave modes.

Detailed processing steps of phase velocity filtering are summarized as follows:

- Take the 3-D Fourier transform: $w(t, x, y) \xrightarrow{\mathcal{F}} W(\omega, k_x, k_y)$.
- Apply a 33 % Tukey window along the frequency axis between 0 and 6 MHz to eliminate spatial aliasing.
- For each discrete frequency, calculate $k_{\min} = 2\pi f / c_{\max}$ and $k_{\max} = 2\pi f / c_{\min}$.
- Apply a 33% Tukey window to smooth k_r between $k_{\min}$ and $k_{\max}$.
- Reconstruct filtered wavefields in the time-space domain via the inverse 3-D FFT:

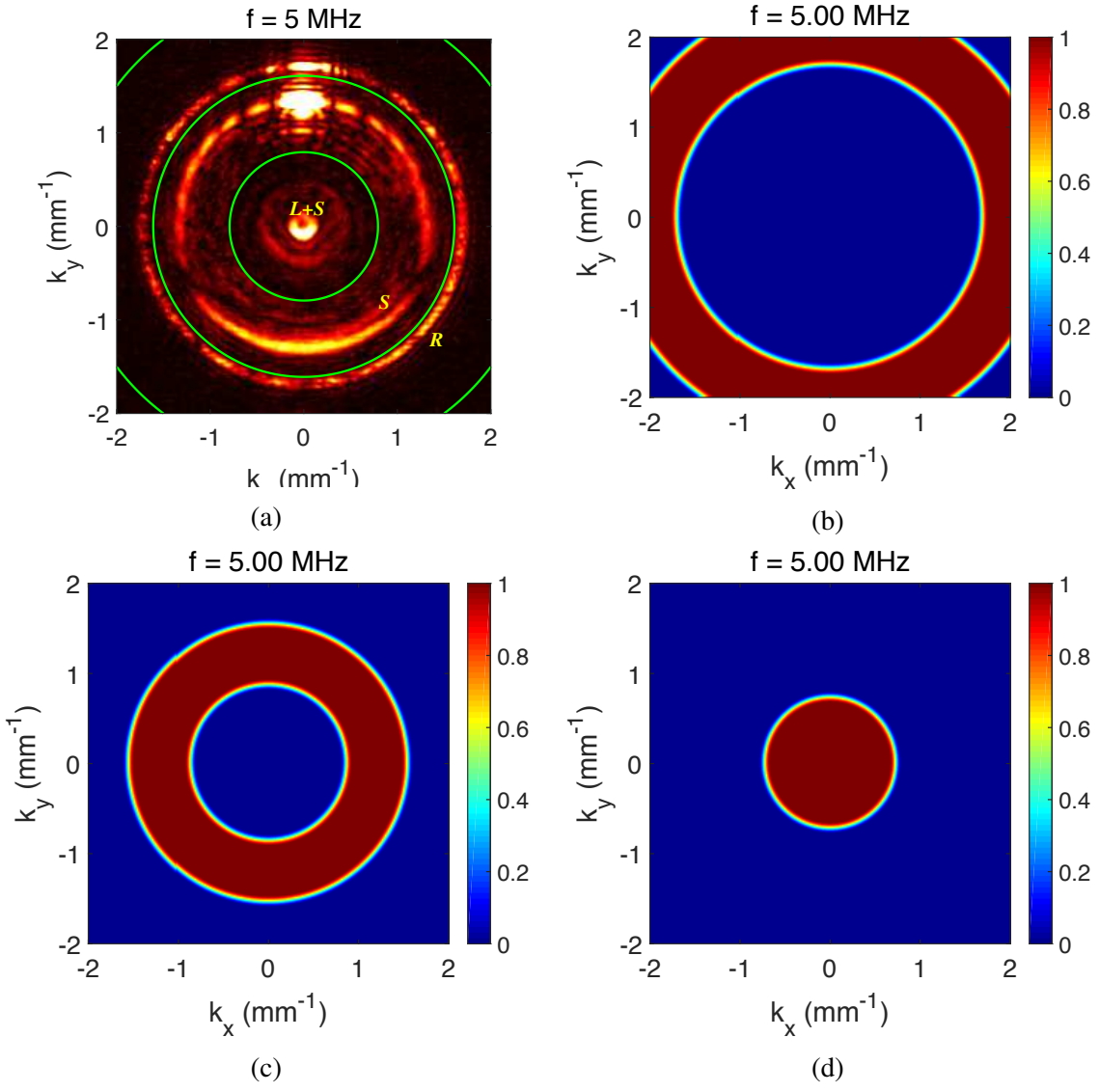

Figure 4.14: (a) Wavefield k_x-k_y slice at a frequency of 5 MHz, and corresponding (b) Rayleigh, (c) shear, and (d) longitudinal filters.

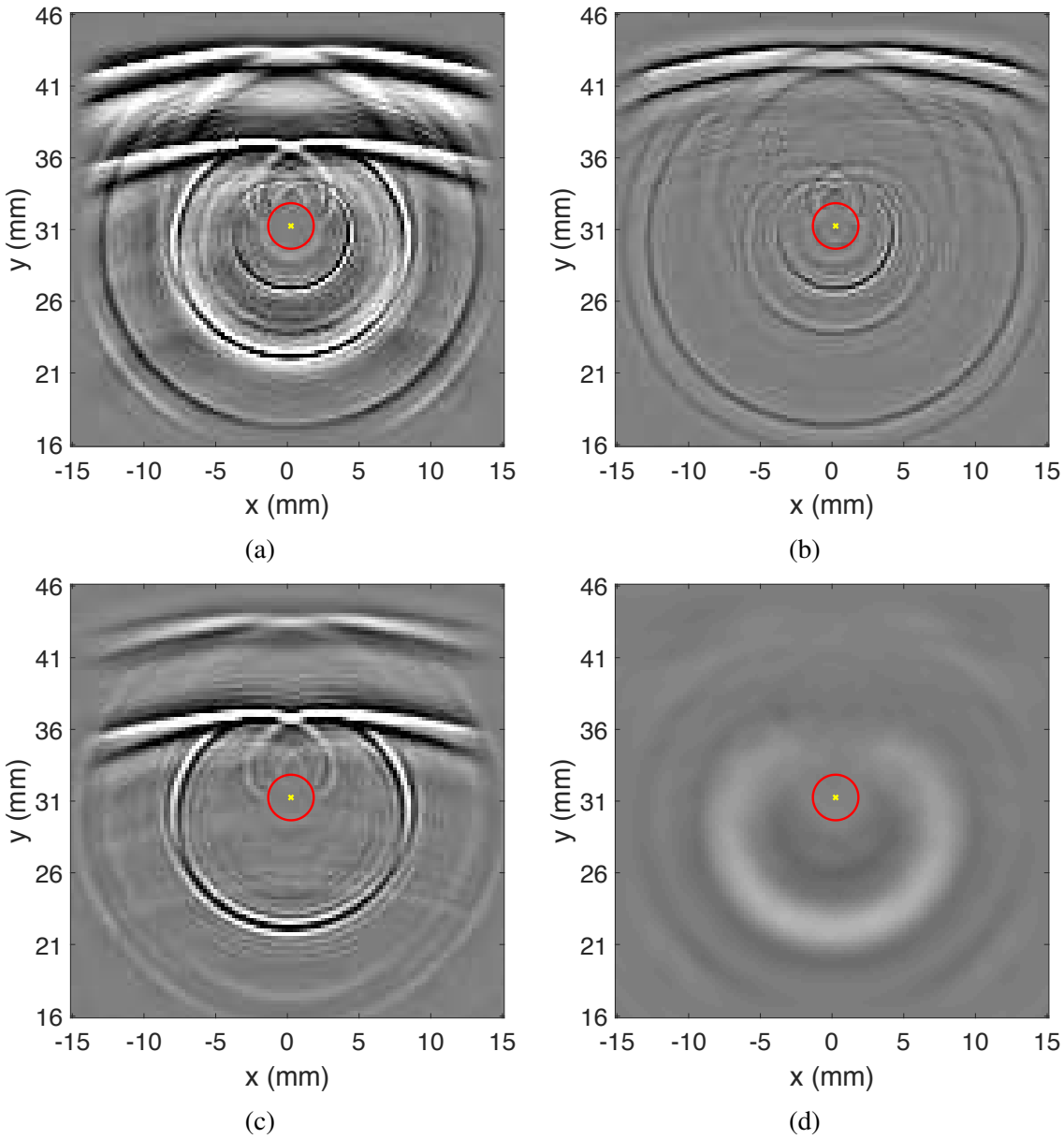

Figure 4.15: Wavefield snapshots of the (a) total, (b) Rayleigh, (c) shear, and (d) longitudinal waves at 18.6 μs.

$$W_{\text{mode}}(\omega, k_x, k_y) \xrightarrow{\mathcal{F}^{-1}} w_{\text{mode}}(t, x, y).$$

4.6 Ray Tracing Analysis

In this thesis, ray tracing is performed to obtain a deeper understanding of wave propagation and scattering behaviors inside the materials. Particularly, for angle-beam inspection, shear waves, as a type of bulk wave, propagate in three spatial dimensions within the plate. However, only the waves returning to the accessible surface can be sensed by a laser Doppler vibrometer in two spatial dimensions. As a result, the waveform information between plate surfaces is unknown. Therefore, ray tracing analysis inside the specimen becomes a complementary means to fill that gap. The goal of this analysis is to simulate how incident rays of shear waves propagate and how the subsequent scattered rays are affected by various scatterers, which include through-holes, part-through holes, and notches emanating from through-holes.

4.6.1 No Hole

This section introduces ray tracing analysis for tracking incident shear waves in pristine plates without any damage. Because of the nature of bulk wave propagation, shear waves are reflected by two plate surfaces, which lead to multiple shear wave skips. Here, one skip refers to a full V-path reflection of shear waves, which travel from the top plate surface, reflect from the bottom plate surface, and return to the top surface. In the experimental data of area scans, four shear wave skips, which are time-space separated, are present in total. For each skip, shear waves actually propagate with a range of different refracted angles because of beam spread. Therefore, in the wavefield videos of time, each shear wave skip has a continuously changing wave trajectory instead of limited discrete wave contours. Each shear wave trajectory at a specific snapshot time corresponds to a unique incident ray propagating with a specific refracted angle. Here, ray tracing analysis aims to build the mathematical relation among the refracted angle, skip number, on-surface propagating

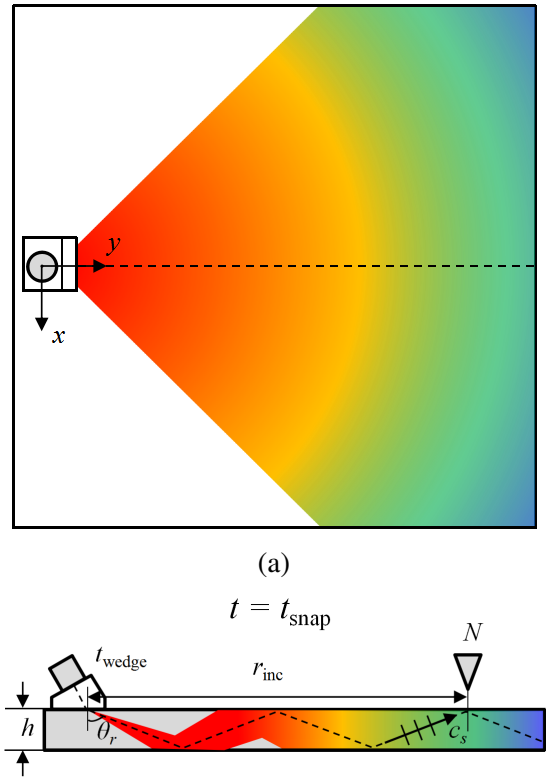

Figure 4.16: Plate specimens from the (a) top view and (b) side view.

distance of incident waves, and snapshot time.

Figure 4.16(a) shows the top view of a plate. As can be seen from the figure, the center of beam incidence is taken to be the origin in the x-y plane. Incident waves are assumed to propagate as circular arcs, so the on-surface propagating distance of the incident shear wave is expressed as a time-dependent radius r_{inc}. Figure 4.16(b) shows the side view of the plate specimen. Given a plate thickness of 6.35 mm, the probe is located at (0, 6.35) in the x-z plane. As shown in the figure, all incident rays are assumed to propagate from the same point source at the same time t_{wedge}. Here t_{wedge} is the wedge offset time for the waves propagating inside the wedge. Actually, there are more complex and comprehensive models to describe beam incidence [99, 100]; however, the model chosen here is not only easier and faster to execute because of its low computational complexity but it also provides good performance for tracking incident waves.

Based on the incident beam model, the traveling path of a specific incident ray can be drawn. As shown in Figure 4.16(b), at a general snapshot time of t_{snap}, an incident ray of refracted angle θ_r returns to the top plate surface after propagating with N skips ($N = 1, 2, 3, 4$). Here, t_{snap} can be also thought as an arrival time of the incident ray on the top surface. Based on the geometric information, the corresponding on-surface distance r_{inc} can be expressed as a function of t_{snap}:

$$r_{\text{inc}} = 2N\sqrt{\left[\frac{(t_{\text{snap}} - t_{\text{wedge}})c_s}{2N}\right]^2 - h^2}. \tag{4.9}$$

Here, the plate thickness h is 6.35 mm and the shear wave speed c_s is taken to be 3.1 mm/μs. In addition, in order to guarantee that Eq. (4.9) is meaningful, t_{snap} has to be larger than a threshold:

$$t_{\text{snap}} \geq t_{\text{wedge}} + \frac{2Nh}{c_s}. \tag{4.10}$$

Similarly, t_{snap} can be expressed as a function of r_{inc},

$$t_{\text{snap}} = t_{\text{wedge}} + \frac{\sqrt{r_{\text{inc}}^2 + (2Nh)^2}}{c_s}. \tag{4.11}$$

The refracted angle of the incident ray at this time can be calculated as,

$$\theta_r = \arctan\left(\frac{r_{\text{inc}}}{2Nh}\right), \tag{4.12}$$

Substituting r_{inc} from Eq. (4.9) yields,

$$\theta_r = \arctan\left(\frac{\sqrt{(t_{\text{snap}} - t_{\text{wedge}})^2 c_s^2 - (2Nh)^2}}{2Nh}\right), \tag{4.13}$$

which directly gives the refracted angle as a function of the snapshot time.

Now, a complete set of mathematical equations is available to describe incident shear wave propagation. According to Eq. (4.9), given a snapshot time t_{snap} and a specific skip

number N (e.g, $N = 1, 2, 3, 4$), the on-surface distance r_{inc} of that skip can be calculated as long as the offset time t_{wedge} is known. If r_{inc} is calculated, the simulated circular wave trajectory of any skip can be applied to the experimental data of area scans as shown in Figure 4.17(a). Here, the constant t_{wedge} is manually estimated by observing how well simulated wave trajectories match the actual area scan data, and is taken to be 4.2 μs for the 60° shear wedge. Note that t_{wedge} depends on the wedge angles and Table 4.3 summarizes the estimated wedge offset time for all used wedges.

Table 4.3: Wedge offset time setup.

Wedge Angle	t_{wedge} (μs)
45°	3.8
60°	4.2
70°	5.7

As can be seen from Figure 4.17(a), the calculated wave trajectories of incident shear wave skips, the 1st skip in red, 2nd skip in green, and 3rd skip in blue, are in good agreement with the actual data. Figure 4.17(b) shows the line scan ($x = 0, +y$ axis), which clearly depicts on-surface hyperbolic shear wave trajectories (distance r_{inc} versus time t_{snap}) along with the calculated curves. Again, calculated results are well matched with the experimental data. For each velocity curve, given a specific snapshot time (e.g., 19 μs), which corresponds to a vertical line marked with a dashed yellow line in Figure 4.17(b), the slope of the curve at that time corresponds to the apparent shear wave phase velocity. Mathematically, because the propagating distance r_{inc} is expressed as a function of time t_{snap} , the derivative of r_{inc} gives to the phase velocity:

$$c_p = \frac{dr_{\text{inc}}(t_{\text{snap}})}{dt_{\text{snap}}} = \frac{(t_{\text{snap}} - t_{\text{wedge}})c_s^2}{\sqrt{(t_{\text{snap}} - t_{\text{wedge}})^2 c_s^2 - (2Nh)^2}}. \tag{4.14}$$

As can be seen Eq. (4.14), the shear wave phase velocity is a function of snapshot time, which means for each shear wave skip, the phase velocity is changing with time. Given t_{snap} of 19 μs as an example, substituting t_{wedge} of 4.2 μs, c_s of 3.1 mm/μs, N of 2,

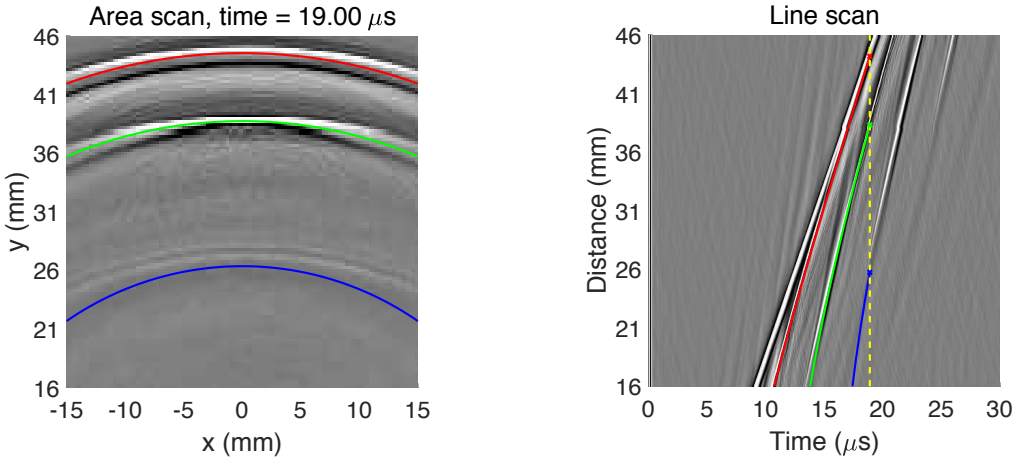

Figure 4.17: (a) Actual wavefield snapshot of 19 μs, (b) the line scan added with simulated wave trajectories of incident shear wave skips, and (c) side view with simulated incident rays at the same time.

and h of 6.35 mm, the phase velocity is calculated by $c_p = \frac{(19-4.2)3.1^2}{\sqrt{(19-4.2)^2 3.1^2-(2\cdot 2\cdot 6.35)^2}} = 3.723$ mm/μs. Based on Eq. (4.13), the refracted angle of this incident ray is $\theta_r = \arctan\left(\frac{\sqrt{(19-4.2)^2 3.1^2-(2\cdot 2\cdot 6.35)^2}}{2\cdot 2\cdot 6.35}\right) = 56.38°$. The answer can be validated by Eq. (4.7). By substituting the calculated refracted angle of $56.38°$ and the shear wave speed of 3.1 mm/μs, the phase velocity also equals to $c_p = \frac{3.1}{\sin(56.38°)} = 3.723$ mm/μs. Recall that all mathematical relations are based on the assumption that all incident rays start traveling from the same point source at the same time. Therefore, the shear wave phase velocity also validates the beam incidence model. Figure 4.17(c) shows the simulated ray paths for the first three shear wave skips from the side view at the same snapshot time of 19 μs. Note that the 4$^{\text{th}}$ incident shear wave skip has not returned to the top surface yet, so it is not drawn in the figure.

Figure 4.18 shows more simulated traveling paths of shear wave skips at different snapshot times, the 1$^{\text{st}}$ in red, 2$^{\text{nd}}$ in green, 3$^{\text{rd}}$ in blue, and 4$^{\text{th}}$ in yellow. Regardless of the skip number, once the incident ray of a specific skip returns to the top surface, a complete V-path can be drawn. At the beginning, refracted angles are small (steep) so that phase velocities are large. In line scan figures, these rays correspond to steep slopes (near to vertical forward lines). Theoretically, the shear wave phase velocity can be infinity with a zero refracted angle. As time progresses, refracted angles become larger so that phase velocities become smaller. As the time approaches infinity, shear wave phase velocities for all skips asymptotically approach the shear wave speed of 3.1 mm/μs. Because of beam spread, incident rays of different refracted angles propagate from the center of beam incidence, which leads to multiple time-space separated incident skips. Incident waves with larger skips need more time to be reflected by the plate surfaces and measured on the top plate surface. As shown in Figure 4.18(a), only the first skip returns to the top surface at 10 μs, but all four skips are observable at 25 μs shown in Figure 4.18(d).

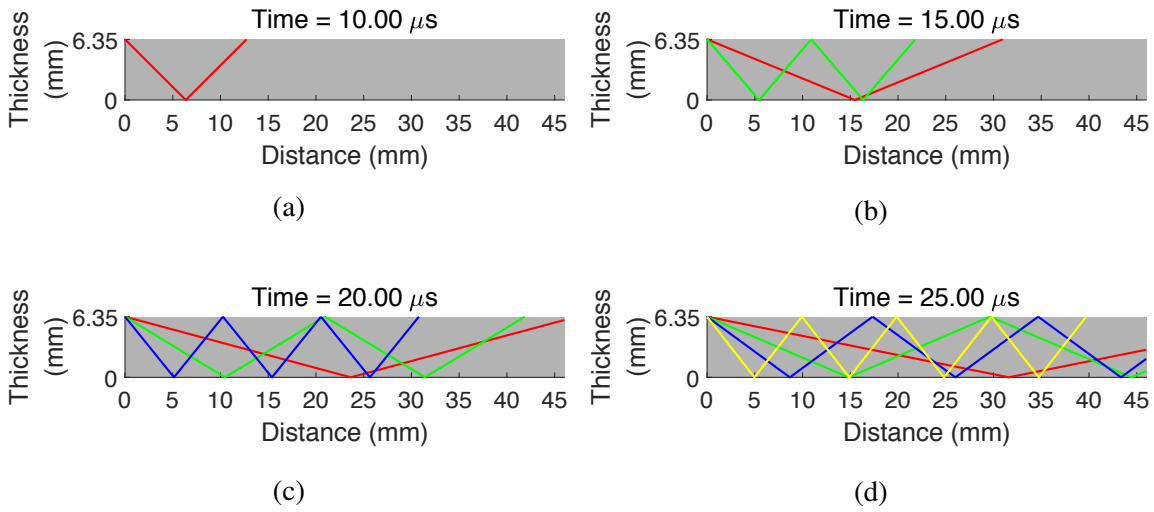

Figure 4.18: Side view with simulated incident rays at (a) 10 μs, (b) 15 μs, (c) 20 μs, and (d) 25 μs.

4.6.2 Through-Holes

This section introduces ray tracing analysis for tracking hole-scattered waves from through-holes. When a through-hole is introduced, time-space separated incident shear wave skips lead to their respective hole-scattered waves as shown in Figure 4.19. As can be seen from the figure, four skips of incident shear waves and their resulting hole-scattered waves are observed. In addition, the 2nd skip, which is the strongest one compared with other three skips, also results in the strongest shear wave scattering by the through-hole. Therefore, the following ray tracing analysis is illustrated by the hole-scattered rays resulting from the 2nd incident skip, but the analysis can also be used to track other skips.

Given a skip number of two, the traveling path of incident shear waves propagating with 2-V paths can be drawn. As previous analysis presented for simulating incident wave propagation under pristine plates, refracted angles become larger with time. When the incident ray hits the hole edge as shown in Figure 4.20(a), hole-scattered waves become visible in the observed wavefield data. Here, a 3.18 mm diameter through-hole is centered at 31 mm expressed by a gray rectangle. Given the on-surface distance between the hole edge and center of beam incidence, 29.41 mm, the refracted angle of this incident ray, $49.2°$,

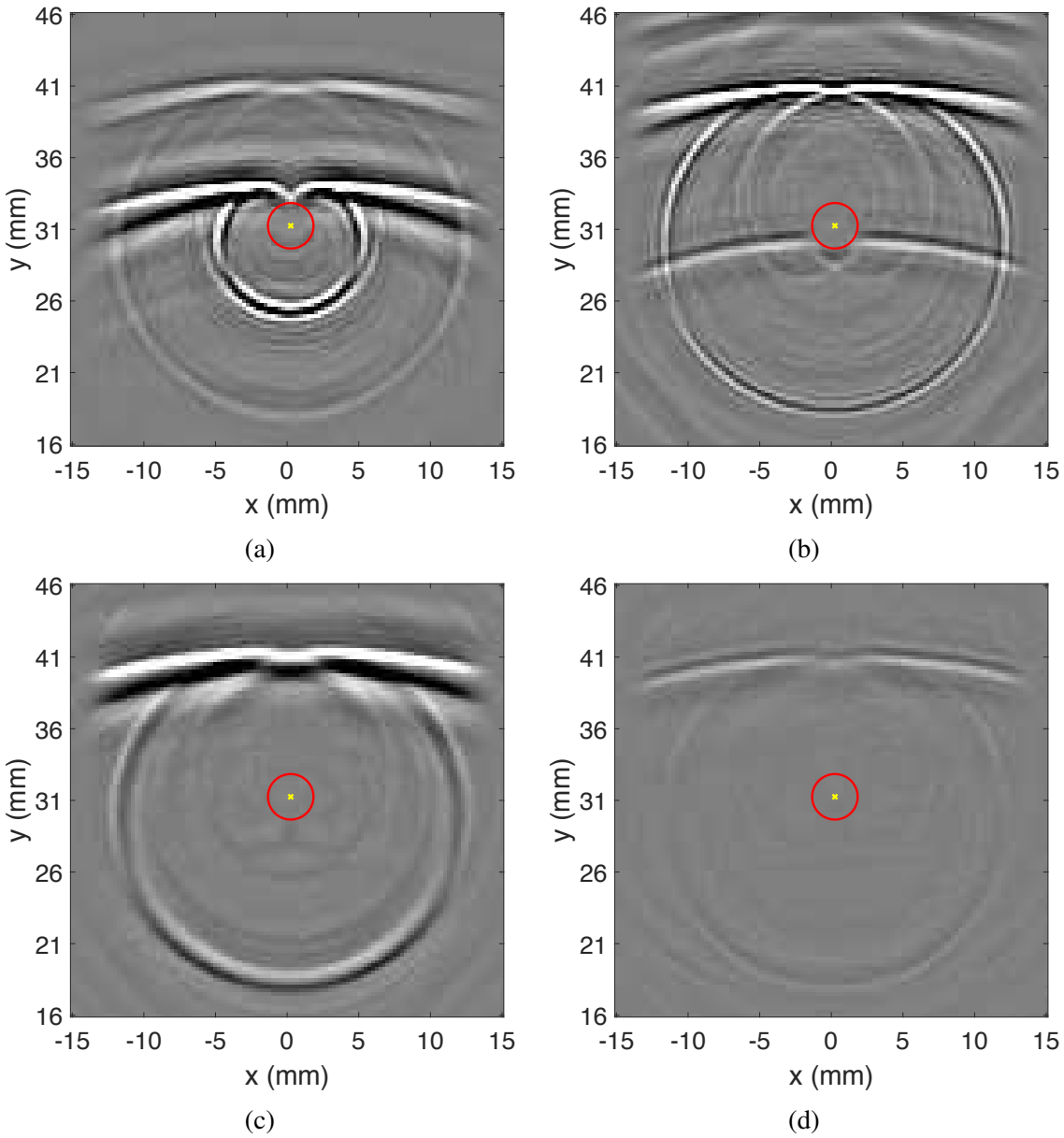

Figure 4.19: Shear wavefield snapshots at (a) 17.8 μs, (b) 19.6 μs, (c) 22.2 μs, and (d) 25 μs.

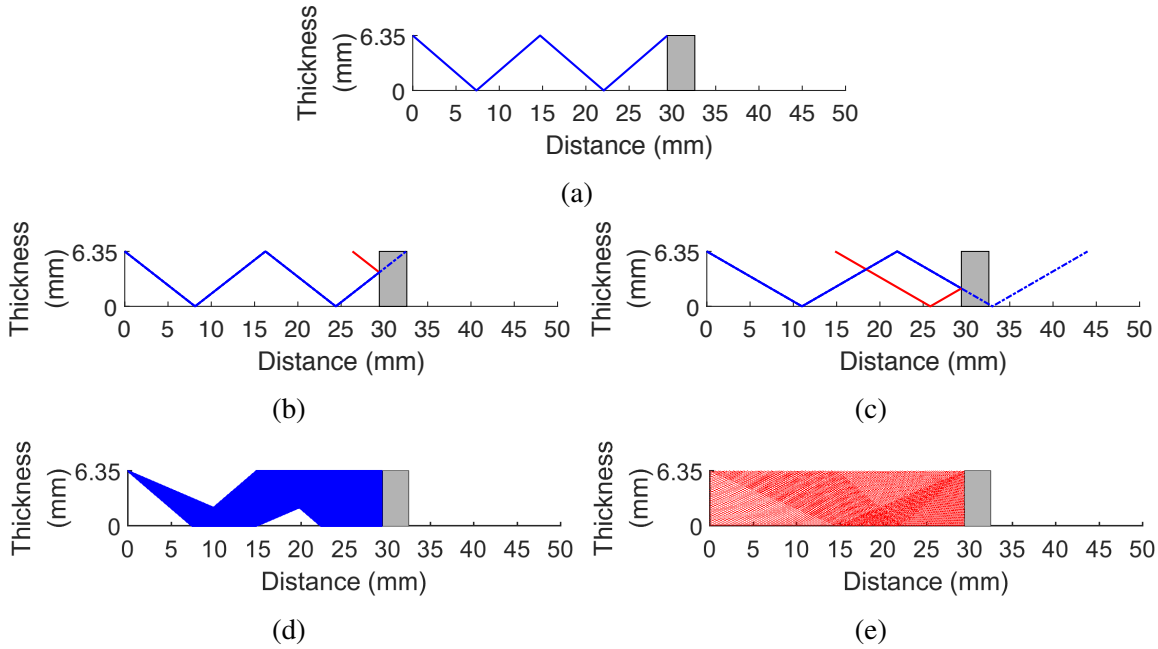

Figure 4.20: (a) Side view with simulated incident rays propagating at refracted angles of (a) 49.2 °, (b) 52°, and (c) 60° in blue and scattered rays in red. (d) Incident rays whose refracted angles are from 49.2 to 66.6° in blue and (e) their corresponding scattered rays in red.

is calculated by Eq. (4.12) and the hitting time equals to 16.74 μs by Eq. (4.11). When the snapshot time is larger than the calculated hitting time, subsequent incident rays with larger refracted angles will hit the front side of the hole. A specular reflection is assumed at the cylindrical front surface of the hole. Under this assumption, given a specific refracted angle of an incident ray that hits the hole, the reflected angle of the corresponding scattered ray is known and a traveling path can be drawn from the side view.

Figures 4.20(b) and 4.20(c) provide two examples of incident rays in blue that hit the front surface of the hole and lead to scattered rays in red. In addition, dashed blue lines show the supposed traveling path of incident rays propagating two skips without hitting the hole. The corresponding on-surface distance is still expressed by r_{inc}, which can be calculated by Eq. (4.9) given a snapshot time or the inverse format of Eq. (4.12) given a refracted angle. As can be seen from the figure, regardless of the refracted angle, the path length of the dashed blue line is the same with the path length of the red line because of

geometrical symmetry. Thus, the time of flight for these two rays is the same. Given this relation, the on-surface distance r_{scat}, which refers to the projected length of the scattered ray path in red, is calculated by,

$$r_{\text{scat}} = r_{\text{inc}} - r_{\text{hit}} = 2Nh\tan(\theta_r) - \big(y_c - r_{\text{hole}}\big). \tag{4.15}$$

Here, r_{hit} refers to the on-surface distance between the center of beam incidence and the hitting point. Here, r_{hit} equals to 29.41 mm, the difference between y_c of 31 mm, the y coordinate of the hole center, and r_{hole} of 1.59 mm, the hole radius. r_{inc} has to be larger than $(y_c - r_{\text{hole}})$ to make this equation meaningful, which indicates when incident rays start hitting the hole surface. For example, Figure 4.20(b) shows an incident ray of 52° hitting the hole. Given N of 2, h of 6.35 mm, θ_r of 52 °, y_c of 31 mm, and r_{hole} of 1.59 mm, r_{scat} equals to 3.1 mm calculated by Eq. (4.15). Similarly, in Figure 4.20(c), r_{scat} = 14.58 mm for an incident ray whose refracted angle is 60°. In addition, based on the known geometric information, all incident rays that hit the hole can be calculated and simulated as shown in Figure 4.20(d). The refracted angle range is calculated from 49.2 to 66.6°, and their respective scattered rays are drawn as shown in Figure 4.20(e). Regardless of the refracted angle, the calculation process of r_{scat} is summarized into two steps as follows:

- Given t_{snap}, r_{inc} is calculated by $r_{\text{inc}} = 2N\sqrt{\left[\frac{(t_{\text{snap}} - t_{\text{wedge}})c_s}{2N}\right]^2 - h^2}, N = 2.$
- Once $r_{\text{inc}} > r_{\text{hit}}$, r_{scat} is calculated by $r_{\text{scat}} = r_{\text{inc}} - r_{\text{hit}}$.

Based on these steps, r_{scat} can be calculated; however, it is not enough to determine the location where the scattered ray reaches the top surface because both incident and scattered shear waves interact with the two plate surfaces in three spatial dimensions. Ray tracing analysis from the top view is also necessary. Figure 4.21(a) shows a diagram of a plate specimen from the top view. The shear probe, located at the origin in the x-y plane, generates angle-beam shear waves propagating as circular arcs as assumed previously. Recall that propagation directions of 90° and 270° represent vertically forward and backward directions. Here, an incident ray propagating along a specific direction is marked in a blue

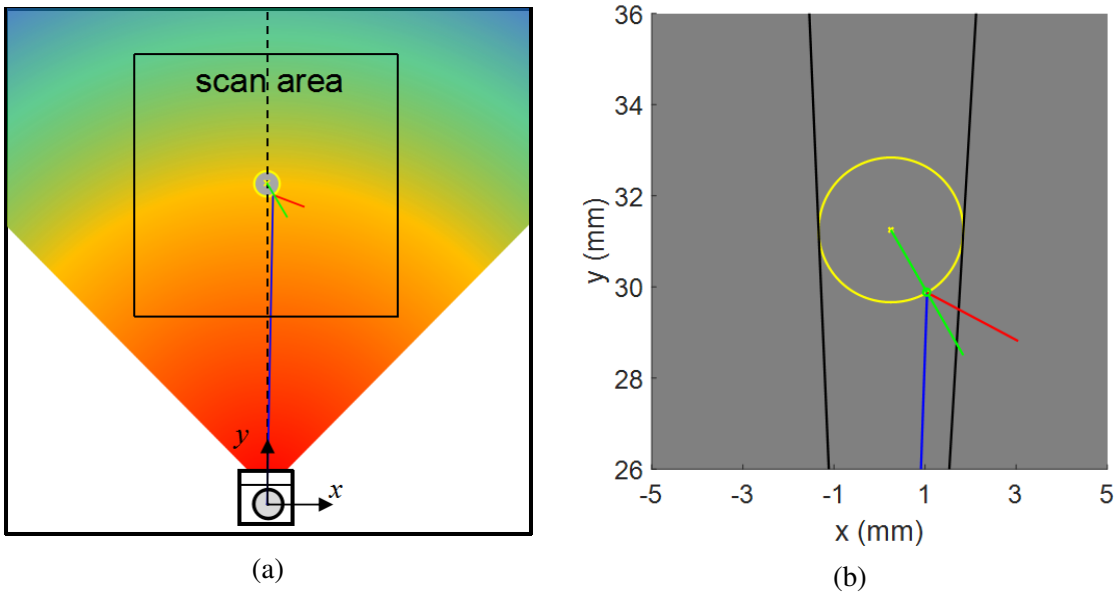

(a) (b)

Figure 4.21: (a) Top view of the plate specimen marked with an incident ray of 88° in blue, normal vector from the hole center in green, and scattered ray in red. (b) Zoom-in top view of hole specular reflection.

line from the origin to a hitting point on the front side of the hole. A specular reflection is assumed again at the hitting point on the hole from the top view. A green line indicates the normal direction with respect to the hole and a red line indicates the scattered (reflected) direction.

Figure 4.21(b) shows a zoomed-in view, which is clearer for describing the angle relation. Two black lines, which are exactly tangent to the hole surface, show the boundaries of incident rays that hit the hole. As long as an incident ray propagates between these two lines, a specular reflection is assumed to obtain the scattered direction in the x-y plane. Specifically, given the hole location and an incident ray with a known propagation direction of 88° shown with a blue line, the hitting point on the hole can be calculated. The normal direction from the hole center to the hitting point is therefore known and is shown with a green line. Based on a specular reflection, the angle between the incident and normal directions should equal the angle between the scattered and normal directions. Then, the corresponding scattered direction can be calculated as shown with a red line. Finally, an angle relation map, which stores propagation directions of any incident rays that hit the

hole and their respective scattered directions, can be built.

By combining the angle relation map and calculated on-surface distance r_{scat} for each scattered ray, the location where scattered waves appear on the top surface can be determined. Figure 4.22(a) shows a shear wavefield snapshot at 19 μs. Based on the previous analysis of tracking incident waves, the wave trajectory of the 2$^{\text{nd}}$ incident shear skip is shown with a blue circular arc expressed by r_{inc}. The hitting point location on the hole (x_{h}, y_{h}) can be calculated for each possible incident ray that can hit the hole based on the geometric information. As an example of an incident ray whose propagation direction is 88° shown in the blue line in Figure 4.22(a), the hitting point (x_{h}, y_{h}) can be calculated as the point where the ray hits the hole circle. The on-surface distance is then calculated by $r_{\text{hit}} = \sqrt{x_{\text{h}}^2 + y_{\text{h}}^2}$. Here, r_{hit} is not equal to the special format of $(y_c - r_{\text{hole}})$ anymore because the propagation direction of this incident ray is not 90° (vertically forward through the hole center). The on-surface distance for the corresponding scattered ray r_{scat} is then calculated by a general format of $(r_{\text{inc}} - r_{\text{hit}})$. Based on a specular reflection, the scattered direction is obtained and expressed by θ_s. Then, the scattered coordinates (x_s, y_s) where the scattered ray is visible on the top plate surface can be calculated by,

$$x_{\text{s}} = x_{\text{h}} + r_{\text{scat}} \cdot \cos\theta_s, \tag{4.16}$$

and

$$y_{\text{s}} = y_{\text{h}} - r_{\text{scat}} \cdot \sin\theta_s. \tag{4.17}$$

As can be seen from the figure, the calculated scattered point expressed by a red dot is in good agreement with the actual scattered wavefront. Figure 4.22(b) shows the calculated incident and scattered rays from the side view at the same snapshot time.

For each incident ray that hits the hole, the corresponding scattered point is obtained by repeating the procedures described above. These resulting scattered points constitute the

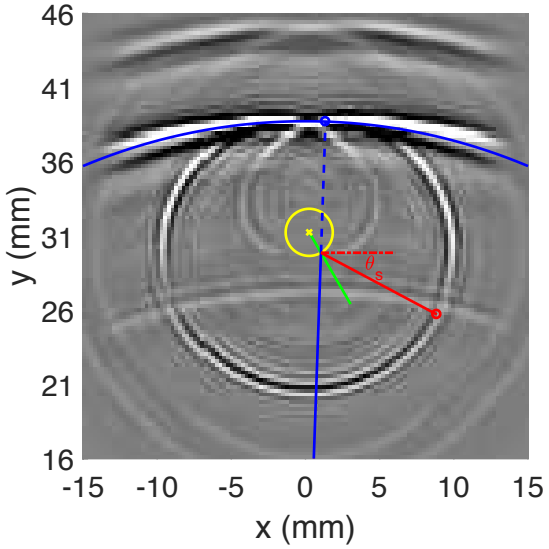

(a)

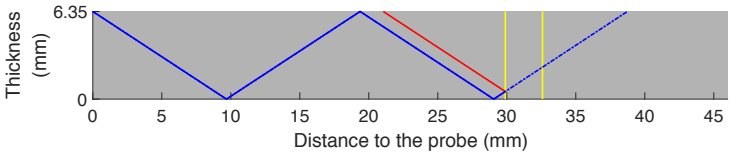

(b)

Figure 4.22: (a) Shear wavefield snapshot of 19 μs added with simulated incident wave trajectory and incident ray of 88° in blue, normal vector in green, and scattered ray in red. (b) Side view of simulated incident and scattered ray paths at 19 μs.

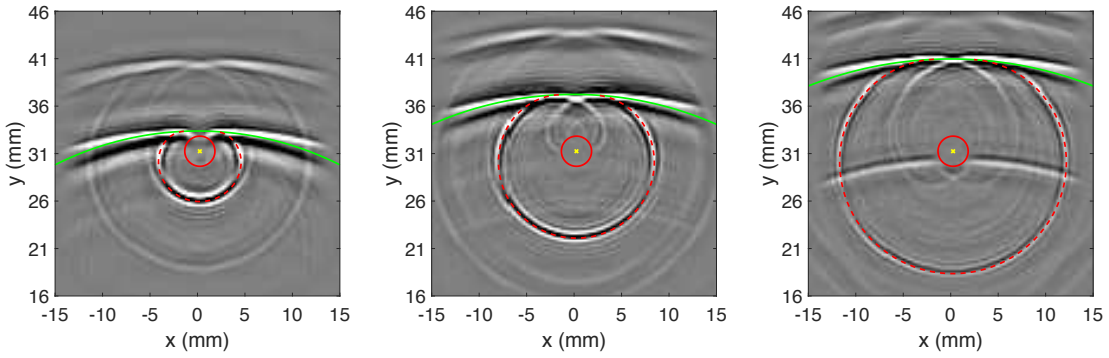

Figure 4.23: Shear wavefield snapshots with calculated trajectories of the second skip of shear incident and scattered waves at (a) 17.6 μs, (b) 18.6 μs, and (c) 19.6 μs.

calculated trajectory of the scattered waves. Figure 4.23 shows the calculated trajectories in red overlaid on snapshots at 17.6 μs, 18.6 μs, and 19.6 μs with the 2$^{\text{nd}}$ incident shear wave skip shown in green. As can be seen from the figure, these calculated trajectories are in excellent agreement with the experimental wavefronts as time progresses, which validates the accuracy of the ray tracing process.

There is an alternative method to calculate the on-surface distance for each scattered ray r_{scat}. Given an incident ray with a specific propagation direction and the hole geometry, the hitting point on the hole (x_h, y_h) and corresponding on-surface distance r_{hit} are known. Then, the time of flight t_{hit} can be calculated by,

$$t_{\text{hit}} = t_{\text{wedge}} + \frac{\sqrt{r_{\text{hit}}^2 + (2Nh)^2}}{c_s}. \tag{4.18}$$

If t_{snap} is larger than t_{hit}, it indicates that incident rays have reached the hole and resulted in scattered rays. The remaining time $(t_{\text{snap}} - t_{\text{hit}})$ is the time for the subsequent scattered waves to propagate with an on-surface distance of r_{scat} along the scattered wave direction. This distance can be estimated using the phase velocity of the shear wave at the nominal refracted angle $\theta_{\text{r\_nom}}$,

$$r_{\text{scat}} = c_{\text{p\_nom}}(t_{\text{snap}} - t_{\text{hit}}), \tag{4.19}$$

where $c_{\text{p\_nom}} = c_s / \sin(\theta_{\text{r\_nom}})$ and c_s is the shear bulk wave speed. This estimation is verified by analyzing radial line scans, which show that the scattered shear waves propagate at very close to the nominal phase velocity. Figure 4.24 shows a set of radial line scans at various polar angles, starting at the center of the hole and ending at a radius of 14 mm (scan area boundary). The dashed green lines indicate the location of the hole boundary (noise inside the hole has been suppressed). In each subfigure, there are three obvious trajectories that correspond to the first three incident shear skips. These trajectories clearly follow curved (hyperbolic) paths as previously discussed in Section 4.6.1. Unlike the incident wave trajectories, the scattered wave trajectories can be well-approximated as straight lines in each subfigure; that is, the phase velocity for each scattered ray can be taken as a constant. The underlying assumption of Eq. (4.19) is that the scattered wavefront propagates at the same nominal shear wave phase velocity even though the refracted angle of the incoming waves is changing with time.

Both methods for calculating r_{scat} work well on tracking the actual hole-scattered waves in the wavefield videos. Both are also fast to execute with no one method being better than the other, but the first method introduced will be utilized for subsequent results. Regardless of the method used, the time-dependent calculated wave trajectories of the hole-scattered skip can be built by combining the resulting scattered points. This technique is robust and effective for tracking different hole-scattered skips caused by various diameter holes. In addition, the technique can be also applied to the wavefield data by utilizing transducers with different angle wedges aimed at different points instead of the hole apex. Figure 4.25 summarizes several time snapshots added with calculated wave trajectories of hole-scattered skips caused by a 6.35 mm diameter through-hole. All probes aim at the right hole edge, which is 3.18 mm horizontally right of the hole center. Figures 4.25(a)-4.25(c) show results from scan C7 using a 45° wedge. Unlike the probe configuration of a 60° wedge, the 45° wedge was placed at a distance of 29.7 mm, which corresponds to 2.5 skips of the 43.1° nominal incident shear waves instead of 1.5 skips, aiming at the right

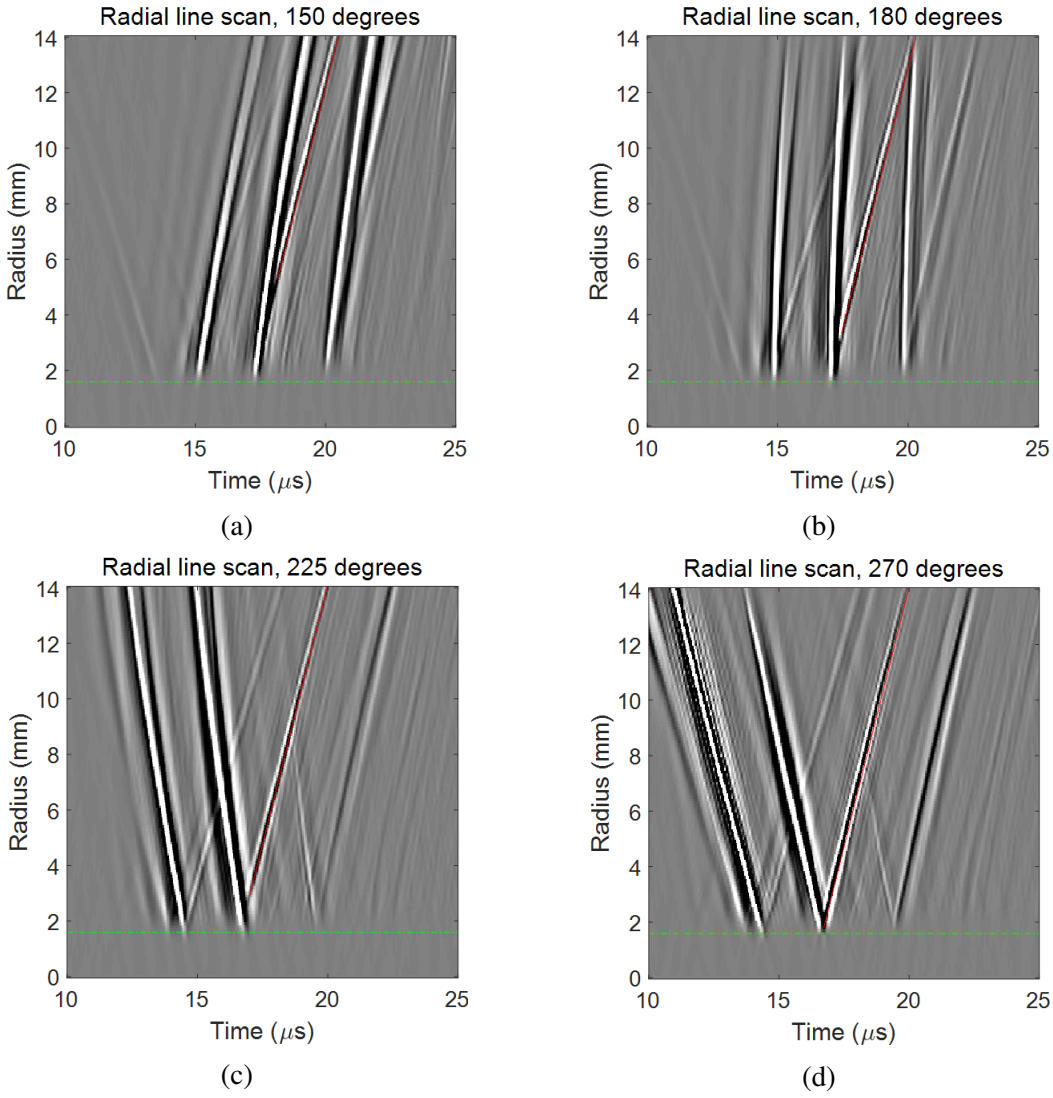

Figure 4.24: Radial line scans at polar angles of (a) 150°, (b) 180°, (c) 225°, and (d) 270°.

hole edge to prevent the probe is within the scan area. Figures 4.25(d)-4.25(f) show results from scan C4 using a 60° wedge located 29.1 mm (1.5 skips) away from the right hole edge. Figures 4.25(g)-4.25(i) show results from scan C10 using a 70° wedge located 41.2 mm (1.5 skips) away from the right hole edge.

For the 45° wedge, the provided time snapshots show hole-scattered waves caused by the third incident shear wave skip. For the 60° and 70° wedges, the provided time snapshots show hole-scattered skips caused by the 2nd incident shear wave skip. As can be seen from the figure, regardless of the wedge angle, aim point, and scattered skip, all calculated wave trajectories match the actual wavefronts of hole-scattered waves very well. This tracking technique is applied to track and extract hole-scattered waves for both undamaged and damaged holes.

4.6.3 Part-Through Holes

The previous section presents ray tracing analysis for tracking hole-scattered waves caused by through-holes. This section focuses on more complex-geometry scatterers: part-through holes with a specific hole depth. Generally, a part-through hole has two scattering surfaces − its sides and its top − which can obviously lead to more scattered waves than through-holes. One group of scattered waves is caused by the hole sides and the other one is caused by the hole top. Figure 4.26 shows several wavefield time snapshots caused by a 3.18 mm diameter, 3.18 mm hole-depth (50% of the plate thickness) part-through hole. As shown in the figure, both groups of scattered waves can be observed. Scattered waves by the hole sides have a near-circular propagation pattern similar to the pattern for through-hole-scattered waves, but forward scattered waves by the hole top surface are manifested as additional wavefronts whose location depends upon the hole depth. In fact, all scattered waves are due to specific incident shear skips, which are separate in the time-space domain. Therefore, ray tracing analysis is performed to track rays reflected from either the hole sides or the hole top. All of the following analyses are illustrated by a 3.18 mm diameter, 3.18

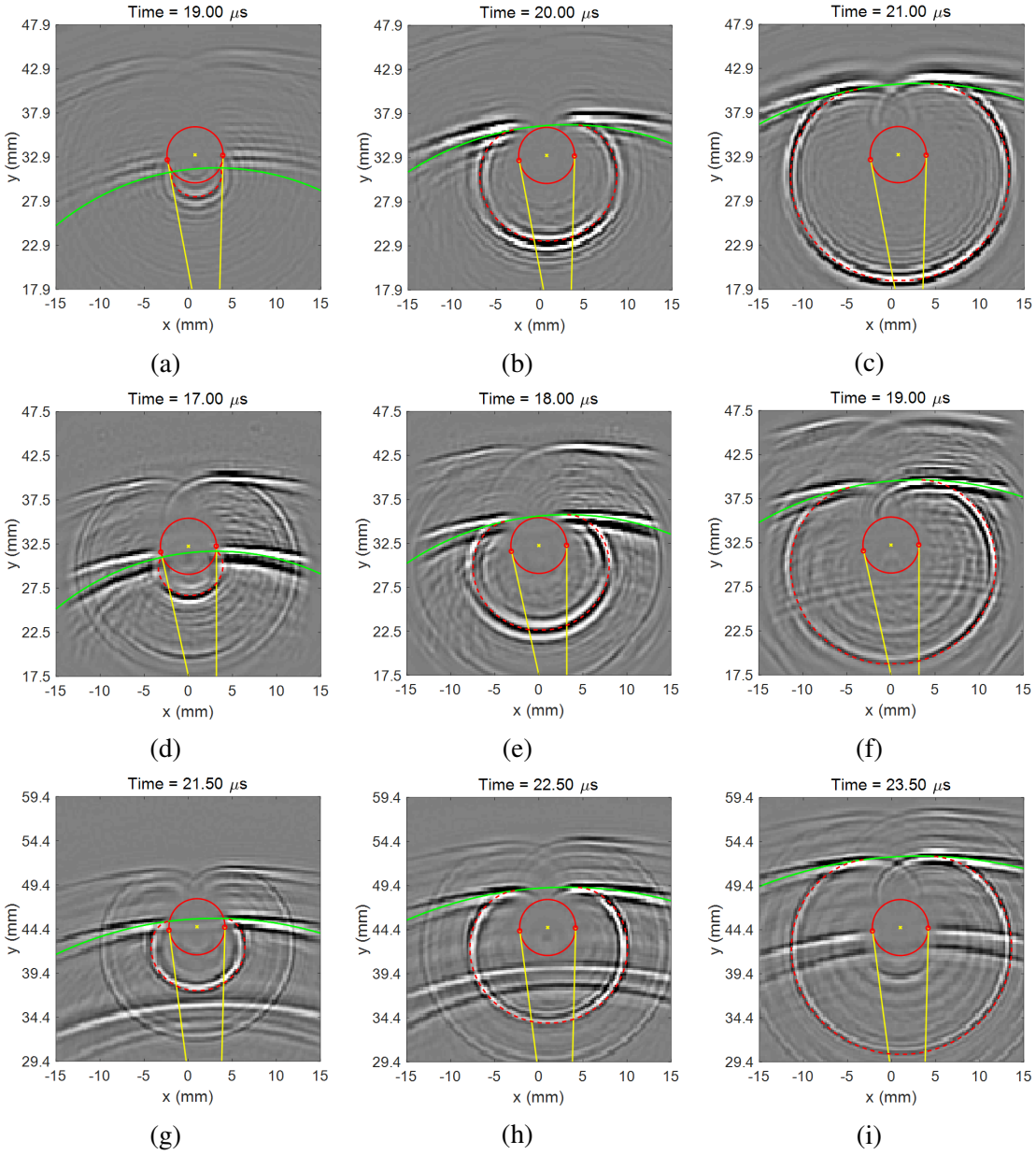

Figure 4.25: Shear wavefield snapshots with calculated trajectories of the second skip of shear incident and scattered waves using different angle probes aimed at right edges of a 6.35 mm diameter through-hole. 45° probe at (a) 19 μs, (b) 20 μs, and (c) 21 μs; 60° probe at (d) 17 μs, (e) 18 μs, and (f) 19 μs; 70° probe at (g) 21.5 μs, (h) 22.5 μs, and (i) 23.5 μs.

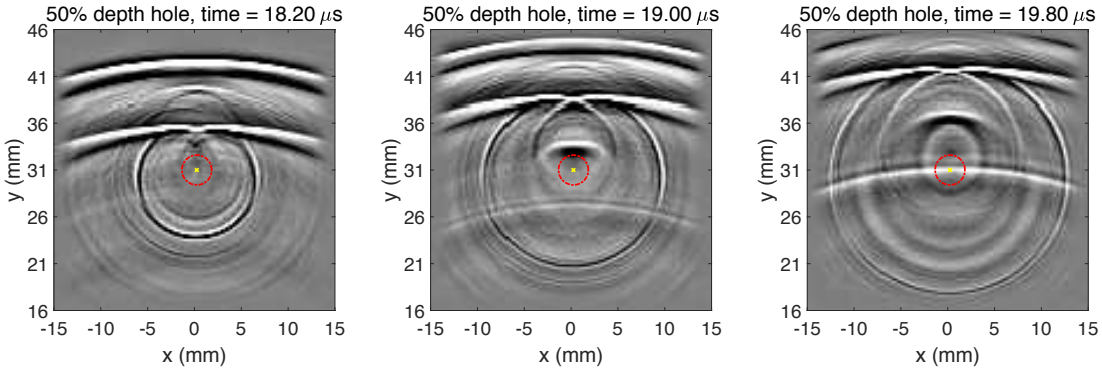

(a) (b) (c)

Figure 4.26: Wavefield time snapshots for a 50% depth part-through holes at (a)18.2 μs, (b)19 μs, and (c)19.8 μs.

mm hole-depth (50% of the plate thickness) part-through hole.

Similar to the ray tracing analysis for through-holes, the analysis here aims to build the relation of specific incident rays and their subsequent scattered rays from the side view of specimens. Figure 4.27(a) shows the side view of a plate specimen. As shown in the figure, a 3.18 mm diameter part-through hole, which is also 3.18 mm (50% of the plate thickness) deep, is expressed by a gray rectangle. As presented in the previous ray tracing analysis of through-holes, the path of a specific incident ray, which hits on the hole front side, is shown in blue and the subsequent scattered ray is shown in red in Figure 4.27(a). Given the geometric information, the angle range of incident rays, which hit the hole front side, can be calculated. Figure 4.27(b) shows these incident rays in blue and the refracted angle range is calculated from 53 to 61.6°. Based on a specular reflection as shown in Figure 4.27(a), paths of all subsequent scattered rays by the hole front side can be traced as shown in Figure 4.27(c). Compared with through-holes, part-through holes have a smaller cylindrical hitting surface, which leads to less incident rays scattered. Other than that, the analysis is exactly the same with through-hole scattered wave tracking. Therefore, the calculated results of tracking through-hole scattered waves can be directly applied to the wavefields of the same diameter part-through holes. As shown in Figure 4.28, the calculated trajectories, which include incident wave trajectories in green and scattered wave trajectories in red, are well

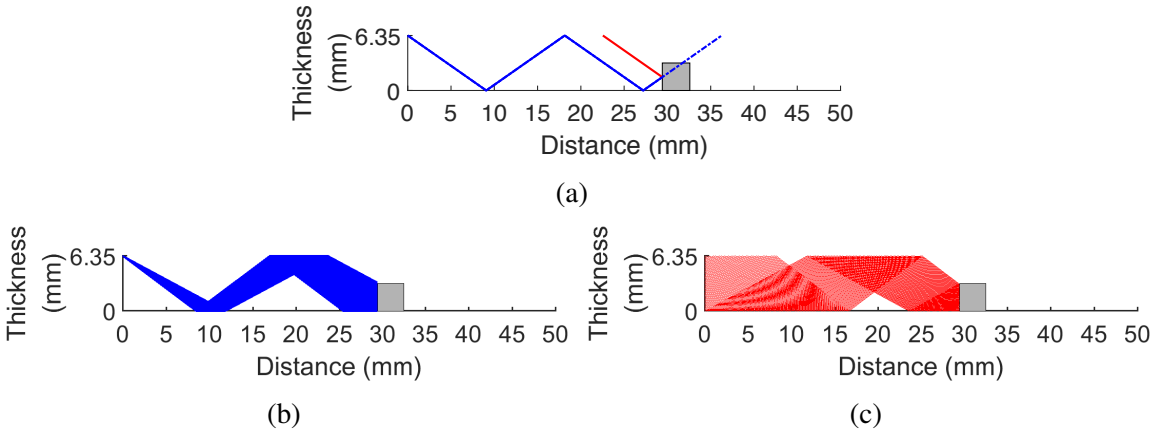

Figure 4.27: (a) Side view with the simulated incident ray of 55° in blue and the resulting scattered ray in red. (b) Incident rays whose refracted angles are from 53 to 61.6° in blue and (c) their corresponding scattered rays in red.

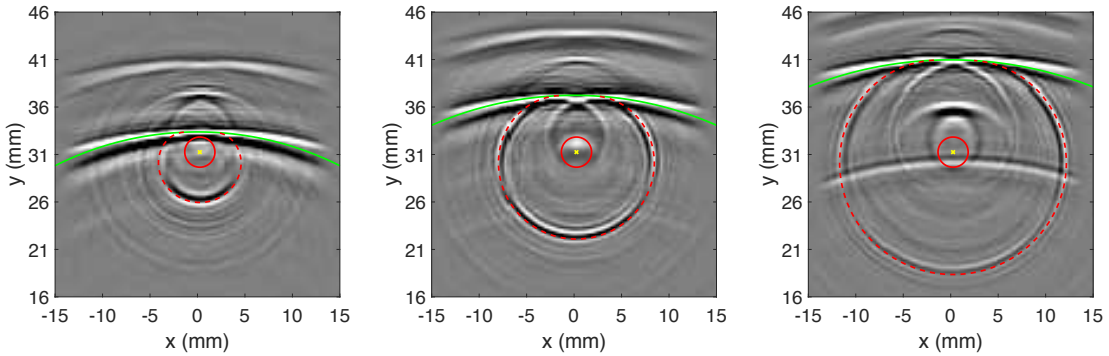

Figure 4.28: Shear wavefield snapshots with calculated trajectories of the second skip of shear incident and scattered waves from a 50% depth part-through hole at (a) 17.6 μs, (b) 18.6 μs, and (c) 19.6 μs.

matched with the experimental wavefield data caused by a part-through hole with time.

Here, ray tracing analysis is presented for tracking scattered waves caused by the top surface of a part-through hole. Generally, there are two groups of incident rays to be tracked and analyzed. The first group is the incident rays that hit the hole top surface after one V-path reflection by plate surfaces. Figure 4.29(a) shows an example of an incident ray whose refracted angle is 63°. A specular reflection is assumed on the hole-top hitting surface. Both incident and scattered rays are shown in blue. As can be seen from the figure, the total path length shown in blue is equivalent to the length that the same incident ray propagates with

1.5 skips. Therefore, the arrival time when the scattered ray returns to the surface can be calculated by the time of flight that the same incident ray propagates after 1.5 skips. Based on the previous ray tracing analysis of tracking incident waves, the on-surface distance r_{s} between the center of beam incidence and the location where the scattered ray returns to the top plate surface can be built by substituting N=1.5 into Eq. (4.9),

$$r_{\mathrm{s}} = 3\sqrt{\left[\frac{(t_{\text{snap}} - t_{\text{wedge}})c_s}{3}\right]^2 - h^2}. \tag{4.20}$$

This relation can be extended to any hole depth scenarios. If the hole depth d_{hole} is known, r_{s} can be estimated by,

$$r_{\mathrm{s}} = 2 \cdot \left(2 - \frac{d_{\text{hole}}}{h}\right)\sqrt{\left[\frac{(t_{\text{snap}} - t_{\text{wedge}})c_s}{2 \cdot \left(2 - \frac{d_{\text{hole}}}{h}\right)}\right]^2 - h^2}. \tag{4.21}$$

The second group includes incident rays that hit the hole top after propagating with two skips. As shown in Figure 4.29(b), an incident ray whose refracted angle is 48° hits the hole. Here, the total path length in blue can be estimated by the length that the same incident ray propagates with 2.5 skips. Similarly, the on-surface distance r_s where the scattered ray returns to the top plate surface can be calculated by,

$$r_{\mathrm{s}} = 2 \cdot \left(3 - \frac{d_{\text{hole}}}{h}\right)\sqrt{\left[\frac{(t_{\text{snap}} - t_{\text{wedge}})c_s}{2 \cdot \left(3 - \frac{d_{\text{hole}}}{h}\right)}\right]^2 - h^2}. \tag{4.22}$$

Here, d_{hole} equals to 3.18 mm (50% plate thickness). In addition, given the geometry, the refracted angle ranges of all incident rays of both groups that hit the hole top can be calculated. The incident rays and their subsequent scattered rays are shown in Figures 4.29(c) and 4.29(d), respectively. The refracted angle range of the first incident ray group is from 61.9 to 64.2° and the second one is from 46.1 to 49°. The calculated distance r_s of each group (e.g., N = 1.5 and N = 2.5 for a 50% hole-depth part-through hole) can be extended to the simulated arc-like wave trajectories. Figure 4.30 shows several

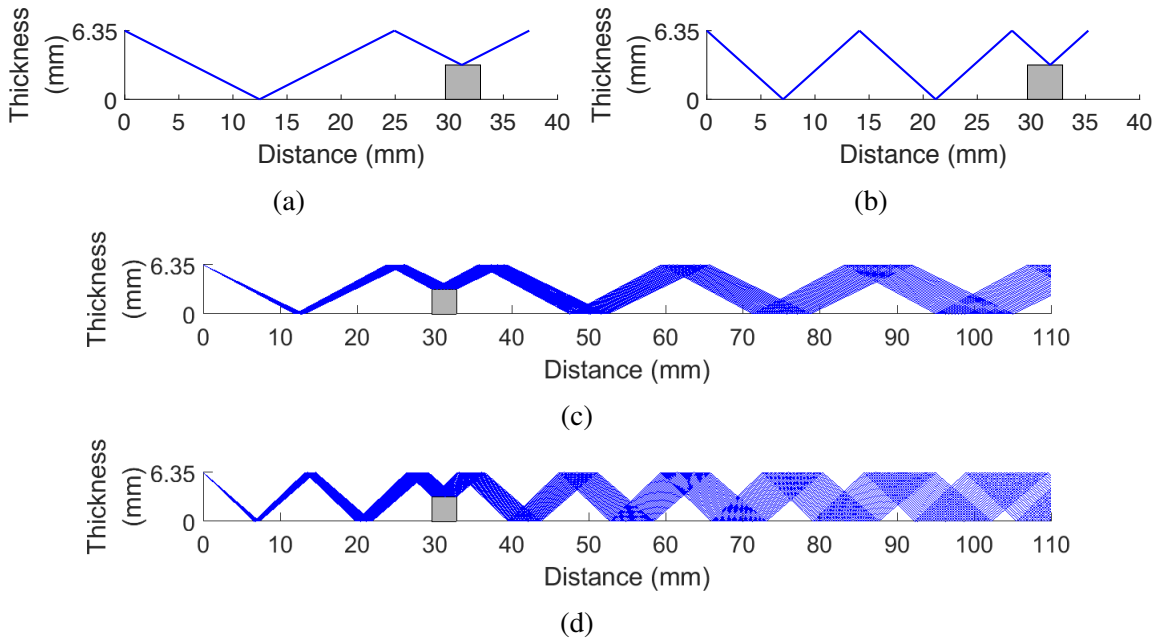

Figure 4.29: Side view with the simulated incident rays of (a) 63° and (b) 48° hitting the hole top and their respective scattered rays. Incident rays whose refracted angles are (c) from 61.9 to 64.2° and (d) from 46.1 to 49° hitting the hole top and their corresponding scattered rays.

wavefield snapshots added with simulated wave trajectories of tracking their respective hole-scattered waves caused by the hole top. As can be seen from the figure, the simulated trajectories match the actual wavefronts very well with time, which validates the reliability of the presented ray tracing process.

4.6.4 Through-Holes with Notches

This section presents how ray tracing can help understanding notch scattering. Unlike previous tracing analyses, which are fundamental and vital to build calculated wave trajectories and track scattered waves from through holes and part-through holes, ray tracing analysis presented here cannot directly track notch-scattered waves because the compound scatterers are so complex that neither scattered directions nor on-surface distances of scattered rays can be estimated by simplifying assumptions as before. However, ray tracing analysis is supportive for estimating when incident waves are scattered by the notches emanating from through-holes. As mentioned previously in Section 3.2.3, notches were made

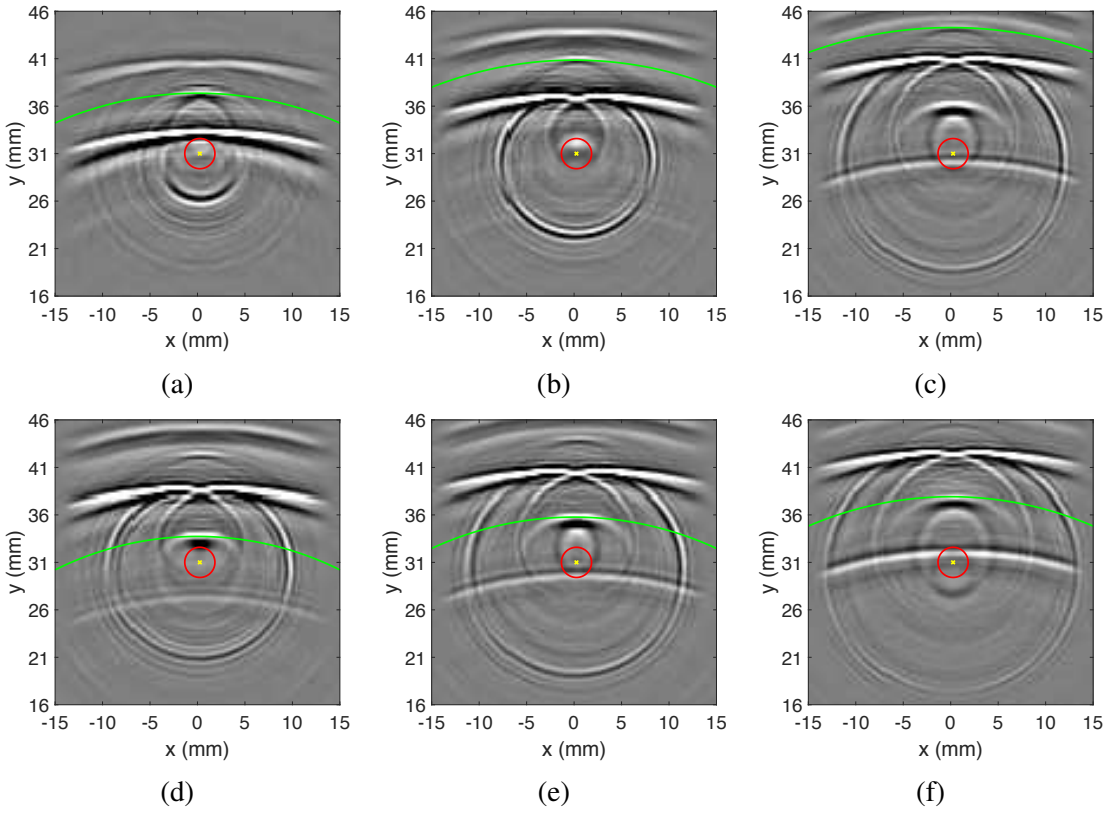

Figure 4.30: Shear wavefield snapshots added with simulated wave trajectories of scattered waves from the hole top caused by incident waves after one-V-path reflection at (a) 17.6 μs, (b) 18.6 μs, and (c) 19.6 μs, and after two-V-path reflection at (d) 19 μs, (e) 19.5 μs, and (f) 20 μs.

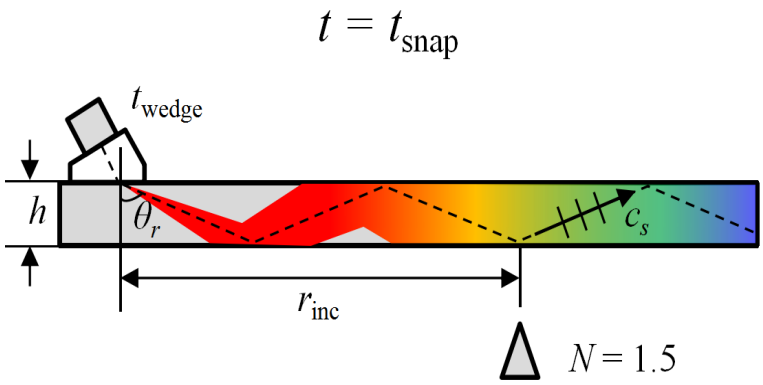

Figure 4.31: Side view for illustrating incident wave skips hitting on the bottom plate surface.

originating inside the holes from bottom plate surfaces. Thus, notch scattering actually occurs near to the bottom plate surface. However, only waves return to the top surface are measured by the laser vibrometer. Therefore, how incident shear waves are reflected by the bottom plate surface is unknown. The purpose of ray tracing analysis here is to fill that gap and then estimate when incident waves interact with notches.

Section 4.6.1 introduced how to track incident shear wave skips returning to the top plate surface by building the relation between the on-top-surface distance r_{inc} and snapshot time t_{snap} from the side view. Similarly, the goal here is to build the relation between the on-bottom-surface distance r_{inc} and snapshot time t_{snap} for each incident shear wave skip. Figure 4.31 shows the side view of the plate specimen. The traveling path of the nominal incident shear ray propagating with 1.5 skips is drawn. As can be seen from the figure, all incident rays reflected by the bottom plate surface propagate with half-integer skips (e.g., N = 0.5, 1.5, 2.5, and 3.5). Because of the same incident beam model that all incident rays propagate from the probe center at the same time, the on-bottom-surface distance r_{inc} can be calculated by the same equation of calculating the on-top-surface distance as shown in Eq. (4.9). Notice that the skip number here is a half-integer instead of an integer. For example, for the incident ray shown in Figure 4.31, substituting a skip number N of 1.5, r_{inc} can be calculated as,

$$r_{\text{inc}} = 2 \cdot 1.5 \sqrt{\left[\frac{(t_{\text{snap}} - t_{\text{wedge}})c_s}{2 \cdot 1.5}\right]^2 - h^2}. \tag{4.23}$$

The calculated r_{inc} can be then extended to arc-like wave trajectories and added to the experimental area scan wavefield data. Figures 4.32(a) and 4.32(b) show two wavefield snapshots from scan C3 (4 mm notch) at 16.91 μs and 18.1 μs, respectively, added with calculated incident wave trajectories on the top surface shown in solid arcs and the back surface in dashed arcs. Keep in mind that any wavefronts on the provided time snapshots are the waves measured on the top plate surface but the dashed arcs mark the location where incident shear waves reach on the bottom plate surface instead. Figures 4.32(c) and 4.32(d) show their respective calculated traveling paths of incident shear wave skips on the bottom plate surface from the side view. By a combination of Figures 4.32(a) and 4.32(c), it is clear to see that incident shear waves hit the notch at 16.91 μs after propagating with 1.5 skips. However, until 18.1 μs, the resulting notch-scattered waves are slightly observable on the top plate surface in Figure 4.32(b). These results cannot be utilized for extracting and quantifying notch-scattered waves, but they are beneficial to obtain a deeper understanding of notch scattering behaviors.

4.7 Incident Wave Subtraction

The purpose of incident wave subtraction is to remove incident waves by utilizing the current wavefield itself instead of applying wavefield baseline subtraction (WBS). This technique is customized particularly for the scattering analysis of compound scatterers (e.g., hole+notch) even though it is also effective and robust for simpler single scatterers (e.g., through-holes). As presented previously, WBS is a common technique to isolate incident waves from scattered waves before scattering characterization. Actually, for single scatterer scenarios (e.g., through-holes), WBS shows good performance in that most of the incident waves are removed as shown in Figures 4.11(c) and 4.11(d). However, several challenges

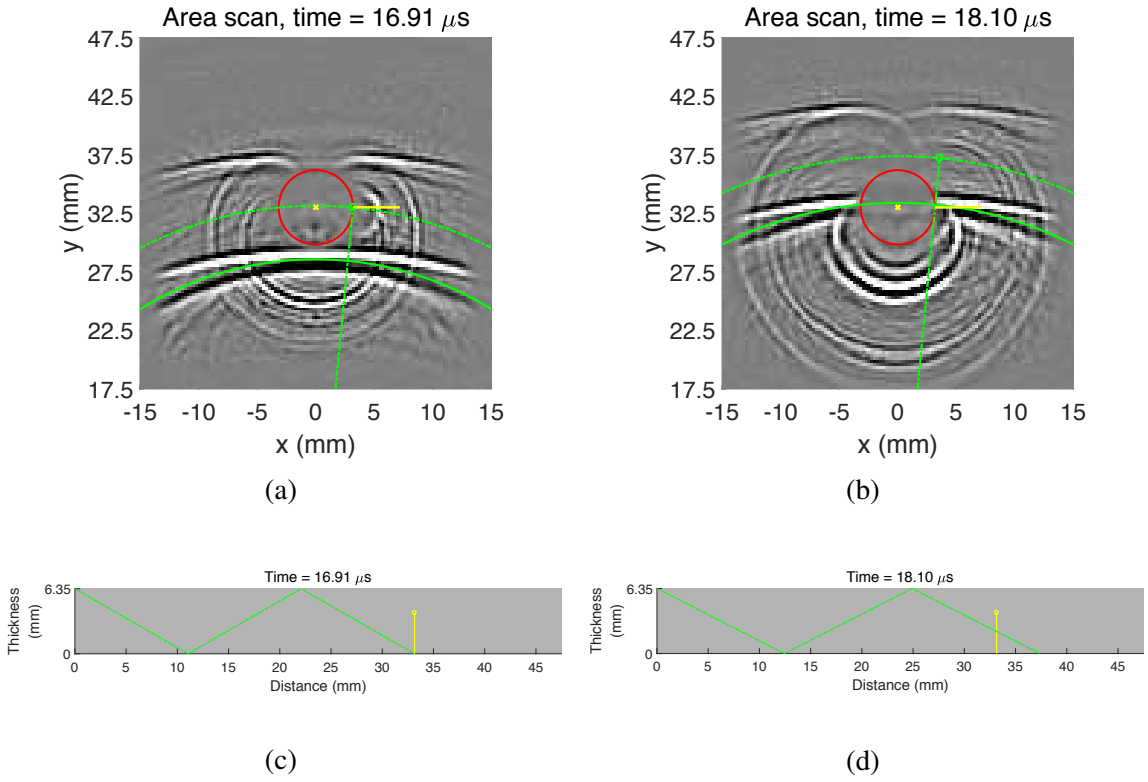

Figure 4.32: Shear wavefield snapshots at (a) 16.91 μs and (b) 18.1 μs added with simulated wave trajectories of incident wave skips hitting on the top and bottom plate surfaces, and their respective side views shown in (c) and (d).

weaken the effectiveness of WBS.

A major challenge is that obtaining a baseline well-aligned with the current wavefield is usually not realistic. In practice, damage-free baseline wavefields are virtually-impossible to acquire because defects have already occurred. Even under laboratory circumstances, nominally identical specimens can be prepared, one with a defect and one without, which are used to acquire current and baseline wavefields, respectively; however, regardless of how carefully the specimens are fabricated and the measurements performed, temporal and spatial misalignment is virtually inevitable between two sets of wavefields. Baseline alignment is one solution to compensate the misalignment as previously discussed in Section 4.4. However, a well-matched baseline is so difficult to obtain particularly for compound scatterers because of the wavefield complexity. Figure 4.33 compares residual wavefield snapshots after WBS without and with baseline alignment, which aims to subtract both incident and hole-scattered waves for isolating notch-scattered waves. As can be seen from the figure, the performance of WBS after baseline alignment is somewhat improved compared with that of direct WBS; however, both incident waves and hole-scattered waves are still dominant compared with the notch-scattered waves of interest. Motivated by this challenge, incident wave subtraction presented here, which combines directional filtering and spatial windowing as introduced previously in Section 4.3, is developed to remove incident waves without using the baseline.

The methodology is illustrated by scan C5 from a 4 mm notch emanating from a 6.35 mm diameter through-hole. As can be seen from Figure 4.34, the 3rd incident skip interferes with the notch-scattered waves of interest. This skip needs to be removed. Different strategies are taken before and after this skip interacts with the hole.

4.7.1 Below the Hole Lower Edge

The goal is to remove the 3rd incident skip by removing all incident shear wave skips before hitting the hole (spatially below the hole lower edge). The general idea is to isolate and

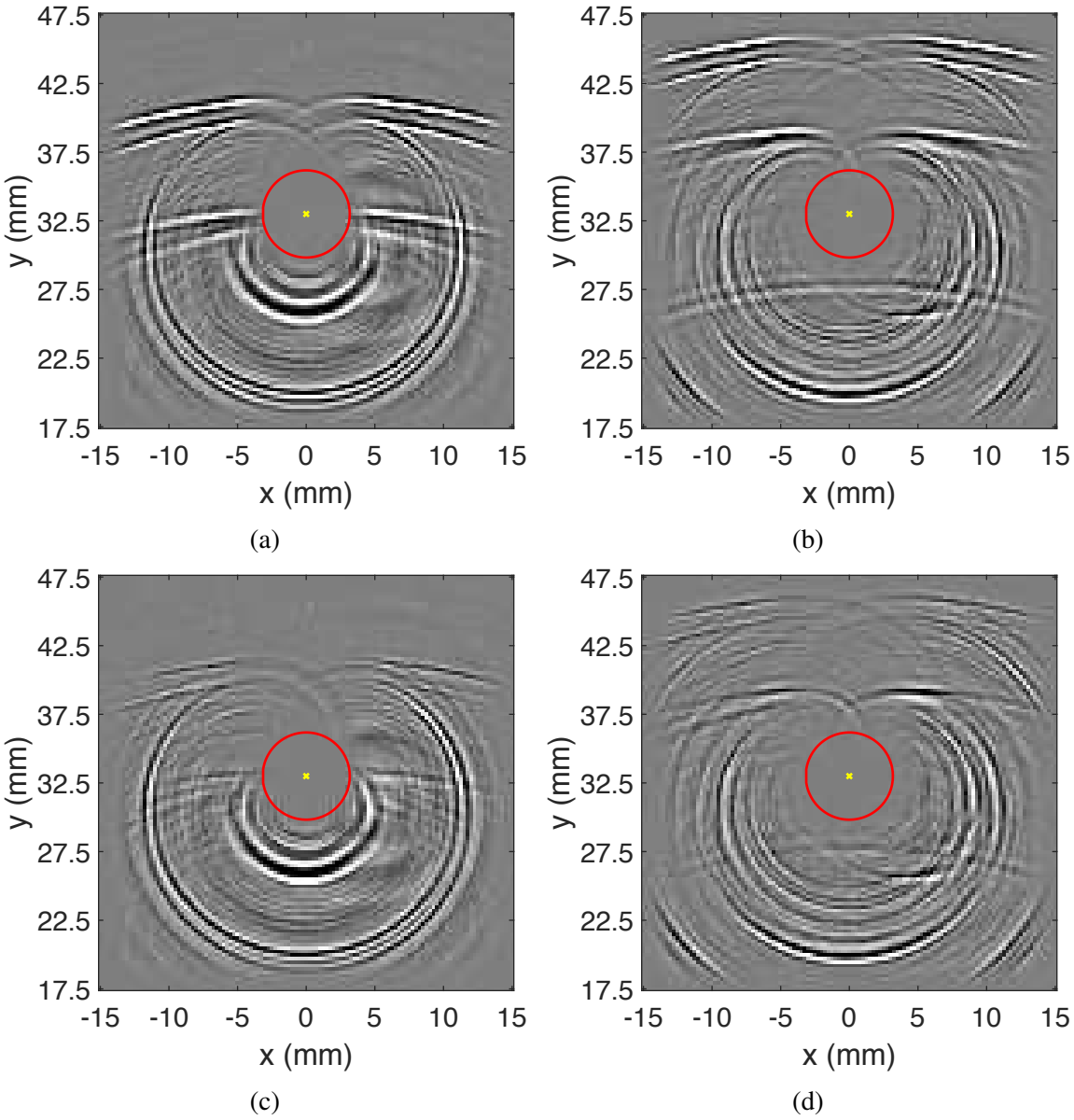

Figure 4.33: Residual wavefield snapshots from a 4 mm notch by direct baseline subtraction at (a) 18 μs and (b) 19.56 μs. Residual wavefield snapshots after baseline alignment at (a) 18 μs and (b) 19.56 μs.

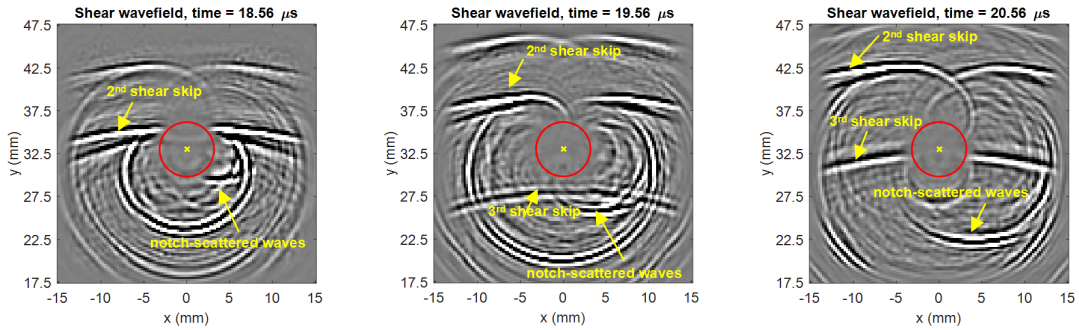

(a) (b) (c)

Figure 4.34: Shear wavefield snapshots for scan C3 of a 0° 4 mm notch emanating from a 6.35 mm diameter through-hole at (a) 18.56 μs, (b) 19.56 μs, and (c) 20.56 μs.

extract incident waves by $+k_y$ directional filtering and then subtract the filtered incident waves from the total wavefield. Specifically, the wavefield data in the time-space domain (t, x, y) are firstly converted into the 3-D frequency-wavenumber domain (ω, k_x, k_y) via the 3-D Fourier transform. Directional filtering, as previously presented in Section 4.3, is then applied to isolate forward-propagating waves, which correspond to the region of the Fourier data where k_y is positive. Here, the propagation direction range is set from 10 to 170° in the k_x-k_y plane to extract all incident waves. A Tukey window is constructed along two boundaries to make a smooth transition from 0 to 1 shown in Figure 4.35(a). The filtered data are then reconstructed via the inverse 3-D FFT. Figures 4.35(b) and 4.35(c) show the comparison before and after directional filtering ($k_y > 0$) at 19.56 μs. As can be seen from Figure 4.35(c), all backward propagating waves are removed and incident waves are remaining below the hole. Finally, spatial windowing is applied to only extract these incident waves. Here, the spatial window, marked with the green rectangle in Figure 4.35(c), is not smoothed because no more Fourier transforms are taken. Then, incident waves below the hole are fully subtracted from the unfiltered wavefield by direct wavefield subtraction as shown in Figure 4.35(d). There is no need to align the filtered waves to the incident waves in the unfiltered wavefield because they are from the same data set.

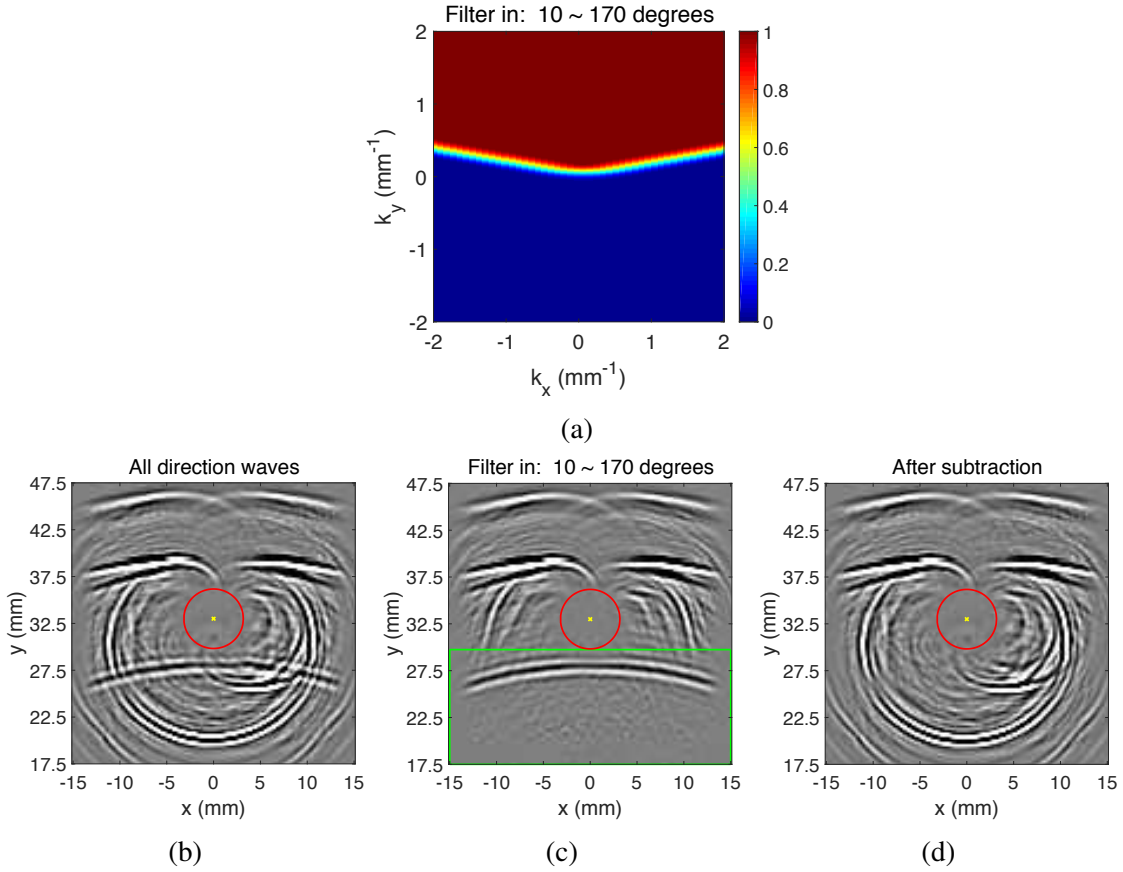

Figure 4.35: (a) Directional filtering to filter in waves propagating from 10 to 170°, (b)-(d) incident wave subtraction below the hole at 19.56 μs.

4.7.2 Above the Hole Lower Edge

Here, the goal is to remove the 3rd incident shear wave skip after hitting the hole (spatially above the hole lower edge), which spatially overlaps with the notch-scattered waves. The strategy is to track and extract the 3rd skip of incident shear waves by ray tracing analysis and then subtract the extracted shear wave skip from the wavefield. The first processing procedure is to extract all forward propagating waves by using the same $+k_y$ directional filter, whose propagation direction range is set from 10 to 170°. The reason is to make sure that no backward propagating waves will be changed with the following steps. Based on the previous ray tracing analysis in Section 4.6.1, each incident skip can be tracked very well as time progresses even after incident waves hit the hole. Here, for the 3rd incident shear wave skip, the calculated wave trajectory can be enlarged to an arc-like spatial filter to fully enclose the 3rd incident shear wave skip by setting a ring width Δr shown in Figure 4.36(a); the binary spatial filter is shown in Figure 4.36(b). Then, spatial windowing is applied to extract this incident wave above the hole. A small portion of the forward-hole-scattered waves is also extracted.

Then, the extracted waves (3rd incident skip with a small portion of forward hole-scattered waves) are subtracted from the wavefield as shown in Figures 4.36(d)-4.36(f) at 20.56 μs. It is clear to see the spatially-overlapped 3rd incident shear wave skip is fully removed after subtraction. Both hole-scattered waves and notch-scattered waves remain for scattering characterization.

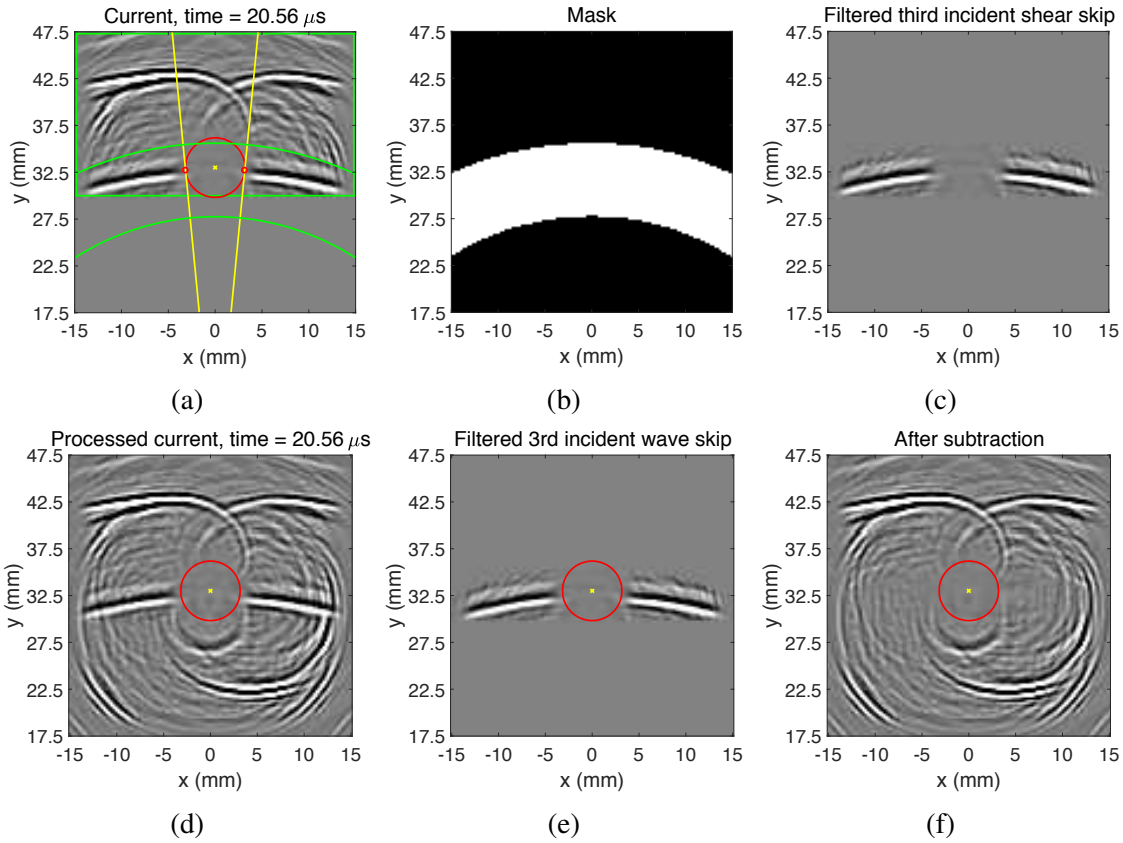

Figure 4.36: The 3rd incident skip extraction. (a) Spatially windowed wavefield snapshot after directional filtering above the hole, (b) spatial filter of the 3rd incident shear wave skip, and (c) extracted wavefield snapshot at 20.56 μs. Incident wave subtraction. (d) Shear wavefield snapshots (d) before and (e) after directional filtering and spatial windowing, and (f) residual wavefield snapshot after incident wave subtraction above the hole at 20.56 μs.

CHAPTER 5
SCATTERING CHARACTERIZATION

This chapter introduces scattering characterization and quantification techniques for analyzing various scatterers, which include through-holes, part-through holes, and notches emanating from through-holes. Overall, two scattering analysis perspectives, one based on energy of residual wavefields and the other on energy comparison, are performed. For specific methodologies, three techniques in total, performed in the 2-D, 3-D frequency-wavenumber domains, and the time-space domain, respectively, are presented to characterize and quantify scattering from through-holes. Scattered waves caused by part-through holes and notches are directly characterized and quantified in the time-space domain.

5.1 Scattering Analysis

Generally, two perspectives are provided for scattering analysis. The first one is to quantify energy of wavefield residuals into energy curves as a function of a polar angle. Analysis of wavefield residuals is able to provide instructive direction-dependent scattering patterns. However, several deficiencies weaken quantification performance. Firstly, residual wavefields are obtained by wavefield baseline subtraction, which is sensitive to slight phase shifts. As a result, scattering patterns obtained from residual wavefields are probably misleading even after baseline alignment. Secondly, an increase in scattered energy is virtually impossible to distinguish from a decrease. An alternative method is to perform an energy comparison of the two wavefields after they are aligned to isolate the effect of a defect. Similar to wavefield baseline subtraction that separates scattered waves, energy subtraction, which quantifies the energy difference before and after a defect is introduced, separates the scattered energy from the original energy.

5.1.1 Energy of Residual Wavefields

Analysis of scattering from the energy of residual wavefields aims to characterize scattering of interest by quantifying energy of residual wavefields obtained by wavefield baseline subtraction (WBS), which is a common technique that isolates the effect of scattered waves before and after a defect of interest is introduced. However, WBS has several disadvantages that limit its effectiveness. As previously discussed in Section 4.7, WBS is sensitive to small phase shifts, which may mislead quantification results. In addition, WBS is generally unable to remove baseline waves for complex compound scatterers (e.g. notches emanating from through-holes).

5.1.2 Energy Comparison

Energy comparison aims to compare scattered energy between the baseline and current wavefields after they are aligned to isolate the effect of the added defect. Unlike energy analysis of residual wavefields, which largely depends on WBS, energy comparison is insensitive to phase changes between two sets of wavefields and an increase in energy is readily distinguished from a decrease after a scatterer of interest is introduced. The strategy is to produce energy curves of current and baseline wavefields separately. Then, energy subtraction is implemented in either the linear or dB domain.

5.2 2-D Frequency-Wavenumber Domain

The methodology here is to quantify scattering in the 2-D frequency-wavenumber domain by lumping all scattered energy together into a single scattering pattern, which is described as a curve of energy versus observer direction. Here, radial interpolation is taken, which aims to transform the area scan data (t, x, y) into radial line scans (t, r, θ_o). The resulting angle-dependent line scans can be transformed into the 2-D frequency-wavenumber domain via the 2-D FFT for quantifying scattered energy into a function of observer direction. The

direction, defined in the time-space domain, is relative to a specific reference point where the observer is located. For example, the reference point is taken to be the hole center for hole-scattering analysis, although that is not a requirement. Given the observer location, the direction is defined radially outward from this location and is in the counterclockwise direction. Therefore, 0° represents the direction horizontally to the right; 90° and 270° refer to vertically forward and backward directions, respectively. Given the definition of the observer direction, hole-scattering can be quantified as a function of angle. Only hole-scattered waves are most of interest; however, both incident and scattered waves exist in the total wavefield. One obvious solution is to apply wavefield baseline subtraction, but the performance is limited as discussed previously in Section 4.7.

An additional processing step presented here is to utilize the 2-D Fourier transform to extract the effect of scattered waves from incident waves. To be noticed, only inward propagating waves relative to the hole center, which also refer to incident waves propagating below the hole, can be removed by this methodology. Incident waves propagating above the hole are only removed via WBS. Figure 5.1 shows the processing steps illustrated by quantifying through-hole scattering from a 3.18 mm diameter, empty through-hole from the residual wavefield of a 3.18 mm diameter, empty through-hole (scans A1 and A2). Here, it is applied to the shear residual wavefield after phase velocity filtering. According to the definition of the observer direction, the wavefield data are radially interpolated outward from the hole center along a line, starting at a radius of 4 mm (hole boundary) and ending at a radius of 13 mm (scan area boundary) as shown in Figure 5.1(a). After radial interpolation, data are transformed from rectangular coordinates (t, x, y) to polar coordinates (t, r, θ_o). Figure 5.1(b) shows the radial line scan of $\theta_o = 270^\circ$, which represents the vertically backward direction from the hole center to the lower vertical boundary ($y_{\min}$). As can be seen from the figure, both inward and outward propagating waves relative to the hole center are present. Here, in the time-space slice of this direction, inward propagating waves, which refer to incident waves below the hole, are identified by the lines of negative

slopes. That is, as time progresses, the incident waves propagate closer to the hole. In contrast, outward propagating waves, which represent backward hole-scattered waves, are recognized by lines of positive slopes in the slice. That is, hole-scattered waves propagate further to the hole with time.

In the time-space slices, inward and outward propagating waves relative to the hole can be differentiated easily by slopes. However, it is difficult to directly separate the waves by building filters in the time-space domain. Here, the core processing step shown in Figure 5.1(c) aims to separate inward and outward propagating waves by the 2-D Fourier transform. Each radially-interpolated line scan (each θ_o) is converted from the 2-D time-space domain (t, r) into the 2-D frequency-wavenumber domain (ω, k_r) via the 2-D FFT. Here, ω is the angular frequency and k_r is the wavenumber. Figure 5.1(c) shows a frequency-wavenumber planar slice of $\theta_o = 270^\circ$ ($-y$ axis).

Because of the Fourier transform, outward propagating waves relative to the hole in the time-space domain correspond to signals distributed in the first quadrant where both ω and k_r are positive. In contrast, inward propagating wave components locate on the second quadrant where ω is positive but k_r is negative. Therefore, in the Fourier slice of $\theta_o = 270^\circ$, incident waves below the hole and backward hole-scattered waves are fully separated. Note that incident and scattered waves cannot be separated when the observer direction θ_o is from 0 to 180°. For example, in the slice of $\theta_o = 90^\circ$ ($+y$ axis), both incident waves above the hole and forward hole-scattered waves propagate outward relative to the hole, so they both distribute in the first quadrant in the Fourier domain. Regardless of the values of the observer direction, hole-scattered waves are always outward propagating to the hole, which correspond to the Fourier data located in the first quadrant where both ω and k_r are positive. Therefore, energy accumulation of data distributed in the first quadrant in each frequency-wavenumber slice (each θ_o) leads to scattering patterns. The obtained curve of scattered energy versus observer direction is shown in Figure 5.1(d).

The procedures of phase velocity filtering described previously in Section 4.5.3 are

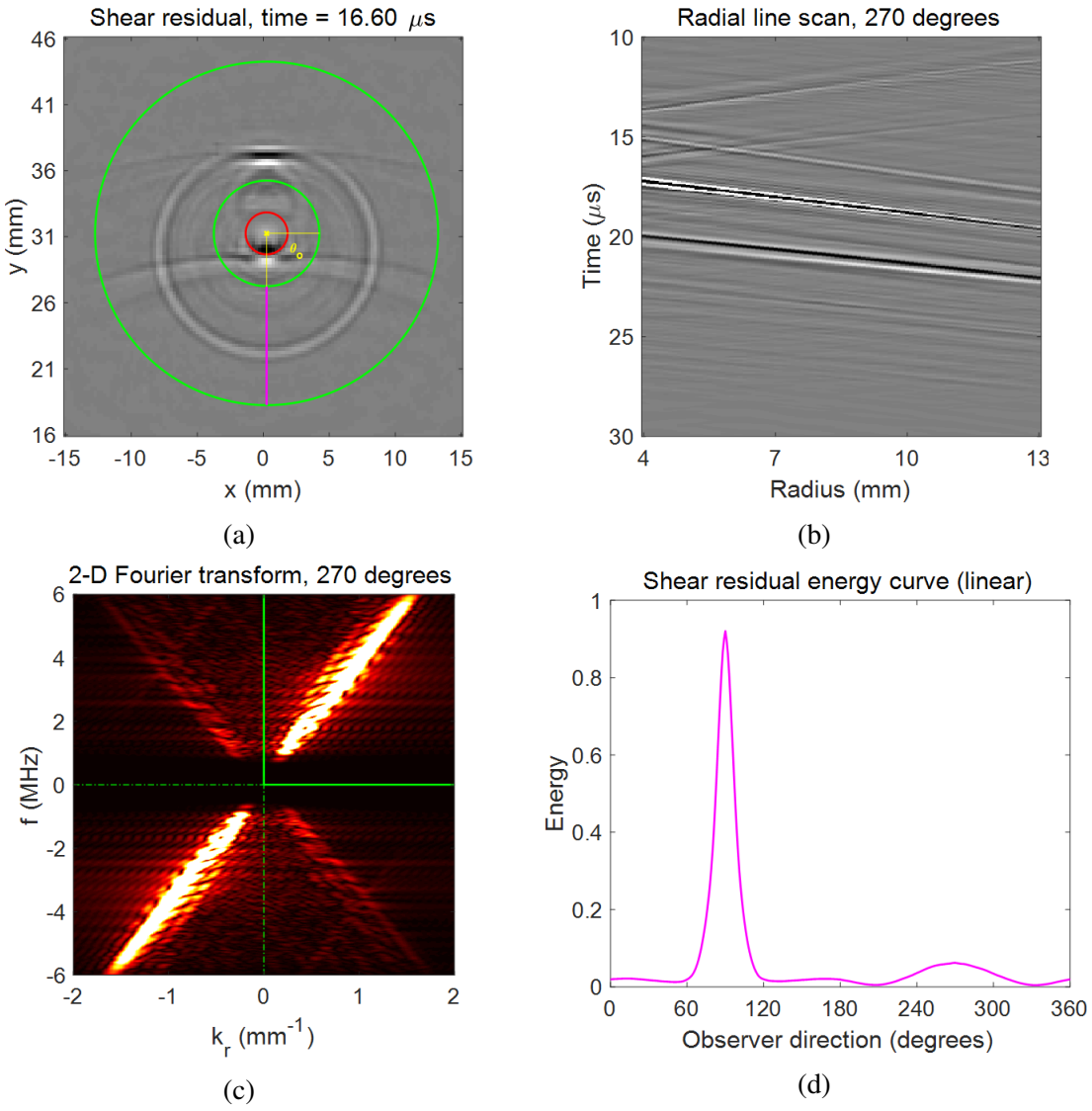

Figure 5.1: Quantification of shear wave scattering in the 2-D frequency-wavenumber domain. (a) Shear residual wavefield snapshot at 16.6 μs, (b) a radial B-scan at an observer direction of 270°, (c) a frequency-wavenumber slice at an observer direction of 270°, and (d) shear scattered energy versus observer direction shown on a linear scale.

implemented first for extracting the shear mode. Then, the restructed shear waves are utilized for the observer direction methodology. Detailed procedures are summarized as follows:

- Radially interpolate the shear residual wavefield from 4 to 13 mm with 0.1 mm radial increment.
- Convert radial line scans (t, r, θ_o) to frequency-wavenumber slices (ω, k_r, θ_o) via the 2-D Fourier transform.
- Sum the squared amplitude values of each frequency-wavenumber slice in the first quadrant for each observer direction to build scattered energy curves as a function of observer direction.

5.3 3-D Frequency-Wavenumber Domain

This section introduces scattering characterization and quantification in the 3-D frequency-wavenumber domain by summing all scattered energy into a single pattern, which is described as an energy curve as a function of propagation direction. Unlike the observer direction defined in the time-space domain, the propagation direction is defined in the 3-D frequency-wavenumber domain. After the 3-D Fourier transform, wavefield data are transformed from the time-space domain (t, x, y) to the frequency-wavenumber domain (ω, k_x, k_y). Figure 5.2(a) shows a k_x-k_y slice at f = 5 MHz. As introduced previously in Section 4.3, the propagation direction is determined by the wavenumber vector, $\boldsymbol{k_r} = k_x\hat{\boldsymbol{e}}_{\boldsymbol{x}} + k_y\hat{\boldsymbol{e}}_{\boldsymbol{y}}$ and is calculated by Eq. (4.4). Therefore, 90° and 270° refer to vertically forward and backward propagation directions, respectively. Given the definition of the propagation direction, 3-D Fourier data are radially interpolated from rectangular coordinates (ω, k_x, k_y) into polar coordinates (ω, k_r, θ_p). Figure 5.2(b) shows a k_r-f planar slice at $\theta_p = 270°$, which refers to the vertically backward propagation direction. Because of the shear wavefield obtained by phase velocity filtering, the Fourier data only distribute between wavenumber boundaries, marked with green lines, in Figure 5.2(b). Similar to the

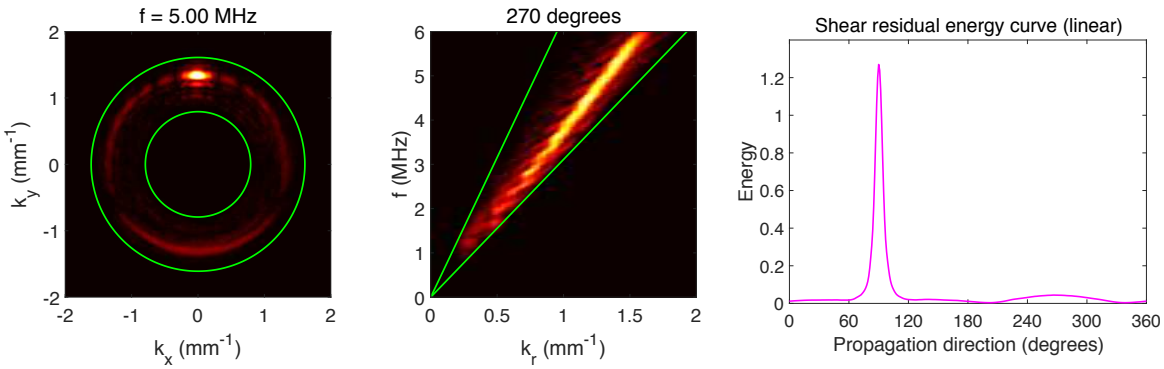

(a) (b) (c)

Figure 5.2: Quantification of shear wave scattering in the 3-D frequency-wavenumber domain. (a) a k_x-k_y slice at a frequency of 5 MHz, (b) a k_r-f slice at a propagation direction of 270°, and (c) shear scattered energy versus propagation direction shown on a linear scale.

curves of energy versus observer direction, the energy versus propagation direction curve shown in Figure 5.2(c) is obtained by energy accumulation in each frequency-wavenumber slice (each θ_p).

The same processing steps are listed in Section 4.5.3 to acquire the reconstructed shear wavefields, which are inputs for the following steps. The detailed procedure is summarized as follows:

- Transform reconstructed shear wavefield data to the 3-D frequency-wavenumber domain via the 3-D FFT, $w_{\text{shear}}(t, x, y) \xrightarrow{\mathcal{F}} W_{\text{shear}}(\omega, k_x, k_y)$.
- Interpolate the 3-D Fourier data along k_x and k_y axes to 8 times the original pixel density in the Fourier domain for each discrete frequency.
- Radially interpolate the data from the rectangular format (ω, k_x, k_y) to the polar format of the propagation direction (ω, k_r, θ_p). Each angle corresponds to a 1° sector in the k_x-k_y plane. For example, an angle of 5° corresponds to a sector from 4.5 to 5.5°.
- Sum the squared amplitude values of each k_r-f slice in each propagation direction to build curves of scattered energy versus propagation direction.

5.4 Time-Space Domain

This section introduces the time-dependent scattering analysis by time-space windowing, which directly quantifies the scattering of interest in the time-space domain. Unlike previous methodologies, which quantify the scattered energy via a single energy curve, the methodology presented here allows the scattering results to be described as a group of time-dependent energy curves. By this means, more scattering details such as how scattering evolves with time are able to be analyzed. It is especially useful and meaningful for compound scatterers (e.g, holes+notches).

5.4.1 Through-Holes

Through-hole scattering characterization and quantification in the 2-D and 3-D frequency-wavenumber domains are introduced in the previous sections. The scattering patterns are described as curves of energy versus either observer direction or propagation direction. Regardless of the direction definition, the last processing step is to accumulate all scattered shear energy into a single energy curve, which provides an overall shear wave scattering pattern. However, once data are transformed into the frequency-wavenumber domain, space and time information is no longer accessible and there is no possibility for identifying separate wave arrivals, but in reality, incident shear wave skips are time-space separated, which leads to their respective scattered waves. The resulting energy distributions of these scattered waves are not necessarily the same, which can be observed in the time-space domain, even if these skips are scattered by the same through-hole. Therefore, even if a single energy curve obtained in the frequency-wavenumber domain is informative to describe an overall scattering pattern, such a pattern is not descriptive enough to explain how waves are scattered by a specific shear wave skip. This limitation makes it difficult to translate wavefield analysis results to an inspection method since the actual ultrasonic inspection methods consider specific signal arrivals rather than an energy accumulation.

Time-space windowing is therefore developed to directly extract and quantify hole-scattered waves in the time-space domain caused by the 2nd incident shear wave skip, which leads to the strongest hole-scattering within the scan area. Based on the ray tracing analysis for tracking through-hole-scattered shear waves presented in Section 4.6.2, a time-space filter is constructed by setting a ring width Δr to broaden the calculated scattered wave trajectory to an arc-like curve that fully encloses the 2nd scattered skip. However, the shadow region blocked by the hole must be taken into account. In Figure 5.3(a), two yellow lines mark the critical incident rays that are tangent to the hole edge, which bound the scattered waves in the shadow region. These waves cannot be directly tracked by the scattered wave trajectory, but the missing region can be completed by applying the corresponding incident wave trajectory. Figure 5.3(b) shows the resulting window (spatial filter), which is edge-smoothed by a radial Tukey window. Figure 5.3(c) shows the 2nd windowed scattered shear skip obtained by multiplication of the wavefield snapshot and the corresponding spatial filter. By radial interpolation and integration of the filtered wavefield data along radial lines, hole-scattering of shear waves at this time snapshot is quantified as a plot of scattered energy versus polar angle relative to the hole center (observer direction) as shown in Figure 5.3(d). Energy comparison of current and baseline wavefields after applying time-space windowing is also performed to obtain the corresponding energy difference curves.

5.4.2 Part-Through Holes

This section introduces time-space windowing techniques for extracting scattered waves caused by the top and side surfaces of part-through holes. As shown previously in Figure 4.26, three groups of scattered waves appear in total in the observed wavefield data, two groups caused by the hole top and one group by the hole sides. As an example of a 50% depth part-through hole, the hole top leads to two groups of forward scattered waves, which are observed after propagating with 1.5 and 2.5 skips, respectively. The hole sides lead to scattered waves, which return to the top surface after 2 skips. Based on the order that

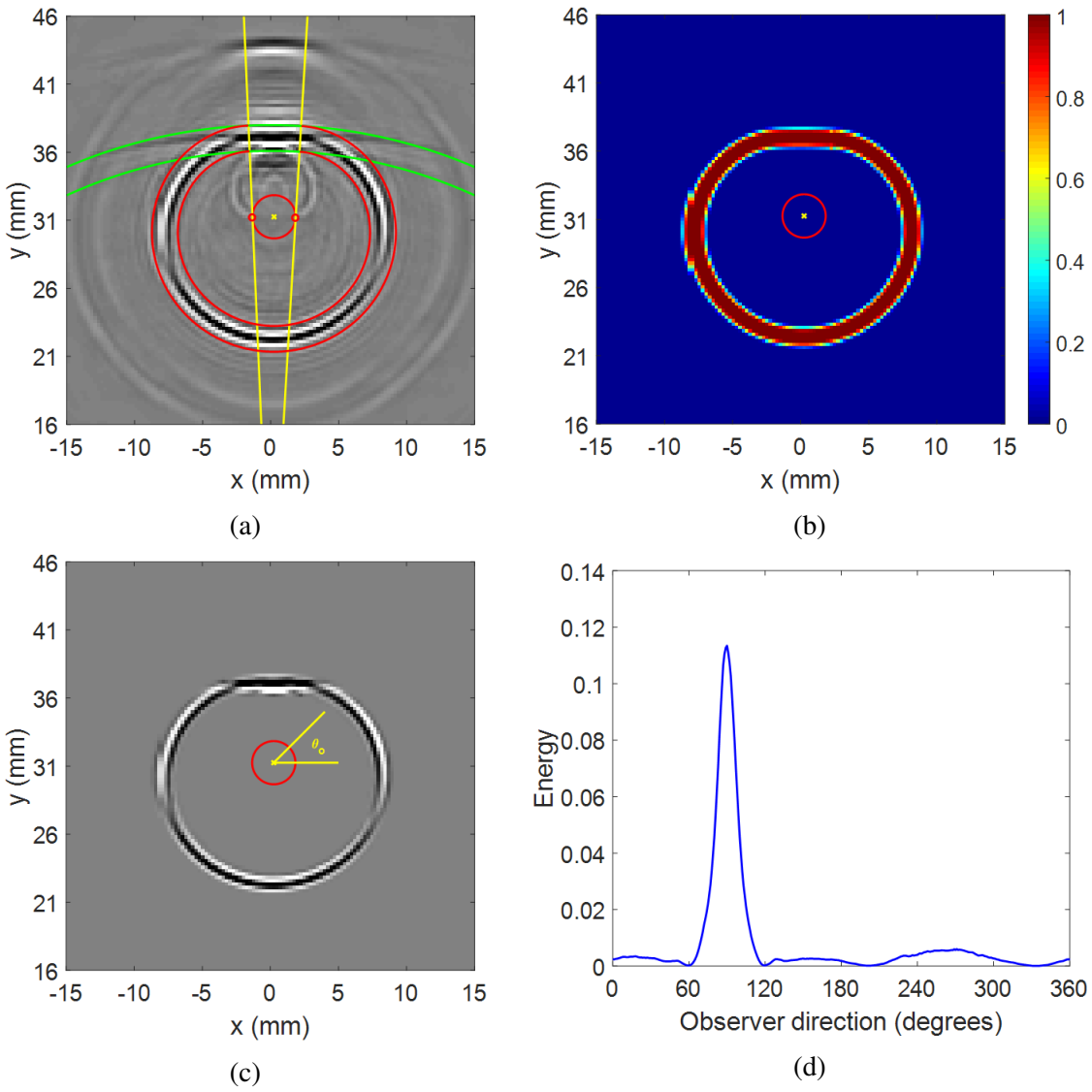

Figure 5.3: (a) Snapshot of the shear residual wavefield at 18.6 μs marked with the time-space filter, (b) time-space filter smoothed by a radial Tukey window, (c) snapshot of filtered second skip of scattered shear waves at 18.6 μs, and (d) energy curves of the second shear scattered skip shown on a linear scale.

they appear, these scattered waves returning to the top surface after 1.5, 2, and 2.5 skips are labeled as “first”, “second”, and “third” scattered skips, respectively, for convenience. As previously discussed in Section 4.6.3, wave trajectories of these three scattered skips are tracked well by the ray tracing analysis. Similar to the through-hole scenarios, the calculated wave trajectories can be enlarged to construct ring-like time-space filters by setting a ring width Δr. Figure 5.4 presents the time-space windowing process by filtering several shear wavefield snapshots from a 50% depth, 3.18 mm diameter part-through hole (scan B3). Figures 5.4(a) and 5.4(c) show forward-hole-scattered waves caused by the hole top resulting from 1.5 and 2.5 incident shear wave skips, respectively; Figure 5.4(b) shows hole-scattered waves by the hole sides (front cylindrical surface). Each figure shows results in a consistent manner the shear wavefield snapshots with superimposed time-spatial filters of both incident and scattered waves, resulting windows (masks), and filtered scattered shear wave skips. For Figure 5.4(b), the simulated spatial filters of both incident waves in green and hole-scattered waves in red are exactly the same as those for the same diameter through-hole. As can be seen from the figure, the spatial filters fully enclose all scattered waves of interest and extract them very well.

Compared to the spatial filters in Figure 5.4(b), the spatial filters shown in Figures 5.4(a) and 5.4(c), which aim to enclose and extract scattered shear wave skips caused by the hole top, are constructed in a different way. Calculated wave trajectories of tracking forward-hole-scattered waves from the hole top are enlarged to arc-like spatial filters shown in green. As can be seen from Figure 5.4(c), a small amount of hole-scattered waves caused by the hole sides are also windowed. For the sake of removing those waves, a smaller-region filter is built. For implementation convenience, an additional annular spatial filter shown in red is constructed similarly to the one in Figure 5.4(b) even though there are no scattered waves caused by the hole sides. The final window is obtained by combining the intersection of the two windows (red+green) and spatial filters (green) in the shadow region (behind the hole). As can be seen from Figures 5.4(a) and 5.4(c), scattered waves by the

hole top resulting from 1.5 and 2.5 incident shear wave skips are effectively extracted.

After time-space windowing of each hole-scattered wave skip separately, their respective hole-scattering at a specific time snapshot is quantified as energy curves versus polar angle relative to the hole center by radial interpolation and integration of the filtered wavefields. Figures 5.5(a), 5.5(b), and 5.5(c) show the filtered wavefield snapshots at 18, 19, and 20 μs, respectively. Here, each snapshot is obtained by combining the three windowed hole-scattered wave skips into a single image. Their respective quantified energy curves are shown in Figures 5.5(d), 5.5(e), and 5.5(f). Energy curves of hole-side-scattered waves, marked with "second", are shown in green and energy curves of hole-top-scattered waves resulting from 1.5 and 2.5 incident shear wave skips, marked with "first" and "third", are shown in red and blue, respectively.

5.4.3 Through-Holes with Notches

Generally, there are two strategies to characterize notch-scattering. Both strategies aim to remove the effect of hole-scattered waves. The first is to indirectly characterize and quantify the change of total scattered energy with and without a notch. The logic is to investigate on how a notch affect the total scattering. The second is to directly extract notch-scattered waves in the time-space domain and then quantify the notch-scattered energy. Energy comparison is taken to quantify notch-scattering for both strategies. In addition, all wavefields are processed after incident wave subtraction steps presented in Section 4.7 to remove incident waves and isolate the effect of scattered waves.

Indirect characterization is aimed to characterize notch-scattering by the change of total scattering with and without a notch, so the goal is to track and extract both hole-scattered waves and notch-scattered waves. Here, time-space windowing, which is presented previously in Section 4.6.2, is applied to reach this goal. The only difference is that time-space filters now must extract not only hole-scattered waves but also notch-scattered waves. Therefore, the ring width Δr is enlarged to make the ring-like filters fully enclose

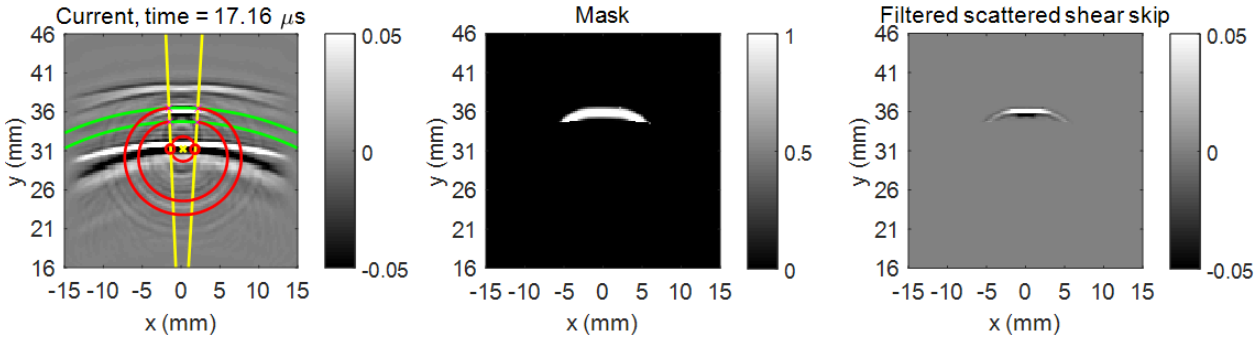

(a)

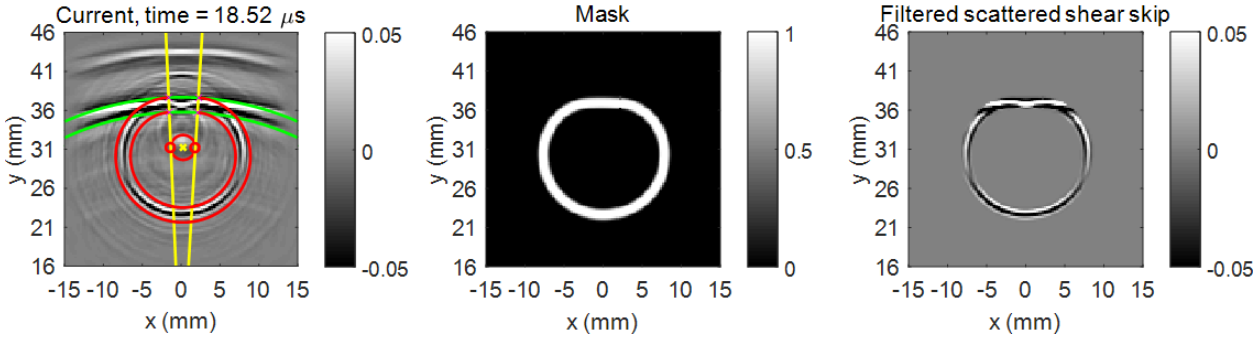

(b)

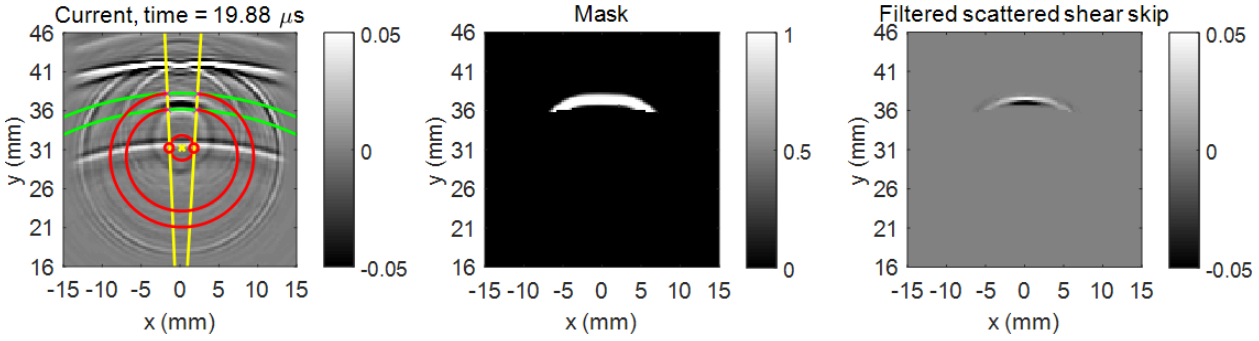

(c)

Figure 5.4: Time-space windowing process of scattered waves caused by a 50% part-through hole at (a) 17.16 μs, (b) 18.52 μs, and (c) 19.88 μs.

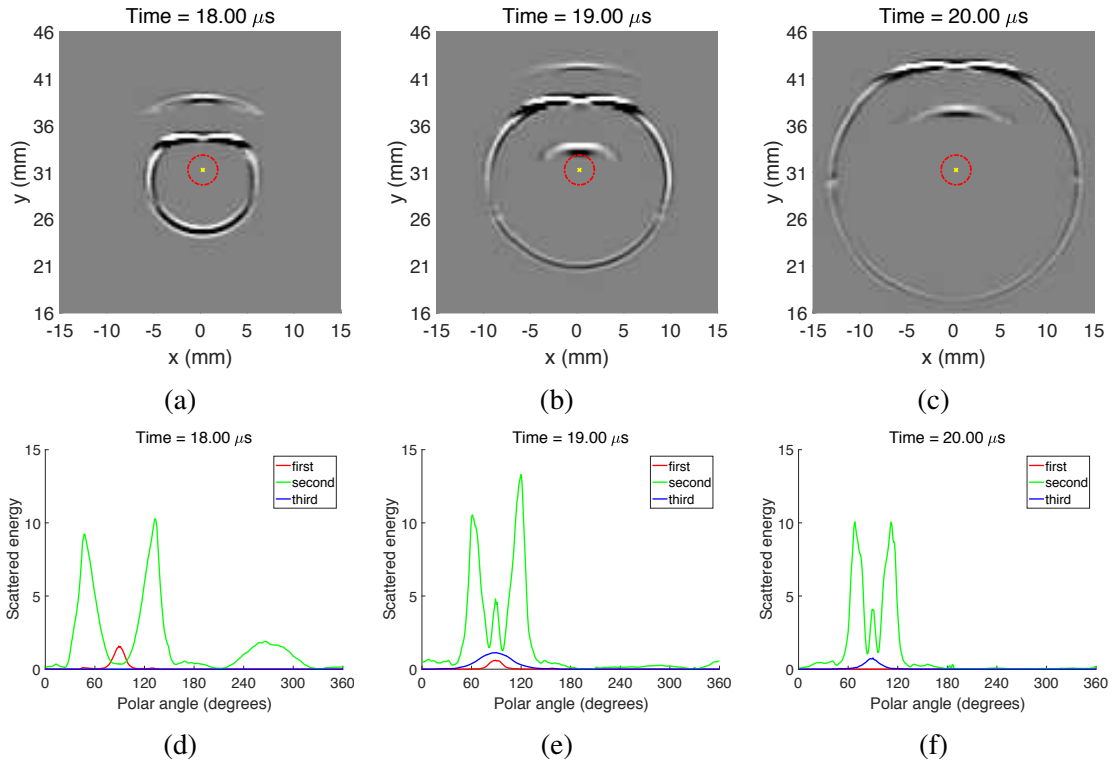

Figure 5.5: Time-space windowed wavefield snapshots at (a) 18 μs, (b) 19 μs, and (c) 20 μs from a 50% depth, 3.18 diameter part-through hole. Their respective energy curves shown on a linear scale in (d)-(f).

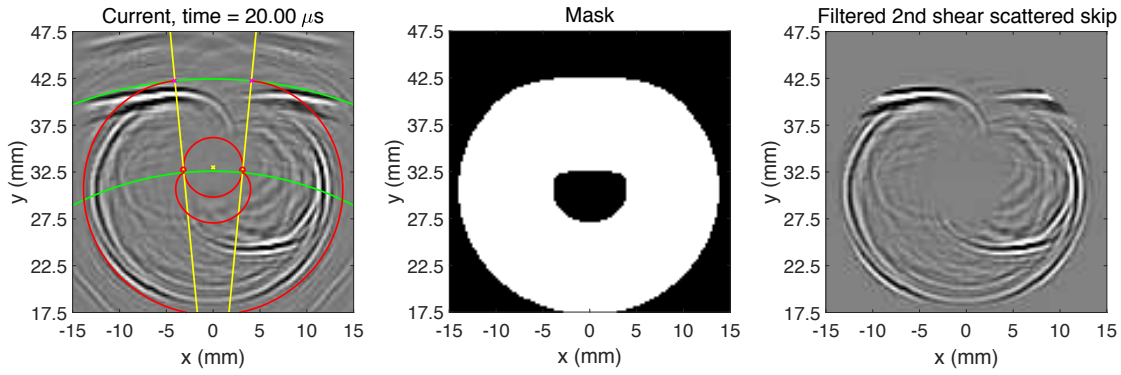

(a) (b) (c)

Figure 5.6: (a) Current wavefield snapshot added with time-space filters, (b) the corresponding mask, and (c) time-space windowed wavefield snapshot at 20 μs.

both scattered waves as shown in Figure 5.6(a). The resulting time-space filter is shown in Figure 5.6(b) and Figure 5.6(c) provides the filtered wavefield snapshot after time-space windowing. The filtered wavefield data only include hole-scattered waves caused by the 2nd incident shear skip and notch-scattered waves caused by the 1.5 incident skip. Then, the scattered energy is quantified as time-dependent energy curves of polar angle referenced to the center of the hole as an example shown in Figure 5.7(c); 90° and 270° refer to the vertically forward and backward directions, respectively.

For the sake of notch-scattering characterization, energy comparison is applied to current (damaged hole) and baseline (undamaged hole) wavefields. The same ring-width time-space filters are applied to the baseline wavefield to obtain filtered hole-scattered waves. Similarly, hole-scattered energy in the baseline is also quantified as energy curves. Then, energy comparison or subtraction can be applied to acquire energy difference curves. However, temporal alignment can be problematic because of differences in transducer mounting. Spatial misalignment is not a severe problem for energy comparison because current and baseline wavefields are quantified as energy curves referenced to the center of their respective holes (damaged or undamaged) rather than an absolute coordinate. However, time misalignment is a concern. Because of mechanical and operational errors, the locations of undamaged and damaged holes are slightly different relative to the transducer, which leads

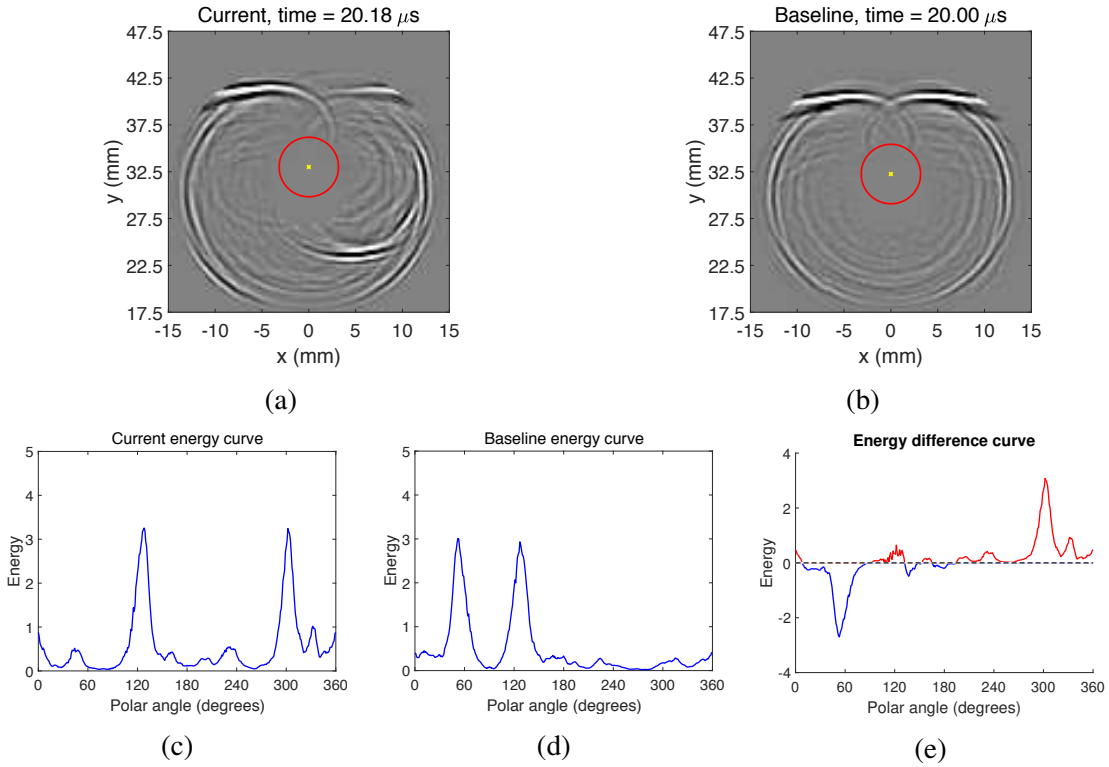

Figure 5.7: Indirect characterization process. (a) Time-space windowed current wavefield snapshot at 20.18 μs, (b) time-space windowed, time-aligned baseline wavefield snapshot at 20 μs, (c) energy curves of current and (d) time-aligned baseline wavefields, and (e) the resulting energy difference curve.

to scattering occuring at slightly different timing points in the current and baseline wavefields. Therefore, the baseline and its energy curves need to be time-aligned before energy comparison.

The time difference Δt between current and baseline wavefields can be estimated by the previous ray tracing analysis. For tracking hole-scattered waves, one primary step is to calculate when incident waves hit the hole t_{hit} based on the geometric information, which includes the exact probe and through-hole locations. The difference of their respective hitting times is used for time alignment. Figures 5.7(a) and 5.7(b) show the time snapshot comparison of current and time-aligned baseline wavefields after time alignment. Then, their respective quantified energy curves are acquired and are shown in Figures 5.7(c) and 5.7(d). Next, energy comparison is implemented to get time-dependent energy different curves, which quantify the energy change of total scattering with and without a notch. As can be seen from Figure 5.7(e), forward and backward notch-scattering is quantified as two lobes in blue and red, respectively, which are approximately located at 60° and 300°.

The purpose of direct characterization is to directly track and extract notch-scattered waves in the time-space domain, which means to remove hole-scattered waves as completely as possible before scattering quantification. The strategy is to build time-space filters for tracking notch-scattered waves as was done for hole-scattered waves. The difference is that here time-space filters are built based on a point-scattering approximation rather than an exact ray tracing analysis. That is, the hole-notch corner is considered to be a point source where notch-scattered waves originate in a near-circular pattern. From the observation of wavefield data, the timing point when notch-scattering occurs can be estimated. Then, standard-circular spatial ring filters are built by setting a ring width Δr to enclose all notch-scattered waves of interest while removing most of the hole-scattered waves as shown in Figure 5.8. The notch-scattered waves are analyzed after time-space windowing and quantified as energy curves versus polar angle referenced to the hole center. Then, time aligned spatial filters can be built using the time difference acquired previously to process

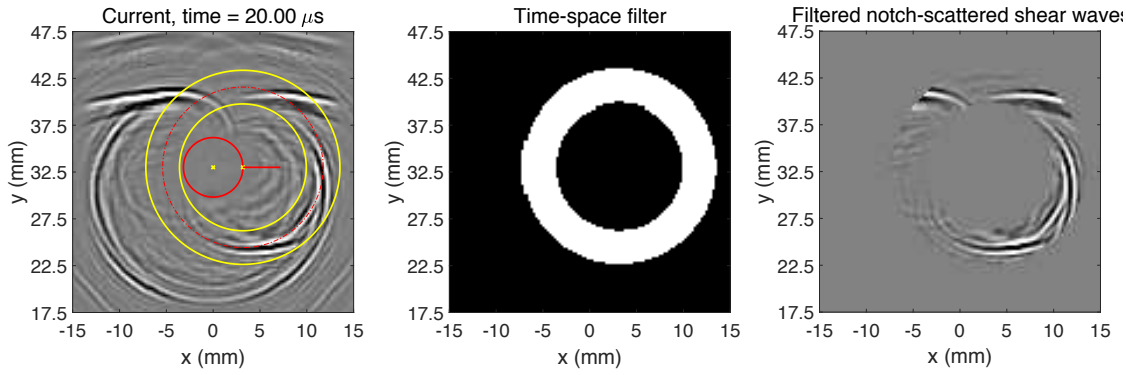

(a) (b) (c)

Figure 5.8: (a) Current wavefield snapshot at 20 μs added with the time-space window trajectories, (b) corresponding time-space filter, and (c) time-space windowed wavefield snapshot.

the baseline wavefield. The time-dependent energy difference curves are acquired by energy comparison of current and baseline energy curves as shown in Figure 5.9. Generally, scattering patterns are consistent with the results of indirect characterization. In addition, energy difference curves are clearly cleaner because most of hole-scattered waves have been removed before quantification.

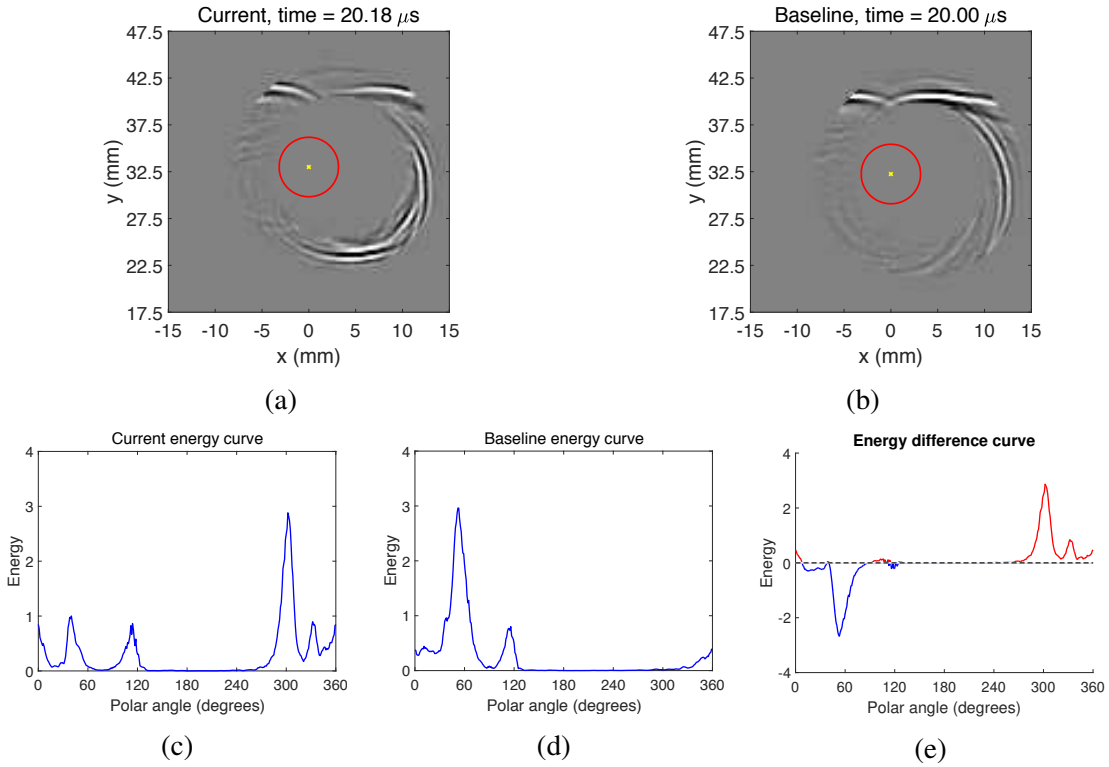

Figure 5.9: Direct characterization process. (a) Time-space windowed current wavefield snapshot at 20.18 μs, (b) time-space windowed, time-aligned baseline wavefield snapshot at 20 μs, (c) energy curves of current and (d) time-aligned baseline wavefields, and (e) the resulting energy difference curve.

CHAPTER 6
RESULTS AND DISCUSSIONS

This chapter summarizes scattering quantification results for a variety of scatterers, which include through-holes, part-through holes, and notches emanating from through holes. Through-hole scattering is characterized in both the frequency-wavenumber and time-space domains. Part-through-hole-scattering and notch-scattering is directly characterized and quantified in the time-space domain.

6.1 Through-Hole-Scattering in the Frequency-Wavenumber Domain

This section presents through-hole-scattering quantified in the frequency-wavenumber domain as energy curves based on four methodologies, which combine two quantification perspectives (residual energy and energy comparison) and two directions (observer direction and propagation direction), as applied to wavefield data after shear wave mode extraction. Firstly, the four methods are compared in the context of quantifying scattering from a 3.18 mm diameter, empty through-hole (scans A1 and A2). Secondly, results are shown for empty holes of varying diameters (scans A3-A6). Thirdly, results for the same hole with various fill conditions (scans A7-A14) are presented. Finally, all results are discussed. The four methods, which combine the techniques described in detail in Sections 5.1-5.3, are listed as follows:

(a) Residual Energy, Observer Direction

(b) Energy Comparison, Observer Direction

(c) Residual Energy, Propagation Direction

(d) Energy Comparison, Propagation Direction

Both residual energy methods require baseline subtraction after baseline alignment; both energy comparison methods compare energy curves of the current wavefields to the

energy curves of the time-space aligned baseline wavefields.

Results obtained by each method are shown on both linear and dB scales. Here, E_C, E_B, and E_R are used to express the energy of current, baseline, and residual wavefields in the linear domain. Their respective dB values are computed as $10\log_{10}$ of the linear energy values. In the linear domain, energy difference curves are obtained by direct energy subtraction of the baseline energy curve from the current energy curve (i.e. $E_C - E_B$). Similarly, in the dB domain, energy difference is calculated by energy subtraction of the dB values. Specifically, energy curves for each wavefield (current and baseline) are first expressed in dB (i.e., $10\log_{10}(E_C)$ and $10\log_{10}(E_B)$) and then subtracted (i.e., $10\log_{10}(E_C) - 10\log_{10}(E_B)$). This is the same as taking the current-to-baseline energy ratio in the linear domain and then converting that to dB (i,e., $10\log_{10}(\frac{E_C}{E_B})$). Notice that energy difference values in the linear domain cannot be directly converted into the dB domain by taking $10\log_{10}$ because of the negative values. For energy difference curves, positive values indicate that the energy of the current wavefield is larger than that of the baseline wavefield in both domains. The energy change is clearly displayed in the energy difference curves with an energy increase shown in red and a decrease in blue.

6.1.1 Comparison of Four Methods

The scattering results shown in this section are based on scans A1 and A2 obtained before and after introducing a 3.18 mm diameter through-hole. Figure 6.1 shows energy curves computed using all four methods in the linear domain. Figure 6.1(a) is the energy of the residual wavefield as a function of observer direction, (b) is the energy difference as a function of observer direction, (c) is the energy of the residual wavefield as a function of propagation direction, and (d) is the energy difference as a function of propagation direction.

Figure 6.2 shows the analogous results to Figure 6.1 but in the dB domain. Each energy curve in both the linear and dB domains is closely symmetrical about 90° and 270°,

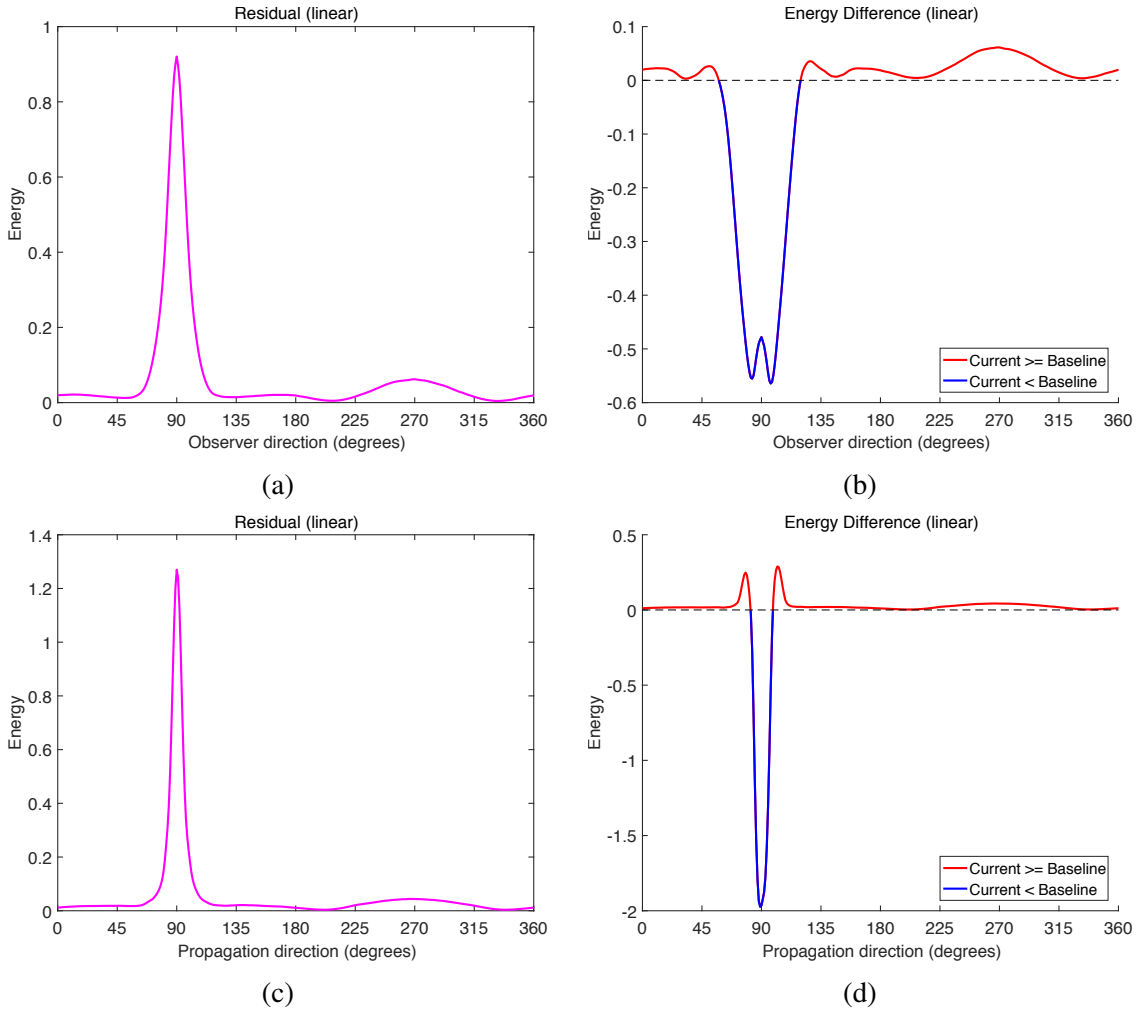

Figure 6.1: Scattering results for a 3.18 mm diameter, air-filled through-hole in the linear domain.

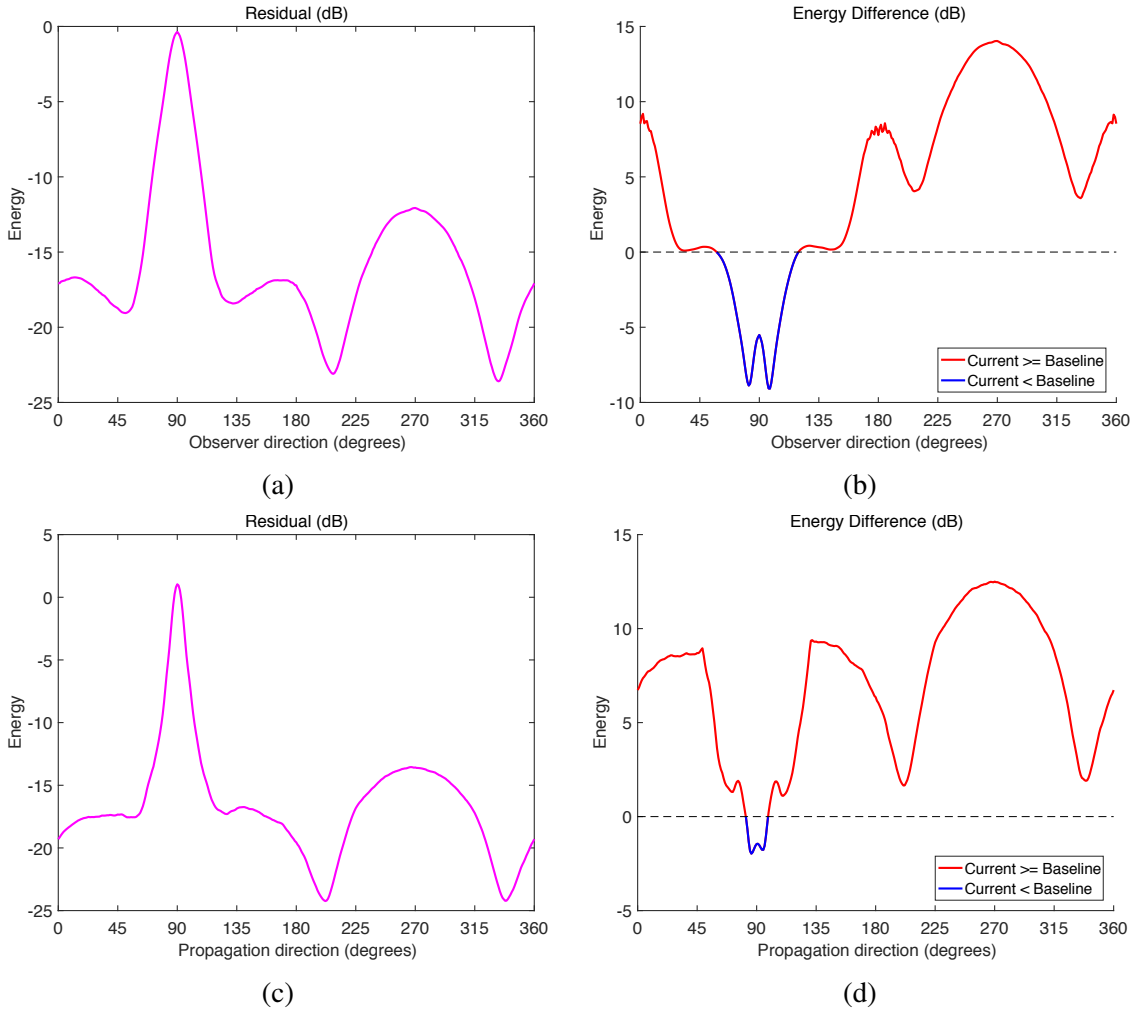

Figure 6.2: Scattering results for a 3.18 mm diameter, air-filled through-hole in the dB domain.

which mark the location of forward- and backward-scattered energy, respectively. In addition, all energy curves consistently show that forward scattering is stronger than backscattering. However, the energy curves for these four methods are obviously different in their details.

The first comparison is between the energy of the residual wavefields and energy difference. For energy curves of the residual wavefields, forward-scattering (shadow region) is described by an angle range between two local minima around 90°; backscattering is similarly indicated by an angle range between two local minima around 270°. For energy difference curves, energy changes (increase in red and decrease in blue) are observable;

that is, more details are provided to show how energy transfers for both forward- and backward-scattering after the hole is introduced. The energy increase mainly occurs in the backscattered direction as expected. There is essentially no backscattered energy in the damage-free baseline wavefield, so the backscattered energy of the current wavefield is unquestionably larger than that of the baseline wavefield. This backscattered range is between two local minima on either side of 270°, which is similar to the energy curves of the residual wavefields. For forward-scattering, most of energy decreases in the shadow region as expected because most of the incident waves of the current wavefield are blocked by the hole. Furthermore, two minima are on either side of 90° and a local maximum is located at 90°, which reveal the actual scattered wave behavior; that is, most incident energy is blocked by the hole but some is diffracted around the hole and combines in the exactly vertically forward direction. This diffraction phenomenon is identified as the Fresnel bright spot as discussed in [101] for a delamination in composites but it has not been previously observed for angle-beam shear waves in aluminum plates. The reason why this bright spot is not observable in Figure 6.1(d) is that for the propagation direction analysis, energy around 90° includes all incident waves (above and below the hole) for both the current and baseline wavefields, and the very small effect of the bright spot is overshadowed by the incident energy. However, it is slightly visible in the dB domain as shown in Figure 6.2(d).

The second comparison is between the observer and propagation directions. The forward-scattering lobe of the propagation direction is narrower ("spikier") than that of the observer direction; the trend is opposite for backscattering. This phenomenon results from the difference of definitions of these two directions. Figure 6.3 shows a residual shear wavefield snapshot at 16.6 μs overlaid with two pairs of arrows, which depict two directions, the observer direction in magenta and the propagation direction in green. These two observer direction vectors in both forward- and backward-scattering areas originate from the hole center according to the definition of the observer direction. However, the propa-

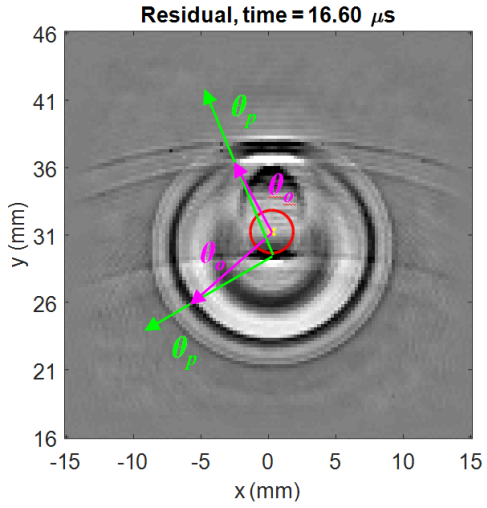

Figure 6.3: Snapshot explaining the difference between the observer and propagation directions.

gation direction for both forward- and backward-scattered waves depends upon where the incident ray hits the hole and then reflects. This interface is the front cylindrical surface of the hole, which corresponds to the semicircle below the hole center in the x-y plane (top view). Thus, for both forward- and backward-scattered waves, their respective propagation directions start from points below the hole. For the same points on the wavefronts that explain the observer direction in Figure 6.3, the propagation direction vectors originate from the hitting point vertically below the hole center. Therefore, for the same wavefronts in the forward-scattering area, the observer direction has a broader angle range than the propagation direction; it is opposite in the backscattering area. This phenomenon can be clearly identified in the energy curves shown in both Figures 6.1 and 6.2.

Additional insight into the energy comparison method in both the linear and dB domains, when using the observer direction, can be obtained by examining the energy curves of both the current and baseline wavefields. Figures 6.4(a)-(c) show these curves, as well as their difference, in the linear domain, and Figures 6.4(d)-(f) show them in the dB domain. The Fresnel bright spot is clearly evident in the current wavefield energy plots in both domains as is the strong shadowing in the forward-scattered directions and the weaker backscattering. The baseline wavefield energy plots show an energy distribution in the

forward-scattered directions that is much broader than the actual range of propagation directions. This artificial broadening is due to the generation of radial B-scans that cut through the incident wavefield in the forward directions along lines that do not correspond to the true directions of propagation. For example, the radial B-scan at 45° intersects the incident wavefield and thus has non-zero energy, but there is actually very little incident wave energy propagating at 45°. However, the same situation is true for the current wavefield, and the energy comparisons shows that the hole has little effect on the 45° observer direction.

Besides, as can be seen from Figure 6.4(b), the baseline energy curves in the linear domain show very little energy between 180° and 360°, which is expected because theoretically no backward-propagating waves occur under a pristine plate. However, Figure 6.4(e) shows a local maximum at 270° (i.e., vertically backward direction) in the dB domain, which indicates that, in fact, the backscattered energy is not strictly equal to zero even without any scatterers. Some of this energy is likely due to spectral leakage during the shear wave phase velocity filtering process, but even prior to filtering, a slight amount of backward-propagating waves, which are probably caused by reflections from surface imperfections, are observed accompanying with the incident shear wave skips in the wavefield videos. This fact may mislead the difference after energy comparison. As shown in Figure 6.4(f), the obtained energy difference curves show a local minimum at 270° where the strongest increase of the backscattered energy is supposed to occur after energy comparison. In order to ignore the effect of this small backscattered energy in the baseline, an energy threshold of -25 dB is applied to both baseline and current energy curves before energy comparison. Notice that this energy threshold is taken subjectively. New current and baseline energy curves in the dB domain are shown in Figures 6.4(g) and 6.4(h), respectively. It is clear to see that current energy curves are the same because all values are larger than -25 dB but any dB values of baseline energy curves smaller than the threshold are forced to be -25 dB. The new energy difference curves are then obtained by energy com-

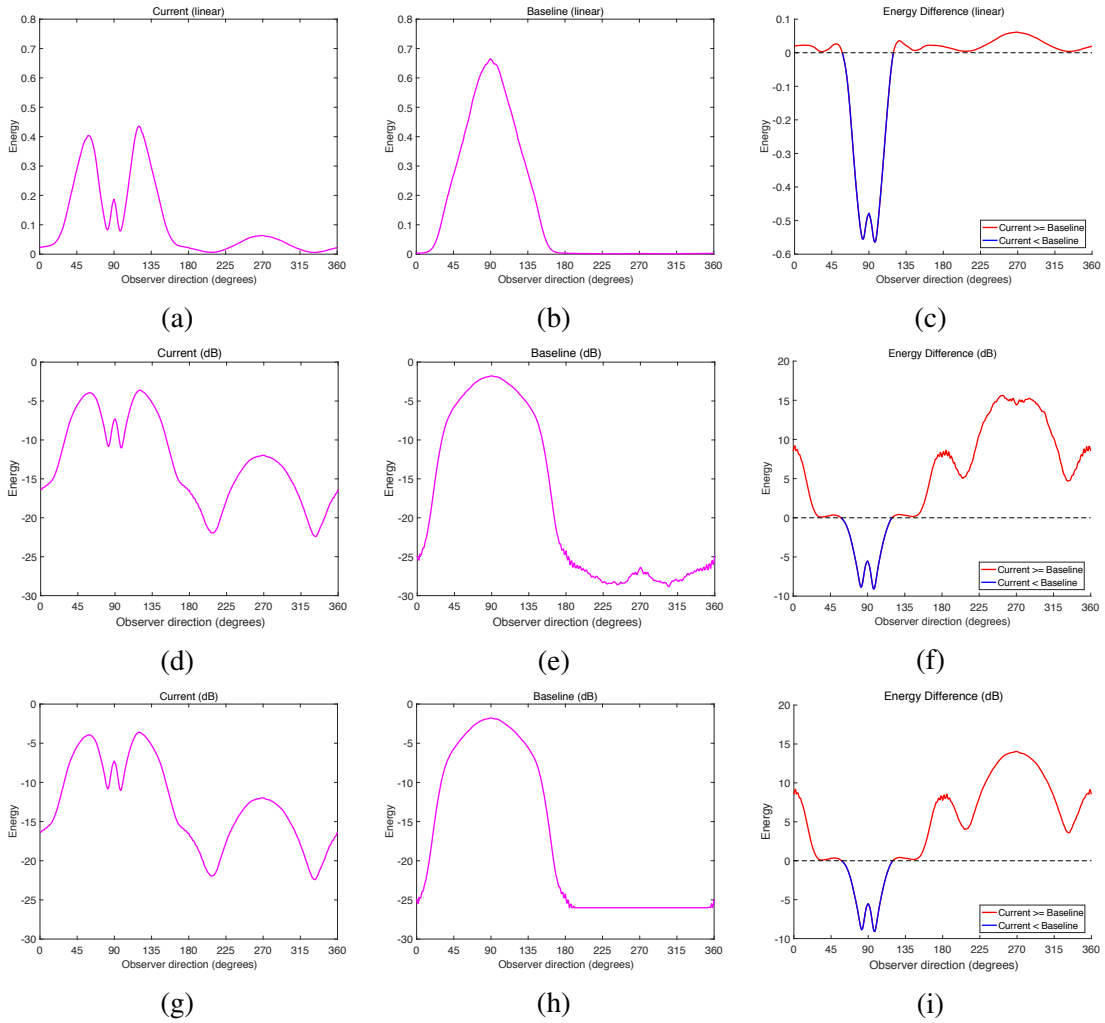

Figure 6.4: Observer direction scattering results for a 3.18 mm diameter, air-filled through-hole: (a/b/c) linear domain, and dB domain before (d/e/f) and after (g/h/i) an energy threshold of -25 dB.

parison. As expected, the strongest backscattering occurs at 270° in Figure 6.4(i), which is consistent with the scattering pattern in the linear domain. Note that Figure 6.4(i) is the same with Figure 6.2(b) previously shown.

Results obtained using the propagation direction can also be better understood by looking more deeply into the constituent parts. Figures 6.5(a)-(c) show these curves, as well as their difference, in the linear domain, and Figures 6.5(d)-(f) show them in the dB domain. In the linear domain, the very narrow baseline energy curve is indicative of the actual range of propagation directions of the incident wave. The current energy curve

is also narrow but reduced in amplitude because of the forward shadowing of the hole. Backscattering is very small in the current energy curve as compared to forward scattering. The energy difference curve is dominated by the negative peak caused by shadowing, and although there is clearly some backscattering, it is much smaller in amplitude. The propagation methodology concentrates the incident energy into a narrow angular range that dominates the results. More details can be seen in energy curves in the dB domain. In contrast to the linear domain, which is dominated by the large-amplitude forward-scattering peak, the dB domain provides a clearer view of lower-amplitude backscattered energy with two local minima on either side of 270° being visible in both the current energy curves and energy difference curves; the Fresnel bright spot is also slightly visible in the energy difference curve. As was the case for the observer direction results, the baseline has non-zero content between 180° and 360°, which shows a local maximum at 270° in dB and leads to a local minimum at 270° in the energy difference curves. Similarly, an energy threshold of -26 dB is thus applied to both current and baseline energy curves. The new curves and the difference after energy comparison are shown in Figures 6.5(g)-(i). As can be seen from Figure 6.5(i), the strongest backscattered energy increase occurs at 270° as expected. Besides, the energy difference curve highlights the increase in energy in all directions except for the shadow region centered at 90°. Note that Figure 6.5(i) is the same with Figure 6.2(d) previously shown.

6.1.2 Empty Holes of Different Diameters

The scattering results presented in this section are based on empty through-holes of different diameters (1.59, 3.18, and 6.35 mm) from scans A3-A6. Scan A3 is the baseline, and scans A4-A6 were recorded after the hole was drilled and then incrementally enlarged. Figure 6.6 shows scattering results for the three hole sizes in the linear domain using the four methods previously compared in Section 6.1.1. Figure 6.7 shows the corresponding results in the dB domain. For the observer direction, radial B-scans for the different hole

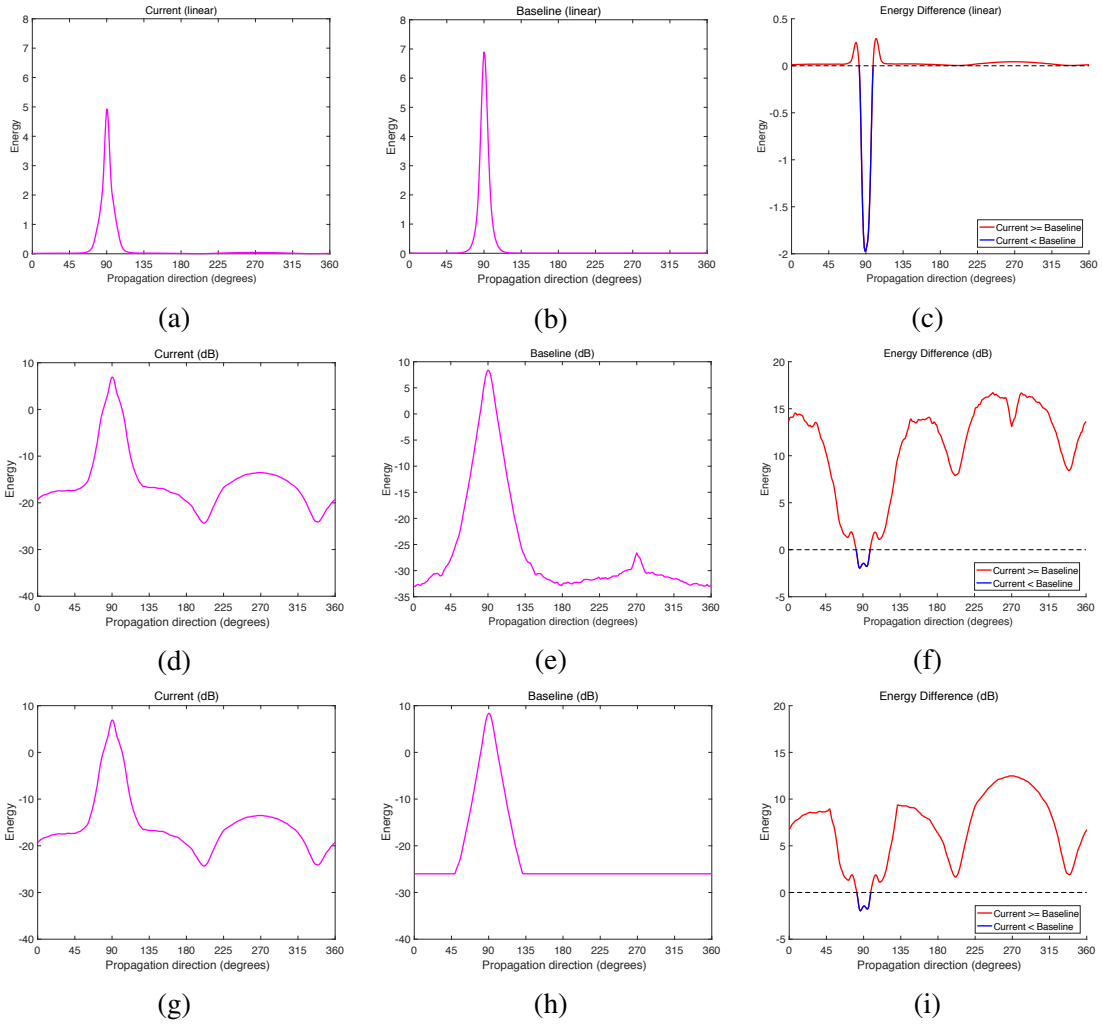

Figure 6.5: Propagation direction scattering results for a 3.18 mm diameter, air-filled through-hole: (a/b/c) linear domain, and dB domain before (d/e/f) and after (g/h/i) an energy threshold of -26 dB.

sizes were all 9 mm in length and consistently started at a distance of 4 mm from the center of the hole for all hole diameters. For both the observer and propagation directions, spatial windowing was performed to reduce spectral leakage as described in Section 4.1 to both smooth the edges and remove noisy data inside each hole prior to taking the 3-D Fourier transform.

With one exception, the energy curves in Figure 6.6 consistently show the expected trend that larger holes lead to stronger forward- and backward-scattering. The exception is Figure 6.6(a), which shows energy curves of observer direction based on the residual wavefields. Here, the forward-scattering lobe of the 3.18 mm diameter hole is taller than that of the 6.35 mm diameter hole. That is, the smaller hole leads to stronger forward scattering, which is unexpected. This same observation holds for the corresponding dB domain curves of Figure 6.7(a). This unexpected result is caused by a phase shift between the current and baseline data for the 6.35 mm diameter hole that results in signal cancellation during baseline subtraction and a subsequent reduction in energy. However, the energy difference results clearly show that this largest hole causes shadowing of more energy than either of the smaller holes. The Fresnel bright spot can be seen for all three hole sizes in the energy difference plots, and it is distinctly more pronounced for the two smaller holes.

The data shown in Section 6.1.1 are from a 3.18 mm diameter through-hole, and although it is from a different specimen and excitation than the corresponding data shown in this section, the shapes of the curves are similar. It is not expected that they would be identical since the signals obtained from the spike excitation have more low frequency content than those obtained with a chirp after post-processing to an equivalent 2-cycle, 5-MHz tone burst excitation.

6.1.3 Through-Holes with Various Fill Conditions

The scattering results of this section are based on a 6.35 mm diameter through-hole with various fill conditions from scans A7-A14, which are divided into two groups with Group

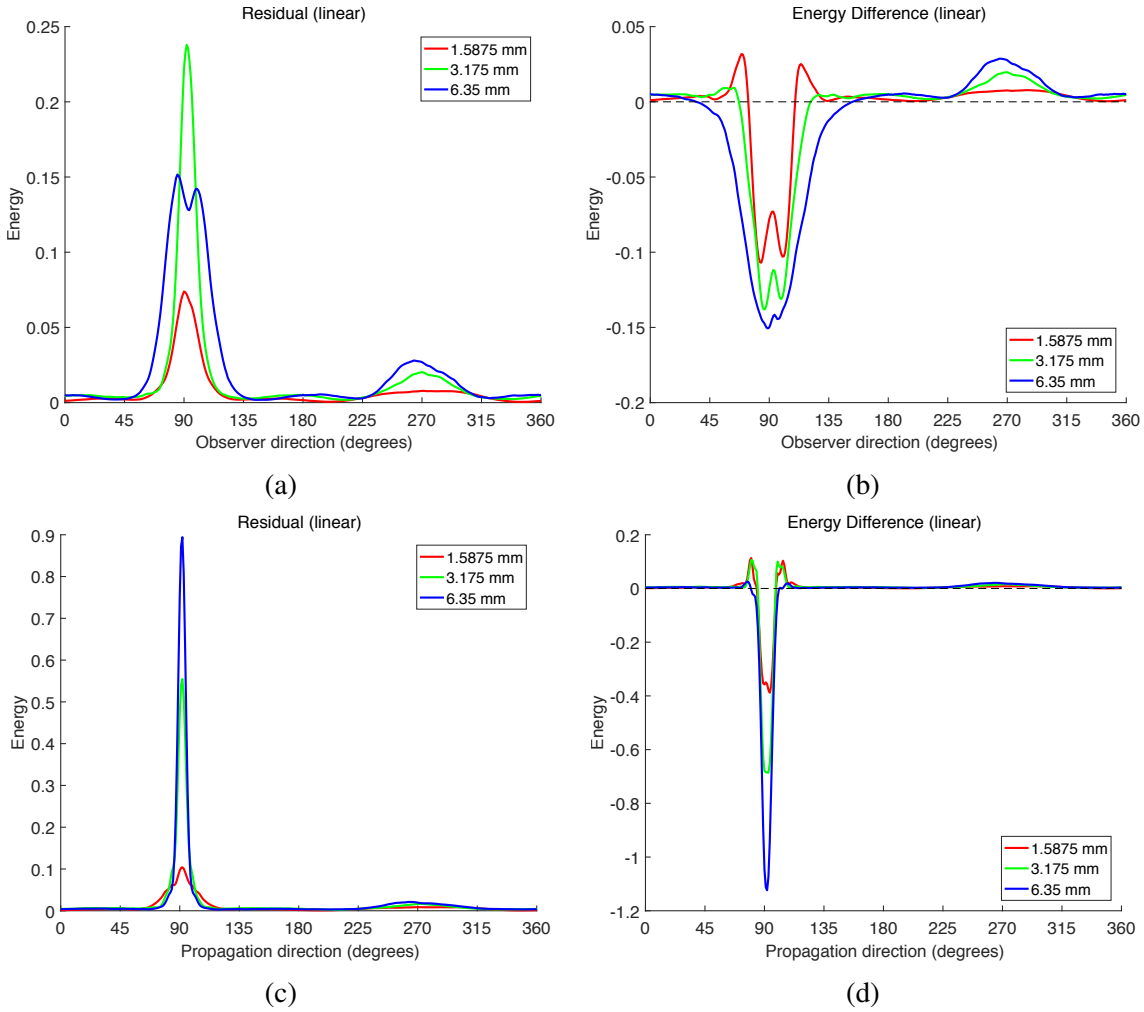

Figure 6.6: Scattering results for air-filled through-holes of different diameters in the linear domain.

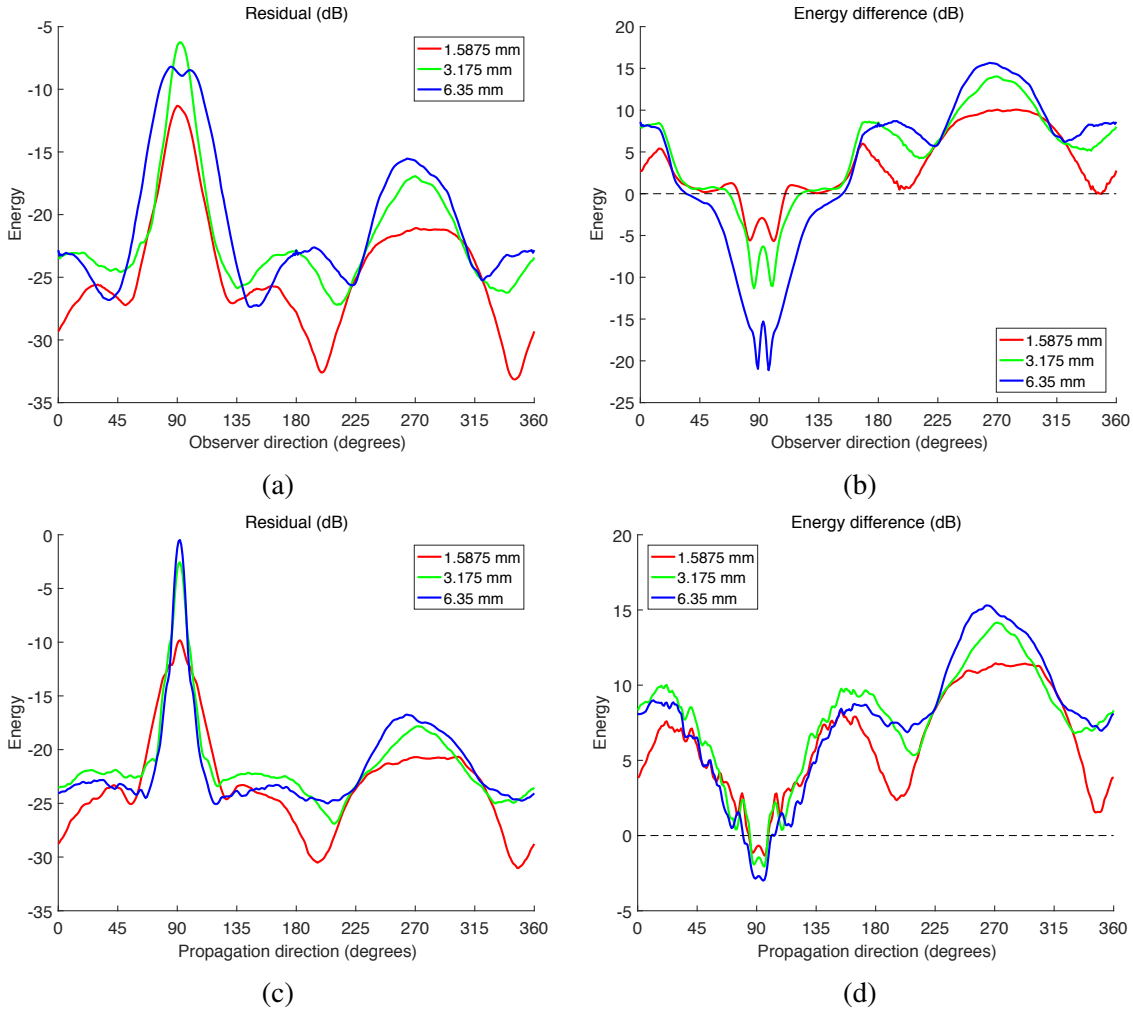

Figure 6.7: Scattering results for air-filled through-holes of different diameters in the dB domain.

#1 containing the epoxy-coupled cases (scans A9-A11) and Group #2 the oil-coupled cases (scans A12-A14); the air-filled hole case (scan A8) is included with both groups for comparison. Note that the baseline for all scans in both groups is scan A7, which is the undamaged specimen.

Figures 6.8 and 6.9 show scattering results for Group #1 in the linear and dB domains, respectively. For the epoxy fill condition, all energy curves show a consistent decrease in energy in most directions as compared to the air-filled hole. This trend is expected because the epoxy absorbs energy, which reduces both forward- and backward-scattering. For the steel- and aluminum-filled inserts with epoxy coupling, forward scattering of the aluminum insert is weaker than that of the steel insert, which indicates the increased transmission of energy through the aluminum as compared to steel. Backscattering is very similar for these two inserts, which is likely due to similarly imperfect epoxy bonds. Compared to the air-filled case, backscattered energy is weaker for both the steel and aluminum inserts because of the increased transmission through the inserts. The comparison of these two inserts to the air-filled case in the forward direction is not clearly displayed except for Figures 6.8(a) and 6.9(b). Figure 6.8(a) shows that the forward-scattered energy for both the steel and aluminum inserts is stronger than the air-filled case, which is not the expected trend. However, the energy comparison of Figure 6.9(b) clearly shows that forward scattering for both inserts is weaker than that for the air-filled hole, and also that it is weaker for aluminum than for steel. This trend is expected, and the seemingly contradictory trends further demonstrate how a phase change can lead to unintuitive results when analyzing residual energy. The Fresnel bright spot can be seen for most fill conditions and is most evident in the dB domain plots of Figure 6.9(b). The epoxy-bonded aluminum and steel inserts reduce the bright spot considerably with it effectively disappearing for the aluminum one.

Figures 6.10 and 6.11 show the scattering results for Group #2 in the linear and dB domains, respectively. Based on the observer direction, both the energy curves from resid-

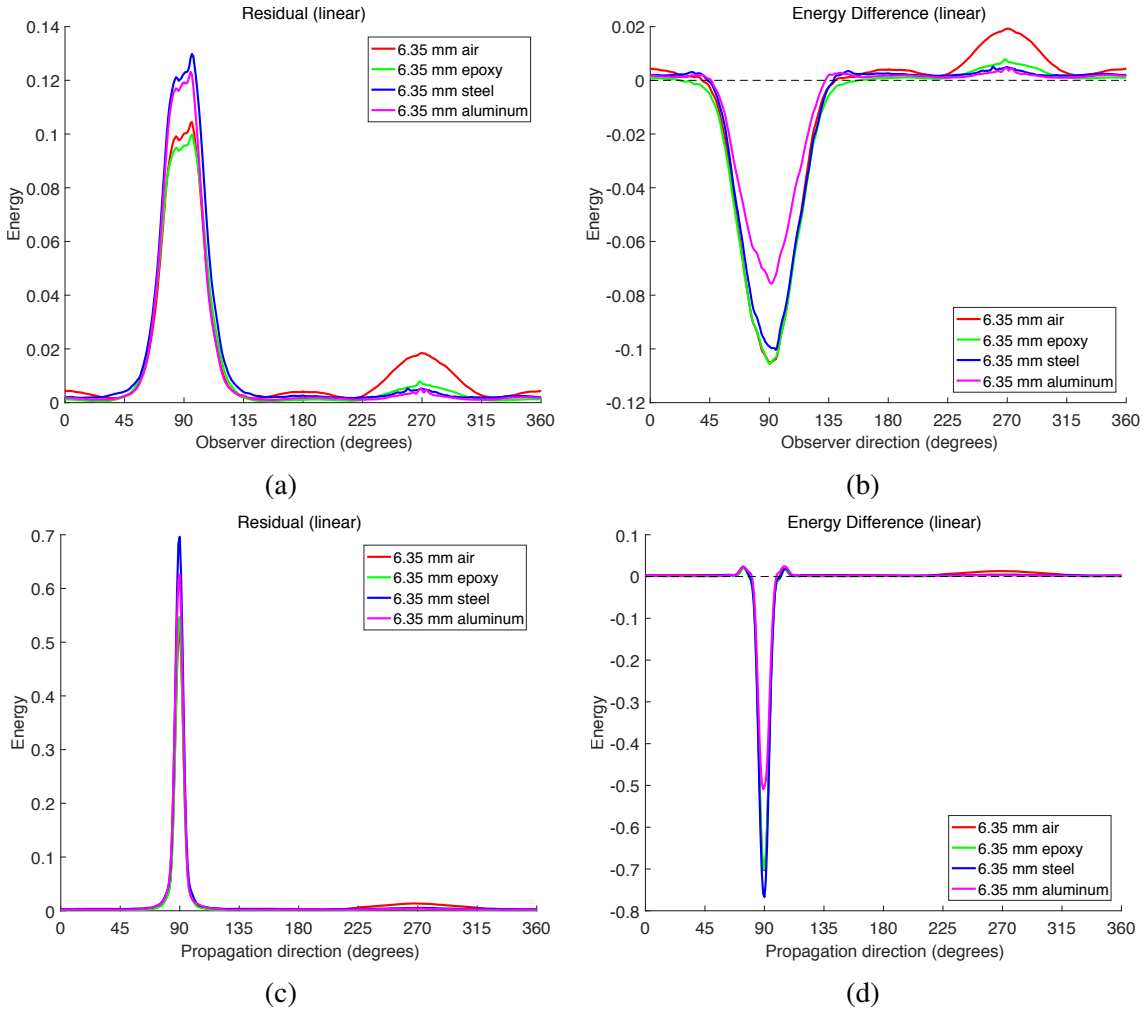

Figure 6.8: Scattering results for through-holes with different fill conditions of air, epoxy, steel, and aluminum in the linear domain.

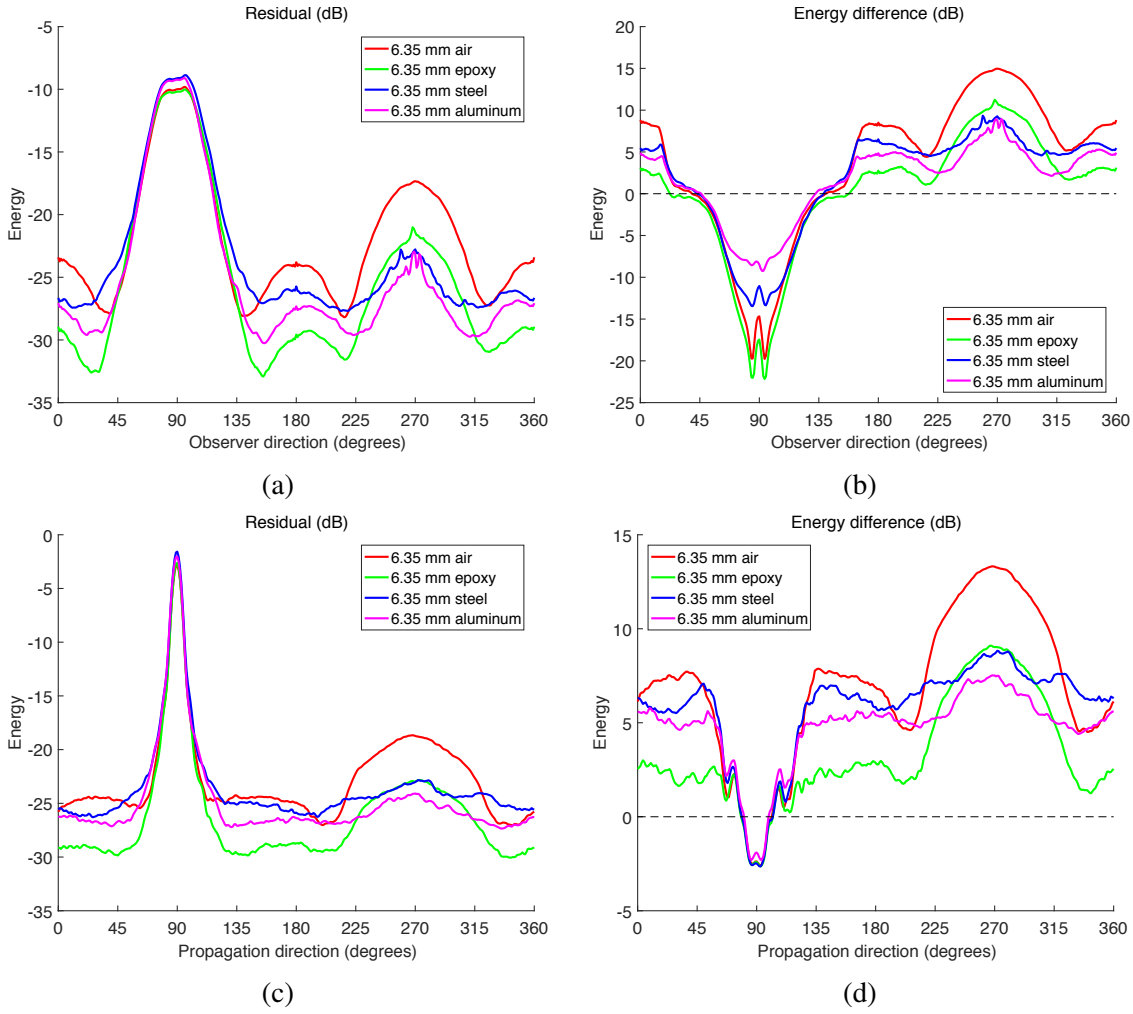

Figure 6.9: Scattering results for through-holes with different fill conditions of air, epoxy, steel, and aluminum in the dB domain.

ual wavefields and the energy difference curves consistently show the backscattering trend. All three inserts (half-steel, steel, and aluminum) with oil coupling lead to the weaker backscattering than the air-filled case, and the backscattering of the steel insert is stronger than that of the half-steel insert, which is stronger than that of the aluminum insert. As expected, the aluminum insert backscatters less energy. For forward scattering, the trend from the energy of residual wavefields is still inconsistent with that from the energy difference, which can most likely be attributed to phase differences between the current and baseline signals. As before, the energy difference yields more intuitive results since it is not sensitive to phase differences. Inspection of energy difference curves in both the linear and dB domains in Figures 6.10(b) and 6.11(b) show that forward scattering for the air-filled case is stronger than for the three inserts, as expected, with the aluminum insert leading to the weakest forward scattering. Half-steel and steel inserts have almost the same impact on forward scattering. The trend confirms that the aluminum insert allows more incident energy to be transmitted through the hole and continue to propagate above the hole than for the other cases. Using the propagation direction, scattering differences from the four cases are not at all visible in the linear domain. Even in the dB domain, the forward scattering is almost the same for the four cases, but the trend of backscattering is consistent with that seen from the observer direction. By the combination of results for Group #1 and Group #2, the epoxy fill does not seem to have much of an effect nor do any of the oil-coupled inserts. This is likely because forward scattering for the epoxy-bonded inserts is dominated by transmission of the shear waves through the insert, whereas there is likely very little transmission of shear energy for the other cases.

6.1.4 Four Method Efficacy Discussion

The results presented in this section not only show how different hole sizes and fill conditions affect scattering, they also give insight as to the strengths and weaknesses of the four methods for characterizing scattering. Overall, scattering profiles are different for the

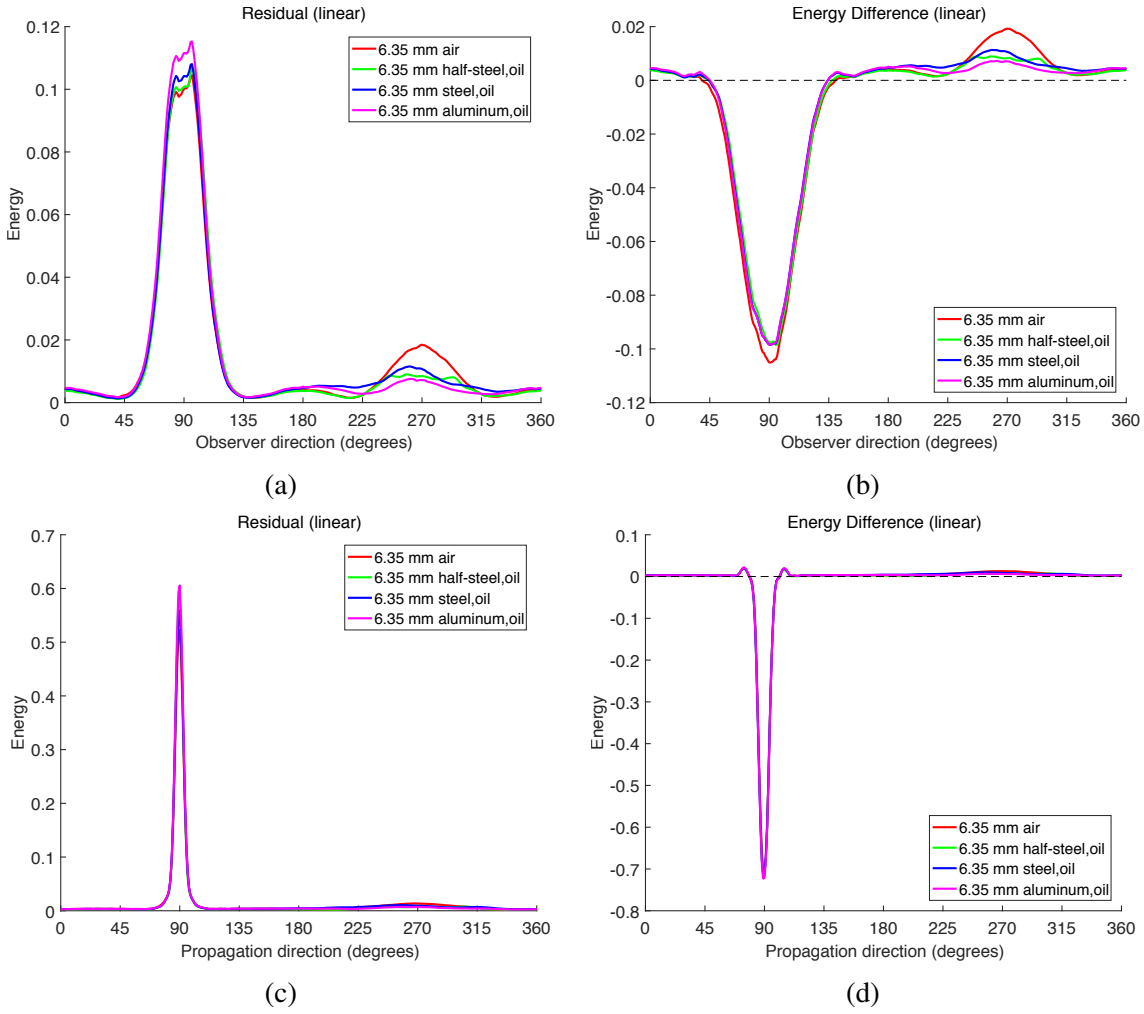

Figure 6.10: Scattering results for through-holes with different fill conditions of air, half-steel with oil, steel with oil, and aluminum with oil in the linear domain.

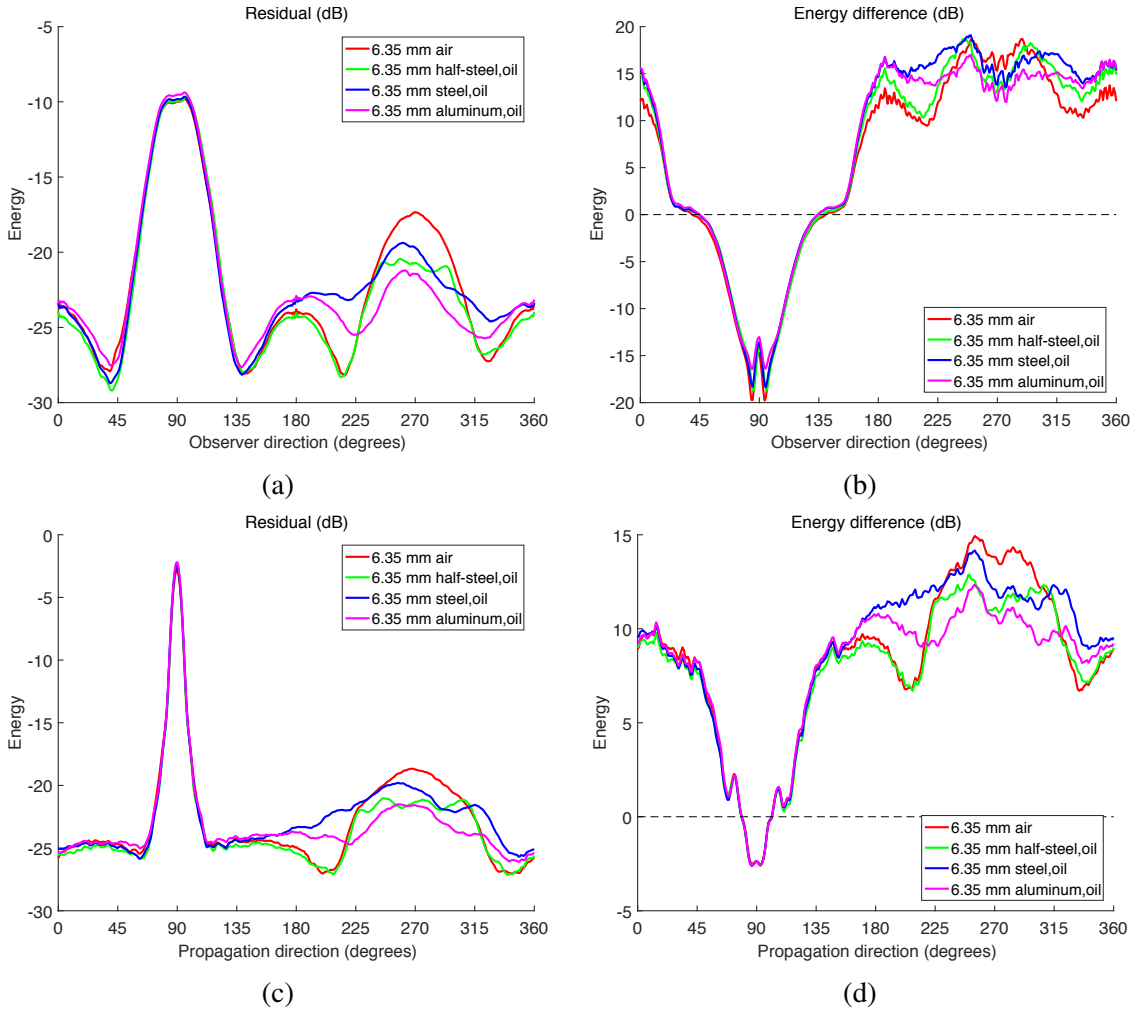

Figure 6.11: Scattering results for through-holes with different fill conditions of air, half-steel with oil, steel with oil, and aluminum with oil in the dB domain.

four methods, but they are generally consistent and complementary if interpreted properly, which can lead to a better understanding of scattering characteristics. The specific strengths and weaknesses of each method are discussed as follows.

Assuming perfect baseline subtraction, the primary strength of analyzing residual wavefields is that incident energy is removed and results clearly quantify scattering. The weaknesses are that an increase in energy cannot be distinguished from a decrease, a phase change can produce a very unintuitive result, and perfect baseline subtraction is rarely achieved. The energy comparison method does clearly discriminate between an energy increase and a decrease and it is not sensitive to phase. Its main weakness is that if the wavefields are not perfectly aligned and scaled, small changes in the incident wavefield can cause significant errors in the scattering results. This potential problem is not clearly evident in the results shown here since wavefields are well-aligned and scaled. Another weakness is that results in the dB domain can be misleading for locations in which the baseline wavefield has little energy primarily the backscattered direction. An energy threshold is subjectively set to mitigate this problem as discussed previously for each specific scattering scenario in Section 6.1.1.

The strengths of the observer direction methodology are that it is very intuitive and one radial line is analyzed at a time. Its main weakness is that the observer direction is generally not the same as the propagation direction, which can cause phase velocity ambiguities. The strength of the propagation direction methodology is that there are no directional ambiguities in the 3-D Fourier domain. The primary weakness is that near the incidence direction it is very difficult to see small changes in forward scattering because the incident energy is dominant below the hole.

6.2 Through-Hole-Scattering in the Time-Space Domain

This section summarizes hole-scattering quantification results in the time-space domain as energy curves based on the two methodologies (residual energy and energy comparison)

described in Section 5.1 and signal processing techniques presented in Section 5.4 as applied to wavefield data after shear wave filtering and time-space windowing. First, the two methods are compared in the context of quantifying scattering from a 3.18 mm diameter, air-filled through-hole (scans A1 and A2). Next, results are shown for empty holes of various diameters (scans A3-A6). Finally, all results are discussed. The two methods, described in detail in Sections 5.1, are listed as follows:

(a) Residual Energy

(b) Energy Comparison

The residual energy methods require baseline subtraction, whereas the energy comparison methods do not. However, the wavefields are globally aligned using the GSTA method before they are compared.

6.2.1 Comparison of Two Methods

Based on the time-space windowing steps as previously presented in Section 5.4.1, through-hole-scattering, caused by a single incident shear wave skip, is quantified as a group of time-dependent energy curves instead of a single scattering pattern with all shear scattered energy lumped together as was previously shown in Section 6.1. Figure 6.12 shows scattering results at several time instances computed from the residual wavefields after baseline subtraction in both the linear and dB domains. As can be seen from the figure, forward- and backward-scattered energy is distributed approximately symmetrically about 90° and 270°, respectively. In addition, forward scattering is consistently stronger than backscattering, which indicates that the energy of the residual wavefield in the shadow region is larger than the energy of backscattered waves. Specifically, it is clear to see how the scattered energy evolves as time progresses. The forward-scattering lobes become narrower and taller with time, which indicates an increasing energy trend in the forward-scattered direction. In contrast, backscattering indicates a decreasing energy trend with time, which is expected because of beam spread.

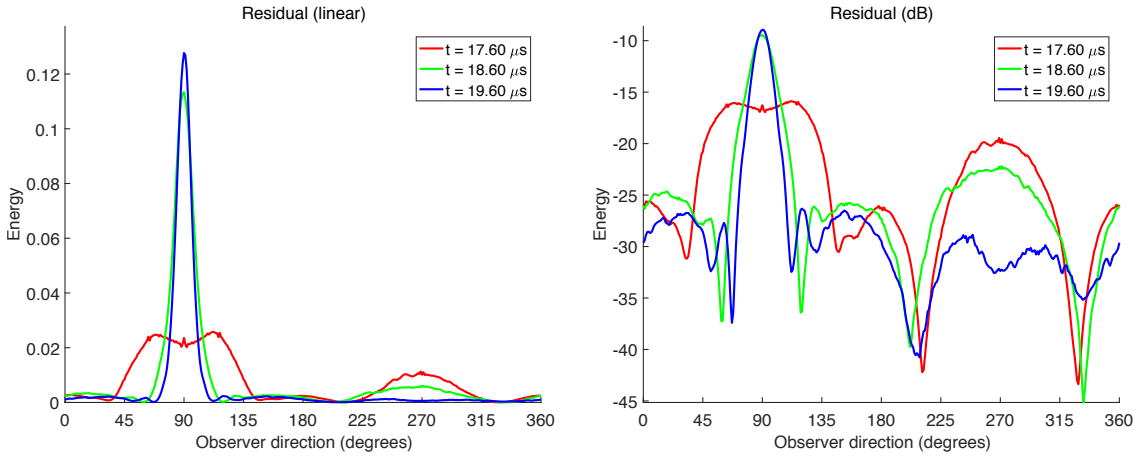

(a) (b)

Figure 6.12: Residual wavefield energy curves at several time instances via time-space windowing in the (a) linear domain and (b) dB domain.

Analysis of the residual wavefields provides instructive scattering information. However, two main deficiencies weaken the performance of scattering quantification via residual wavefields as previously discussed. The first is that an increase in scattered energy is virtually impossible to distinguish from a decrease. The second is that wavefield baseline subtraction is sensitive to slight phase shifts, which may mislead the scattering results. An alternative method is to compare the energy of the two wavefields after they are aligned to quantify the effect of the scatterer. The strategy is to apply the same time-space windowing steps to both current and baseline wavefields. Figures 6.13(a) and 6.13(b) show the filtered 2^{nd} shear skips of current and baseline wavefields, respectively, after time-space windowing at a time snapshot of 18.6 μs. The corresponding energy versus angle curves are shown in Figures 6.13(c) and 6.13(d). The energy difference curve is obtained by energy subtraction shown in Figure 6.13(e). The energy change is clearly displayed with an increase in red and a decrease in blue. In addition, as expected, more details of how scattered energy distributes in the shadow region are shown in both the energy curve of the current wavefield and the energy difference curve. Specifically, in the shadow region, two maxima are approximately located at 45° and 135°, which indicate where the strongest scattering occurs. Besides, the Fresnel bright spot, the local maximum at 90°, is clearly shown in both Figures 6.13(c) and

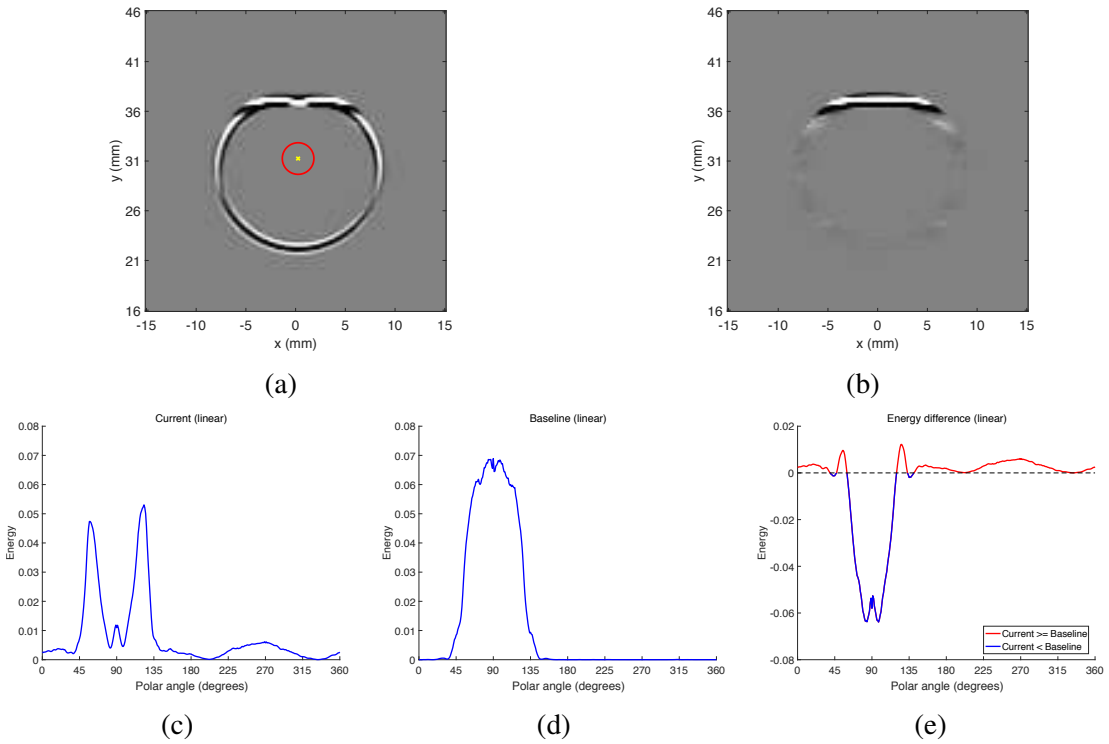

Figure 6.13: Snapshots of shear (a) current and (b) baseline wavefields at 18.6 μs. Energy curves of (c) filtered current, (d) baseline wavefields, and (e) energy difference shown on a linear scale using the time-space filter of the second shear scattered skip.

6.13(e), which is a consequence of diffraction around the hole.

Similar to the single energy curve at a time snapshot, a group of energy curves can be obtained at multiple times within a window of interest by time-space windowing for both current and baseline wavefields. Figure 6.14 shows scattering results acquired from the energy subtraction process in both the linear and dB domains, which includes energy curves of the current and baseline wavefields as well as the energy difference curves after energy subtraction. Energy curves of the current wavefield are of interest because they include the hole and can be directly interpreted. The Fresnel bright spot is visible in the shadow region at most time instances. In particular, forward scattering shows an increasing trend with time and backscattering shows a decreasing trend, which is consistent with scattering profiles of the residual wavefields.

For the energy curves of the baseline wavefield, as can be seen from the figure in the

linear domain, the incident lobes centered at 90° become narrower and taller with time. This narrowing trend is due to the polar angle being referenced from the hole center rather than the transducer. As time progresses, the incident wavefronts propagate further and further above the hole, so the angle range of observer directions referenced to the hole center become narrower. In addition, energy between 180° and 360° is very small in comparison. The non-zero backscattered energy is possibly due to imperfect surface reflections as mentioned previously in Section 6.1.1. Therefore, an energy threshold of -45 dB is set for baseline energy curves in the dB domain to ignore those small-amplitude waves that are not of interest. This processing step is also beneficial to obtain cleaner and smoother curves of both the baseline energy and energy difference in the dB domain.

For the energy difference curves, in both the linear and dB domains, positive values show that the energy of the current wavefield is larger than that of the baseline wavefield. Figures 6.14(c) and 6.14(f) show the energy difference curves in the linear and dB domains, respectively. Both figures show a consistent scattering pattern. An energy decrease occurs in the forward-scattered region because the hole blocks most of incident energy. In contrast, backscattered energy increases after the hole is introduced. Similar to the indication from energy curves of the current wavefield, energy difference curves show an increasing trend of forward scattering and a decreasing trend of backscattering with time. In addition, the Fresnel bright spot, a local maximum, is identified at a polar angle of 90°.

6.2.2 Empty Holes of Different Diameters

This section shows time-dependent hole-scattering quantification results based on different hole sizes (i.e., 1.59, 3.18, and 6.35 mm) by time-space windowing from scans A3-A6. Figure 6.15 shows results of tracking waves hole-scattered from through-holes of different hole diameters caused by the 2nd incident shear wave skip at several time values. Calculated wave trajectories of tracking the 2nd incident and scattered shear skips are shown in solid green and dashed red, respectively. The hole center is marked with a yellow cross and the

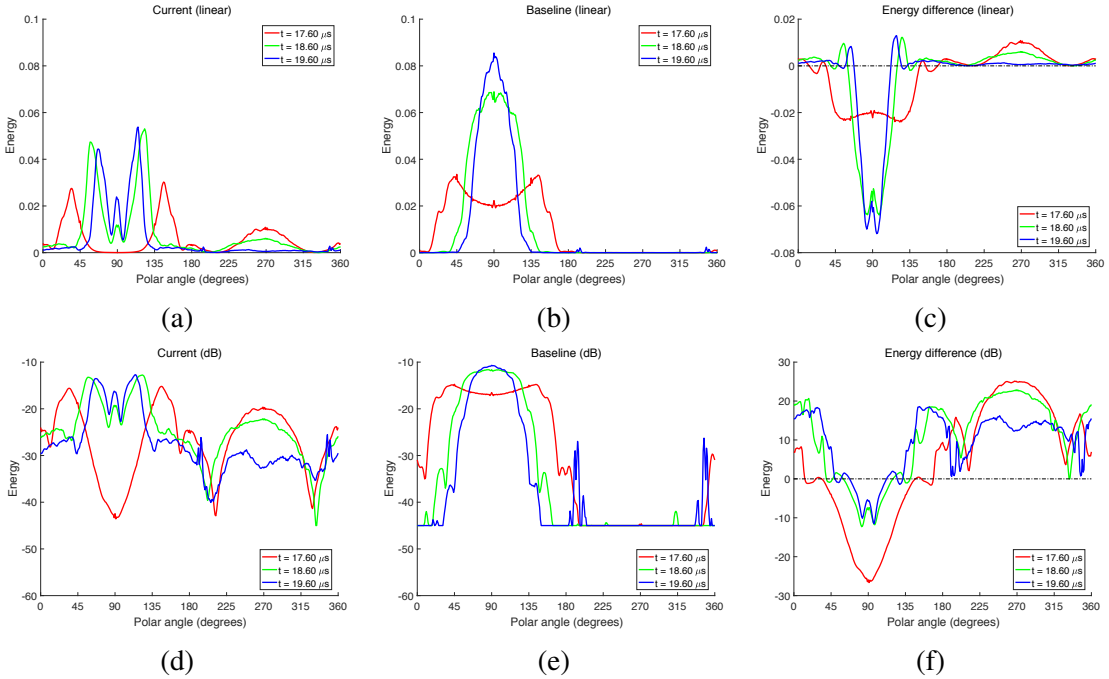

Figure 6.14: Energy subtraction process via time-space windowing in the (a/b/c) linear domain and (d/e/f) dB domain.

edge of each hole is shown with a solid red circle. The time instances selected for the three hole sizes are different, although the smallest time for all three is 18.6 μs. This smallest time results in different locations of the scattered wavefronts for the three hole sizes since scattering occurs earlier in time as the hole diameter increases. The largest time chosen for the 1.59 mm hole was 20.2 μs; it was not feasible to choose a time this large for the other two hole sizes because the scattered wavefronts propagated outside of the scan area. For all hole sizes and time snapshots, the calculated wave trajectories are well-matched to the actual wavefields. These results prove that ray tracing analysis from the side view previously described in Section 4.6.2 is effective and robust for tracking the scattered shear skip of interest for through-holes regardless of the hole size.

Time-dependent hole-scattering results are quantified as energy curves of polar angle referenced to the hole center from two quantification perspectives (residual energy and energy comparison) as previously discussed in Section 5.1. Figure 6.16 shows scattering results acquired from the energy of the residual wavefields after baseline subtraction in

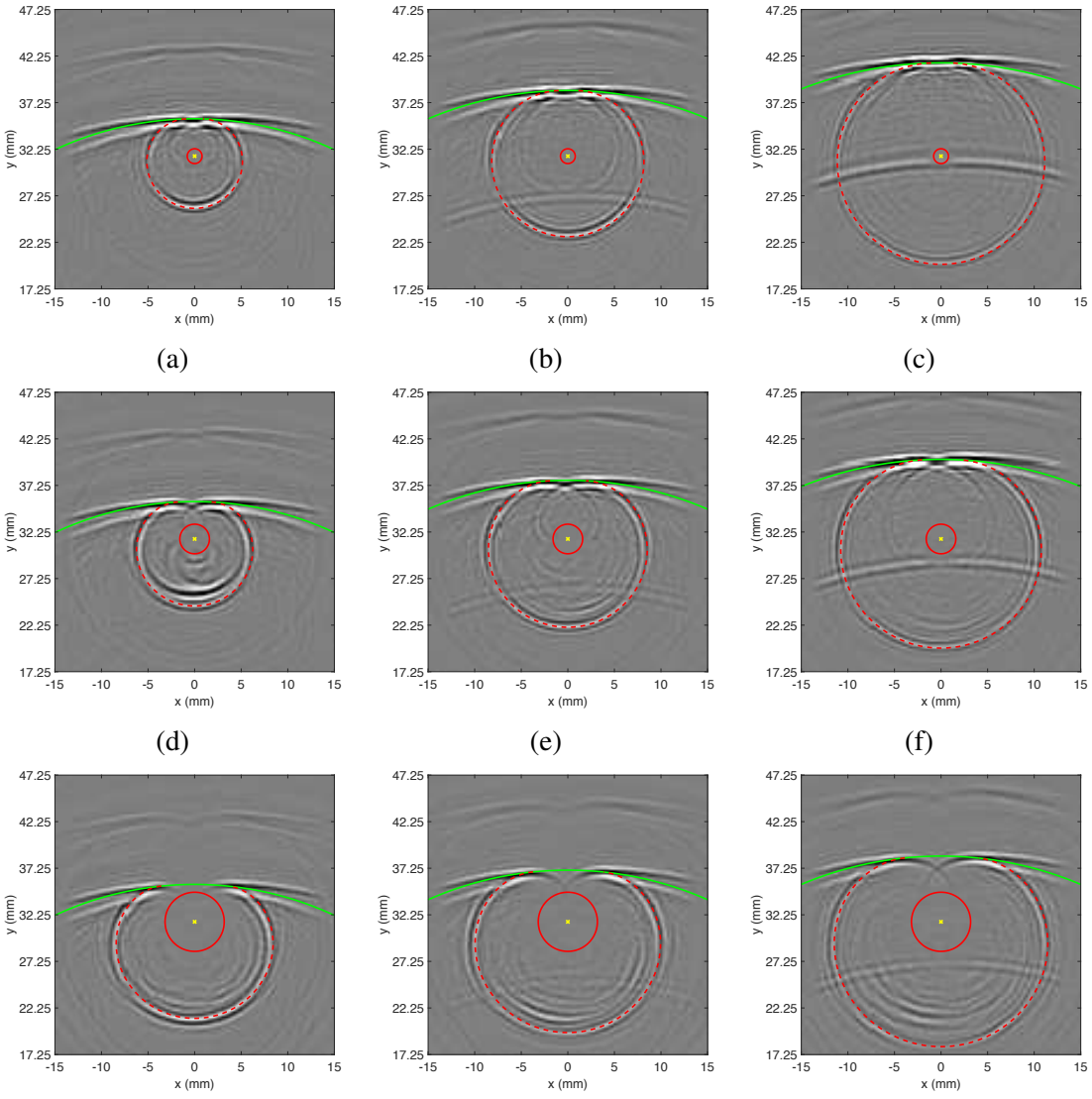

Figure 6.15: Snapshots of current wavefield with calculated trajectories of the second skip of shear incident and scattered waves. 1.59 mm diameter hole at (a) 18.6 μs, (b) 19.4 μs, and (c) 20.2 μs. 3.18 mm diameter hole at (d) 18.6 μs, (e) 19.2 μs, and (f) 19.8 μs. 6.35 mm diameter hole at (g) 18.6 μs, (h) 19.0 μs, and (i) 19.4 μs.

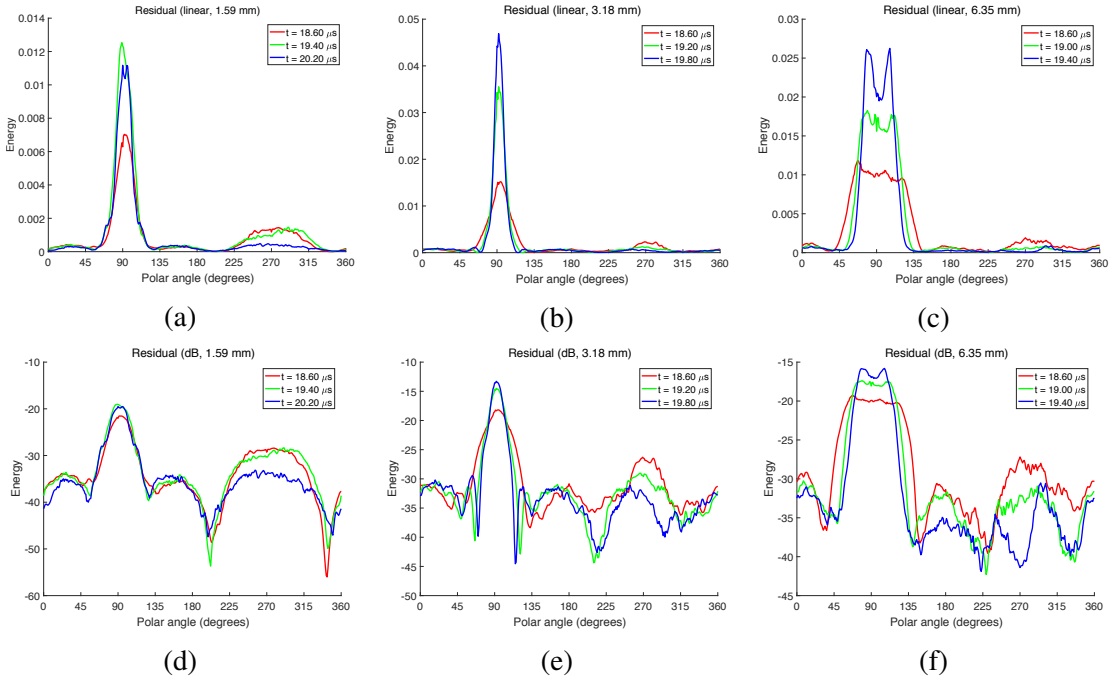

Figure 6.16: Energy curves of the residual wavefields for different hole sizes via time-space windowing in the (a/b/c) linear domain and (d/e/f) dB domain.

both the linear and dB domains. Generally, for all three hole sizes, two dominant lobes show the patterns of forward- and backward-scattering. Forward-scattering is consistently stronger than backscattering. The hole-scattering is shown in patterns grouped by hole sizes. For each hole size, quantified energy curves are similar to each other at the different time instances provided. The patterns shown here are generally consistent with the single pattern for the same hole size quantified in the frequency-wavenumber domain as shown in Figures 6.1(a) and 6.2(a). This similarity is especially evident for the hole size of 3.18 mm, particularly given that the patterns here were acquired by the scattering of only the 2nd incident shear wave skip whereas the previous ones were generated from all incident shear wave skips. Furthermore, it is clear to see how the scattered energy evolves with time for each hole size. For all three holes, the forward-scattering lobes become narrower and taller with time. Backscattering shows a decreasing energy trend as time progresses, likely caused by a combination of beam spread and where the skip reaches the measurement surface with time.

Figure 6.17 shows scattering results computed by comparing the energy between the current and baseline wavefields in both the linear and dB domains. Similar to the scattering profiles obtained from energy curves of the residual wavefields, the two dominant lobes correspond to forward- and backward-scattering for all three hole sizes. As can be seen from the figure, forward-scattering is again consistently stronger than backscattering. Another similarity is that for each hole size, forward scattering shows an increasing trend in amplitude as time progresses whereas backscattering shows a decreasing trend. In contrast to the residual energy results, at most of the provided time instances, the Fresnel bright spot is clearly shown regardless of the hole size, as was discussed in Section 6.1.1. For the hole size of 3.18 mm, the patterns at both 19.2 and 19.8 μs shown here are similar to the single patterns of the same hole size shown in Figures 6.1(b) and 6.2(b) that were obtained by the scattering of all incident shear wave skips. Here, for baseline energy curves in the dB domain, an energy threshold of -50 dB is set to ignore the smaller energy of backward-propagating waves, which leads to cleaner quantification results in the backscattered direction as previously discussed.

Figure 6.18 gives additional insight into the time-dependent scattering process by showing the energy curves of current and baseline wavefields prior to energy comparison in the linear domain. In particular, the energy plots of current wavefields are of interest since they include the hole and can be interpreted directly. The Fresnel bright spot is visible in the shadow region in the current wavefield plots for the 1.59 and 3.18 mm hole sizes. In particular, forward-scattering shows an increasing trend with time for both of these holes. For the 6.35 mm hole, neither the Fresnel bright spot nor an increasing trend in forward-scattered energy with time can be observed, which is likely due to the limited scan area. However, for the baseline wavefield energy curves, the incident lobes centered at 90° for all three hole sizes consistently become narrower and taller with time. The lobes become narrower because the angle is referenced from the center of the hole rather than the transducer, and they become larger in amplitude because the enlarging spatial window better matches

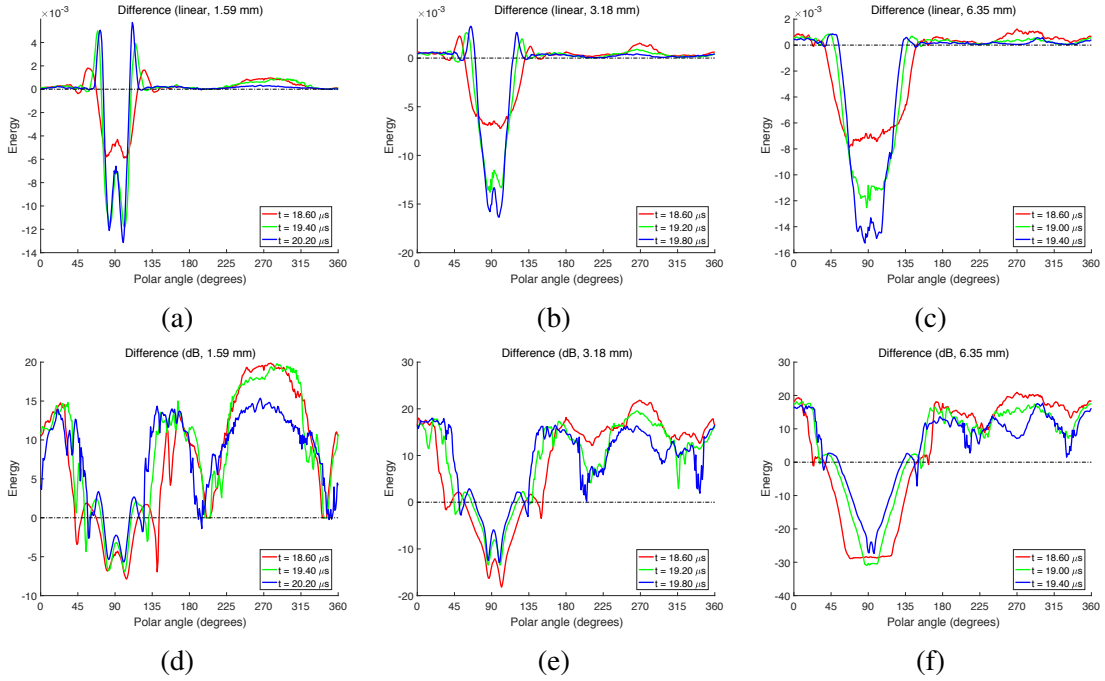

Figure 6.17: Energy difference curves for different hole sizes via time-space windowing in the (a/b/c) linear domain and (d/e/f) dB domain.

the distance of the 2nd incident shear wave skip from the transducer. Backscattered energy between 180° and 360° is very small in comparison as expected.

Similarly, Figure 6.19 shows the time-dependent scattering process in the dB domain, which provides better visualization of small energy values. Keep in mind, an energy threshold of -50 dB is set for baseline energy curves, which makes backscattered energy less noisy. In the linear domain, the Fresnel bright spot is not visible for the 6.35 mm diameter hole in the current wavefield energy curves, but the bright spot is visible for all hole sizes in the dB domain for most of the provided time instances. For the 6.35 mm hole, the Fresnel bright spot only occurs at 19.4 μs because forward hole-scattered waves have not propagated far enough from the hole before that time, which can be directly identified in the wavefield snapshots as shown in Figures 6.15(g)-(i). In addition, the trend of increasing energy with time for forward-scattering is also visible for the 6.35 mm hole.

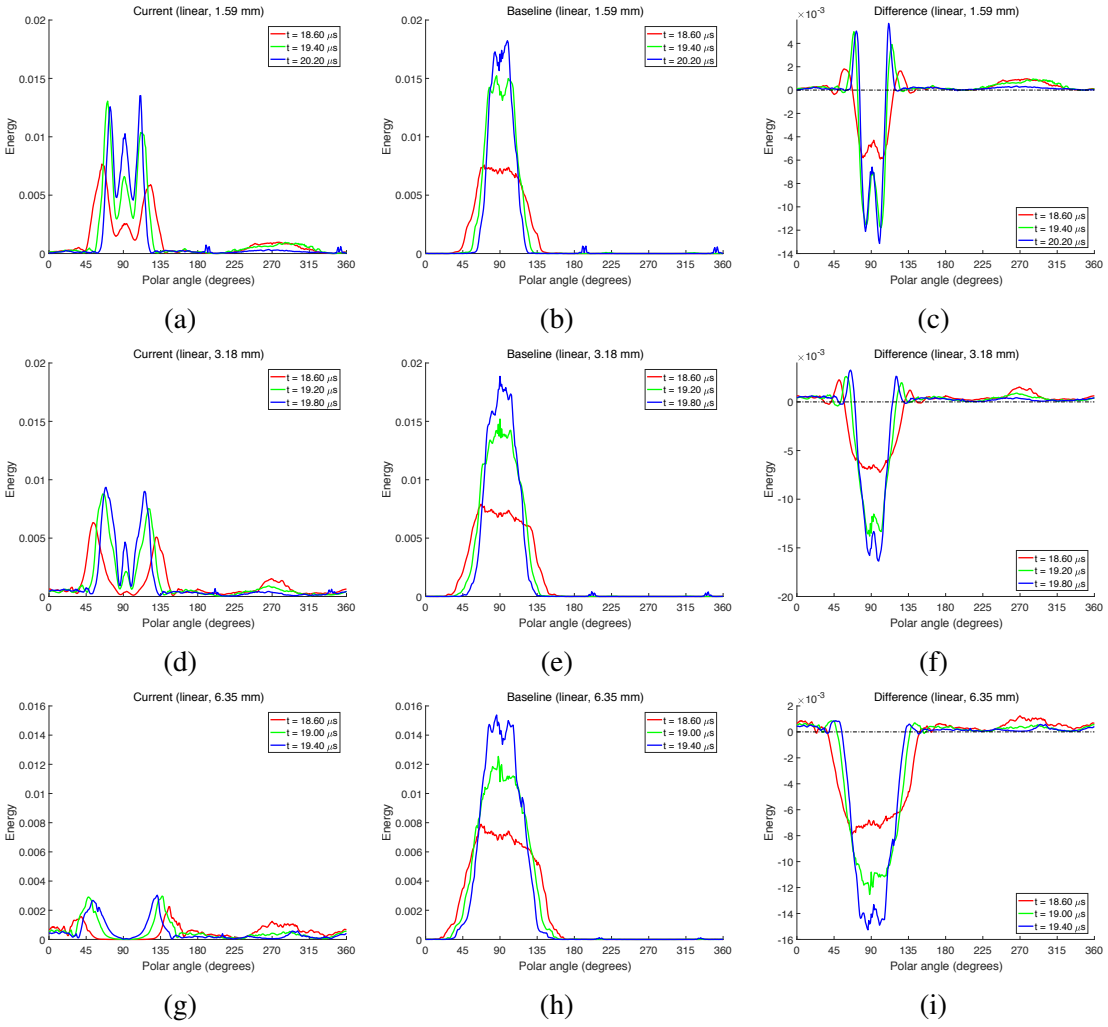

Figure 6.18: Energy subtraction process with different hole sizes in the linear domain via time-space windowing.

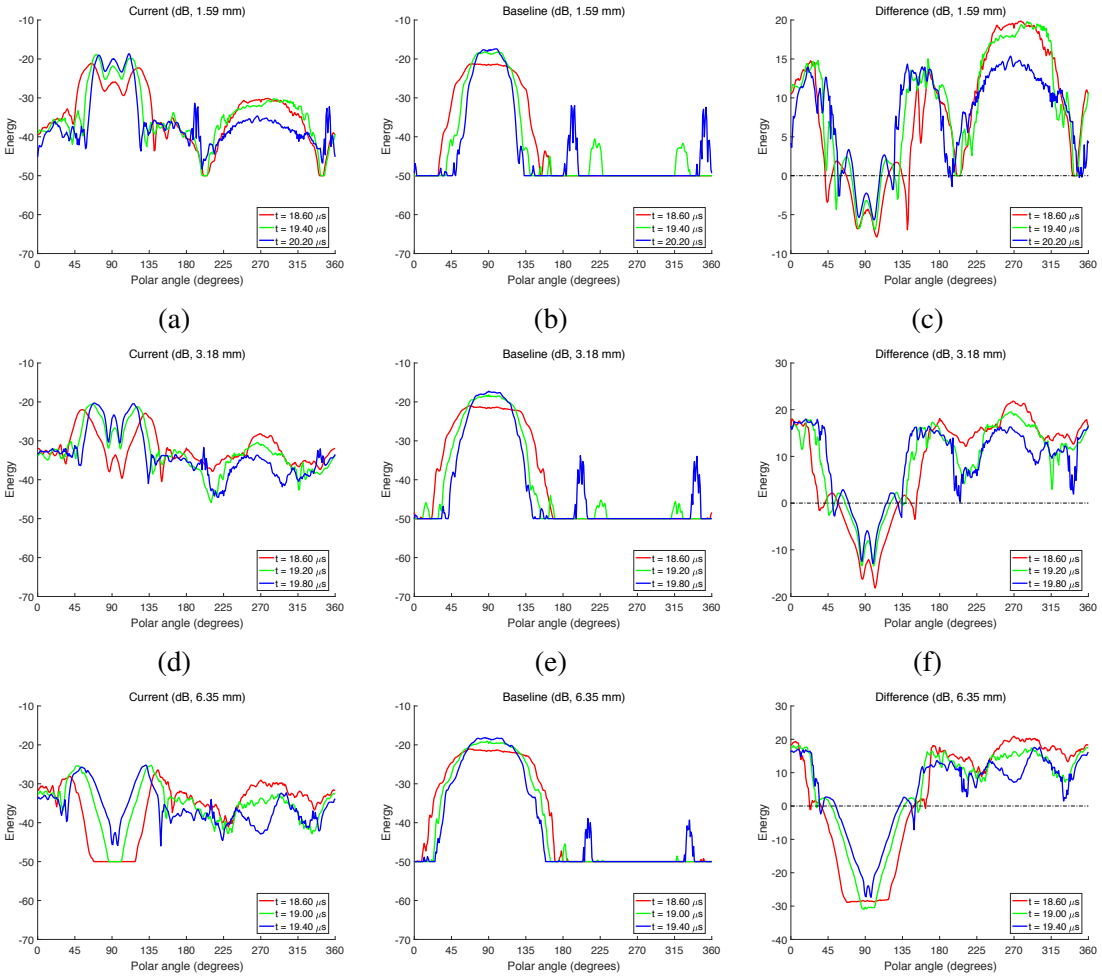

Figure 6.19: Energy subtraction process with different hole sizes in the dB domain via time-space windowing.

6.2.3 Discussion

Time-space windowing allows for extracting a specific incident shear skip and the resulting scattered skip from through-holes, which leads to the scattered energy being quantified directly in the time-space domain. The quantified scattering results are described as a family of time-dependent energy curves instead of a single curve obtained from an accumulation of all shear skips. Both methods (residual energy and energy comparison) are utilized to quantify hole-scattering in both the linear and dB domains. All results consistently show that forward scattering is stronger than backscattering. Such scattering patterns also present how scattering evolves as time progresses. Specifically, all scattering patterns consistently show an increasing energy trend in the forward-scattered direction whereas a decreasing trend in the backscattered direction with time regardless of the hole size. In addition, the Fresnel bright spot is visible in the shadow region in both current energy curves and energy difference curves at most time instances. The scattering profiles shown in this section complete the through-hole-scattering behavior at each time snapshot, mutually support the previous overall scattering patterns from all shear skips, and provide additional insights into how scattered energy changes with time.

6.3 Part-Through-Hole-Scattering

This section summarizes quantification results of part-through-hole scattering as energy curves in the time-space domain as previously described in Sections 4.5 and 5.4.2 as applied to wavefield data after shear wave filtering and time-space windowing. Scattering quantification results are from 3.18 mm diameter, air-filled part-through holes of 25%, 50%, and 75% hole depths (scans B2-B4). Finally, all results are discussed.

6.3.1 Part-Through Holes of Different Hole Depths

Based on the time-space windowing steps described previously in Section 5.4.2, three groups of part-through-hole-scattered waves in total can be effectively extracted in the time-space domain, two groups caused by the hole top and one group by the hole sides. For example, for a 50% depth part-through hole, the group of scattered waves caused by the hole sides return to the measured top surfaces after two skips; the other two groups of waves scattered by the hole top return to the top surface after 1.5 and 2.5 skips, respectively. For convenience, first, second, and third scattered skips are used to refer to these scattered waves returning to the top surface after 1.5, 2, and 2.5 skips, respectively, according to the order that they are observed in the wavefield data. This convention is extended to other hole depth cases. Then, three scattered wave skips are quantified as their respective energy curves as a function of polar angle referenced to the hole center.

Unlike through-hole scattering profiles, which show either residual energy curves or energy difference curves after energy comparison, here part-through-hole scattering patterns are directly shown by the current wavefields. Compared with through-hole-scattered waves, the main difference for part-through holes is the scattered waves caused by the hole top, and they have been time-space separated from incident waves. Therefore, there is no need to isolate the effect of these scattered waves via wavefield baseline subtraction. Here, scattering patterns of part-through holes are shown at three snapshot times, 17.6, 18.6, and 19.6 μs, to describe how scattering changes as time progresses. Figures 6.20(a)-(c) show time-space windowed wavefield snapshots at 17.6 μs from 25%, 50%, and 75% hole depth part-through holes, respectively, and Figure 6.20(d) shows the time-space windowed snapshot from the same size through-hole as a reference for comparing scattered waves caused by the hole sides. Their respective quantified energy curves are shown in Figures 6.20(e)-(h).

As can be seen from time-space windowed snapshots in the figure, both the first and second scattered skips are visible for all three hole depth part-through holes at this snapshot

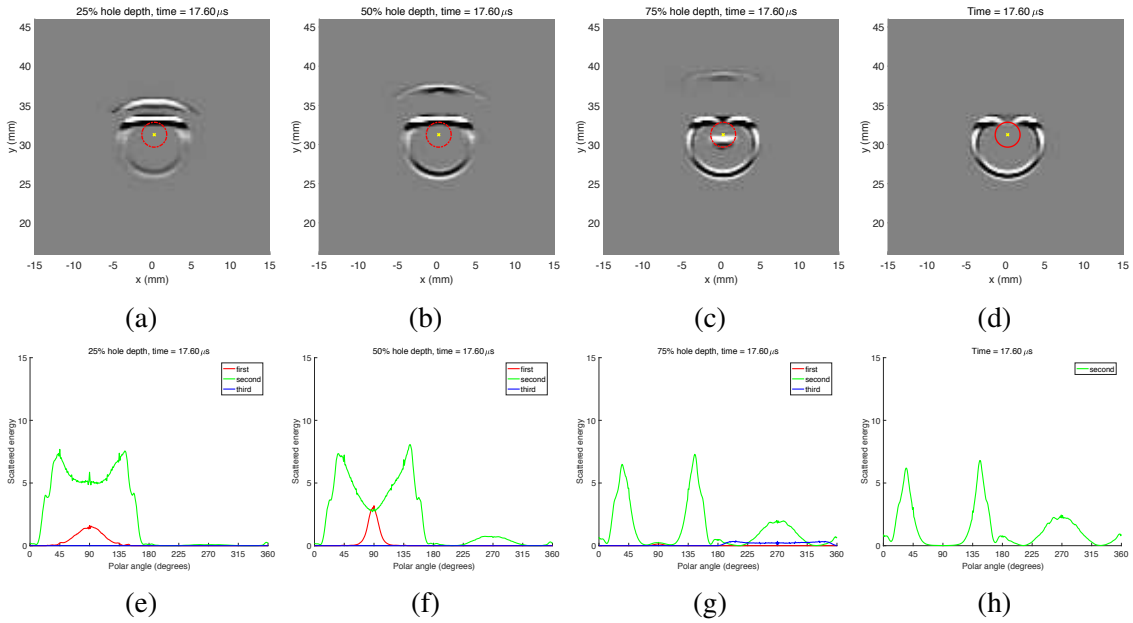

Figure 6.20: Time-space windowed snapshots at 17.6 μs of (a) 25%, (b) 50%, (c) 75% part-through holes, and (d) the same size through hole; their respective energy curves are shown in (e)-(h).

time. For the 75% hole depth one, the third scattered skip begins to appear inside the dashed red circle, which shows the location of part-through holes. More details of how scattered energy distributes can be found from energy curves. For the 25% depth hole, forward-scattering of the first scattered skip is characterized by a lobe roughly from 45 to 135°. The maximum locates at 90°, which is the vertically forward propagation direction. Forward-scattering of the second scattered skip is symmetrical about 90°. Two maxima are located at around 30° and 150°, and the minimum locates at 90°. Backscattered energy is almost zero and slightly visible. For the 50% depth hole, scattering patterns are similar, but details are a little different. For the first scattered skip, as can be seen from the red lobe, forward-scattered energy is stronger and is distributed within a narrower angle range roughly from 60 to 120°. For the second scattered skip, the minimum of forward-scattered energy, located at 90°, is weaker but the backscattering lobe is observable from 225 to 315° and the maximum locates at 270°.

For the 75% depth hole, the energy of the first scattered skip almost decays to zero

in the forward direction. For the second scattered skip, scattering patterns are generally similar to those for the through-hole of the same diameter. Backscattered energy is slightly weaker but the forward-scattered energy distribution is almost the same compared to the through-hole. Compared to other two shallower part-through holes, forward scattering is weaker and the energy minimum of forward-scattered waves is near zero but backscattering is the strongest one .

Figure 6.21 shows time-space windowed wavefield snapshots and quantification results at 18.6 μs. As can be seen from the provided snapshots, both the first and second scattered skips are visible for the 25% and 50% depth part-through holes. For the 75% depth hole, the second and third scattered skips are visible. Quantified energy curves show more details of forward- and backward-scattering. For the 25% depth hole, the forward-scattering lobe of the first scattered skip is taller and narrower than that at 17.6 μs. The scattering of the second scattered skip in both the forward- and backward-scattered directions is also stronger than that at 17.6 μs. For the 50% depth hole, the energy of the first scattered skip obviously dies out but the energy of the second scattered skip is stronger. In addition, the Fresnel bright spot is visible as a local maximum at 90°. For the 75% depth hole, the scattered energy distribution of the second scattered skip is similar to both the 50% depth hole and the through-hole. The Fresnel bright spot is also clearly visible. The energy of the third scattered skip is present in a lobe from 45 to 135° and with an energy maximum at 90°.

Figure 6.22 shows time-space windowed wavefield snapshots and quantification results at 19.6 μs. In general, for the second scattered skip, the Fresnel bright spot appears in the forward-scattering for all part-through holes and all backscattered energy monotonically decays. Specifically, for the 25% depth hole, the local maximum at 90° is strongest as compared to other two depth holes and is almost as strong as the two global maxima located at 60° and 120°, respectively. The first scattered skip lobe is weaker than that at 18.6 μs. The third scattered skip occurs in the wavefield data but the energy is very weak

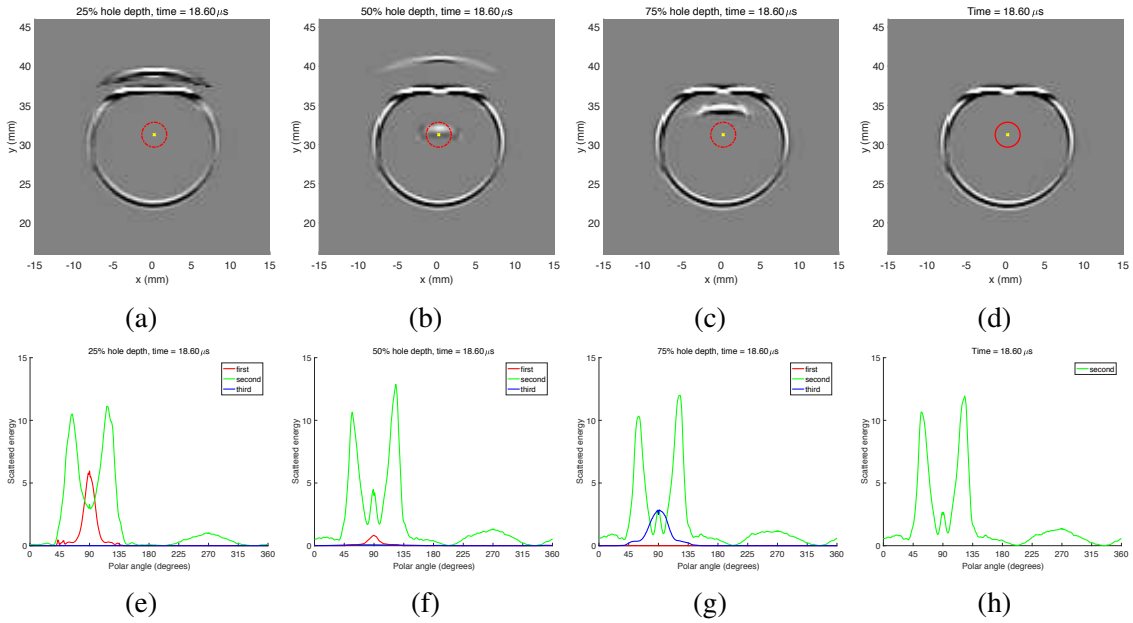

Figure 6.21: Time-space windowed snapshots at 18.6 μs of (a) 25%, (b) 50%, (c) 75% part-through holes, and (d) the same size through hole; their respective energy curves are shown in (e)-(h).

and hardly visible in scattering patterns. For the other two part-through holes, the scattering patterns are similar to that of the through-hole. In addition, for the 50% depth hole, the third scattered skip is characterized as a lobe from 45 to 135°.

6.3.2 Discussion

Time-space windowing, which is enabled from the ray tracing analysis of part-through holes, is a powerful tool to track and extract scattered waves in the time-space domain caused by different incident shear skips interacting with specific scatterer surfaces (i.e., the hole top and hole sides). This technique is applied to the wavefield data of various hole depths. The scattered energy is directly quantified in the time-space domain described as a group of time-dependent energy versus direction curves. The hole scattering caused by the hole sides is most of interest. A 75% part-through hole leads to the most similar scattering patterns as compared to the same size of a through-hole. However, more shallow part-through holes show more different scattering patterns. As an example shown in

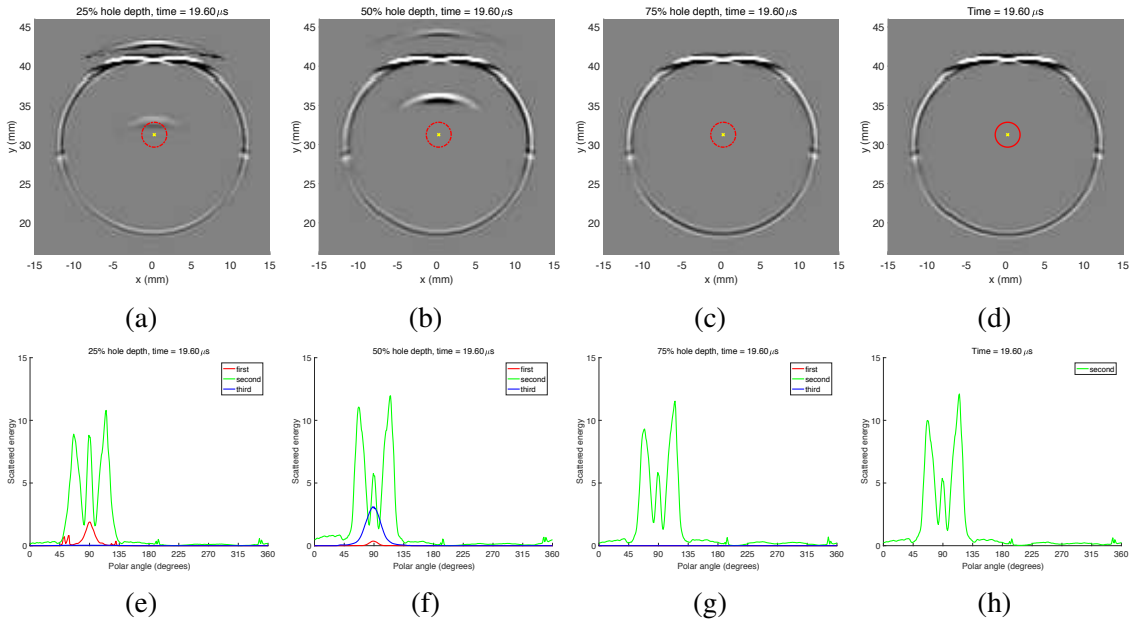

Figure 6.22: Time-space windowed snapshots at 19.6 μs of (a) 25%, (b) 50%, (c) 75% part-through holes, and (d) the same size through hole; their respective energy curves are shown in (e)-(h).

Figure 6.22(e), the 25% part-through hole leads to the strongest Fresnel bright spot in the forward scattered direction as compared to other two part-through holes and the same diameter through-hole. This scattering behavior is expected because more shallow part-through holes have smaller scatterer surfaces, which can block less incident energy. Scattering profiles also show that more shallow holes lead to weaker backscattered energy as expected.

6.4 Notch-Scattering

This section summarizes quantification results of notch scattering as energy curves in the time-space domain as previously described in Sections 4.5 and 5.4.3 as applied to wavefield data after shear wave filtering and time-space windowing. Both indirect and direct characterization methodologies are applied to notch lengths of 2 mm and 4 mm. Scattering profiles are energy difference curves after energy comparison between wavefields of damaged and undamaged holes. Finally, all results are discussed.

6.4.1 Hole Apex Aim Point

Figure 6.23 shows selected wavefield snapshots after time space-windowing based on indirect characterization, which aims to extract both hole-scattered and notch-scattered waves. Figures 6.23(a)-(c) and Figures 6.23(d)-(f) show filtered wavefield snapshots for the 2 mm and 4 mm notches, respectively, at 19, 20, 21 μs. In general, as can be seen from the figure, both hole-scattered waves caused by the second incident skip and notch-scattered waves of main interest caused by the 1.5 incident skip are effectively extracted. As expected, the 4 mm notch leads to clearly stronger backscattered waves and more energy loss in the forward direction. There is a more interesting phenomenon that the Fresnel bright spot in the shadow region behind the damaged holes is not located at the vertically forward direction anymore but is shifted towards to the notch placement direction even though the probe is aimed at the hole apex. In contrast, Sections 6.1 and 6.2 show that the Fresnel bright spot occurs at the vertical forward direction for undamaged holes. The difference implies that the introduction of notches not only leads to additional notch-scattering in both the forward and backward directions but also affects hole-scattering. This observation also explains why wavefield baseline subtraction fails to remove hole-scattered waves by aligning two sets of data from an undamaged hole and a damaged hole.

More details of notch-scattered waves can be shown in quantified energy curves. Figure 6.24 shows quantification results by indirect characterization at 19, 20, and 21 μs with a decrease in energy shown in blue and an increase in red as compared to the no-notch case. As described previously in Section 5.4.3, both time-aligned baseline (undamaged hole) and current (damaged hole) wavefields are time-space windowed and quantified as energy versus direction curves.

Generally, forward-scattering and backward-scattering are characterized by two lobes located around 45° and 270°, respectively. For the 2 mm notch, forward-scattering is stronger than backscattering for all three time snapshots provided. Backscattering shows a decreasing trend with time but forward-scattering does not, and the angle range of backscat-

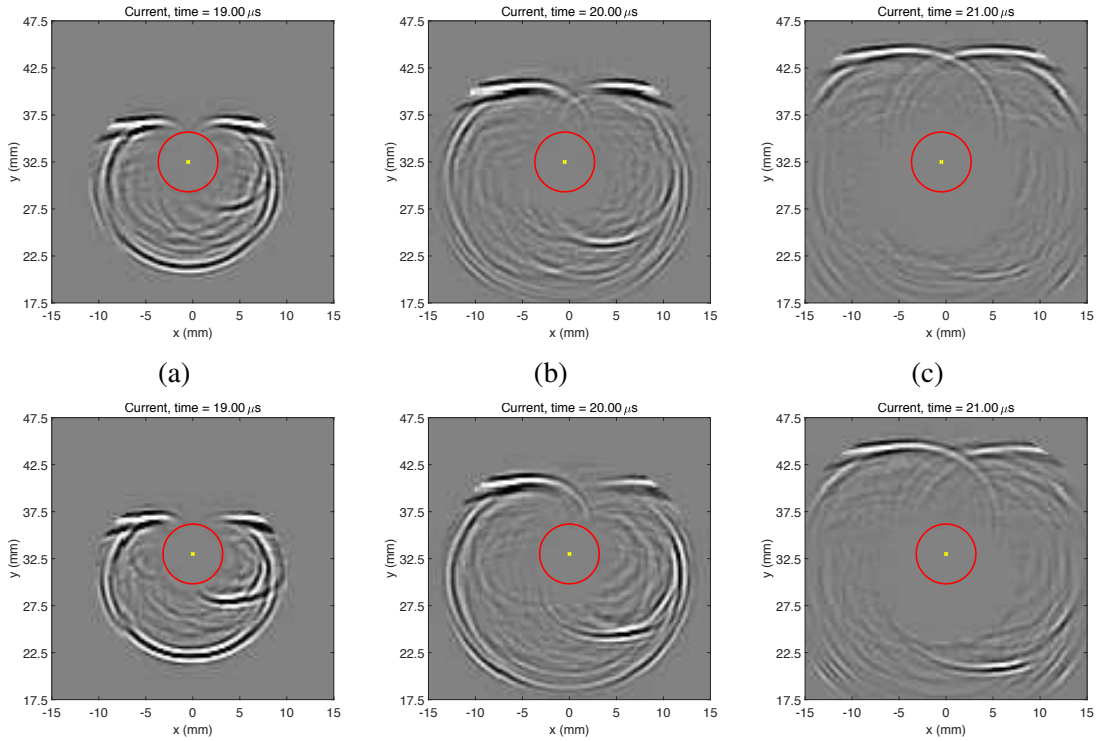

Figure 6.23: Indirect characterization based on the 60° wedge aiming at the hole apex. Time-space windowed wavefield snapshots for a 2 mm notch at (a) 19 μs, (b) 20 μs, and (c) 21 μs; 4 mm notch at (d) 19 μs, (e) 20 μs, and (f) 21 μs.

tering is broader than that of forward scattering. For the 4 mm notch, there are also two main lobes located around 45° and 270° that show forward- and backward-scattering, respectively, caused by the notch. Because the notch length is longer, both forward- and backward-scattering is stronger than that caused by the 2 mm notch. In addition, it is clearer to see the energy trend in both the forward- and backward-scattered directions as time progresses than for the 2 mm notch. Forward-scattering occurs primarily from 40 to 90° and shows a decreasing trend with time. Backscattering is more interesting. At a time snapshot of 19 μs, backscattered energy is slightly weaker than forward-scattered energy but the angle range, which is roughly from 230 to 330°, is obviously broader than that in the forward-scattered direction. One reason may be imperfect energy subtraction of hole-scattered waves. Even though undamaged and damaged holes are ideally the same except for the notches, the actual geometric details of the holes cannot be exactly the same. As a result, hole-scattered energy cannot be fully removed by energy comparison even with a time-aligned baseline. At a time snapshot of 20 μs, the two lobes of forward- and backward-scattering are nearly anti-symmetrical. That is, the energy loss in the forward-scattered direction is very similar to the energy increase in the backward-scattered direction. At a time snapshot of 21 μs, the energy of backward-scattered waves has decayed more than that of forward-scattered waves.

Figure 6.25 shows several wavefield snapshots after time space-windowing based upon direct characterization, which aims to extract notch-scattered waves according to a hole-notch point scattering approximation. Figures 6.25(a)-(c) and Figures 6.25(d)-(f) show filtered wavefield snapshots of 2 mm and 4 mm notches, respectively, at 19, 20, 21 μs. Unlike indirection characterization, which also extracts hole-scattered waves, direction characterization is targeted to the notch-scattered waves of interest. As can be seen from the figure, the windowed waves mainly consist of notch-scattered waves and a small amount of hole-scattered waves in the forward directions. The effect of hole-scattering is mostly removed even before energy comparison between damaged and undamaged holes.

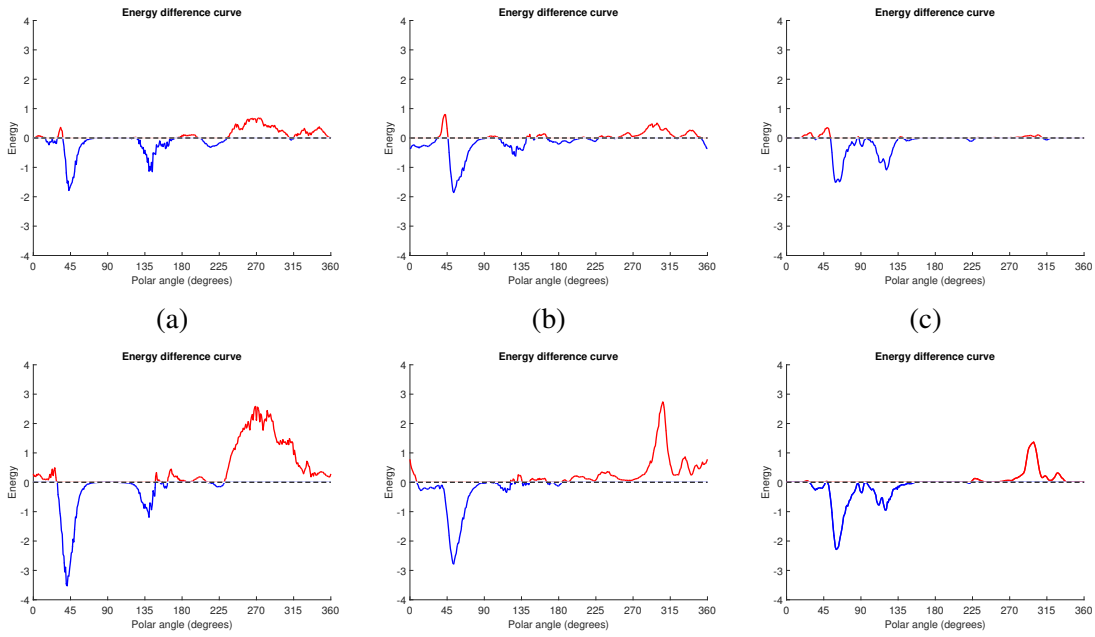

Figure 6.24: Indirect characterization based on the 60° wedge aiming at the hole apex. Scattered energy curves for a 2 mm notch at (a) 19 μs, (b) 20 μs, and (c) 21 μs; 4 mm notch at (d) 19 μs, (e) 20 μs, and (f) 21 μs.

Figure 6.26 shows quantification results for 2 mm and 4 mm notches by direct characterization. As can be seen from the figure, compared to energy difference curves shown in Figure 6.24, all energy difference curves shown here are much cleaner than those by indirect characterization from 90 to 270° because more hole-scattered waves have been removed before quantification. For each energy difference curve, there are two lobes that show an energy decrease for forward-scattering and an increase for backscattering. For the 2 mm notch, results of both 20 and 21 μs are consistent with the results by indirect characterization, but the energy difference curve at 19 μs is different. The energy of both forward-scattered and backward-scattered waves shown in Figure 6.26(a) is weaker than that shown in Figure 6.24(a). The main reason is that most of the hole-scattered waves are removed by direct characterization, which means that the energy difference shown in Figure 6.26(a) is less affected by the energy residual of hole-scattered waves after energy comparison. Thus, results from direct characterization are likely to be more accurate and

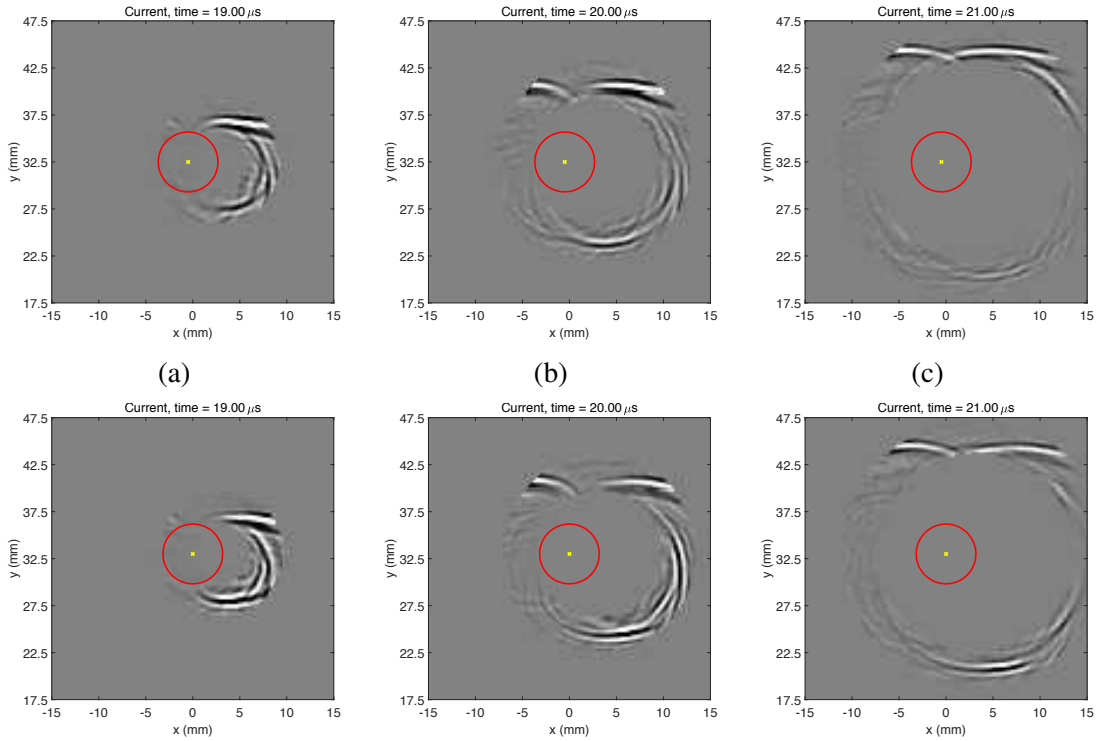

Figure 6.25: Direct characterization based on the 60° wedge aiming at the hole apex. Time-space windowed wavefield snapshots for a 2 mm notch at (a) 19 μs, (b) 20 μs, and (c) 21 μs; 4 mm notch at (d) 19 μs, (e) 20 μs, and (f) 21 μs.

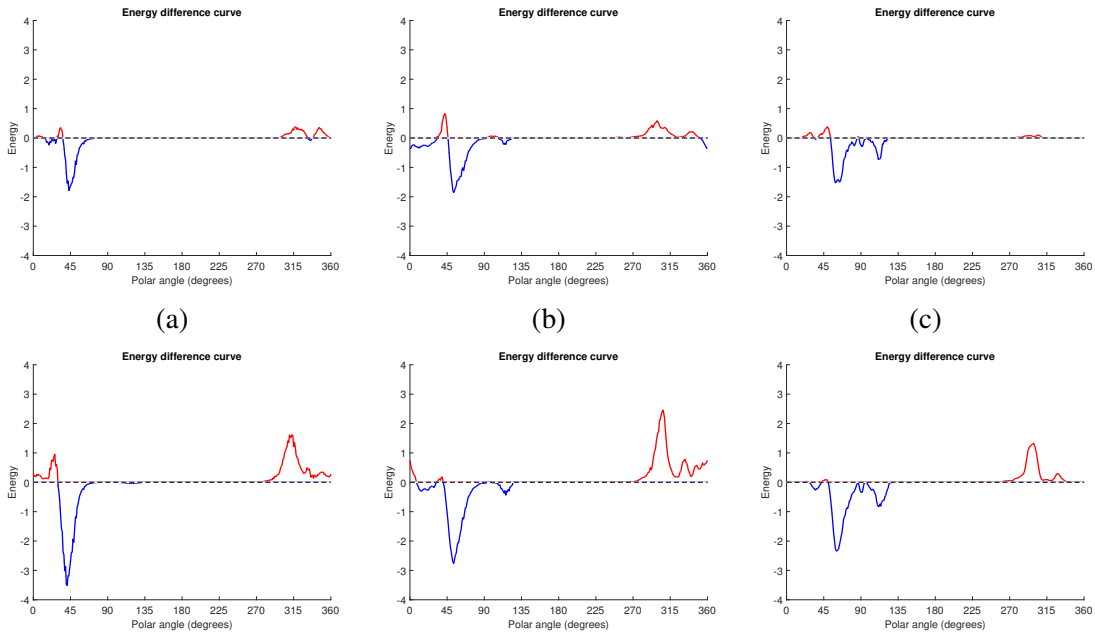

Figure 6.26: Direct characterization based on the 60° wedge aiming at the hole apex. Scattered energy curves for a 2 mm notch at (a) 19 μs, (b) 20 μs, and (c) 21 μs; 4 mm notch at (d) 19 μs, (e) 20 μs, and (f) 21 μs.

reliable for quantifying notch-scattering.

Unlike the differences between Figures 6.24(a) and 6.26(a) for the 2 mm notch, quantification results for the 4 mm notch are basically consistent with results obtained by indirect characterization. The explanation is that notch-scattered waves are much stronger when the notch is longer, which leads to stronger notch-scattered energy. Even though the energy residual of hole-scattered waves is still probably present to some extent in both Figures 6.24(d)-(f) and Figures 6.26(d)-(f) for the 4 mm notch, notch-scattered energy is dominant compared to unwanted hole-scattered energy residual and thus it can be characterized effectively by both methods. In conclusion, the direct characterization method is generally more effective to characterize and quantify notch-scattered waves because more hole-scattered waves are filtered out before quantification. Therefore, only direct characterization is applied for analyzing the following scattering scenarios.

6.4.2 Hole-Notch Corner Aim Point

The previous section presented time-space windowed wavefield snapshots when the probe (transducer+wedge) is aimed at the hole apex. This section shows results when the probe is aimed at the hole-notch corner. Figure 6.27 shows time-space windowed wavefield snapshots using the direct characterization methodology. Figures 6.27(a)-(c) and Figures 6.27(d)-(f) show filtered wavefield snapshots of 2 mm and 4 mm notches, respectively, at 18, 19, 20 μs. Compared to wavefield snapshots shown in Figure 6.25 for the probe aimed at the hole apex, wavefield snapshots presented here show notch-scattered waves occur earlier and they are clearly stronger for both notch sizes. Because the probe is aimed at the hole-notch corner with a shorter distance such that the nominal incident ray hits the notch corner after 1.5 skips, the resulting notch-scattering is observable earlier. Stronger notch-scattering indicates that this probe placement is better and generally preferred.

Figure 6.28 shows quantification results for 2 mm and 4 mm notches. Compared to energy difference curves shown in Figure 6.26, one main difference is that the overall notch-scattered energy is quantitatively larger. In addition, two cleaner lobes, located around 45° and 270°, respectively, characterize forward- and backward-scattering. In general, for both notch sizes, the lobes in blue clearly show an energy decrease in the forward-scattered region and the lobes in red effectively show an increase in the backward-scattered region compared to the energy of undamaged holes. For the 2 mm notch, forward scattering in blue is consistently stronger than backscattering at provided time snapshots, which indicates that notches block more incident energy than they scatter. In addition, forward scattering shows an increasing trend with time. Unlike forward scattering, backscattering does not show an increasing or decreasing trend. The backscattered energy increases from 18 to 19 μs and decays from 19 to 20 μs. For the 4 mm notch, both forward-scattering and backscattering is stronger than that from the 2 mm notch for all selected snapshot times, as expected. Energy difference curves also show an increasing trend for both forward- and backward-scattering as time progresses. In addition, an interesting phenomenon is that the

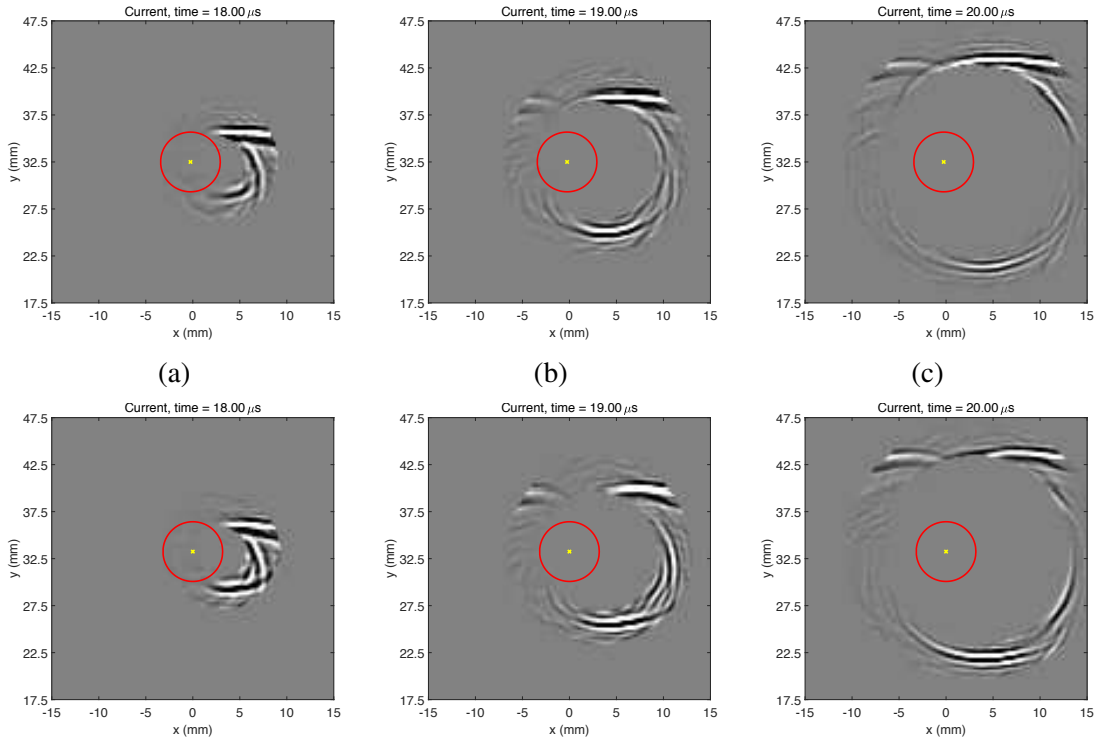

Figure 6.27: Direct characterization based on the 60° wedge aiming at the hole-notch corner. Time-space windowed wavefield snapshots for a 2 mm notch at (a) 18 μs, (b) 19 μs, and (c) 20 μs; 4 mm notch at (d) 18 μs, (e) 19 μs, and (f) 20 μs.

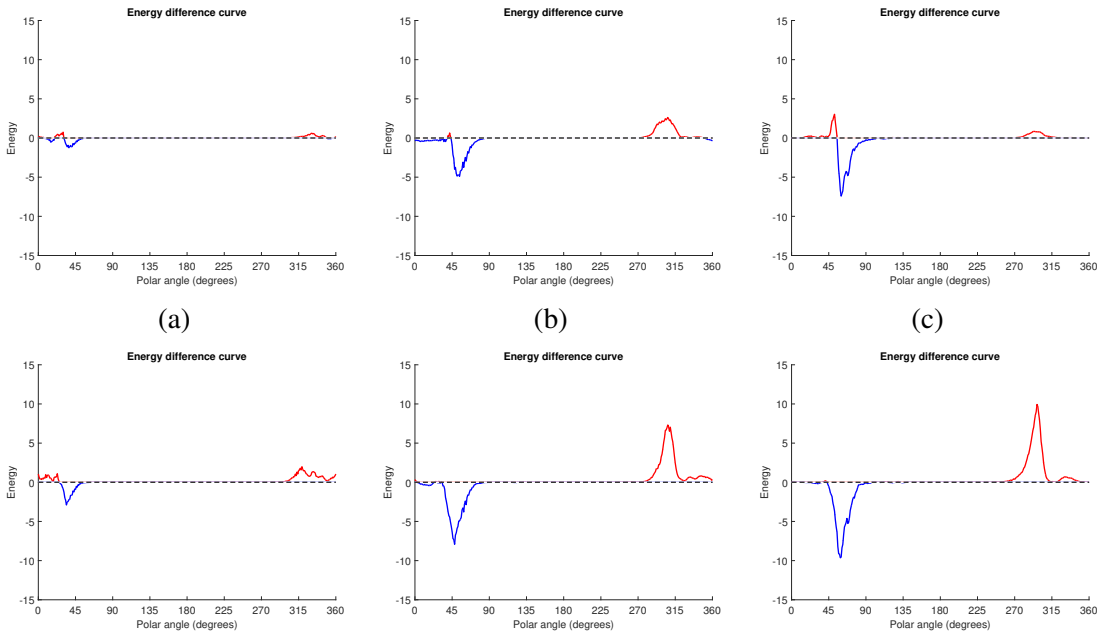

Figure 6.28: Direct characterization based on the 60° wedge aiming at the hole-notch corner. Scattered energy curves for a 2 mm notch at (a) 18 μs, (b) 19 μs, and (c) 20 μs; 4 mm notch at (d) 18 μs, (e) 19 μs, and (f) 20 μs.

two lobes of forward- and backward-scattering are nearly anti-symmetrical, which implies that the energy loss blocked by the notch is almost equal to the energy increase scattered from the notch.

6.4.3 Different Angle Wedges

This section presents notch-scattering quantification results by using different angle wedges aimed at the hole-notch corner. Figure 6.29 shows time-space windowed wavefield snapshots for 2 and 4 mm notches, respectively, at 19.5, 20.25, and 21 μs using the 45° angle wedge. Unlike the 60° probe, the 45° probe was placed 2.5 skips away from the hole-notch corner instead of 1.5 skips to avoid spatial interference of the wedge within the scan region. As can be seen from the figure, the 4 mm notch blocks more incident energy and leads to more backscattered waves. More details are shown in the energy difference curves.

Figure 6.30 shows quantified energy difference curves for the 2 mm and 4 mm notches

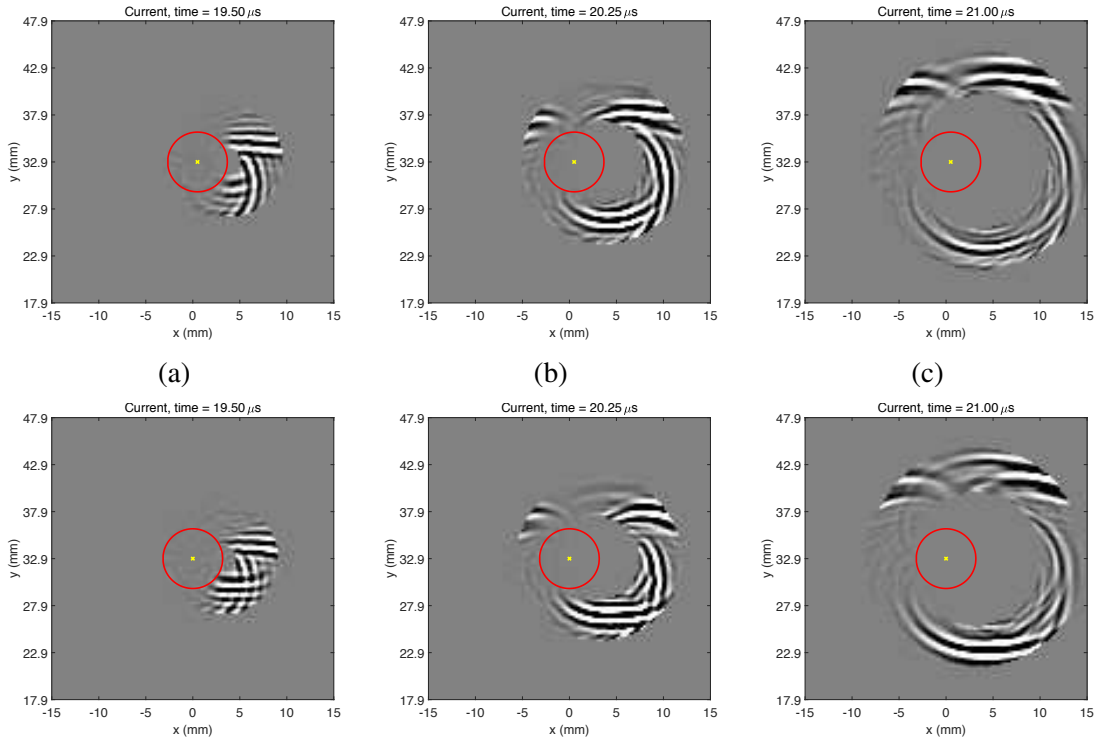

Figure 6.29: Direct characterization based on the 45° wedge aiming at the hole-notch corner. Time-space windowed wavefield snapshots for a 2 mm notch at (a) 19.5 μs, (b) 20.25 μs, and (c) 21 μs; 4 mm notch at (d) 19.5 μs, (e) 20.25 μs, and (f) 21 μs.

after energy comparison. Forward-scattering and backscattering are characterized by two lobes at around 45° in blue and 315° in red, respectively. However, an obvious additional lobe in red shows an energy increase in the forward direction. In particular, for scattering patterns of the 2 mm notch shown in Figure 6.30(b), the energy increase is even larger that the energy loss blocked by the notch, which is unexpected and most likely caused by experimental issues. One issue is possible misalignment between wavefield data of undamaged and damaged holes, which results in a large energy residual of hole-scattered waves after energy subtraction. Another issue is possible geometry differences between damaged and undamaged holes even though they are supposed to be exactly the same.

Regardless of the misleading forward-scattered lobes, time-dependent energy difference curves still provide instructive information of how scattering evolves with time. For the 2 mm notch, forward-scattered energy increases from 19.5 to 20.25 μs and slightly decreases from 20.25 to 21 μs. The strongest backscattering occurs at 20.25 μs and it is even stronger than forward scattering, which is different than the 60° wedge. For the 4 mm notch, both scattered energy are clearly larger than that for the 2 mm notch. Generally, backscattering is consistently stronger than forward scattering. At a time of 20.25 μs, backscattered energy increases and it is about three times as large as forward-scattered energy. At a time of 21 μs, forward-scattered energy slightly decreases but backscattered energy decreases in a large degree.

Unlike the 45° wedge, the 70° wedges was placed at 1.5 nominal incident skips away from the hole-notch corner. Figure 6.31 shows time-space windowed wavefield snapshots for 2 and 4 mm notches, respectively, at 22, 23, and 24 μs using the 70° wedge. As can be seen from the figure, notch-scattered waves are effectively extracted by time-space windowing. In addition, the 4 mm notch results in more scattered waves than the 2 mm notch. More scattering details are described by energy difference curves after energy comparison between damaged and undamaged holes. Figure 6.32 shows their respective energy difference curves. As can be seen from the figure, for both notch sizes, forward scattering is

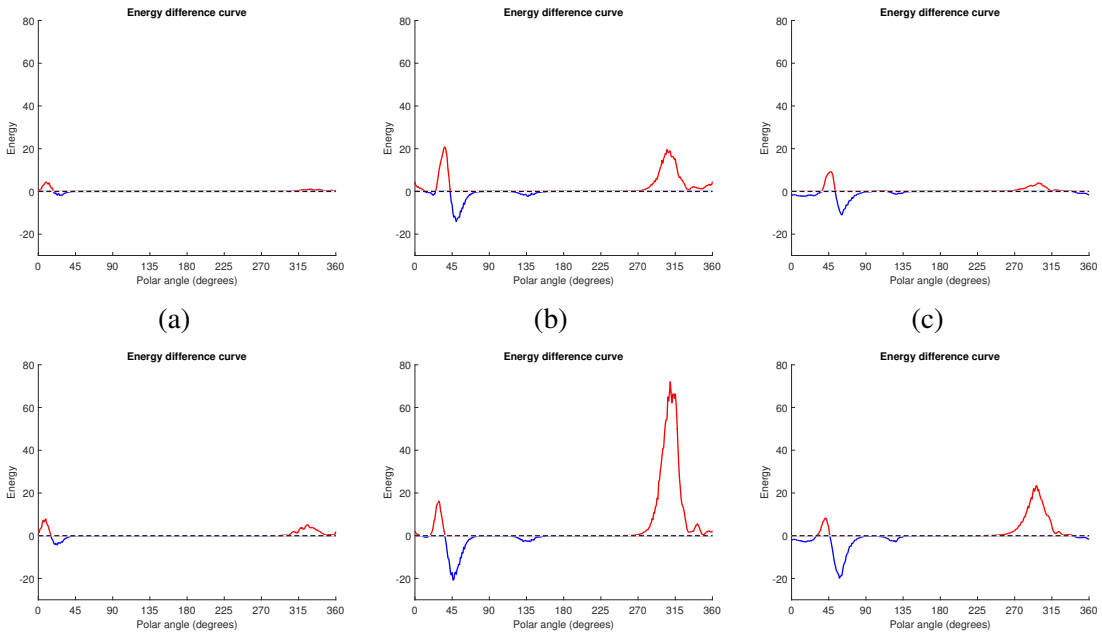

Figure 6.30: Direct characterization based on the 45° wedge aiming at the hole-notch corner. Scattered energy curves for a 2 mm notch at (a) 19.5 μs, (b) 20.25 μs, and (c) 21 μs; 4 mm notch at (d) 19.5 μs, (e) 20.25 μs, and (f) 21 μs.

characterized by a lobe in blue located around 45° but backscattering is much weaker than forward scattering, which is different than scattering patterns obtained using either the 45° or 60° wedge. For the 2 mm notch, backscattered energy slightly increases as shown in red but it is quite small. Unlike scattering patterns of the 2 mm notch, both forward and backward scattering are clearly characterized by two lobes located around 45° and 315°, respectively. Specifically, forward-scattered energy increases in a large degree from 22 to 23 μs and slightly decreases from 23 to 24 μs. Backscattered energy consistently shows this trend but the energy is still much weaker than that of forward-scattered energy.

6.4.4 Discussion

Incident wave subtraction is a reliable means to remove unwanted incident waves particularly for compound scatterers (e.g., holes+notches). This technique is applied to all notch-scattering scenarios presented here. Then, two characterization methods, one indi-

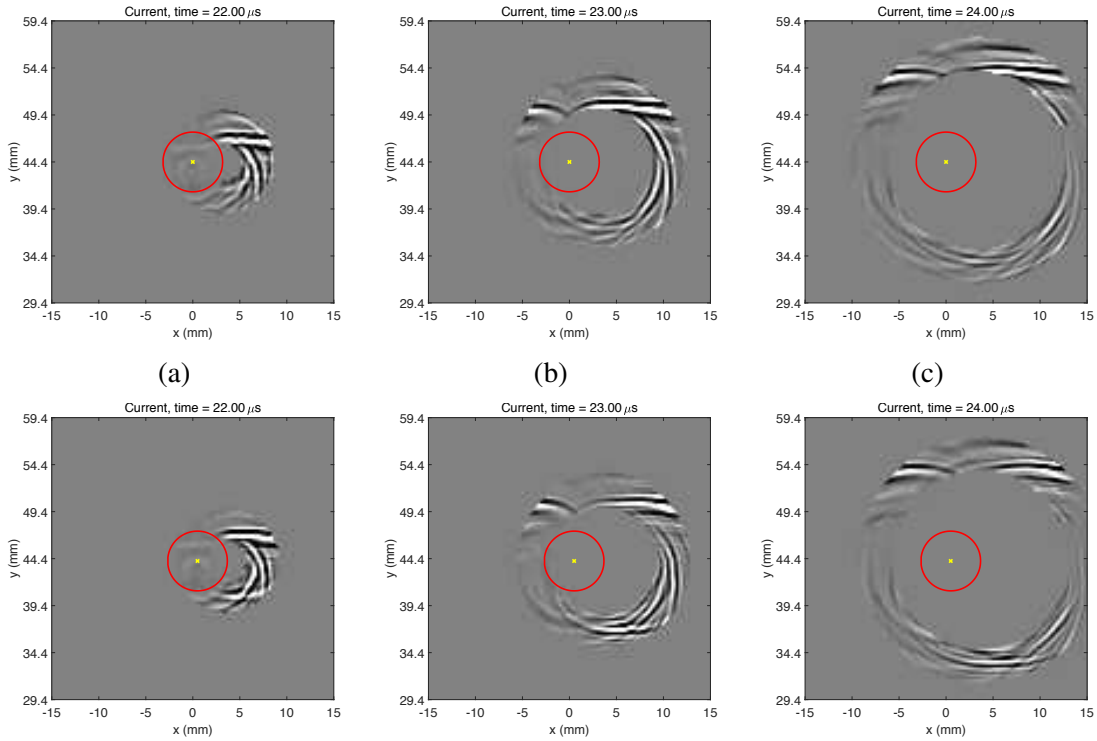

Figure 6.31: Direct characterization based on the 70° wedge aiming at the hole-notch corner. Time-space windowed wavefield snapshots for a 2 mm notch at (a) 22 μs, (b) 23 μs, and (c) 24 μs; 4 mm notch at (d) 22 μs, (e) 23 μs, and (f) 24 μs.

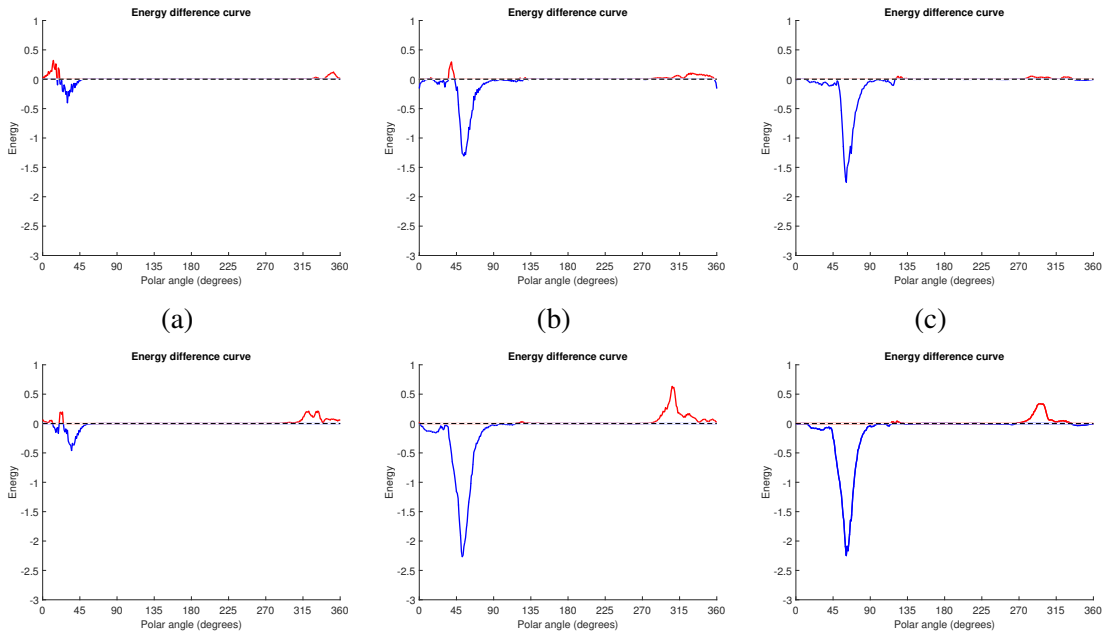

Figure 6.32: Direct characterization based on the 70° wedge aiming at the hole-notch corner. Scattered energy curves for a 2 mm notch at (a) 22 μs, (b) 23 μs, and (c) 24 μs; 4 mm notch at (d) 22 μs, (e) 23 μs, and (f) 24 μs.

rect and the other direct, are utilized to the wavefield data using a 60° wedge aiming at the hole apex. The indirect characterization, as its name imply, aims to indirectly quantify notch-scattering via the time-space windowing of hole-scattered waves. However, direct characterization is to directly extract and quantify notch-scattered waves via the other time-space windowing technique, which is build based on a hole-notch point scattering approximation. Even though both characterization methodologies effectively quantify forward- and backward-scattering by energy comparison, direct characterization provides more reliable energy difference curves, which are less affected by the unwanted energy residual of hole-scattered waves. Therefore, direct characterization is applied to different scattering scenarios for quantitative comparison.

In terms of aim points, both the hole apex and hole-notch corner are investigated using the 60° wedge. The scattering results show that the hole-notch corner is preferred over the hole apex because of stronger backscattering from notches. In terms of wedge angles,

the quantified results show very different scattering patterns. As an example of the 4 mm notch, the 45 ° wedge leads to stronger backscattering than forward scattering; the strengths of forward- and backward-scattered energy are basically the same using the 60° wedge; however, the 70° wedge causes much weaker backscattering than forward scattering. In terms of notch lengths, the 4 mm notch generates stronger forward- and backward-scattered energy than the 2 mm notch at all provided time instances as expected regardless of the aim point and wedge angle.

CHAPTER 7
CONCLUSIONS AND RECOMMENDATIONS

This chapter presents concluding remarks and recommendations for future work. Generally, this thesis focuses on wavefield-based characterization of ultrasonic shear wave scattering caused by a variety of scatterers in aluminum plates. The scatterers investigated here are through-holes, part-through holes, and notches. Experimental wavefield data of each scatterer were acquired by a wavefield measurement system, originally developed by previous colleagues Dawson $et\ al.$ [34]. Compared with prior work by previous colleagues, this research focuses more on scattering analysis. This thesis develops a set of effective signal processing techniques and demonstrates a comprehensive and systematic approach for shear wave scattering characterization.

7.1 Conclusions

In this thesis, the main signal processing techniques, which are beneficial to scattering analysis, include directional filtering, phase velocity filtering, dynamic ray tracing analysis, and time-space windowing. Directional filtering is a powerful tool to extract waves propagating within a specific direction range, which is defined in the 3-D frequency-wavenumber domain. The main application here is the separation of incident waves and backscattered waves, which is further applied to both baseline wavefield subtraction and incident wave subtraction. Directional filters are demonstrated that can robustly extract waves propagating at any angle range with minimal artifacts. Phase velocity filtering is effective to separate most of the shear waves from the total wavefield, which also includes Rayleigh and longitudinal waves, according to their respective phase velocity ranges. Even though mode conversion between shear and longitudinal waves is obviously observed in the wavefield videos as waves are reflected by scatterers, only shear waves exist in the reconstructed

wavefield data after phase velocity filtering, which is helpful for characterizing shear wave scattering. Although both directional filtering and phase velocity filtering have been previously applied to ultrasonic guided waves, their application and implementation here on bulk waves are novel.

Ray tracing analysis is another useful technique for both characterizing scattering in the time-space domain and obtaining a deeper understanding of shear wave propagation and scattering process. Firstly, ray tracing analysis is demonstrated that can accurately track incident shear wave skips and specific wavefronts scattered from either a through-hole or a part-through hole. The enlarged trajectories of these wavefronts lead to time-space windows, which characterize and quantify scattering caused by a specific incident skip into a group of time-dependent energy curves. The time-space windowing is further applied to indirectly characterize notch-scattering by the energy change of total scattered waves. Secondly, ray tracing analysis is a supportive way to explain and analyze shear wave propagation and scattering process in 3-D. The obtained wavefield data are measured in two spatial dimensions but shear waves, as one type of bulk wave, interact with the two plate surfaces and scatterers in three spatial dimensions. Ray tracing analyses for pristine plates, through-holes, part-through holes, and notches definitely provide complementary perspectives to fill the gap between the visible data on the plate surface and propagation process within the plate. In addition, it is noteworthy that the ray tracing models developed here under several simplifying assumptions are easier to implement and faster to execute than a more comprehensive model.

Incident wave subtraction is another improvement as compared to prior work. Unlike wavefield baseline subtraction, which aims to align and subtract damage-free baseline wavefields to isolate scattered waves, incident wave subtraction developed here directly utilizes the current wavefield itself regardless of the geometric complexity of scatterers. The technique is demonstrated that can effectively remove unwanted incident waves without affecting scattered waves of interest for notch scattering scenarios. It is anticipated that the

technique is practically helpful to remove incident waves if the baseline wavefields cannot be well aligned to the current wavefields.

This thesis presents multiple methods for characterizing and quantifying shear wave scattering in the form of scattering patterns. Through-hole scattering is characterized in both the frequency-wavenumber domain and time-space domain. In the frequency-wavenumber domain, two definitions of direction (observer direction and propagation direction) and two quantification methods (energy of residual wavefields and energy comparison), are proposed and implemented. Combining these methods pairwise results in four distinct methodologies for generating scattering patterns that are energy-versus-direction curves. Their strengths and weaknesses are discussed and they are complementary with no one method being the clear favorite. It is further found to be useful to view results of all methods in both the linear and dB domains. In the time-space domain, hole-scattering caused by a specific incident skip is directly characterized by time-space windowing. Scattering patterns are a group of time-dependent energy curves instead of a single overall energy curve in the frequency-wavenumber domain. The quantified scattering profiles are more instructive to display how scattering evolves as time progresses and how the hole diameter affects scattering. Even though this research only shows the hole-scattering caused by the 2^{nd} incident skip, which is most affected by through-holes, it is robust to apply to scattered waves caused from each incident skip. It is even powerful to track and quantify Rayleigh waves in a similar way.

Motivated by through-hole scattering characterization, the scattering caused by more complex scatterers such as part-through holes and notches investigated here is directly characterized in the time-space domain. Resulting scattering profiles clearly show how scattering changes with time and allow for more detailed evaluations. For part-through-hole scattering, quantification results of different hole depths are compared and discussed. For notch scattering, various factors such as notch length, probe location, and wedge angle are investigated and how these factors affect notch scattering is discussed in detail.

In addition, the Fresnel (or Poisson) bright spot, which is a valuable indicator of the hole diffraction process, is clearly observed in the shadow region behind both through-holes and part-through holes. Although not pursued here, there may be NDE applications related to how a defect may influence the existence, amplitude, and location of the bright spot.

7.2 Recommendations for Future Work

This research has developed a set of systematic signal processing techniques, established a comprehensive approach for shear wave scattering characterization for a variety of scatterers, and made a contribution to the field of ultrasonic NDE. However, there is still a considerable amount of research to be explored. The most obvious recommendation is to apply the developed techniques and methodologies for scattering characterization to more complex angle-beam shear wave scattering problems. This thesis focuses on various scatterers in single-layer specimens. In particular, crack-like notches are of practical interest. However, in practice, these crack-like defects usually occur between bonded layers instead of single layers. Therefore, scattering of ultrasonic waves from buried defects emanating from through-holes in bonded plate-like structures is of particular interest for aerospace applications and it is strongly recommended to be researched for future work.

It is also recommended that additional transducer frequencies be considered. Here, only one transducer frequency of 5 MHz was investigated. One natural extension would be to consider higher transducer frequencies and see how transducer frequencies affect the scattering behaviors especially for the scattering of smaller notches. Another would be to investigate the sensitivity of the scattering patterns to other experimental factors such as transducer orientation and location. The purpose is to optimize the transducer configuration for the sake of multiple scattering separation. For example, for notch-scattering analysis, one main challenge is how to separate and extract notch-scattered energy from hole-scattered energy. The methodologies presented here, which include indirect and direct characterization methods, are effective to characterize and quantify notch scattering

by energy comparison, but it would be much easier if these two types of scattered waves were time-space separated in the current wavefield. The notch scattering can then be directly characterized and quantified in the time-space domain without the need of recording a baseline from an undamaged hole. In addition, in terms of sensitivity study of notch scattering, various fill conditions and notch geometries would be considered.

In addition, it would be more meaningful to improve angle-beam inspection performance in practice in terms of multiple scattering separation. For example, pulse-echo and pitch-catch inspection methods are often used in industrial applications. Regardless of the method, the observed signals from the receiving transducer can show possible echoes caused by a flaw or geometrical feature. However, returning echoes from multiple scatterers (e.g., a crack originating from a through-hole) may overlap, which makes flaw detection difficult. In this case, it will be helpful if there is specific guidance to place transducers in such a way that leads to multiple scattering separation in the time-space domain.

It is strongly recommended that ultrasonic wave propagation models be developed. Accurate models are key to the development of future NDE quantification methods and they can explain bulk wave interactions from structures and scatterers with more detail. Such models must be validated by experimental data. The experimental wavefield data presented in this thesis and corresponding scattering quantification results by the various methods can be utilized for validating these simulated models. Unfortunately, data from models are not yet available that are comparable to data obtainable via wavefield experiments because of computational requirements. As computing power continues to increase and model data become available, the quantification performance will be improved further.

Finally, it is recommended that both signal processing techniques and wavefield analysis methods presented in this thesis be applied to other ultrasonic scattering problems because the methodologies are quite general in nature. For example, characterization of Lamb wave scattering is particularly suited to wavefield measurements via wavefield imaging so that it could particularly benefit from the various techniques for processing acquired

wavefields and methodologies for generating scattering patterns.

REFERENCES

[1] C. J. Hellier, *Handbook of Nondestructive Evaluation*. New York: McGraw-Hill, 2003.

[2] J. Krautkrämer and H. Krautkrämer, *Ultrasonic Testing of Materials*. New York: Springer-Verlag, 1997.

[3] P. J. Shull, *Nondestructive Evaluation: Theory, Techniques, and Applications*. New York: Marcel Dekker, 2002.

[4] American Society for Nondestructive Testing, *Introduction to Nondestructive Testing*. [Online] Available: https://www.asnt.org/MinorSiteSections/AboutASNT/Intro-to-NDT (last accessed 11/01/2017).

[5] L. W. Schmerr Jr., *Fundamentals of Ultrasonic Nondestructive Evaluation*. Springer, 2016.

[6] J. L. Rose, *Ultrasonic Guided Waves in Solid Media*. New York: Cambridge University Press, 2014.

[7] Lord Rayleigh, "On waves propagated along the plane surface of an elastic solid," *Proceedings of the London Mathematical Society*, vol. 1, no. 1, pp. 4–11, 1885.

[8] H. Lamb, "On waves in an elastic plate," *Proceedings of the Royal Society of London. Series A*, vol. 93, no. 648, pp. 114–128, 1917.

[9] R. Stoneley, "Elastic waves at the surface of separation of two solids," *Proceedings of the Royal Society of London. Series A, Containing Papers of a Mathematical and Physical Character*, vol. 106, no. 738, pp. 416–428, 1924.

[10] J. G. Scholte, "The range of existence of Rayleigh and Stoneley waves," *Geophysical Supplements to the Monthly Notices of the Royal Astronomical Society*, vol. 5, no. 5, pp. 120–126, 1947.

[11] A. E. H. Love, "Some problems of geodynamics," *Bulletin of the American Mathematical Society*, vol. 20, no. 8, pp. 432–434, 1914.

[12] D. A. Cook and Y. H. Berthelot, "Detection of small surface-breaking fatigue cracks in steel using scattering of Rayleigh waves," *NDT & E International*, vol. 34, no. 7, pp. 483–492, 2011.

[13] R. S. Edwards, S. Dixon, and X. Jian, "Depth gauging of defects using low frequency wideband Rayleigh waves," *Ultrasonics*, vol. 44, no. 1, pp. 93–98, 2006.

[14] D. E. Chimenti, "Guided waves in plates and their use in materials characterization," *ASME Applied Mechanics Reviews*, vol. 50, no. 5, pp. 247–284, 1997.

[15] P. Wilcox, M. Lowe, and P. Cawley, "The effect of dispersion on long-range inspection using ultrasonic guided waves," *NDT & E International,*, vol. 34, no. 1, pp. 1–9, 2001.

[16] J. L. Rose, *Ultrasonic Nondestructive Evaluation Technology for Adhesive Bond and Composite Inspection*. Springer, 1991.

[17] P. M. Shearer, *Introduction to Seismology*. Cambridge, United Kingdom: Cambridge University Press, 2009.

[18] Olympus Corporation, *Ultrasonic Flaw Detection Tutorial*. [Online] Available: http://www.olympus-ims.com/en/ndt-tutorials/flaw-detection/angle-beam-probe-selection/ (last accessed 11/01/2017).

[19] J. Blitz and G. Simpson, *Ultrasonic Methods of Non-destructive Testing*. Chapman & Hall, 1996.

[20] C.-P. Chiou, F. J. Margetan, and J. H. Rose, "Ultrasonic detection of cracks below bolts in aircraft skins," *Review of Progress in Quantitative Nondestructive Evaluation*, vol. 10B, pp. 1891–1898, 1991.

[21] J. P. Sargent, "Ultrasonic imaging of cracks around fastener holes," *Insight*, vol. 39, no. 11, pp. 790–794, 1997.

[22] A. McNab and M. Campbell, "Ultrasonic phased arrays for nondestructive testing," *NDT International*, vol. 20, no. 6, pp. 333–337, 1987.

[23] S. C. Wooh and Y. Shi, "Optimum beam steering of linear phased arrays," *Wave Motion*, vol. 29, no. 3, pp. 245–265, 1999.

[24] J. J. Selman, J. T. Miller, M. D. C. Moles, O. Dupuis, and P. G. Herzog, "Inspection of aircraft fastener holes using a conically shaped multi-element phased array probe," *AIP Conference Proceedings*, vol. 615, no. 1, pp. 886–893, 2002.

[25] D. Bray and R. Stanley, *Nondestructive Evaluation: A Tool in Design, Manufacturing and Service*. Taylor & Francis, 1996.

[26] K. Imielińska, M. Castaings, R. Wojtyra, J. Haras, E. Le Clezio, and B. Hosten, "Air-coupled ultrasonic C-scan technique in impact response testing of carbon fibre and

hybrid: glass, carbon and Kevlar/epoxy composites," *Journal of Materials Processing Technology*, vol. 157-158, pp. 513–522, 2004.

[27] T. Hasiotis, E. Badogiannis, and N. G. Tsouvalis, "Application of ultrasonic C-scan techniques for tracing defects in laminated composite materials," *Journal of Mechanical Engineering*, vol. 57, no. 3, pp. 192–203, 2011.

[28] W. Staszewski, B. Lee, L. Mallet, and F. Scarpa, "Structural health monitoring using scanning laser vibrometry: I. Lamb wave sensing," *Smart Materials and Structures*, vol. 13, no. 2, pp. 251–260, 2004.

[29] T. E. Michaels, J. E. Michaels, B. Mi, and M. Ruzzene, "Damage detection in plate structures using sparse ultrasonic transducer arrays and acoustic wavefield imaging," *AIP Conference Proceedings*, vol. 760, no. 1, pp. 938–945, 2005.

[30] E. B. Flynn, S. Y. Chong, G. J. Jarmer, and J.-R. Lee, "Structural imaging through local wavenumber estimation of guided waves," *NDT & E International*, vol. 59, pp. 1–10, 2013.

[31] J. Takatsubo, H. Miyauchi, H. Tsuda, N. Toyama, K. Urabe, and B. Wang, "Generation laser scanning method for visualizing ultrasonic waves propagating on a 3-D object," *1st International Symposium on Laser Ultrasonics: Science, Technology and Applications*, 2008.

[32] Y. Fukushima, O. Nishizawa, and H. Sato, "A performance study of a laser Doppler vibrometer for measuring waveforms from piezoelectric transducers," *IEEE Transactions on Ultrasonics, Ferroelectrics, and Frequency Control*, vol. 56, no. 7, pp. 1442–1450, 2009.

[33] E. B. Flynn and G. S. Jarmer, "High-speed, non-contact, baseline-free imaging of hidden defects using scanning laser measurements of steady-state ultrasonic vibration," *Structural Health Monitoring*, vol. 1, pp. 1186–1193, 2013.

[34] A. J. Dawson, J. E. Michaels, R. M. Levine, X. Chen, and T. E. Michaels, "Acquisition and analysis of angle-beam wavefield data," *AIP Conference Proceedings*, vol. 1581, no. 1, pp. 1716–1723, 2014.

[35] T. E. Michaels and J. E. Michaels, "Application of acoustic wavefield imaging to non-contact ultrasonic inspection of bonded components," *AIP Conference Proceedings*, vol. 820, no. 1, pp. 1484–1491, 2006.

[36] J. E. Michaels, "Ultrasonic wavefield imaging: Research tool or emerging NDE method?" *AIP Conference Proceedings*, vol. 1806, pp. 020001(14pp), 2017.

[37] D. Algernon, B. Gräfe, F. Mielentz, B. Köhler, and F. Schubert, "Imaging of the elastic wave propagation in concrete using scanning techniques: Application for impact-echo and ultrasonic echo methods," *Journal of Nondestructive Evaluation*, vol. 7, pp. 83–97, 2008.

[38] M. D. Rogge and C. Leckey, "Local guided wavefield analysis for characterization of delaminations in composites," *AIP Conference Proceedings*, vol. 1511, no. 1, pp. 963–970, 2013.

[39] J. A. Scales and A. E. Malcolm, "Laser characterization of ultrasonic wave propagation in random media," *Physical Review E*, vol. 67, pp. 046618(7pp), 2003.

[40] H. Sohn, D. Dutta, J. Y. Yang, M. DeSimio, S. Olson, and E. Swenson, "Automated detection of delamination and disbond from wavefield images obtained using a scanning laser vibrometer," *Smart Materials and Structures*, vol. 20, pp. 045017(10pp), 2011.

[41] M. D. Rogge and C. Leckey, "Characterization of impact damage in composite laminates using guided wavefield imaging and local wavenumber analysis," *Ultrasonics*, vol. 53, pp. 1217–1226, 2013.

[42] Y.-K. An, B. Park, and H. Sohn, "Complete noncontact laser ultrasonic imaging for automated crack visualization in a plate," *Smart Materials and Structures*, vol. 22, pp. 025022(10pp), 2013.

[43] T. E. Michaels, J. E. Michaels, and M. Ruzzene, "Detection and sizing of subsurface impedance discontinuities using acoustic wavefield imaging," *Proceedings of the 8^{th} International Workshop on Structural Health Monitoring*, pp. 2215–2222, 2011.

[44] H. Sohn, D. Dutta, J. Yang, H. Park, M. DeSimio, S. Olson, and E. Swenson, "Delamination detection in composites through guided wave field image processing," *Composites Science and Technology*, vol. 71, no. 9, pp. 1250–1256, 2011.

[45] Z. Tian, L. Yu, C. Leckey, and J. Seebo, "Guided wave imaging for detection and evaluation of impact-induced delamination in composites," *Smart Materials and Structures*, vol. 24, pp. 105019(13pp), 2015.

[46] T. E. Michaels and J. E. Michaels, "Monitoring and characterizing corrosion in aluminum using Lamb waves and attached sensors," *Proceedings of the SPIE*, vol. 6532, pp. 65321G(11pp), 2007.

[47] L. Hörchens, C. Wassink, and H. Haines, "Ultrasound imaging of stress corrosion cracking," *AIP Conference Proceedings*, vol. 1650, no. 1, pp. 891–898, 2015.

[48] M. Ruzzene, "Frequency-wavenumber domain filtering for improved damage visualization," *Smart Materials and Structures*, vol. 16, pp. 2116–2129, 2007.

[49] T. E. Michaels, J. E. Michaels, and M. Ruzzene, "Frequency-wavenumber domain analysis of guided wavefields," *Ultrasonics*, vol. 51, pp. 452–466, 2011.

[50] Z. Tian and L. Yu, "Lamb wave frequency-wavenumber analysis and decomposition," *Journal of Intelligent Material Systems and Structures*, vol. 25, no. 9, pp. 1107–1123, 2014.

[51] J. C. Aldrin, M. P. Blodgett, E. A. Lindgren, G. J. Steffes, and J. S. Knopp, "Scattering of obliquely incident shear waves from a cylindrical cavity," *Journal of the Acoustical Society of America*, vol. 129, no. 6, pp. 3661–3675, 2011.

[52] E. Glushkov, N. Glushkova, A. Ekhlakov, and E. Shapar, "An analytically based computer model for surface measurements in ultrasonic crack detection," *Wave Motion*, vol. 43, pp. 458–473, 2006.

[53] R. K. Chapman, "A system model for the ultrasonic inspection of smooth planar cracks," *Journal of Nondestructive Evaluation*, vol. 9, no. 2/3, pp. 197–210, 1990.

[54] M. Darmon, S. Chatillon, S. Mahaut, P. Calmon, L. J. Fradkin, and V. Zernov, "Recent advances in semi-analytical scattering models for NDT simulation," *Journal of Physics: Conference Series*, vol. 269, no. 1, pp. 1–12, 2011.

[55] A. Velichko and P. D. Wilcox, "A generalized approach for efficient finite element modeling of elastodynamic scattering in two and three dimensions," *Journal of the Acoustical Society of America*, vol. 128, no. 3, pp. 1004–1014, 2010.

[56] A. H. Harker, "Numerical modelling of the scattering of elastic waves in plates," *Journal of Nondestructive Evaluation*, vol. 4, no. 2, pp. 89–106, 1984.

[57] R. M. White, "Elastic wave scattering at a cylindrical discontinuity in a solid," *Journal of the Acoustical Society of America*, vol. 30, no. 8, pp. 771–785, 1958.

[58] L. Flax, V. K. Varadan, and V. V. Varadan, "Scattering of an obliquely incident acoustic wave by an infinite cylinder," *Journal of the Acoustical Society of America*, vol. 68, no. 6, pp. 1832–1835, 1980.

[59] A. J. Niklasson and S. K. Datta, "Scattering by an infinite transversely isotropic cylinder in a transversely isotropic medium," *Wave Motion*, vol. 27, pp. 169–185, 1998.

[60] A. Boström and P. Bövik, "Ultrasonic scattering by a side-drilled hole," *International Journal of Solids and Structures*, vol. 40, pp. 3493–3505, 2003.

[61] V. Schmitz, K. J. Langenberg, and S. Chakhlov, "Calculation of high frequency ultrasonic signals for shear wave insonification in solid material," *Ultrasonics*, vol. 42, no. 1, pp. 249–252, 2004.

[62] J. Ye, H. J. Kim, S. J. Song, S. S. Kang, K. Kim, and M. H. Song, "The far-field scattering response of a side drilled hole in single/layered anisotropic media in ultrasonic pulse-echo setup," *Wave Motion*, vol. 48, no. 3, pp. 275–289, 2011.

[63] A. L. Lopez-Sanchez, H. J. Kim, L. W. Schmerr, and A. Sedov, "Measurement models and scattering models for predicting the ultrasonic pulse-echo response from side-drilled holes," *Journal of Nondestructive Evaluation*, vol. 24, no. 3, pp. 83–96, 2005.

[64] D. Placko and T. Kundu, *DPSM for Modeling Engineering Problems*. John Wiley & Sons, Inc., 2006.

[65] S. Das, S. Banerjee, and T. Kundu, "Modeling of elastic wave scattering by a hole in a half-space," *the 15th International Symposium on: Smart Structures and Materials & Nondestructive Evaluation and Health Monitoring*, vol. 6935, pp. 69350K(12pp), 2008.

[66] S. Das, S. Banerjee, and T. Kundu, "Elastic wave scattering in a solid half-space with a circular cylindrical hole using the Distributed Point Source Method," *International Journal of Solids and Structures*, vol. 45, pp. 4498–4508, 2008.

[67] K. Harumi and M. Uchida, "Computer simulation of ultrasonics and its applications," *Journal of Nondestructive Evaluation*, vol. 9, pp. 81–99, 1990.

[68] P. Fellinger, R. Marklein, K.J. Langenberg, and S. Klaholz, "Numerical modeling of elastic wave propagation and scattering with, EFIT−elastodynamic finite integration technique," *Wave Motion*, vol. 21, pp. 47–66, 1995.

[69] J. Zhang, B. W. Drinkwater, and P. D. Wilcox, "Defect characterization using an ultrasonic array to measure the scattering coefficient matrix," *IEEE Transactions on Ultrasonics, Ferroelectrics and Frequency Control*, vol. 55, no. 10, pp. 2254–2265, 2008.

[70] J. Zhang, B. W. Drinkwater, and P. D. Wilcox, "The use of ultrasonic arrays to characterize crack-like defects," *Journal of Nondestructive Evaluation*, vol. 29, no. 4, pp. 222–232, 2010.

[71] C. Travaglini, C. Bescond, D. R. Franca, S. E. Kruger, M. Viens, and P. Bélanger, "Scattering of high order guided wave modes around a through-thickness circular hole," *AIP Conference Proceedings*, vol. 1706, pp. 030017(7pp), 2016.

[72] O. Diligent, T. Grahn, A. Bostrom, P. Cawley, and M. Lowe, "The low-frequency reflection and scattering of the S_0 Lamb mode from a circular through-thickness hole in a plate: Finite element, analytical and experimental studies," *Journal of the Acoustical Society of America*, vol. 112, no. 6, pp. 2589–2601, 2002.

[73] J. C. Aldrin and J. S. Knopp, "Modeling and simulation for nondestructive testing with applications to aerospace structures," *Materials Evaluation*, vol. 66, no. 1, pp. 53–59, 2008.

[74] D. A. Mendelsohn, J. D. Achenbach, and L. M. Keer, "Scattering of elastic waves by a surface-breaking crack," *Wave Motion*, vol. 2, pp. 277–292, 1980.

[75] J. D. Achenbach and A. N. Norris, "Interference of corner reflected and edge diffracted signals for a surface-breaking crack," *Journal of the Acoustical Society of America*, vol. 70, no. 1, pp. 165–171, 1981.

[76] J. D. Achenbach, A. K. Garutesen, and D. A. Mendelsohn, "Ray analysis of surface-wave interaction with an edge crack," *IEEE Transactions on Sonics & Ultrasonics*, vol. SU-27, no. 3, pp. 124–129, 1980.

[77] Y. C. Angel and J. D. Achenbach, "Reflection and transmission of obliquely incident Rayleigh waves by a surface-breaking crack," *Journal of the Acoustic Society America*, vol. 75, pp. 313–319, 1984.

[78] Ch. Zhang and J. D. Achenbach, "Scattering of body waves by an inclined surface-breaking crack," *Ultrasonics*, vol. 26, pp. 132–138, 1988.

[79] C. L. Scandrett and J. D. Achenbach, "Time-domain finite difference calculations for interaction of an ultrasonic wave with a surface-breaking crack," *Wave Motion*, vol. 9, pp. 171–190, 1987.

[80] S. K. Datta and A. H. Shah, "Ultrasonic scattering by planar and non-planar cracks," *Review of Progress in Quantitative Nondestructive Evaluation*, vol. 6A, pp. 69–78, 1987.

[81] M. V. Felice, A. Velichko, and P. D. Wilcox, "Accurate depth measurement of small surface-breaking cracks using an ultrasonic array post-processing technique," *NDT & E International*, vol. 68, pp. 105–112, 2014.

[82] M. Silk, "The transfer of ultrasonic energy in the diffraction technique for crack sizing," *Ultrasonics*, vol. 17, no. 3, pp. 113–121, 1979.

[83] F. A. Ravenscroft, K. Newton, and C. B. Scruby, "Diffraction of ultrasound by cracks: Comparison of experiment and theory," *Ultrasonics*, vol. 29, no. 1, pp. 29–37, 1991.

[84] L. Adler and J. D. Achenbach, "Elastic wave diffraction by elliptical cracks: Theory and experiment," *Journal of Nondestructive Evaluation*, vol. 1, pp. 87–99, 1980.

[85] J. Zhang, B. W. Drinkwater, and P. D. Wilcox, "Longitudinal wave scattering from rough crack-like defects," *IEEE Transactions on Ultrasonics, Ferroelectrics and Frequency Control*, vol. 58, no. 10, pp. 2171–2180, 2011.

[86] P. Fromme and C. Rouge, "Directivity of guided ultrasonic wave scattering at notches and cracks," *Journal of Physics: Conference Series*, vol. 269, pp. 012018(11pp), 2011.

[87] A. H. Shah, K. C. Wong, and S. K. Datta, "Surface displacements due to elastic wave scattering by buried planar and non-planar cracks," *Wave Motion*, vol. 7, pp. 319–333, 1985.

[88] Y. Lu, L. Ye, Z. Su, and C. Yang, "Quantitative assessment of through-thickness crack size based on Lamb wave scattering in aluminum plates," *NDT & E International*, vol. 41, pp. 59–68, 2008.

[89] Z. Chang and A. Mal, "Scattering of Lamb waves from a rivet hole with edge cracks," *Mechanics of Materials*, vol. 31, no. 3, pp. 197–204, 1999.

[90] F. Shi, W. Choi, E. A. Skelton, M. J. S. Lowe, and R. V. Craster, "A time-domain finite element boundary integration method for ultrasonic nondestructive evaluation," *IEEE Transactions on Ultrasonics, Ferroelectrics, and Frequency Control*, vol. 61, no. 12, pp. 2054–2066, 2014.

[91] M. Darmon, V. Dorval, A. Kamta Djakou, L. Fradkin, and S. Chatillon, "A system model for ultrasonic NDT based on the physical theory of diffraction (PTD)," *Ultrasonics*, vol. 64, pp. 115–127, 2016.

[92] A. J. Dawson, *Acquisition and Analysis of Ultrasonic Wavefield Data to Characterize Angle-Beam Propagation and Scattering in Plates*. Ph.D. Thesis, Georgia Institute of Technology, 2015.

[93] J. W. Kummer, *Signal Processing Methods to Quantify Scattering of Angle-Beam Shear Waves from Through-Holes in Plates*. M. S. Thesis, Georgia Institute of Technology, 2015.

[94] C. T. Maki, *Quantification of Ultrasonic Shear Wave Scattering from an Element of a Compound Scatterer in a Bonded Plate via Wavefield Imaging*. M. S. Thesis, Georgia Institute of Technology, 2017.

[95] J. E. Michaels, S. J. Lee, A. J. Crawford, and P. D. Wilcox, "Chirp excitation of ultrasonic guided waves," *Ultrasonics*, vol. 53, pp. 265–270, 2013.

[96] F. J. Harris, "On the use of windows for harmonic analysis with the discrete Fourier transform," *Proceedings of the IEEE*, vol. 66, pp. 51–83, 1978.

[97] A. J. Dawson, J. E. Michaels, and T. E. Michaels, "Isolation of ultrasonic scattering by wavefield baseline subtraction," *Mechanical Systems and Signal Processing*, vol. 70-71, pp. 891–903, 2016.

[98] A. J. Dawson, J. E. Michaels, J. W. Kummer, and T. E. Michaels, "Quantification of shear wave scattering from far-surface defects via ultrasonic wavefield measurements," *IEEE Transactions on Ultrasonics, Ferroelectrics, and Frequency Control*, vol. 64, no. 3, pp. 590–601, 2017.

[99] H. Jeong and L. W. Schmerr, "Ultrasonic transducer fields modeled with a modular multi-Gaussian beam and application to a contact angle beam testing," *Research in Nondestructive Evaluation*, vol. 19, no. 2, pp. 87–103, 2008.

[100] H.-J. Kim, J.-S. Park, S.-J. Song, and L. W. Schmeer, Jr., "Modeling angle beam ultrasonic testing using multi-Gaussian beams," *Journal of Nondestructive Evaluation*, vol. 23, no. 3, pp. 81–93, 2004.

[101] V. Kommareddy, J. J. Peters, V. Dayal, and D. K. Hsu, "Air-coupled ultrasonic measurements in composites," *AIP Conference Proceedings*, vol. 700, pp. 859–866, 2004.